UVSOR ACTIVITY REPORT 2003

UVSOR II
since 2003

UVSOR Facility
Institute for Molecular Science
National Institutes of Natural Sciences

UVSOR

ACTIVITY REPORT

2003

edited by

A. Mochihashi, H. Hagiwara, T. Ito

Preface

On December 2, 2003, we celebrated the twentieth anniversary of the UVSOR facility. It is a great pleasure to publish this new series of the UVSOR Activity Report at the beginning of the third decade from the first light observation in November 10, 1983. This volume describes the research activities at the UVSOR facility in the Institute for Molecular Science (IMS) in FY2003. This is also the first report by use of the UVSOR-II ring with eight straight sections, which was upgraded in the spring of 2003. We hope we will be able to have a daily operational mode at the minimum emittance around 27 nmrad from the UVSOR-II ring after the replacement of the main RF cavity in the winter of 2004.

In April 2004, our organization has been changed. The Okazaki National Research Institutes involving IMS, NIBB (National Institute for Basic Biology), and NIPS (National Institute for Physiological Sciences) were disorganized in March. IMS now belongs to a new organization, National Institutes of Natural Sciences (NINS) together with NAO (National Astronomical Observatory) and NIFS (National Institute for Fusion Science) in additional to NIBB and NIPS. Director General of IMS is now Prof. Hiroki Nakamura. According to a master plan of the IMS organization, we have started to strengthen the organization of the UVSOR facility. We have gotten a new position of full professor of the accelerator division. Assoc. Prof. Dr. Masahiro Katoh was promoted to this professor in January 2004. In October 2003, Dr. Yasumasa Hikosaka joined the photochemistry division as research associate from Photon Factory.

We lost an excellent technical associate, Mr. Osamu Matsudo at the age of 53, on December 26, 2003 after long medical treatment. His first job here was the design work for proposal of the UVSOR facility and he had been a walking dictionary about the UVSOR facility. I would like to pay my deepest and last respects to him together with all of the UVSOR users and staff members since 1980.

May, 2004

Nobuhiro Kosugi
Director of UVSOR

Memories of
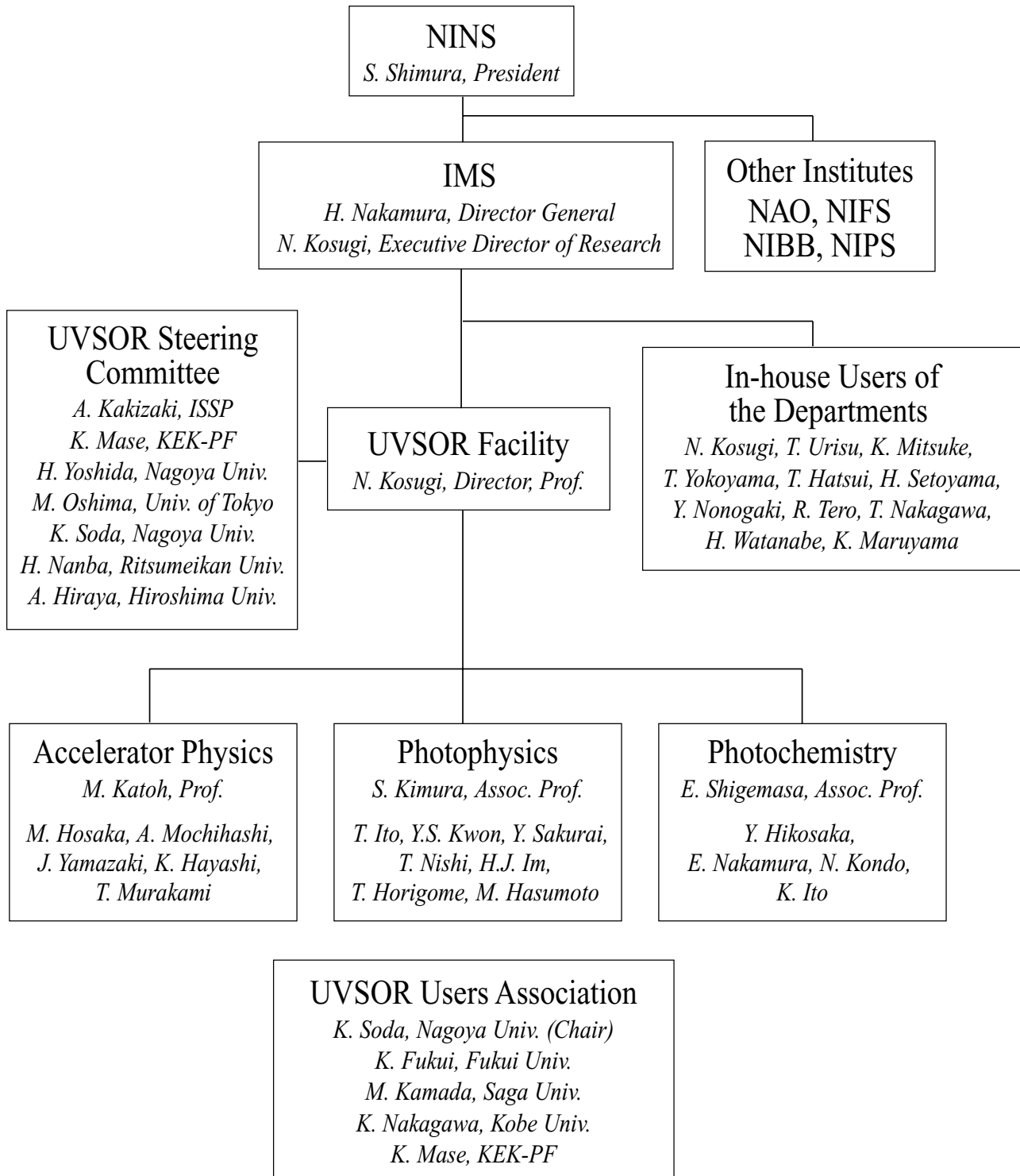# Mr. Osamu Matsudo (1950-2003)

(Center) Mr. Osamu Matsudo, UVSOR chief engineer, with (right) Mr. Eiken Nakamura, unit chief engineer at BL8A in the UVSOR facility.

   Mr. Osamu Matsudo was one of the pioneers of the UVSOR facility. As soon as he arrived at his position in the Institute for Molecular Science in 1980, he started to work for construction of the UVSOR facility. After the UVSOR was born, he devoted himself to upgrade and develop various kind of experimental systems, and moreover, he always worked with his devotion to support of user's experiments and maintainance of equipment for the experimental instrumentation. 'If you have troubled, call Matsudo-san' - most of the UVSOR users have been supported by his appropriate advice, tolerance and smile.

   Not only he was a very skillful technician but also good at drawing. He often selected beautiful nature and flowers as a motif of his drawings. Now we can see his fruitful imagination not only in his impressive drawings but also in all of the experimental instrumentation that he designed and made.

   We all miss his smile, open-minded attitude and pioneering spirit.

UVSOR Organization   April 2004

NINS
S. Shimura, President

IMS
H. Nakamura, Director General
N. Kosugi, Executive Director of Research

Other Institutes
NAO, NIFS
NIBB, NIPS

UVSOR Steering Committee
A. Kakizaki, ISSP
K. Mase, KEK-PF
H. Yoshida, Nagoya Univ.
M. Oshima, Univ. of Tokyo
K. Soda, Nagoya Univ.
H. Nanba, Ritsumeikan Univ.
A. Hiraya, Hiroshima Univ.

UVSOR Facility
N. Kosugi, Director, Prof.

In-house Users of the Departments
N. Kosugi, T. Urisu, K. Mitsuke,
T. Yokoyama, T. Hatsui, H. Setoyama,
Y. Nonogaki, R. Tero, T. Nakagawa,
H. Watanabe, K. Maruyama

Accelerator Physics
M. Katoh, Prof.

M. Hosaka, A. Mochihashi,
J. Yamazaki, K. Hayashi,
T. Murakami

Photophysics
S. Kimura, Assoc. Prof.

T. Ito, Y.S. Kwon, Y. Sakurai,
T. Nishi, H.J. Im,
T. Horigome, M. Hasumoto

Photochemistry
E. Shigemasa, Assoc. Prof.

Y. Hikosaka,
E. Nakamura, N. Kondo,
K. Ito

UVSOR Users Association
K. Soda, Nagoya Univ. (Chair)
K. Fukui, Fukui Univ.
M. Kamada, Saga Univ.
K. Nakagawa, Kobe Univ.
K. Mase, KEK-PF

ORGANIZATION STAFF

1

UVSOR Facility Staff List (2003)

Director

KOSUGI, Nobuhiro	Professor	kosugi@ims.ac.jp

Light Source Division (Accelerator Physics)

KATOH, Masahiro	Professor	mkatoh@ims.ac.jp
HOSAKA, Masahito	Research Associate	hosaka@ims.ac.jp
MOCHIHASHI, Akira	Research Associate	mochi@ims.ac.jp
YAMAZAKI, Jun-ichiro	Unit Chief Enginner	yamazaki@ims.ac.jp
HAYASHI, Kenji	Engineer	h-kenji@ims.ac.jp
MURAKAMI, Takayuki	Supporting Engineer	tmurakami@ims.ac.jp

Beam Line Division (Photochemistry, Photophysics)

SHIGEMASA, Eiji	Associate Professor	shigemasa@ims.ac.jp
KIMURA, Shin-ichi	Associate Professor	kimura@ims.ac.jp
ITO, Takahiro	Research Associate	tito@ims.ac.jp (Apr. 2003~)
HIKOSAKA, Yasumasa	Research Associate	hikosaka@ims.ac.jp (Oct. 2003~)
MATSUDO, Osamu	Section Chief Engineer	matsudo@ims.ac.jp (~Dec. 2003)
HORIGOME, Toshio	Section Chief Engineer	horigome@ims.ac.jp
HASUMOTO, Masami	Unit Chief Engineer	hasumoto@ims.ac.jp
NAKAMURA, Eiken	Unit Chief Engineer	eiken@ims.ac.jp
KONDO, Naonori	Engineer	nkondo@ims.ac.jp
MATSUO, Suekichi	Supporting Engineer	matsuo@ims.ac.jp (~Mar. 2004)
KAMIMOTO, Bun-ichi	Supporting Engineer	kamimoto@ims.ac.jp (~Sep. 2003)

Guest Researcher (Photochemistry, Photophysics)

ITO, Kenji	KEK-PF	(Apr. 2003~)
KWON, Yong-seung	Sungkyunkwan Univ.	(Sep. 2003~)

The Graduate University for Advanced Studies (Photophysics)

NISHI, Tatsuhiko	Student	tnishi@ims.ac.jp
IM, Hojun	Student	hojun@ims.ac.jp (Oct. 2003~)

Secretary

HAGIWARA, Hisayo		hagiwara@ims.ac.jp
ONITAKE, Naoko		onitake@ims.ac.jp

ORGANIZATION STAFF

UVSOR Steering Committee (April 2003 ~ March 2004)

KOSUGI, Nobuhiro	UVSOR, IMS	Chairperson
KIMURA, Shin-ichi	UVSOR, IMS	
KATOH, Masahiro	UVSOR, IMS	
SHIGEMASA, Eiji	UVSOR, IMS	
ITO, Kenji	UVSOR, IMS	(Guest Researcher from KEK-PF)
YOKOYAMA, Toshihiko	IMS	
TSUKUDA, Tatsuya	IMS	
KOBAYASHI, Hayao	IMS	
MITSUKE, Koichiro	IMS	
KINOSHITA, Toyohiko	Univ. of Tokyo	
YAGISHITA, Akira	KEK-PF	
UENO, Nobuo	Chiba Univ.	
OSHIMA, Masaharu	Univ. of Tokyo	
SODA, Kazuo	Nagoya Univ.	
NAMBA, Hidetoshi	Ritsumeikan Univ.	
HIRAYA, Atsuya	Hiroshima Univ.	

Joint Studies (Fiscal Year 2003)

Special Projects	3
Cooperative Research Projects	19
Use-of-UVSOR Projects	129
Machine Time Weeks for Users	27
Workshop	1
	(in 20th anniversary)

ORGANIZATION STAFF

3

Light Source in 2003

Masahiro KATOH

UVSOR Facility, Institute for Molecular Science

1. Construction and Commissioning of UVSOR-II

The original UVSOR (UVSOR-I) had been operated for about 20 years as a national VUV light source in Japan. About 20 beam-lines, including a few infrared ones, were utilized for performing various kinds of experiments in the research field for molecular science. After the 20 years, the accelerator components had become less reliable. With the relatively large emittance (160 nm-rad) and only two undulators, it seemed difficult for the facility to survive in the next decade as a national light source, and thus, became our proposal for an upgrade plan in 2000 [1]. The magnetic lattice of the storage ring would be modified to have small emittance of 27 nm-rad. The ring would have eight straight sections, six of which would be available for insertion devices. The circumference would be kept same, and modification of the existing beam-lines would be unnecessary. The super-conducting wiggler and one of two undulators, both old and partly malfunctioned, would be replaced with two short period undulators of in-vacuum type. New beam-lines would be constructed for these undulators. Some components of the injector would be replaced.

The configuration of the upgraded storage ring, UVSOR-II, is illustrated in Figure 1. The quadrupole triplets between the bending magnets are replaced with two quadrupole doublets and a short straight section 1.5 m long. To save space, sextupole magnets are integrated in the quadrupole magnets. The doublets on the both sides of the longer straight sections are also replaced. As a result, the lengths of the sections are increased from 3 m to 4 m.

The optical functions of UVSOR-I and II are compared in Figure 2. The horizontal betatron function and the dispersion function of UVSOR-II have their minima in the bending magnets, and thus a small emittance of 27 nm-rad is realized. The vertical betatron function is small at all the straight sections, which enables insertion devices with narrow pole gaps to be installed. The lattice has a large dynamic aperture in a wide range of the betatron tunes. The parameters of UVSOR-II are summarized in Table 1.

Fortunately, in the fiscal year 2002, the project was funded and all the necessary accelerator components were constructed, such as 32 multi-pole magnets, 16 vertical steering magnets, their power supplies, their girders, their beam ducts, vacuum pumps, an in-vacuum undulator, an electron gun, a klystron pulse modulator and so on. The control systems for the magnets and the undulator were also constructed.

In the end of March 2003, the operation of UVSOR-I was terminated and the reconstruction work was begun. After the old components were removed, the new magnets and their girders were installed. Then, the beam ducts and the vacuum pumps were installed. The magnet power supplies, the new undulator and the new components for the injector were also installed in parallel. All the installations were completed at the end of June. All the vacuum components of the storage ring were baked in the first week of July.
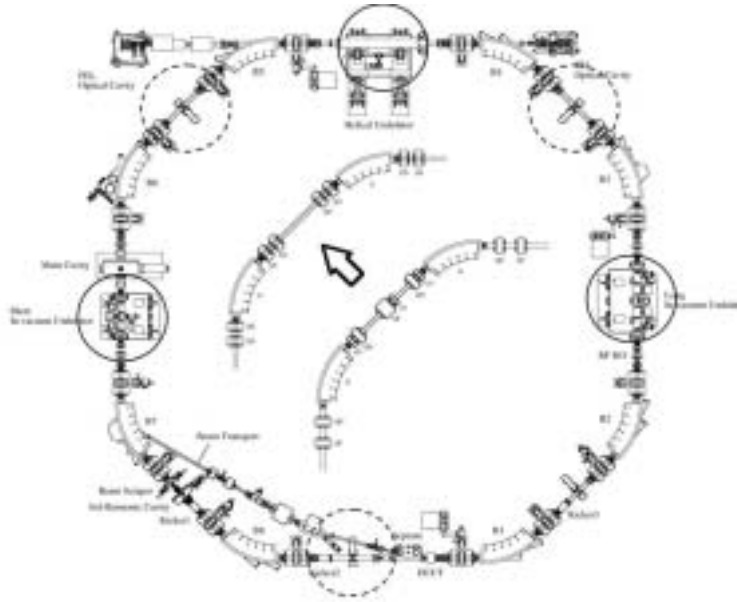
FIGURE 1. Configuration of UVSOR-II Storage Ring. Three undulators indicated by solid circles are in operation. Three short straight sections indicated by dashed circles are reserved for future insertion devices.
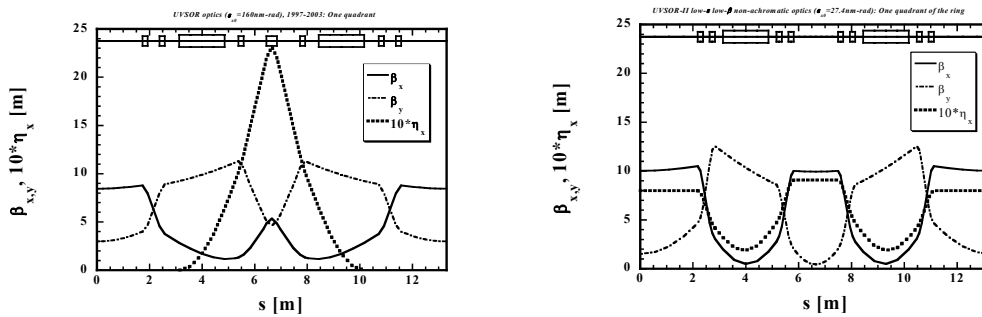

FIGURE 2. Electron Beam Optics of UVSOR-I (left) and II (right). One quadrant of the ring is shown.

TABLE 1. Parameters of UVSOR-I and II

	UVSOR-I	UVSOR-II
Electron Energy	750 MeV	750 MeV
Circumference	53.2 m	53.2 m
Number of Super-periods	4	4
Straight Sections	3 m x 4	4 m x 4, 1.5 m x 4
Emittance	165 nm-rad	27.4 nm-rad
Energy Spread	4.2×10^{-4}	4.2×10^{-4}
Betatron Tunes (ν_x, ν_y)	(3.16, 1.44)	(3.75, 3.20)
Natural Chromaticity (ξ_x, ξ_y)	(-3.4, -2.5)	(-8.1, -7.3)
Momentum Compaction Factor	0.026	0.028
XY Coupling (presumed)	10%	10%

FIGURE 3. UVSOR just after removing old accelerator components
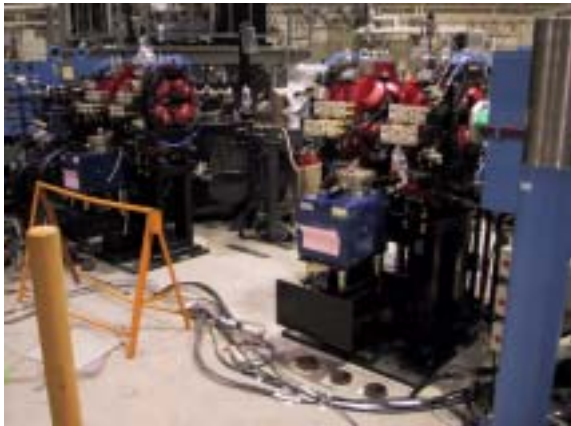
FIGURE 4. New multi-pole magnets and their girders just after the installation
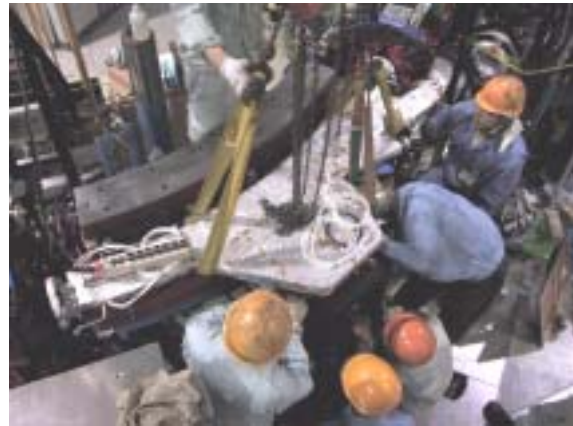
FIGURE 5. Installation of the beam duct for the bending magnet B07

FIGURE 6. Installation of the beam duct for the multi-pole magnets

FIGURE 7. Alignment of the accelerator components

FIGURE 8. New In-vacuum undulator being transported in the storage ring room

FIGURE 9. A part of the storage ring (between B02 and B04) just after finishing the installation. New in-vacuum undulator between B02 and B03, and a short free space reserved for future undulator can be seen.

FIGURE 10. New control system for the magnets

FIGURE 11. New controllers and power supplies for vacuum pumps and gauges

FIGURE 12. New magnet power supplies
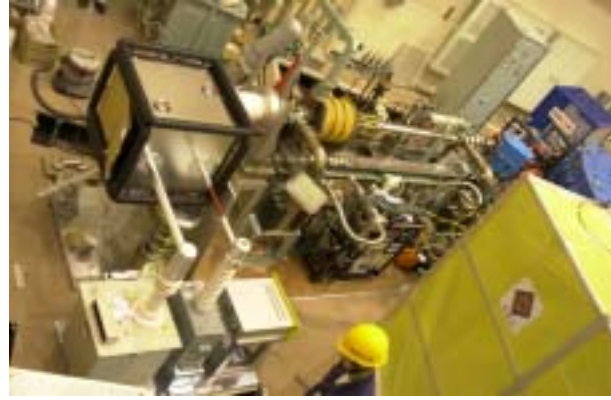
FIGURE 13. Installation of the new electron gun for the injection linac

FIGURE 14. UVSOR-II just after finishing the installation

We started the commissioning of the injector during the first week of July. Within two days, we were able to accelerate the electron beam up to 600 MeV, the normal injection energy into the storage ring. The injection efficiency into the booster-synchrotron from the linac was much improved. The beam intensity at the exit of the synchrotron was larger by a factor of 2 than before the upgrade.

In the second week of July, we started to inject the beam into the storage ring. We started the commissioning using the same betatron tunes and nearly the same optical functions as we had prior to the upgrade. On 14th July, we succeeded in storing the beam in the storage ring. One week later, the maximum beam current reached 500 mA. On 30th July, we succeeded in operating the ring in the low emittance mode of 27 nm-rad. There was no difficulty in injection and storage. Preliminary measurements on the optical functions and the beam sizes suggested that the design goal of 27 nm-rad was likely achieved. The beam profile in the low emittance mode (27nm-rad) and the high emittance mode (190nm-rad) are compared in Fig. 15. More precise measurement is under preparation.
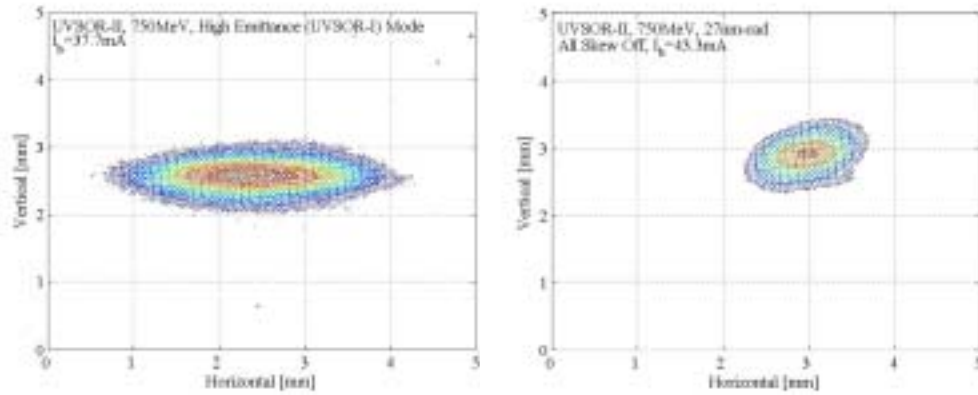
FIGURE 15. Beam Profile observed at the bending B03 in the high emittance (190nm-rad) mode (left) and the low emittance (27nm-rad) mode (right).

In August, the machine tuning and the vacuum conditioning were continued in parallel with the conditioning of the beam-lines. Since almost two thirds of the beam ducts in the storage ring were replaced, the pressure rise due to the irradiation of synchrotron radiation was very large. However, as the integrated beam current increased, the beam lifetime recovered as shown in Figure 16.
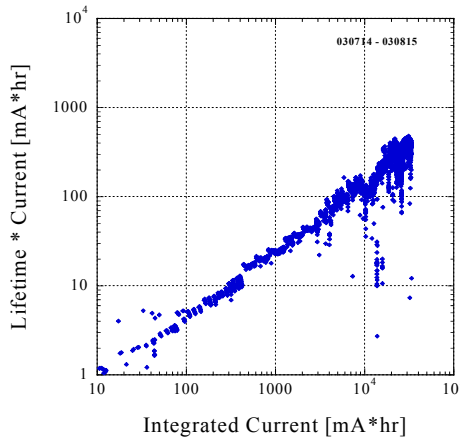
FIGURE 16. Recovery of the beam lifetime during the first one month. The lifetime multiplied by the beam current is illustrated versus time-integrated beam current. The normal lifetime of UVSOR-I was about 1000-1500 mA

2. Operation of UVSOR-II

After the conditionings of the machine and the beam-lines in July and August, the operation for the users was re-started in the first week of September. A moderately small emittance of 60 nm-rad was chosen for the initial stage of the users operation as considering the short Touschek lifetime. After the RF cavity is reinforced, users operation with the smaller emittance of 27 nm-rad will be started.

From the first week of September to the last week of March, 2004, the machine has been operated for users. The operation was stopped only for two weeks around the New Years Day. Normally, from Tuesday to Friday, the machine is operated for users. The injection is twice a day, at 9:00 and 15:00. The initial beam current of each run is 350 mA in multi-bunch condition and about 100 mA in single bunch condition. There was no serious trouble on the machine in the first 7 month operation of UVSOR-II. The monthly statistics of the operation time and the integrated beam current are shown in Figures 17 and 18.
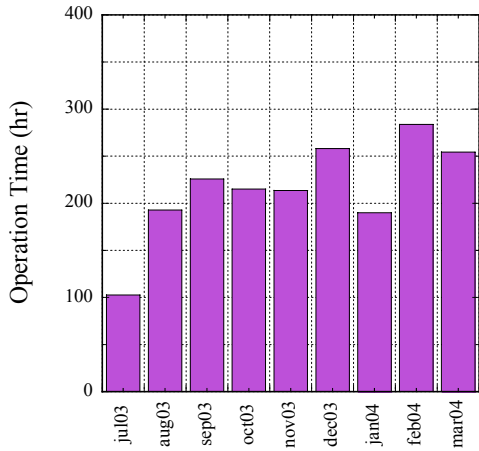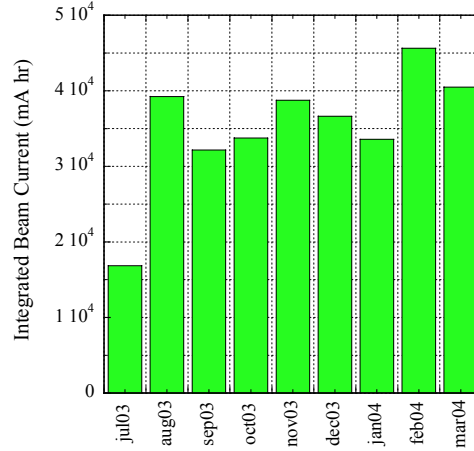
FIGURE 17. Monthly statistics of the operation time

FIGURE 18. Monthly statistics of the integrated beam current

3. Improvements

Second In-vacuum Undulator for BL3U

In parallel with the reconstruction of the storage ring, an in-vacuum undulator was installed at a straight section between the bending magnet B02 and B03, as shown in Figure 19. This undulator provides intense VUV radiation to the BL3U, which was also newly constructed during the reconstruction of the ring. The main parameters of the undulator are shown in the Table 2. The period length is 38 mm and the number of the periods is 50.

The minimum pole gap is 15 mm for the beam optics shown in Figure 2. The minimum gap is a very important parameter which limited the tunability. We made a measurement on the pole gap and the beam lifetime and got an unexpected result. A reduction of the beam lifetime was observed for the pole gap smaller than 20 mm, which was larger than expected. We made various measurements and were convinced that the undulator had some problem. Later, in April 2004, we opened the vacuum chamber and found that a small bolt of a few mm was on the lower pole that came out of the upper pole. After removing the bolt, we could confirm that the pole gap of 15 mm did not affect the lifetime.
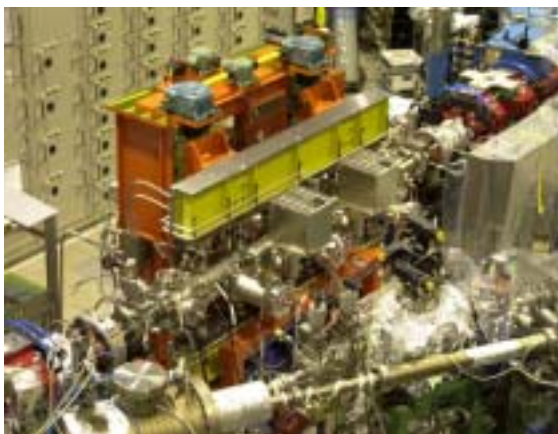

FIGURE 19. In-vacuum undulator for BL3U

TABLE 2. Parameters of Undulator for BL3U

Type	in-vacuum
Polarity	linear
Number of Periods	50
Period Length	38 mm
Pole Length	1.9 m
Max. K Parameter	2.0

11

New Optical Station for Beam Diagnostics

At the bending magnet B03 and B07, there are SR ports for beam diagnostics. New optical station was constructed near B03, inside of the ring. Visible light from B03 is introduced to the station. The beam profile can be monitored by a CCD camera. The beam sizes can be measured precisely by an interferometer. Purity of the RF bucket can be monitored by a PM tube.

4. Researches and Developments

Free Electron Laser

The smaller emittance of UVSOR-II has a great advantage on the free electron laser, especially to oscillate in the shorter wave length region [2]. In November, we re-started the FEL experiment with the re-alignment of the optical cavity. In December 1st, we could oscillate in the visible region. A preliminarily measurement on the FEL gain indicated an increase of the gain due to the smaller emittance.

Design of the new RF cavity

In the fiscal year 2004, the new RF cavity will be constructed. As the result of the design study, main parameters of the new cavity was decided to be as shown in Table 3. With the present RF power source whose maximum output power is 20 kW, the new cavity will produce 150 kV accelerating voltage for the beam current of 500 mA. This will greatly improve the Touschek lifetime as shown in Figure 20. The new cavity will be installed in the ring in April 2005.

TABLE 3. Basic specification of present/planned RF cavity.

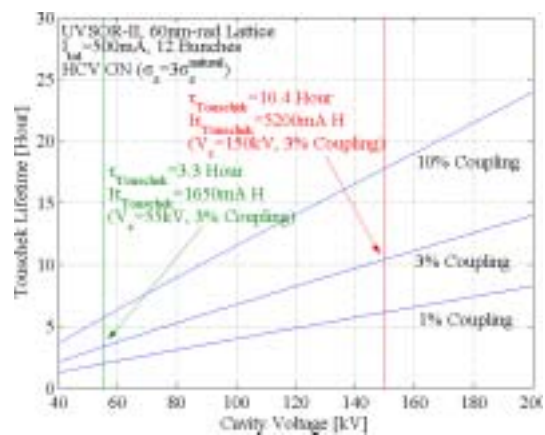|	Present Cavity	Planned Cavity
Frequency	90.1 MHz	90.1 MHz
Cavity voltage	55 kV	150 kV
Shunt impedance	0.5 MΩ	2.2 MΩ
Material	SUS + Cu	Cu (OFHC)
Cells	Re-entrant×1	Re-entrant×1
Coupler	Air-cooled	Water-cooled
Tuner	Plunger×1	Plunger×2

FIGURE 20. Change in Touschek lifetime on the caviti voltage. Green and red lines correspond to the present and planned cavity voltage, respectively.

[1] M. Katoh et al., Nuclear Instruments and Methods in Physics Research A, 467-468 (2001), 68-71

[2] M. Hosaka et al., presented at the 2003 FEL Conference (Tsukuba, 2003)

UVSOR Accelerator Complex 2003

Parameters of UVSOR-II Storage Ring (Upgraded UVSOR)

Energy	750 MeV
Injection Energy	600 MeV
Maximum Stored Current	500 mA (multi bunch)
	100 mA (single bunch)
Natural Emittance	27.4 nm-rad
Circumference	53.2 m
RF Frequency	90.1 MHz
Harmonic Number	16
Bending Radius	2.2 m
Lattice	Extended DBA × 4
Straight Section	(4m × 4) + (1.5m × 4)
RF Voltage	55 kV
Betatron Tune	
Horizontal	3.75
Vertical	3.20
Momentum Compaction	0.028
Natural Chromaticity	
Horizontal	-8.1
Vertical	-7.3
Energy Spread	4.2×10^{-4}
Natural Bunch Length	160 ps

Parameters of Injector

Injection Linear Accelerator

Energy	15 MeV
Length	2.5 m
Frequency	2856 MHz
Accelerating RF Field	$2\pi/3$ Traveling Wave
Klystron Power	1.8 MW
Energy Spread	~ 1.6 MeV
Repetition Rate	2.6 Hz

Booster Synchrotron

Energy	**600 MeV**
Injection Energy	**15 MeV**
Beam Current	**32 mA (uniform filling)**
Circumference	**26.6 m**
RF Frequency	**90.1 MHz**
Harmonic Number	**8**
Bending Radius	**1.8 m**
Lattice	**FODO × 8**
Betatron Tune	
Horizontal	**2.25**
Vertical	**1.25**
Momentum Compaction	**0.138**
Repetition Rate	**2.6 Hz**
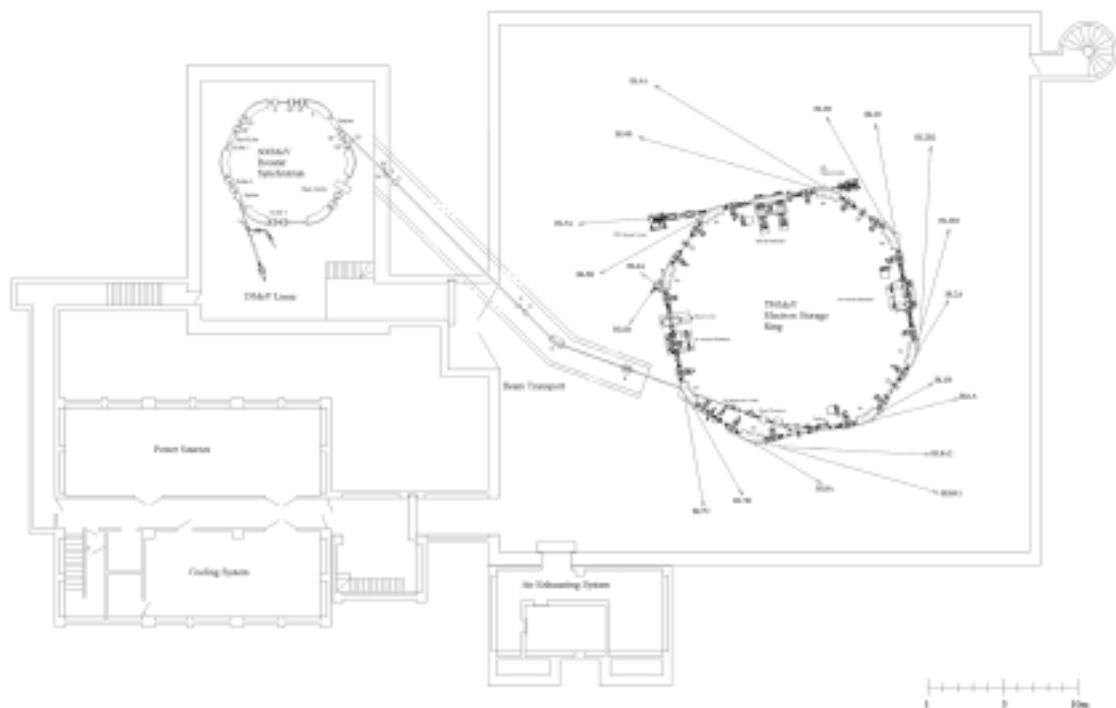
Fig. 1 Accelerator complex in the UVSOR facility.

Electron Beam Optics of UVSOR-II Storage Ring
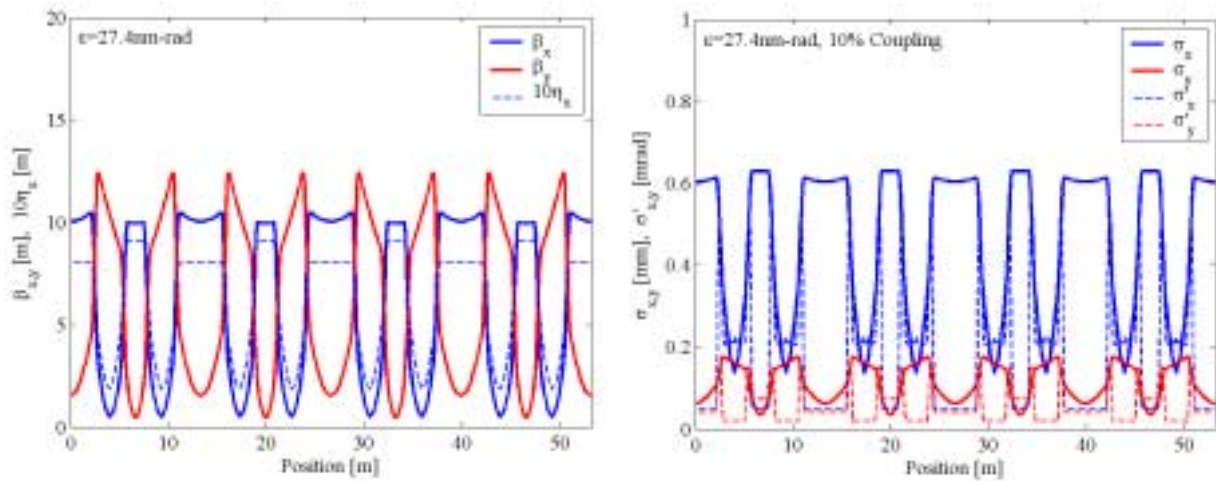
Fig. 2. (Left)Horizontal/vertical betatron functions and dispersion function, and (right) horizontal/vertical electron beam sizes and beam divergences of the UVSOR-II electron storage ring.

Synchrotron Radiation Spectra & Light Source Parameters
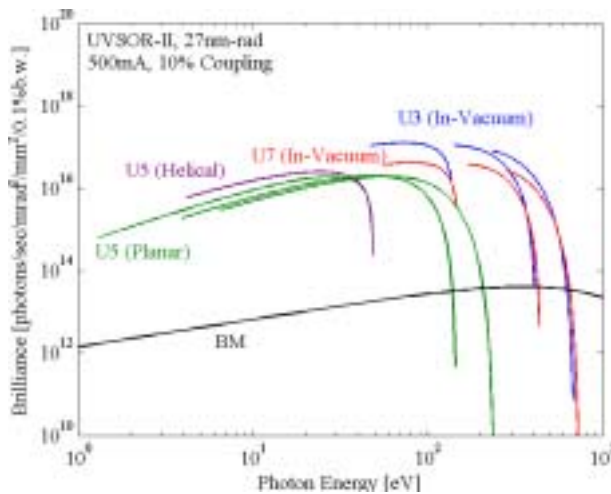
Fig. 3. Brilliances of light sources in UVSOR-II electron storage ring.

Bending Magnets

Bending Radius	2.2 m
Critical Energy	425 eV

BL3U In-vacuum Undulator

Number of Periods	50
Period Length	38mm
Pole Length	1.9 m
Pole Gap	15~40mm
Deflection Parameter	2.0~0.24

BL5U Helical Undulator / Optical Klystron

Number of Periods	21 / 9+9(Opt. Kly.)
Period Length	110mm
Pole Length	23.5mm
Pole Gap	30~150mm
Deflection Parameter	4.6~0.07(Helical)
	8.5~0.15(Linear)

BL7U In-vacuum Undulator

Number of Periods	26
Period Length	36mm
Pole Length	0.94m
Pole Gap	15~40mm
Deflection Parameter	2.0~0.19

Beamlines in 2003

Eiji SHIGEMASA

UVSOR Facility, Institute for Molecular Science

Eight bending magnets and three insertion devices are available for utilizing Synchrotron Radiation at UVSOR. There is a total of sixteen operational beamlines, which are classified into two categories. Eight of them are so-called "Open beamlines", which are open to scientists of universities and research institutes belonging to the government, public organizations, private enterprises and those of foreign countries. The rest of the eight beamlines are so-called "In-house beamlines", and are dedicated to the use of research groups within IMS. We have one soft X-rays station equipped with a double-crystal monochromator, seven extreme ultraviolet and soft X-rays stations with a grazing incidence monochromator, three vacuum ultraviolet stations with a normal incidence monochromator, one infrared (IR) station equipped with Fourier-Transform interferometers, one station with a multi-layer monochromator, and three non-monochromatized stations for irradiation of white-light, as shown in the appended table for all available beamlines at UVSOR.

Discussion with users, concerning the improvements and upgrades of the beamlines at UVSOR, has been continuously held as series of UVSOR workshops. Recently, discussion for the reconstruction and rearrangement of several old beamlines has been initiated, on the basis of the review and evaluation report on the present status of UVSOR in 2000. The upgrade project of the UVSOR storage ring, in which the creation of four new straight sections and the achievement of much smaller emittance (27 nm-rad) were planned, has been approved in the fiscal year of 2002. Keeping pace with this project, a new in-vacuum undulator and monochromator for BL3 and a new high-resolution photoelectron energy analyzer for the end station at BL5U have successfully been installed. Correspondingly, in order to achieve effective utilizations of the straight sections, the operations of two old beamlines, BL2A and BL2B1, have been terminated and all the beamline components and end stations of these beamlines have been completely removed till the end of FY 2003. Parallel to the UVSOR upgrade project, the renewal of the vacuum duct at BL6 was initially scheduled in the spring of 2003, but has been postponed until the regular shutdown in the spring of 2004. In coincidence with this, a so-called magic mirror will be installed as the first mirror for BL6B, to realize the highest intensity in the wavelength range from sub-milli to near IR region all over the world. The front-end part of BL6B will be renewed to make place for BL6A. As a result, we have two vacant lots at BL2A and BL6A to construct novel beamlines. The short straight section between B01 and B02 is planned to utilize for a new RF cavity; BL2A will be a bending-magnet beamline while BL6A is to be an undulator one. Accordingly, the long straight section between B06 and B07, where the in-vacuum undulator of 1-m long for BL7U and the present RF cavity lie, will be available for a new undulator with the length more than 2 m. Further serious discussion toward utilizing the available straight sections most effectively and formulating a basic plan on the beamline construction, will be made in the near future.
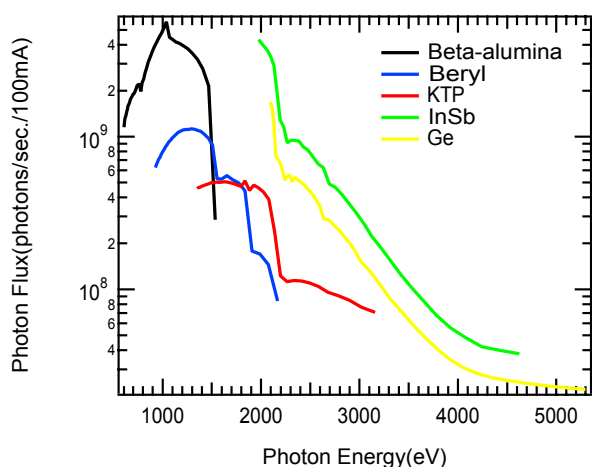
All users are required to refer to the beamline manuals and the UVSOR guidebook (latest revision in 1999), on the occasion of conducting the actual experimental procedures. Those wishing to use the open and in-house beamlines are recommended to contact the stationmaster/supervisor and the representative, respectively. For updated information of UVSOR, http://www.uvsor.ims.ac.jp/.

BL1A

Soft X-Ray Beamline for Photoabsorption Spectroscopy

BL1A is a soft X-ray beamline for photoabsorption spectroscopy. The beamline is equipped with a focusing premirror and a double crystal monochromator [1]. The monochromator serves soft X-rays in the energy region from 585 to 4000 eV by using several kinds of single crystals such as β-Al_2O_3, beryl, KTP ($KTiOPO_4$), quartz, InSb, and Ge. The throughput spectra measured by a Si photodiode (AXUV-100, IRD Inc.) are shown in Fig. 1. Typical energy resolution (E/ΔE) of the monochromator is about 1500 for beryl and InSb. There are no experimental setups specific of this beamline, except for a small vacuum chamber equipped with an electron multiplier (EM) detector. Photoabsorption spectra for powdery samples are usually measured in a total electron yield mode, with the use of the EM detector.

[1] Hiraya at al, *Rev. Sci. Instrum*., 63, 1264 (1992).

Beamline Specifications

Monochromator	Double crystal monochromator
Monochromator crystals: (2d value, energy range)	β-Al_2O_3 (22.53 Å, 585-1609 eV), beryl (15.965 Å, 826-2271 eV), KTP (10.95 Å, 1205-3310 eV), quartz (8.512 Å, 1550-4000 eV), InSb (7.481 Å, 1764-4000 eV), Ge (6.532 Å, 2094-4000 eV)
Resolution	E/ΔE = 1500 for beryl and InSb
Experiments	Photoabsorption spectroscopy

BL1B

Seya-Namioka Monochromator for General Purposes.

BL1B has been constructed to perform various spectroscopic investigations such as absorption, reflectivity, and luminescence in condensed matters.   This beamline consists of a pre-focusing mirror, a 1-m Seya-Namioka type monochromator, and post-focusing mirrors with different focal lengths.   Three gratings of 600, 1200, and 2400 l/mm can cover the wavelength region ranging from 40 to 650 nm ($h\nu = 2 - 30$ eV).   The post mirror with a longer focal length is usually used with an LiF window to separate the vacuum condition of the monochromator from a main experimental station, which make experiments for liquids and bio-specimens possible, while the other is mainly utilized for solid-state spectroscopy.   The output flux from this monochromator is about 10^{10} photons/sec. around 200 nm with 0.1 mm slit openings.   The spectral distributions for two gratings measured by a conventional photomultiplyer are shown in Fig. 1.   A second monochromator (Spex 270M) and a LN-cooled CCD detector (Princeton Inc.) are available for luminescence measurements, together with a liquid helium-flow type cryostat. To perform time-resolved experiments, a TAC system is also available.
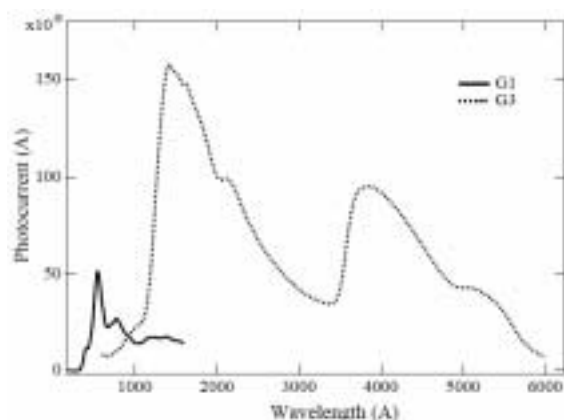
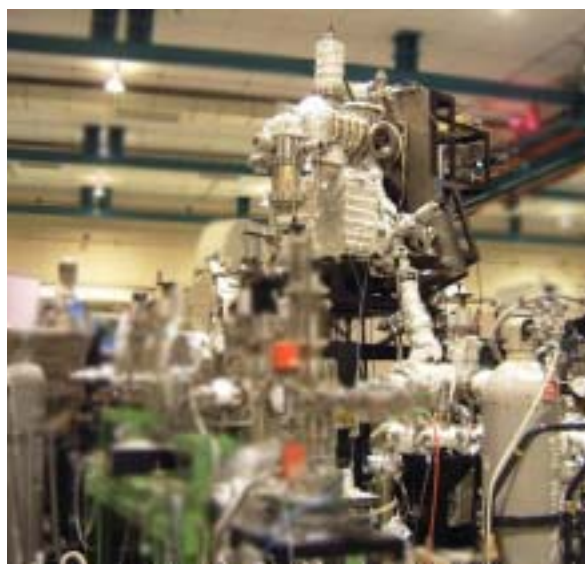

Fig. 1.   Photocurrent at the sample position at BL1B.

Fig. 2.   Photo of BL1B.

Beamline Specifications

Monochromator	1-m Seya-Namioka type
Wavelength Range	40 to 600 nm (2-30 eV)
Resolution	E/ΔE~1000 at 100 nm (10 eV)
Experiment	Absorption, reflection, luminescence spectroscopy for solids

BL2B

Beamline for Gas Phase Photoionization and Reaction Dynamics

This beamline has been developed for the purpose of studying ionization, excitation and decay dynamics involving inner-valence electrons, $2p$ electrons of the third row atoms, and $4d$ electrons of the lanthanides. The monochromator is a spherical grating Dragon-type with 18-m focal length. High throughput (1×10^{10} photons s^{-1}) and high resolution ($E/\Delta E$ = 2000 - 8000) are achieved simultaneously under the condition of the ring current of 100 mA [1]. A second-order light of 7 % is contained at a photon energy of 45.6 eV (G3). The optical system consists of two prefocusing mirrors, an entrance slit, three spherical gratings (G1 - G3), two folding mirrors, a movable exit slit and a refocusing mirror [2]. The monochromator is designed to cover the energy range of 23 - 205 eV with the three gratings: G1 (2400 lines mm^{-1}, R = 18 m) at 80 - 205 eV; G2 (1200 lines mm^{-1}, R = 18 m) at 40 - 100 eV; G3 (2400 lines mm^{-1}, R = 9.25 m) at 23 - 50 eV.

We have been taking photoion yield curves of various fullerenes. Geometrical structures and electronic properties of fullerenes have attracted widespread attention because of their novel structures, novel reactivity, and novel catalytic behaviors as typical nanometer-size materials. However, spectroscopic information is very limited in the extreme UV region, which has been probably due to difficulties in acquiring enough amount of sample. This situation has been rapidly changed in these few years, since the techniques of syntheses, isolation, and purification have been advanced so rapidly that appreciable amount of fullerenes can be readily obtained.

[1] M. Ono *et al.*, *Nucl. Instrum. Meth. Phys. Res. A* **467-468**, 577 (2001).

[2] H. Yoshida and K. Mitsuke, *J. Synchrotron Radiat.* **5,** 774 (1998).
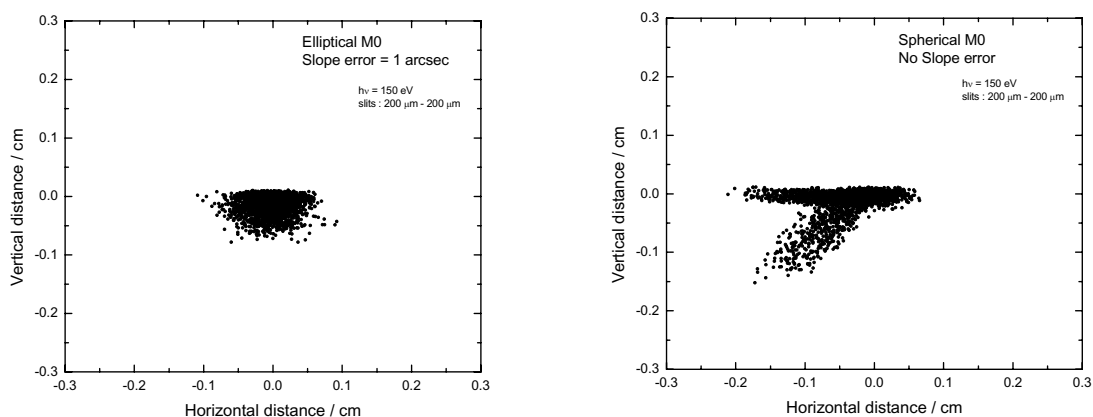

Figure 1. Spot profiles at the sample point. (Left) employing meridional elliptical M0 prefocusing mirror with a slope error of 1 arcsec RMS. (Right) employing spherical M0 mirror without slope error.

Beamline Specifications

Monochromator	18-m spherical grating Dragon-type
Wavelength Range	6 – 55 nm
Resolution	2000-8000
Experiment	Mass spectrom.; Photoelectron spectrosc.

BL3U

Varied-line-spacing Plane Grating Monochromator

for Molecular Soft X-ray Spectroscopy

The beamline BL3U is equipped with an in-vaccum undulator composed of 50 periods of 3.8 cm period length. The emitted photons are monochromatized by the varied-line-spacing plane grating monochromator (VLS-PGM) designed for various spectroscopic investigations in the soft x-ray range including soft x-ray emission studies. Three holographically ruled laminar profile plane gratings are designed to cover the photon energy range from 60 eV to 800 eV. The beamline has two endstations, namely XES setup and Multi-purpose setup. The XES setup is used for soft x-ray emission spectroscopy. The beam is horizontally focused on the exit slit by plane-elliptical mirror in order to produce beam size less than 50 micron. In the Multi-purpose setup, the beam is focused by the toroidal mirror M2. Between the sample position and M2, the differential pumping is placed.
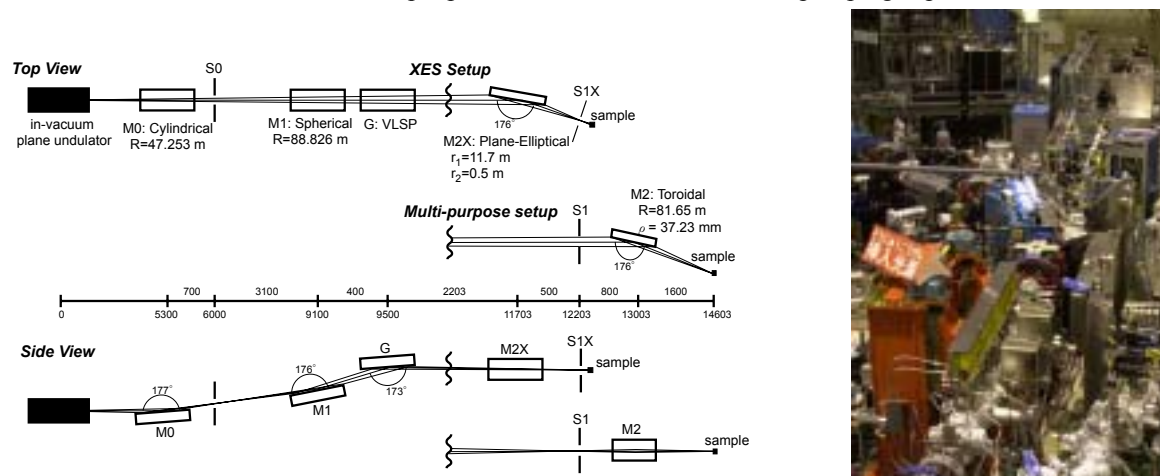
Fig. 1. Schematic layout (left) and the photography (right) of the BL3U. The distances along the beam from the center of the in-vacuum plane undulator are shown in mm. S1X and M2X can be replaced with the other exit slit S1 so that experiments can be carried out at either the XES or multi-purpose endstation. In the XES setup, the sample is placed at 5-10 mm downstream of S1X.

Beamline Specifications

Monochromator	Varied-line-spacing plane grating monochromator
Energy Range	60-800 eV
Resolution	$E/\Delta E > 7000$
Experiment	Soft X-ray spectroscopy (XPS, XES, XAS)

BL3B

Beamline for Gas Phase Photoelectron Spectroscopy

This beam line is devoted to studies of elementary atomic and molecular processes induced by excitation of valence electrons. A monochromator is a vertically dispersed normal incidence type with 3m focal length and 10° angle between the incident and diffracted photon beams. The maximum wavelength resolution of 0.007nm is narrow enough to separate vibrational levels of excited states for various molecules. A main component in an experimental chamber is a spherical sector electrostatic energy analyzer which has been designed and setup for photoelectron spectroscopy. One can perform two-dimensional photoelectron spectroscopy with good resolution (≤ 30meV) in which the photoelectron yield is measured as a function of both photon energy and electron kinetic energy (binding energy). A two-dimensional spectrum, usually represented as a contour plot, contains rich information on photoionization dynamics and properties of superexcited states. A great variety of interesting high-lying states involved in autoionization have been studied (please see the references).

[1] K. Mitsuke *et al.*, *J. Electron Spectrosc. Rel. Phenom.* **79**, 395 (1996).
[2] H. Hattori and K. Mitsuke, *ibid.* **80**, 1 (1996); H. Hattori *et al.*, *J. Chem. Phys.* **106**, 4902 (1997).
[3] Y. Hikosaka *et al.*, *J. Chem. Phys.* **105**, 6367 (1996); *ibid.* **107**, 2950 (1997); *ibid.* **110**, 335 (1999).
[4] K. Mitsuke *et al.*, *J. Electron Spectrosc. Rel. Phenom.* **112**, 137 (2000).
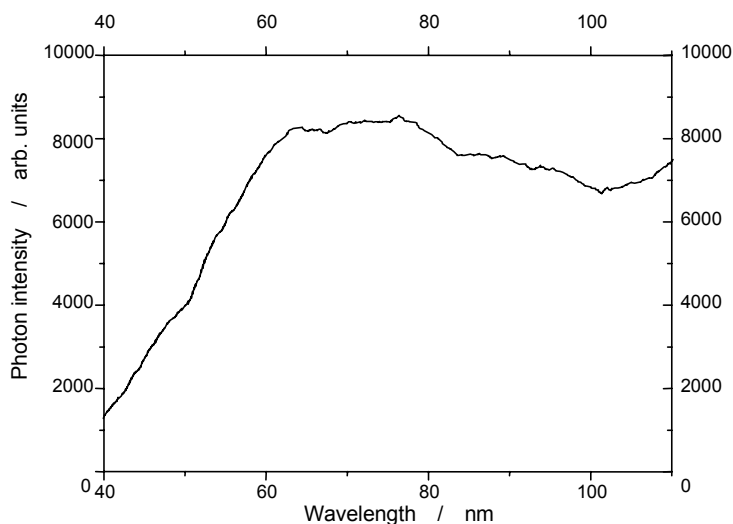[5] Y. Hikosaka and K. Mitsuke, *J. Phys. Chem.* **105**, 8130 (2001); *J. Chem. Phys.* **121**, xxxx (2004).

Fig. 1.   Relative photon intensity at the sample point of BL3B.

Beamline Specifications

Monochromator	3-m normal incidence
Wavelength Range	30 – 200 nm
Resolution	14000 at 100 nm
Experiment	Photoelectron Spectroscopy

CURRENT STATUS OF
LIGHT SOURCE

BL4A2

SR-CVD beam line

This beam line is used for synchrotron radiation chemical vapor deposition (SR-CVD) and photo-etching experiments.   The beam line has no monochromator for high photon flux to irradiate and consists of only two mirrors.   One is for focusing and the other is for branching.   At the beam line, the gas supply and extinction system is equipped for using legally controlled high pressure gasses such as SiH_4, Si_2H_6 and GeH_4.   They are commonly used to CVD of semiconductor crystals.

The SR-CVD and photo-etching chambers are connected to the beam line as shown in Fig. 1.   In those chambers, infrared reflection absorption spectroscopy (IRRAS) system is installed to study the surface photochemistry on Si surfaces modified with various kinds of molecules.
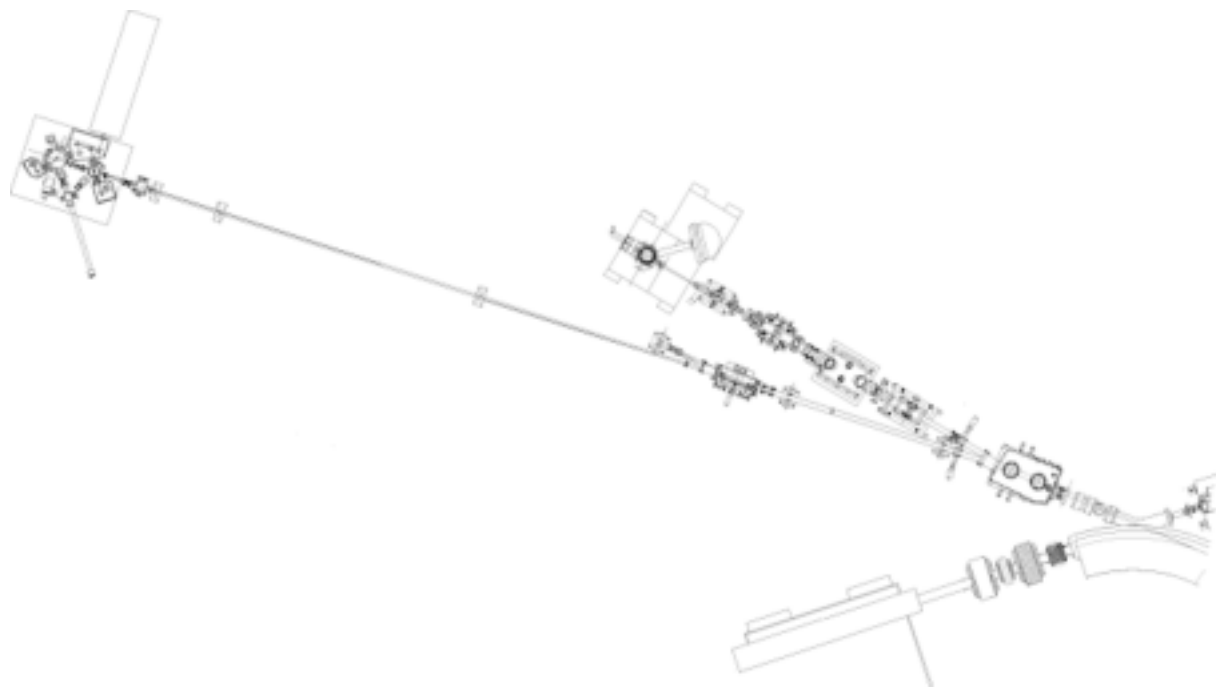
Figure 1   Top view of BL4A2

Specifications

Spectral range: whole range of synchrotron radiation from UVSOR

BL4B

Varied-line-spacing Plane Grating Monochromator for Molecular Soft X-ray Spectroscopy

  The beamline BL4B equipped with a varied-line-spacing plane grating monochromator (VLS-PGM) was constructed for various spectroscopic investigations in a gas phase and/or on solids in the soft X-ray range. Two holographically ruled laminar profile plane gratings with SiO_2 substrates are designed to cover the photon energy range from 80 eV to 800 eV. The gratings with the groove densities of 267 and 800 l/mm cover the spectral ranges of 60-300 and 200-1000 eV, respectively, and are interchangeable without breaking the vacuum. Fig. 1 shows the absolute photon flux for each grating measured by a Si photodiode (IRD Inc.), with the entrance- and exit-slit openings set at 25 and 10 μm, respectively. Under this condition, the corresponding resolving power (E/ΔE) for the 800 l/mm grating is expected to be more than 8000 at 400 eV.
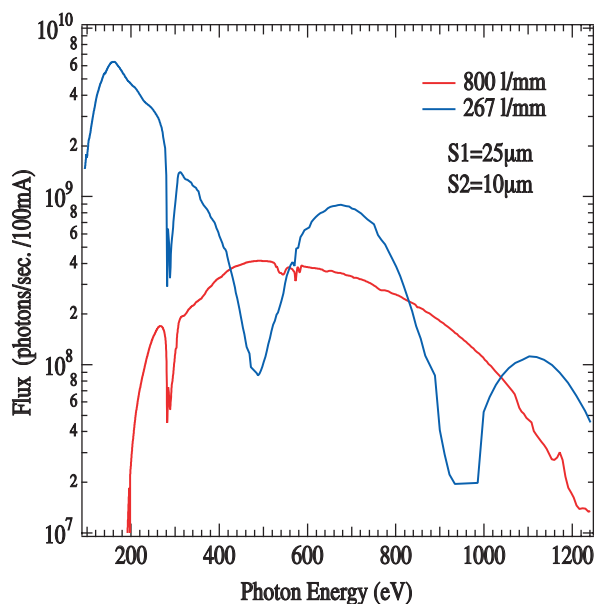
Fig. 1 Throughput from the VLS-PGM monochromator on BL4B.

Fig. 2 A photo of BL4B taken from the upper platform of BL3B.

Beamline Specifications

Monochromator	Varied-line-spacing Plane Grating Monochromator
Energy range	60-1000 eV
Resolution	E/ΔE > 5000 (at maximum)
Experiments	Soft X-ray spectroscopy (mainly, angle-resolved photoion spectroscopy for gaseous targets and photoelectron spectroscopy for gaseous and solid targets)

BL5U

Photoelectron Spectrometer for Solids and Surfaces

This beamline is designed for high-resolution angle-resolved photoemission study for solids and surfaces with the linearly and circularly polarized synchrotron radiation from a helical undulator.   The beamline consists of a Spherical Grating Monochromator with Translational and Rotational Assembly Including a Normal incidence mount (SGM-TRAIN), and a high-resolution angle-resolved photoemission spectrometer.

The SGM-TRAIN is an improved version of a constant-length SGM to aim the following points; (1) wide energy range of 5-250 eV, (2) high resolving power, (3) use of linearly and circularly polarized light, (4) reduction of second-order light, and (5) two driving modes by a computer control.   The second-order light is well suppressed by using laminar profile gratings and combinations of mirrors and gratings.
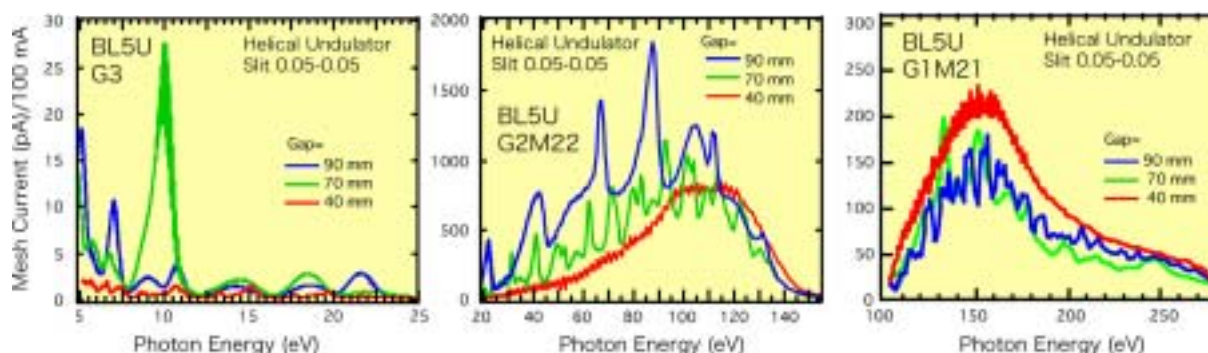
Fig. 1. Throughput from the SGM-TRAIN monochromator on BL5U.

Beamline Specifications

Monochromator	SGM-TRAIN
Energy Range	5-250 eV
Resolution	0.5-80 meV (with slits width of 0.01 mm)
Experiment	ARPES, AIPES, XAS
Flux	1x 10^{12} photons/s for undulator radiation in MPW mode
Main Instruments	Hemispherical photoelectron analyzer (MBS-Toyama, A-1), LEED of reverse type (OMICRON), Liq-He flow qryostat (5 – 400 K)

Fig. 2. High-resolution angle-resolved photoemission apparatus for BL5U

BL6B (IR)

Infrared and terahertz spectroscopy of solids

SR has a good performance (high brilliance and high flux) not only in VUV and SX regions but also in IR and terahertz regions.   This beamline covers in the IR and terahertz regions.   The previous beamline BL6A1 that has been constructed in 1985 is the pioneer of the infrared SR research.   The beamline was upgraded in the spring of 2004 and the name was changed to be BL6B (IR).   The front-end part including the bending duct #6 was replaced to a new one with higher acceptance angle using a magic mirror as shown in Fig. 1.

The beamline is equipped with two interferometers, one is Michelson-type (Bruker IFS-66v) and the other Martin-Puplett-type (JASCO FARIS-1), for the wide spectral region from several to 20,000 cm^{-1} ($h\nu$ = several 100 μeV – 2.5 eV) as shown in Fig. 2.   The experimental chamber in which users bring can be equipped at the free port.   In the near future, an IR microscope covering down to terahertz region will be set up.
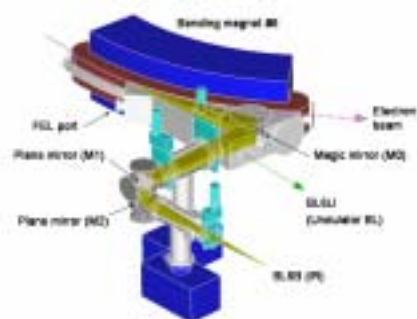
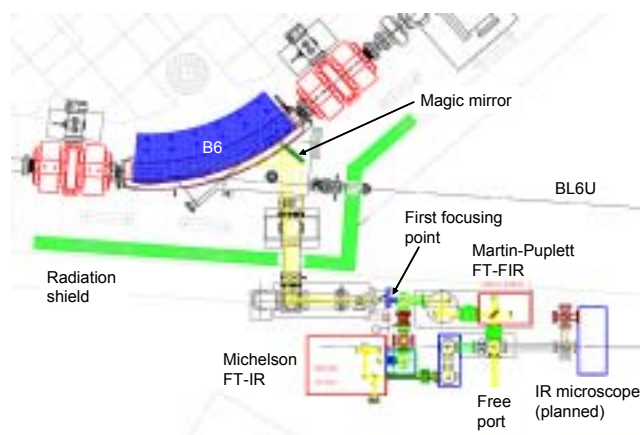**Fig. 1.**   The design of optics and front end of BL6B.

Fig. 2.   Schematic figure of top view of BL6B.

Beamline Specifications

Interferometer	Michelson (Bruker IFS66v), Martin-Puplett (JASCO FARIS-1)
Wavenumber Range (Energy range)	several – 20,000 cm^{-1} (several 100 μeV – 2.5 eV)
Resolution in cm^{-1}	0.1cm^{-1} for IFS66v 0.25cm^{-1} for FARIS-1
Experiments	Reflectivity and transmission Magneto-optics (Microspectroscopy)
Miscellaneous	Users can bring their experimental system in this beamline.

BL7U

Undulator Irradiation Beamline for STM Observation

This beamline has been constructed for STM observation of surface photochemical reactions stimulated by undulator irradiation.   The schematic drawing of the BL7U is shown in Fig. 1.   The undulator is in-vacuum type, of which the period is 36 mm and the number of the period is 26.   The 1st harmonic is tuned from 70 eV to 140 eV [4].   Two Pt-coated cylindrical mirrors are used for the vertical and horizontal focusing.   These two mirrors also suppress the higher harmonics of the undulator radiation into ~10% with respect to the first harmonic.   The focus point is set at the point of 9100 mm downstream from the middle of the undulator.   The spot size on the sample surface was 1.0 mm (H) x 0.4 mm (V) and the estimated photon flux density was 10^{18} photons $(cm^2 \, sec \, 100 \, mA)^{-1}$.
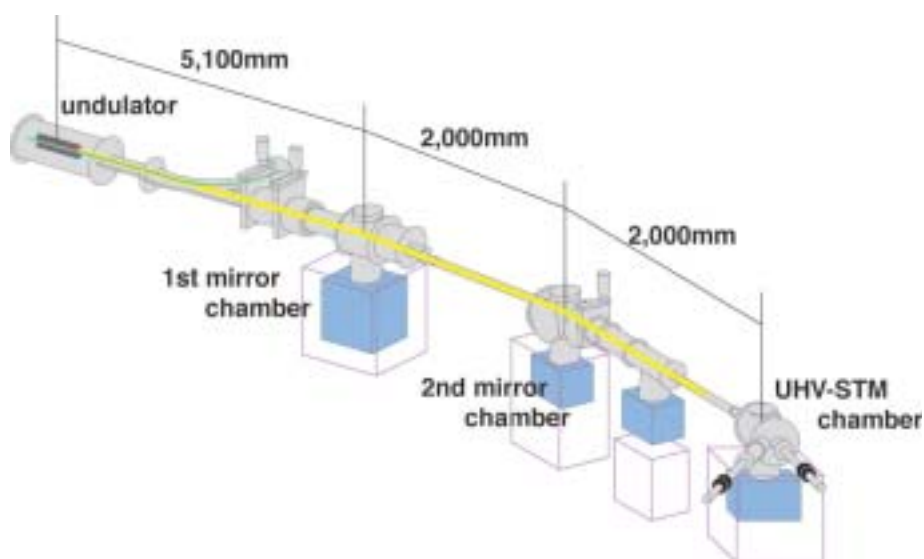
Fig. 1.Schematic drawing of BL7U

Beamline Specifications

Monochromator	None
Wavelength Range	70 – 140 eV (1st harmonic)
Resolution	~10 -
Experiment	Undulator Irradiation and STM Observation
Miscellaneous	

BL7B

3-m Normal Incidence Monochromator for Solid-State Spectroscopy.

   BL7B has been constructed to provide sufficiently high resolution for conventional solid-state spectroscopy, enough intensity for luminescence measurements, a wide wavelength coverage for Kramers-Kronig analyses, and the minimum deformation to the polarization characteristic of the incident synchrotron radiation.   This beamline consists of a 3-m normal incidence monochromator which covers the vacuum ultraviolet, ultraviolet, visible and infrared, *i.e.* the wavelength region of 40 -1000 nm, with three gratings (1200, 600, and 300 l/mm). Two interchangeable refocusing mirrors provide two different focusing positions.   For the mirror with the longer focal length, an LiF or a MgF2 window valve can be installed in between the end valve of the beamline and the focusing position.   Figure 1 shows absolute photon intensity for each grating with the entrance and exit slit openings of 0.5 mm.   A silicon photodiode (AXUV-100, IRD Inc.) was utilized for measuring the photon intensity and the absolute photon flux was estimated, taking the quantum efficiency of the photodiode into account.
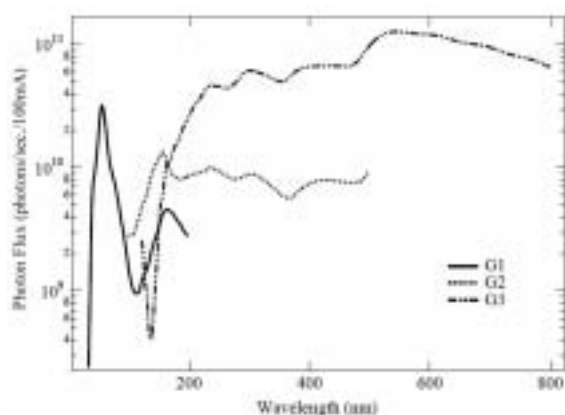

Fig. 1.   Throughput spectra of BL7B measured by a silicon photodiode.
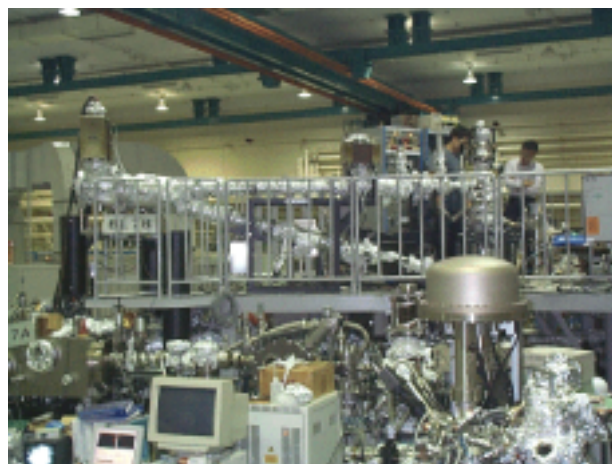

Fig. 2.   Photo of BL7B.

Beamline Specifications

Monochromator	3-m Normal Incidence Monochromator
Wavelength Range	50 to 1000 nm (1.2 - 25 eV)
Resolution	$E/\Delta E = 4000 - 8000$ for 0.01 mm slits
Experiment	absorption, reflection, fluorescence spectroscopy, mainly for solids

BL8A

Irradiation Beamline for Studies of Photochemical Reaction on Solids

The beamline BL8A was constructed for providing synchrotron radiation without monochromatizaion. The white synchrotron radiation is focused into a 3.5 mm × 2.5 mm size by use of a toroidal mirror. The focusing mirror can be removed for obtaining a bigger irradiation area. A differential pumping system with three stages is introduced, which enables users to perform experiments under a very low vacuum condition (<0.5 Torr). The intense white light available at this beamline is suitable for studies on photochemical reaction, chemical vapor deposition, photo-etching and irradiation damage effects. No standing experimental stations are placed at the beamline; users may install their own experimental chambers, while some standard chambers are arranged by UVSOR.
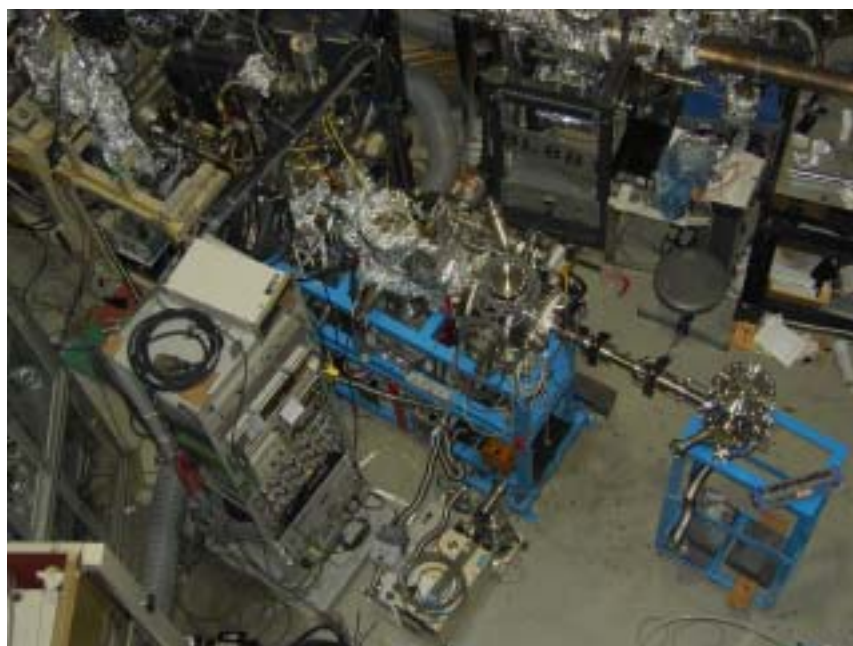

Fig. 1. A top-view photo of the beamline.

Beamline Specifications

Monochromator	None
Energy Range	The whole energy range of the synchrotron radiation
Resolution	—
Experiments	Photochemical reaction, chemical vapor deposition and photo-etching experiments
Miscellaneous	Beam spot size: (H)3.5 mm × (V)2.5 mm

BL8B1

Spherical Grating Monochromator for Soft X-Ray Spectroscopic Studies on Solids and Surfaces

The beamline BL8B1 equipped with a constant-deviation constant-length spherical grating monochromator [1] provides soft X-ray photons in the energy range 30-800 eV with medium energy resolution. The photon energy range is covered by using three gratings (R=15 m; 1080 l/mm, R=15 m; 540l/m, and R=7.5m; 360 l/mm) which are interchangeable in vacuum. Figure 1 shows a throughput spectrum measured with the entrance- and exit-slit openings of 10 μm. Under this condition, the achievable resolving power is about 4000 at 400 eV and 3000 at 245 eV, respectively.

Two experimental chambers are arranged for users. One of them has recently been placed at BL8B1, which used to be at BL2B1 for a long time. This chamber is equipped with an electron-ion coincidence spectrometer, a double-pass cylindrical mirror analyzer, a LEED of reverse type, a quadrupole mass spectrometer, an ion-gun for sputtering, and a liquid helium cryostat. Photoelectron and Auger spectroscopies for solids and surfaces are feasible under ultra-high vacuum (~1×10^{-10} Torr). The other experimental chamber is for conventional measurements of electron yield spectra, or pseudo-photoabsorption spectra, under a ~1×10^{-6} Torr vacuum condition.

[1] Hiraya at al, *Rev. Sci. Instrum*., <u>66</u>, 2104 (1995).
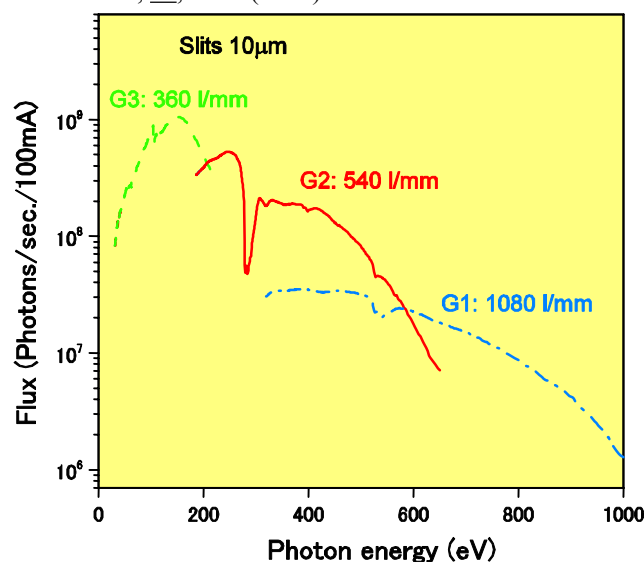

Fig. 1   Throughput from the constant-deviation constant-length spherical grating monochromator on BL8B1.

Beamline Specifications

Monochromator	Constant-deviation constant-length spherical grating type
Energy range	30-800 eV
Resolution	E/ΔE = 4000 at 400 eV and 3000 at 245 eV
Experiments	Photoabsorption spectroscopy, electron spectroscopy and electron-ion coincidence spectroscopy for solids and surfaces

BL8B2

Angle-Resolved Ultraviolet Photoelectron Spectrometer for Solids

BL8B2 is a beamline for angle-resolved ultraviolet photoemission spectroscopy (ARUPS) system which is designed for measuring various organic solids such as molecular crystals, organic semiconductors, and conducting polymers. This beamline consists of a plane-grating monochromator (PGM), a sample preparation chamber with a fast entry Load-Lock chamber, a measurement chamber with an accurate for temperature dependence (base pressure 1×10^{-10}Torr), a cleaning chamber (base pressure 1×10^{-10}Torr), and a sample evaporation chamber (base pressure 3×10^{-10}Torr). The cleaning chamber is equipped with a back-view LEED/AUGER, an ion gun for Ar^+ sputtering, and an infrared heating unit. The PGM consists of premirrors, a plane grating, focusing mirror, and a post-mirror, with an exitslit. It covers the wide range from 2 to 150eV with exchanging two gratings (G1: 1200l/mm, G2: 450l/mm) and five cylindrical mirrors. The toroidal mirror focuses the divergent radiation onto the sample in the measurement chamber. The spot size of the zeroth-order visible light at the sample surface is about $1\times1mm^2$. Figure 1 shows the throughput spectra of PGM (slit=100μm). The energy resolution at a slit width of 100μm was found to be 0.004-0.3eV in the wavelength range from 2 to 130eV. A hemi-spherical electron energy analyzer of 75mm mean radius with an angular resolution less than 2° can be rotated around vertical and horizontal axes. The sample mounted on a manipulator can be also rotated around two axes.
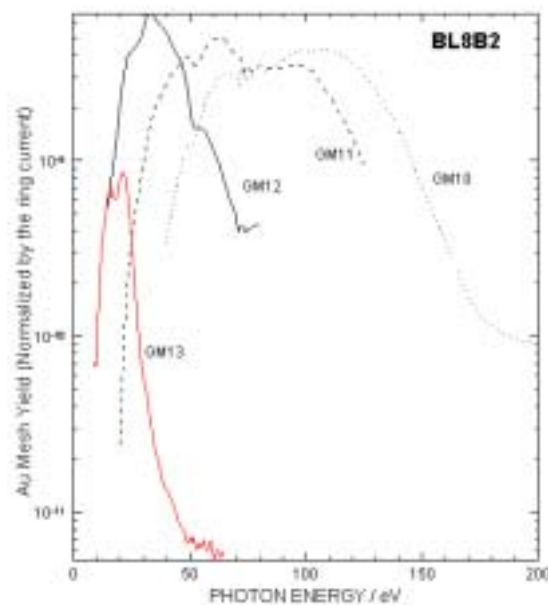

Figure 1 Throughput spectra of plane-grating monochromator at BL8B2(slit=100um).

Beamline Specifications

Monochromator	Plane-grating monochromator
Wavelength Range	9- 600nm
Resolution	E/ΔE = 1000
Experiment	Angle-resolved UPS

Beamlines at UVSOR-II

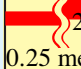| Beam-line	Monochromator, Spectrometer	Energy Region (eV)	Experiments	Beamline master
1A	Double-Crystal	600 eV — 4 keV	Solid (Absorption)	N. Kondo nkondo@ims.ac.jp
1B	1m Seya-Namioka	1.9 eV 40 eV	Solid (Reflection & Absorption)	M. Hasumoto hasumoto@ims.ac.jp
2B	18m Spherical Grating	20 eV 200 eV	Gas (Photoionization, Photodissociation)	K. Mitsuke mitsuke@ims.ac.jp
3U	Varied-Line-Spacing Plane Grating Monochromator	40 eV 600 eV	Gas (Photoionization, Photodissociation) & Solid (Photoemission)	T. Hatsui hatsui@ims.ac.jp
3B	3m Normal Incidence	3 eV 40 eV	Gas (Photoemission)	K. Mitsuke mitsuke@ims.ac.jp
4A1	Multi-Layered-Mirror Monochromator	50 eV 95 eV	Irradiation	T. Urisu urisu@ims.ac.jp
4A2	None		Irradiation	T. Urisu urisu@ims.ac.jp
4B	Varied-Line-Spacing Plane Grating Monochromator	80 eV 800 eV	Gas (Photoionization, Photodissociation) & Solid (Photoemission)	E. Shigemasa sigemasa@ims.ac.jp
5U (FEL*)	None	(OK****)	FEL*	J. Yamazaki yamazaki@ims.ac.jp
5U	SGM-TRAIN**	5 eV 250 eV	Solid (Photoemission)	T. Ito tito@ims.ac.jp
5B	Plane Grating	5 eV 600 eV	Calibration, Gas (Photodissociation) & Solid (Absorption)	M. Hasumoto hasumoto@ims.ac.jp
6B (IR)	Martin-Puplett FT-TIR, Michelson FT-IR***	2.5 eV 0.25 meV	Solid (Reflection & Absorption)	S. Kimura kimura@ims.ac.jp
7U	None		Irradiation	Y. Nonogaki nonogaki@ims.ac.jp
7B	3m Normal Incidence	1.2 eV 30 eV	Solid (Reflection & Absorption)	M. Hasumoto hasumoto@ims.ac.jp
8A	None (Filter)		Irradiation & User's Instruments	E. Nakamura eiken@ims.ac.jp
8B1	15m Constant Deviation Grazing Incidence	30 eV 600 eV	Gas (Photoionization, Photodissociation) & Solid (Absorption)	Y. Hikosaka hikosaka@ims.ac.jp
8B2	Plane Grating	1.9 eV 150 eV	Solid (Photoemission)	D. Yoshimura daisukey@ims.ac.jp

FEL*: Free Electron Laser
FT-IR***:
Fourier Transform interferometer in the Infrared
OK*****: with an Optical Klystron
U: with an Undulator

E (eV) <1 200 400 600 800 1000< 1keV<
λ (m) >10⁻⁶ 10⁻⁸   10⁻⁹>
>1μm 10nm   1nm>
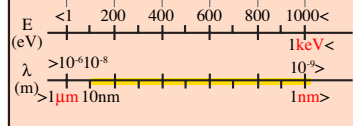
SGM-TRAIN**:
Spherical Grating Monochromator with Translating and Rotating Assembly Including Normal incidence mount

CURRENT STATUS OF LIGHT SOURCE

Table I. Station masters and supervisors of open beamlines in 2003

Beamline	Station Master	Sub Master	Supervisor
1A	N. Kondo	E. Shigemasa	E. Shigemasa
1B	M. Hasumoto	S. Kimura	S. Kimura
5U	T. Ito	S. Kimura	S. Kimura
5B	M. Hasumoto	E. Nakamura	E. Shigemasa
6B	S. Kimura	E. Nakamura	S. Kimura
7B	M. Hasumoto	S. Kimura	S. Kimura
8A	E. Nakamura	Y . Hikosaka*	E. Shigemasa
8B1	Y . Hikosaka*	E. Nakamura	E. Shigemasa

*Dr. Y . Hikosaka arrived at his post on October 1, thereafter the name of "E. Shigemasa" in Table I is replaced by "Y . Hikosaka" accordingly.

Table II. Representatives of in-house beamlines in 2003.

Beamline	Representative	Affiliation
2B	K. Mitsuke	Dep. VUV Photoscience
3U	N. Kosugi	Dep. VUV Photoscience
3B	K. Mitsuke	Dep. VUV Photoscience
4A	T. Urisu	Dep. VUV Photoscience
4B	E. Shigemasa	UVSOR
7U	T. Urisu	Dep. VUV Photoscience
8B2	T. Urisu	Dep. VUV Photoscience

Feasibility Study of Generation and Observation of Far Infrared Coherent Synchrotron Radiation at UVSOR

Y.Takashima, M.Katoh[A], M.Hosaka[A], A.Mochihashi[A] and S.Kimura[A]

Graduate School of Engineering, Nagoya University, Chikusa-ku Nagoya 464-8603 Japan

A)UVSOR Facility, Institute for Molecular Science, Okazaki 444-8585 Japan

We have been considering a method for the generation of far infrared coherent synchrotron radiation from UVSOR storage ring.

Far infrared coherent radiations can be emitted when the electron bunches have density modulations [1]. In order to obtain intense far infrared synchrotron radiations, we have been studying the feasibility to generate coherent radiations by using the bunch slicing technique [3,4,5].

The bunch slice can be achieved by using a laser pulse passing together with an electron bunch through in an undulator [5]. We tune the undulator to the wavelength of the laser, so that the energy of electrons overlapped with the laser are modulated by the interaction with the laser field. If the energy modulation is several times lager than the r.m.s. energy spread of the electron beam, the modulated electrons are separated spatially and a dip is made in the bunch when the electrons pass through a dispersive section. The modulated electron bunch with a dip can emit coherent radiations of which wavelength is in the same order of the size of the dip.

Experimental Equipment

We will use the existing BL5U undulator as an energy modulator in which circulating electrons interact with the laser pulses.

A mode-locked Ti-sapphire laser and an ultrafasst regenerative amplifier is used to make femtosecond laser pulses which should have enough power to make sufficient energy modulation in order to make a dip [5,6].

Intensity of Coherent Radiation

The ratio of the coherent to incoherent radiation intensity is expressed by the following equations [1,2],

$$\frac{P(\omega)_{coherent}}{P(\omega)_{incoherent}} \cong N \cdot f(\omega),$$

where ω is the frequency and N is the number of electrons within a bunch. $P(\omega)_{incoherent}$ and $P(\omega)_{coherent}$ are the power of incoherent and coherent radiations, respectively, emitted from a electron bunch. Because of the large number of N ($\sim 10^{10}$), coherent radiations can dominate over the incoherent radiations.

The beam tracking simulations has confirmed that a dip can be made in the bunch at the exit of BM6 [6]. The electrons of the width of 1 ps in a bunch were modulated their energy up to 0.8 % in the existing BL5U undulator (modulator) and then traveled to the BM6. The ratio of the coherent to incoherent radiation intensity generated from the bunch is abut 2 $\times 10^5$ at the wavenumber of 20 cm-1 (wavelength is 0.5 mm) when the beam current is 18mA/bunch (N is 2×10^{10}).

In order to observe the infrared radiation, we plan to use the InSb semiconductor bolometer at BL6. The detector can be used to detect the radiation of wavenumber from 5 to 50 cm^{-1}; in the region the coherent radiations are expected to be yielded much more than incoherent radiations [6].

Summary

We have been planning to generate and observe far infrared coherent synchrotron radiation using the bunch slicing technique at UVSOR. A commercial short pulse laser can be used to slice electron bunches and make dips which are indispensable to generate the coherent radiations. The averaged intensity of the far infrared coherent radiation is about ten times larger than the incoherent radiation if we use the laser of 5 kHz repetition rate and make one dip in each bunch. We can observe the coherent radiation at BL6 using the InSb bolometer.

For further studying, we should consider methods to improve the intensity of the radiation, for example, how to make dips periodically in a bunch.

[1] G.L.Carr et al., Nucl. Instr. and Meth. A463, 387 (2001)
[2] H.Weidemann, "Particle Accelerator Physics", Springer-Verlag, (1993)
[3] A.A.Zholents and M.S.Zolotorev, Phys. Rev.Lett., 76, 912 (1996)
[4] R.W.Schoenlein et al., SCIENCE, 287, 2237 (2000)
[5] Y.Takashima et al., UVSOR Activity Report, (2001)
[6] Y.Takashima et al., UVSOR Activity Report, (2003)

ACCELERATOR AND BEAM PHYSICS

The First FEL Lasing on the UVSOR-II Storage Ring

M. Hosaka, M. Katoh, A. Mochihashi, J. Yamazaki, K. Hayashi, Y. Takashima*

UVSOR Facility, Institute for Molecular Science, Okazaki 444-8585 Japan
*Depertment of Materials Processing Engineering, Graduate School of Engineering,
Nagoya University, Chikusa-ku, Nagoya 464-8603 Japan

The upgraduation of the UVSOR storage ring was successfully done in Spring 2003 and the emittance of the electron beam has been reduced by factor 6 comparing the previous value [1]. The improved performance of the UVSOR-II electron beam is of great advantage for the free electron laser experiment and we expect lasing in much shorter wavelength.

The FEL experiment using UVSOR-II was begun in October 2003. Before the lasing experiment we determined a beam trajectory for the FEL experiment by measuring spontaneous radiation spectra from the helical optical klystron (HOK) [2]. On December 1st the first lasing was achieved after an adjustment of the optical cavity. The lasing wavelength was visible region around 420 nm. Looking at an extracted FEL power, we made more accurate adjustment of the cavity mirror. In the experiment, multi-layers of Ta_2O_5/SiO_2 was employed for the cavity mirrors. The round-trip reflectivity of the cavity mirror was evaluated by a ring-down method and the deduced value was 99.25 %. Reducing an electron beam current, a threshold beam current was measured and the obtained value was 16 mA/2-bunch. Thus the FEL gain is estimated to be 0.75 % at the electron beam current of 16 mA/2-bunch. This value is compared with calculated FEL gain in Fig. 1. As seen in the figure, although the measured gain was higher than previous value of the UVSOR-I, it is smaller than the calculated one of the UVSOR-II. This indicates that the optimization of the FEL system has not been done satisfactory.
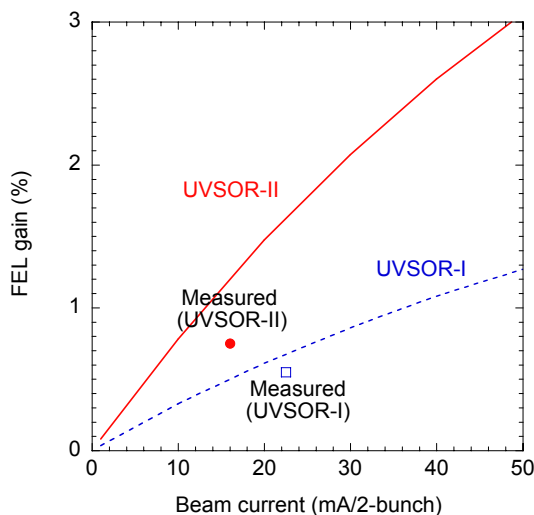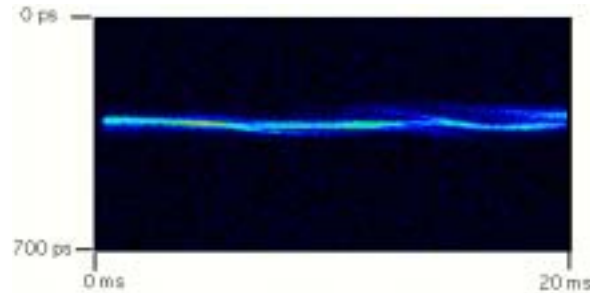

Figure 2: Temporal profile of the FEL at the beam current of 68 mA measured using a dual sweep streak camera.

We suppose that the adjustment of the overlap between the laser and the electron beam whose size is reduced in the upgraduation of the storage ring is not sufficient. We are going to employ correction magnets equipped inside HOK to maximize the overlap.

In order to investigate characteristics of the lasing, we measured a temporal profile of the FEL using a dual-sweep streak camera. Figure 2 shows one of obtained profiles. The shortest temporal width was 5 ps, but the stable lasing did not last more than 10 msec. This is because the electron beam was suffered by the transverse/longitudinal instability during the measurement. The source of the instability is supposed to the interaction with the RF cavity system (main cavity and 3rd harmonic cavity). We are going to optimize the operating point of the storage ring to suppress the instability.

In summary, we have successfully obtained the FEL lasing with UVSOR-II, however its performance is not satisfactory. More studies are needed for lasing in shorter wavelength.

[1] M. Katoh, SYNCHROTRON RADIATION NEWS, Vol. 16, No. 6, 33 (2003).
[2] M. Hosaka et al., Proc. of the 3rd Asian Particle Accelerator Conference (2004).

Fig. 1: FEL gain as a function of the beam current. Measured gains for the UVSOR-I and UVSOR-II are compared with calculated ones.

ACCELERATOR AND BEAM PHYSICS

Improvement Plan of RF Cavity in UVSOR-II Electron Storage Ring

A. Mochihashi, M. Katoh, M. Hosaka, K. Hayashi, J. Yamazaki, *Y. Takashima

UVSOR, Institute for Molecular Science, Okazaki 444-8585 Japan
Graduate School of Engineering, Nagoya University, Chikusa-ku Nagoya 464-8603 Japan

The improvement of the UVSOR electron storage ring[1] has been finished successfully, and a transverse emittance of the electron beam has been decreased from 165nm-rad to 27nm-rad. Users runs have been performed since September 2003 with high brilliance beam optics, and since then high brilliance SR beams have been supplied routinely for users. Because of the decrease in the transverse emittance, however, Touschek effect becomes prominent and a condition for a beam lifetime becomes severe; before the improvement (ε=165nm-rad) the beam lifetime was about 1700mA·Hour at the multibunch operation, and after the improvement the beam lifetime decreases to 1000mA·Hour in the low-emittance operation (ε=60nm-rad in the achromatic optics). To increase the beam lifetime and make full use of the improved SR beams, we have planned to improve the main RF cavity of the UVSOR-II electron storage ring.

The aim of the plan is to increase the beam lifetime by increasing in accelerating voltage and easing the Touschek effect. Figure 1 shows change in the Touschek lifetime on the accelerating cavity voltage (V_c) at the achromatic low emittance beam optics (ε=60nm-rad). At the present cavity voltage (V_c=55 kV) the I·$\tau_{Touschek}$ product becomes 1650mA·H in the x-y coupling of 3%; on the other hand, the I·$\tau_{Touschek}$ product is estimated to be 5200 mA·H at the cavity voltage of 150 kV, as seen in the figure. Figure 2 shows calculated value of change in transmitter power on the cavity voltage. In the calculation, the shunt impedance (R_s) of the RF cavity is assumed to be R_s=2.2MΩ, that is one of appropriate values from the calculation with Poisson/Superfish[2] for typical re-entrant RF cavity whose resonant frequency is around 90 MHz. As seen in the figure, the transmitter power to generate the cavity voltage of 150 kV is estimated to be less than 20 kW, that is the maximum power of the transmitter that is in operation in the UVSOR now. From the estimation, the target values of the accelerating voltage and the I·$\tau_{Touschek}$ product have been settled to be above 150kV and 5000 mA·H, that is comparable to the designed parameter of MAX-III[3].

To realize those target values, it is necessary to renew the RF cavity because the shunt impedance of the present RF cavity has only 0.5MΩ. On the other hand, the transmitter that is in use now can be applied to the new RF cavity because it is estimated the transmitter has enough output power to realize the target value of the cavity voltage. Table 1 shows the basic specification of the new RF cavity. As seen in the table, the basic parameters of the RF system such as the RF frequency will not be changed even in the new cavity. The new cavity would be build with pure oxigen-free-copper chamber to stabilize temperature of the cavity easily. The target value of the shunt impedance is 2.2MΩ to realize enough cavity voltage. The cavity will be built in 2004 and installed in S2 section (B1~B2) in the spring of 2005. After the installation and tuning of the new cavity, the present cavity will be removed from the ring.

Table 1. Basic specifications of present/planned cavity.

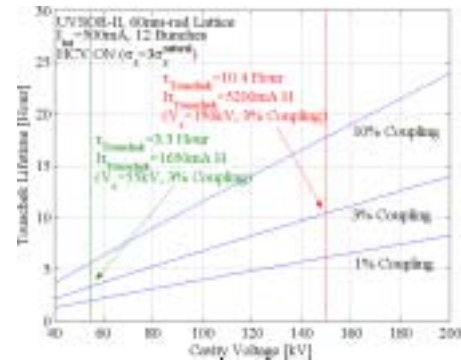|	Present	Planned
Frequency	90.1 MHz	90.1 MHz
Cavity voltage	55 kV	150 kV
Shunt impedance	0.5 MΩ	2.2 MΩ
Material	SUS + Cu	Cu (OFHC)
Cells	Re-entrant×1	Re-entrant×1
Coupler	Air-cooled	Water-cooled
Tuner	Plunger×1	Plunger×2

Fig. 1. Dependence of the calculated Touschek lifetime on the cavity voltage.
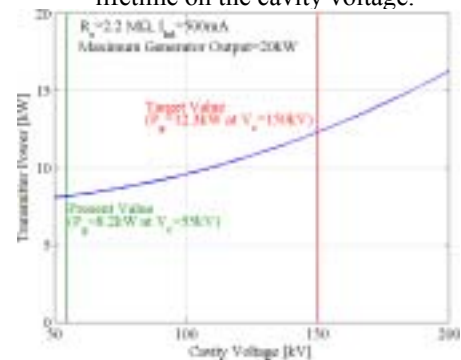

Fig. 2. Transmitter power for the cavity voltage.

[1] M. Katoh, in this report.
[2] J. H. Billen and L. M. Young, Poisson/Superfish version 7.11.
[3] Å. Andersson *et at.,* Proc. of the 8th European Particle Accelerator Conference, p.36-38.

Estimation of the Impedance of UVSOR-II Electron Storage Ring

A. Mochihashi, M. Hosaka, M. Katoh, K. Hayashi, J. Yamazaki, *Y. Takashima

UVSOR, Institute for Molecular Science, Okazaki 444-8585 Japan
*Graduate School of Engineering, Nagoya University, Chikusa-ku Nagoya 464-8603 Japan

In the improvement of the UVSOR electron storage ring[1], almost all of beam ducts, especially the beam ducts for straight sections, have been replaced, and moreover, two in-vacuum undulators[2] have been installed in the straight sections. We have measured effective impedance of the UVSOR-II electron storage ring by measuring threshold beam current of longitudinal microwave instability. Another values associated with the effective impedance have been estimated, too.

Measurement

To measure the threshold current of the microwave instability, we have stored single bunch and observed a modulation factor of the spectrum emitted from the optical klystron. Because the modulation factor depends on the energy spread of the electron beam, the threshold current of the microwave instability can be measured by observing the change in the modulation factor of the undulator radiation from the optical klystron on the beam current. Figure 1 shows change in the energy spread on the beam current by measuring the modulation factor by Hosaka[3] in the beam energy of 600 MeV. As seen in the figure, it is clearly seen that the energy spread drastically increases around the beam current of 70 mA.
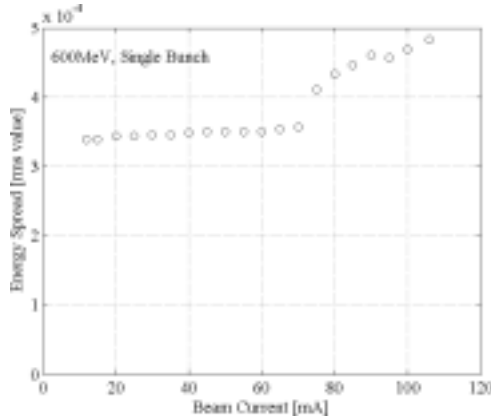

Fig. 1. Measured value of the change in the energy spread on the beam current in UVSOR-II.

Estimation of the Impedance

The threshold current[4] I_{th} of the microwave instability is written as

$$I_{th} = \frac{\sqrt{2\pi}\,k_b v_{s0}^2 E}{e\alpha |Z/n|_{crit}} \left(\frac{\sigma_0}{R}\right)^3 \left(\frac{\sigma_{th}}{\sigma_0}\right)^2 , \qquad (1)$$

where k_b is the RF wave number, v_{s0} is the synchrotron tune, E is the beam energy, e is the electron charge, α is the momentum compaction factor, $|Z/n|_{crit}$ is the critical impedance[4], R is the average ring radius, and σ_0 and σ_{th} are the natural bunch length and the bunch

length at the threshold current, respectively. From the measurement of the bunch length with a streak camera, the ratio σ_{th}/σ_0 is estimated to be 2.12 in case of I_{th}=70mA. From Eq. 1, the critical impedance is estimated to be $|Z/n|_{crit}$=1.2Ω.

The effective impedance[4] $|Z/n|_{eff}$ is given by

$$\left|\frac{Z}{n}\right|_{eff} = \left|\frac{Z}{n}\right|_{crit} \left\{ \left(\frac{\sigma_{th}}{\sigma_0}\right)^2 - 1 \right\} = 4.2\,\Omega ,$$

which is larger than the measured value before the improvement of the UVSOR[5]. The cause of the increase in the effective impedance has not yet become clear; it might be because of the two in-vacuum undulators that have been installed at the improvement.

From the longitudinal effective impedance, the transverse broad band impedance Z_T can be estimated by the approximate relation:

$$Z_T = \frac{2R}{b^2} \left|\frac{Z}{n}\right|_{eff} , \qquad (2)$$

where b is the effective radius of the beam duct. For the beam duct which has an elliptical cross section the effective vertical radius is written as[4]

$$b = \frac{a}{2\{2(\xi_1 - \varepsilon_1)\}^{1/3}} , \qquad (3)$$

where $2a$ is the horizontal width of the beam duct, and ξ_1 and ε_1 are the Laslett parameters[6], respectively. From Eq. 3, the transverse broad band impedance is estimated to be Z_T=1.8×10⁵ Ω/m. From the broad band transverse impedance, the dependence of the vertical tune on the beam current can be given by

$$\frac{dv_y}{dI_b} = -\frac{r_0 bc Z_T}{16\pi e f_{rev}^2 \gamma C \omega_\beta} , \qquad (4)$$

where r_0 is the classical electron radius, c is the speed of light, f_{rev} is the revolution frequency of the beam, γ is the Lorentz factor, C is the circumference of the ring and $\omega_\beta/2\pi$ is the vertical betatron oscillation frequency, respectively. From Eq. 4, the change in the vertical tune on the beam current by the transverse broad band impedance is estimated to be -3.3×10⁻⁵ /mA in UVSOR-II.

[1]M. Katoh, in this report.
[2]in *the Proc. of 8th Int. Conf. on Synchrotron Radiation Instrumentation* (to be printed)..
[3]M. Hosaka, private communications.
[4]A. Hofmann and J. R. Maidment, LEP-Note 168 (1979).
[5] A. Mochihashi, UVSOR Activity Report 2001.
[6]L. J. Laslett, PUB-616, Lawrence-Barlkeley Laboratory.

Construction of the 2m-Long in-Vacuum Undulator Beamline BL3U

T. Hatsui, H. Setoyama, S. Masuda, N. Kondo[*], E. Nakamura[*], Shigemasa[*], N. Kosugi

Dept. of Vacuum UV photoscisence, Institute for Molecular Science, Okazaki 444-8585 Japan
*UVSOR facility, Institute for Molecular Science, Okazaki 444-8585 Japan

The undulator beamline BL3U has been designed and constructed for photoelectron spectroscopy (PES), soft x-ray absorption spectroscopy (XAS), and soft x-ray emission spectroscopy (XES) for the energy range from 60 to 800 eV. A soft x-ray emission spectrometer generally requires small beam size at the sample position, because a smaller opening of the spectrometer entrance slit is needed to achieve higher energy resolution. Such a beam is usually produced by refocusing optics downstream of the exit slit. In our case, the adoption of such refocusing optics is impossible, due to the very limited space. On the other hand, a monochromator with short arm lengths is utilized with a small exit-slit opening for obtaining practical resolution. It is feasible to carry out XES studies at the exit-slit position, if the monochromator has a constant exit-arm length. We have designed a varied-line-spacing plane (VLSP) grating monochromator in order to satisfy high energy resolution and small width of the exit-slit opening. Figure 1 represents the layout of the beamline BL3U at the UVSOR facility. The in-vacuum plane undulator composed of 50 periods of 3.8 cm period length is installed in a straight section, where the electron beam parameters are $s_x=602$ mm, $\sigma_x'=49.9$ mrad, $\sigma_y=61.3$ μm, and $\sigma_y'=40.6$ mrad. The brilliance and total flux calculated by using SPECTRA ver. 7.0.5 [1] are shown in Figure 2. The cylindrical mirror M0 vertically focuses the beam on the entrance slit S0 with the demagnification of 1/7.57. The typical beam size at the entrance slit S0 is a full width at half maximum (FWHM) of 22 μm. Due to the short arm length, the entrance-slit opening corresponding to the resolving power of $E/\Delta E=10^4$ becomes smaller than the beam size. This mismatch causes the beam loss of 12-63%. Varied-line-spacing parameters are calculated by minimizing the aberrations in the energy range of interest. The analytical solution of the aberrations for an S0-M1-VLSP-S1 optical system derived by Amemiya et. al. [2] is used. The obtained parameters give resolving power higher than $E/\Delta E=10^4$ in the photon energy range of 50-800 eV by using three interchangeable gratings with the center groove densities of 1200, 600, and 240 l/mm.

In the XES setup of Figure 1, the beam is horizontally focused on the exit slit by a plane-elliptical mirror M2X, which is located downstream of the VLSP gratings. A sample is placed at 5-10 mm downstream of the exit slit S1X. In the multi-purpose setup, the beam is focused on the exit slit S1 only vertically and then refocused in the both directions on the sample by a toroidal mirror M2. The

M2X mirror and the exit slit S1X are designed to be easily interchangeable with the exit slit S1. In the XES setup, the beam on the sample is designed to have a gaussian distribution with FWHM of 60 μm horizontally. The vertical beam size is close to the opening of the exit slit S1X. Although the beam is diffracted by the exit slit S1X, the vertical size of the beam can be down to ~10 μm; in the multi-purpose setup, the beam size at the sample position is typically 30(v) x 170 (h) μm^2.

The commissioning has started from March 2004. The fitting of the N 1s $\rightarrow\pi*$ resonance spectrum (Fig.3) gives the monochromator resolution of 7200, where the Lorentzian width of 109 meV was assumed [3]. The resolution is lower than the designed value. The reason was found to be the misalignment of the gratings. Improvement of the alignment is now under progress.
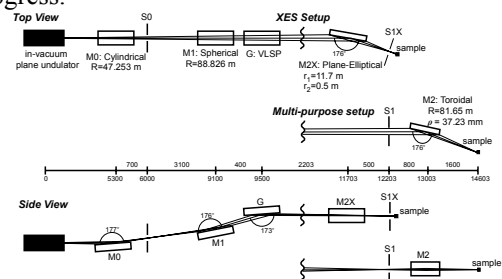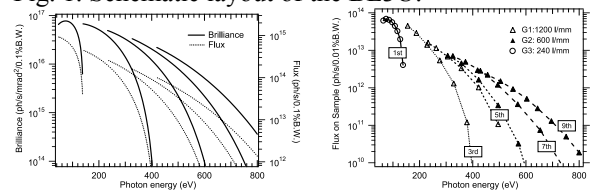

Fig. 1. Schematic layout of the BL3U.

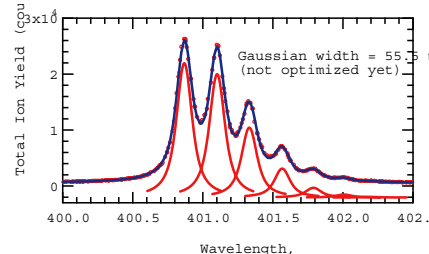Fig. 2. Theoretical estimates of the undulator brilliance and flux, and the photon flux at sample position.

Fig. 3. Total ion yield spectrum of nitrogen molecule using the grating with groove density of 1200 l/mm.

[1] T. Tanaka, and H. Kitamura, J. Synchrotron Rad. 8, (2001) 1221.
[2] K. Amemiya, et. al., J. Synchrotron Rad. 3, (1996) 282.
[3] H. Ohashi et. al., Nucl. Instr. And Meth. A 467–468 (2001) 533.

INSTRUMENTAL DEVELOPMENT

Design of a Transmission Grating Spectrometer for X-ray Emission Studies

T. Hatsui, E. Shigemasa[*], N. Kosugi

Dept.of Vacuum UV photoscience, Institute for Molecular Science, Okazaki 444-8585 Japan
*UVSOR facility, Institute for Molecular Science, Okazaki 444-8585 Japan

High resolution soft x-ray emission spectroscopy (XES) in combination with synchrotron radiation as incident soft x-rays has been extensively studied since the development of a high energy resolution spectrometer by J. Nordgren et. al [1]. The design of their grazing-incidence spectrometer is based on the Rowland circle mount. In this case, the horizontal acceptance angle is mainly limited by the detector size. In order to achieve higher resolution, the Rowland radius, R, or the spectrometer size, should be larger due to the relationship of $\lambda/\Delta\lambda \propto R$. The detector size is however limited. It is therefore desirable to design a novel optical system which can focus the emitted x-rays not only in the (vertical) dispersion direction but also in the other (horizontal) direction. In addition, recent advances make the charge-coupled devices (CCD) a promising soft-x-ray detector. It is however not a trivial problem to adopt it in the high resolution Rowland spectrometer, since the CCD detectors have low quantum efficiency at the small grazing-incidence angle. In this report, we propose a novel spectrometer design for high resolution soft x-ray emission studies.

Figure 1 shows the schematic layout of a transmission-grating spectrometer (TGS). In order to focus the emitted x-ray both horizontally and vertically, a Wolter type I mirror is introduced as the prefocussing mirror with a magnification of 10. The Wolter mirror consists of hyperboloidal and elliptical surfaces. The grazing-incidence angle of 1 degree gives a collection angle of 1.5×10^{-3} sr. A free-standing transmission plane grating with its groove density of 10 000 lines/mm is placed at 67 mm downstream at the edge of the Wolter mirror, in
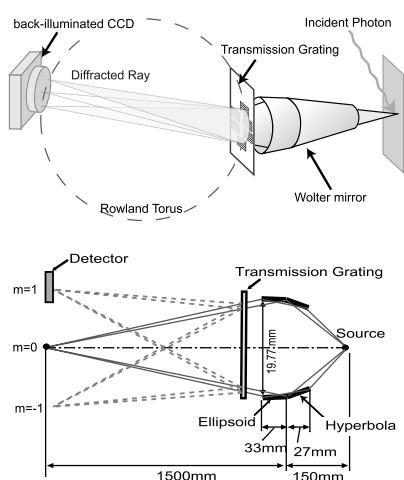
the normal incidence geometry. A back-illuminated CCD, of which the position is changed along the Rowland torus with scanning the photon energy, is located at 1400 mm downstream from the grating.

For evaluating the aberrations of TGS, a ray-tracing code TGSGUI is originally developed by one of the authors (T.H.). In the case of a rectangular source, the Wolter mirror has considerable amount of the aberration. Figure 4 presents a spot diagram at the detector position for the 0th order diffraction with a rectangular source of $1(v) \times 200(h)$ μm^2. This result suggests that the aberration is negligible for this source size. Figure 4 (right) indicates a spot diagram of the 1st order diffracted rays of 320 eV at the detector with a rectangular source of 1×200 μm^2. Other aberrations arise from the plane figure of the grating [2]. The diagram however indicates that the present TGS has small amount of the aberrations. The resolving power better than 5000 is possible. The spatial resolution of the detector should be very high, which is estimated to be about 1 μm, in order to achieve such a high resolution.

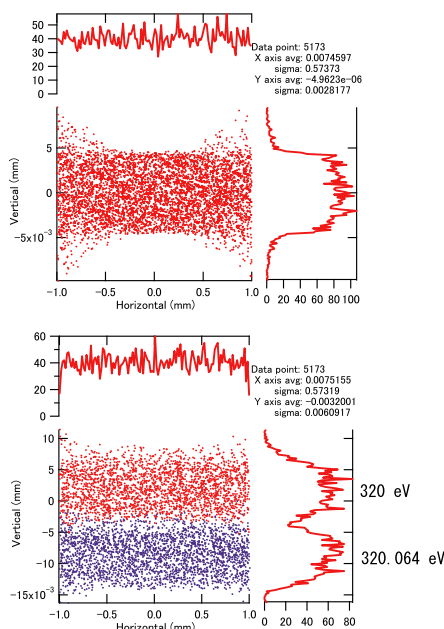Fig. 1. Spot diagram of the 0th (top) and 1st (bottom) order diffraction at the detector with a rectangular source of $1(v) \times 200(h)$ μm^2 (top).

[1] Nordgren, et.al., Rev. Sci. Instrum. 60, 1690-1696 (1989).
[2] Beuermann, K.P. et.al., Applied Optics 17, 2304-2309 (1978).

Fig. 1. Schematic layout of the transmission-grating spectrometer (TGS) (up). A cross sectional view is also shown (bottom).

X-ray Magnetic Circular Dichroism Measurements at BL4B

T. Nakagawa, H. Watanabe, K. Maruyama, T. Yokoyama

Department of Molecular Structure, Institute for Molecular Science, Okazaki 444-8585 Japan

X-ray magnetic circular dichroism (XMCD) is a powerful technique to investigate element-specific magnetization. Moreover, by using so-called sum rules, orbital and spin magnetic moments are separately obtainable, which are hardly derived by other conventional magnetic measurements. We have constructed a new ultrahigh vacuum (UHV) chamber for XMCD and surface XAFS (X-ray absorption fine structure) measurements at BL4B in upgraded UVSOR-II. Here, basic performance of our XMCD measurement system is described.

Apparatus

BL4B is a bending magnet station, where a varied-line-spaced grating monochromator is installed. Circularly polarized X rays are obtained by placing a newly installed slit (located in the upstream of the first mirror) upward or downward with respect to the electron orbit plane. A polarization factor P_c of ~0.70 was obtained with a reasonable photon intensity and an energy resolution $E/\Delta E$ of ~700 at the energy range of 600-1000 eV.

Figure 1 shows the inside of the UHV chamber. An Au-coated Fe electromagnet allows us to apply a static magnetic field of maximum 3000 G during XMCD measurements. The X ray is introduced through the holes at the center of the magnet poles, and its propagating direction is thus always parallel or antiparallel to the magnetic field.

The UHV chamber is evacuated by turbo molecular pumps, a non- evaporation getter and a Ti sublimation pump. The base pressure is around 1×10^{-10} Torr. Standard surface cleaning equipments such as an ion gun, a heater and a LEED/RHEED optics are installed. Metals and gases can be deposited by commercial evaporators and leak valves, respectively. A sample can be cooled down to ~100 K using liq. N_2. The sample can be rotated in both the polar and azimuthal directions with respect to surface normal.

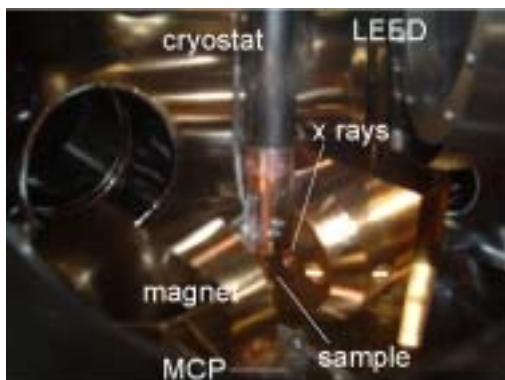The signals were detected usually by a drain current from the sample, and a microchannel plate (MCP) is also available for the partial electron yield detection with a retarding field under the remanent condition. XMCD spectra are taken by changing the helicity of the X rays or the direction of the magnetic field. Most equipments such as the upstream slit, the monchromator, the magnet and the detection systems are controlled by the LabView software.

Results

In order to show the performance of BL4B and the XMCD system, we have recorded Co $L_{III,II}$-edge XMCD of 3 monolayer (ML) Co on Cu(001). The substrate Cu(001) was cleaned by repeated cycles of Ar^+ sputtering and annealing to ~900 K (electron bombardment from the rear side). Cleanliness and order of Cu(001) were verified by XAFS and LEED, respectively. Co was deposited from the Omicron EFM3 evaporator. Co is known to grow epitaxially on Cu(001) with a layer-by-layer pseudomorphic fashion and to show the in-plane easy axis.

Figure 2 show the XMCD spectra, taken at the x-ray incidence angles of 30° (grazing incidence, close to the easy axis) and 90° (normal incidence, along the hard axis). It took around 12 min. to record a parallel or antiparallel spectrum. A signal-to-noise ratio is fairly well. The normal incidence spectra show much weaker XMCD signals because the magnetization is not saturated at 2000 G.

We have performed the sum rule analysis. The orbital moment m_l of 0.164 (μ_B) and the effective spin moment m_s of 1.65 (μ_B) for the θ=30° spectra, while m_l/m_s= 0.095 for the θ=90° ones. These values are consistent with previously reported values.

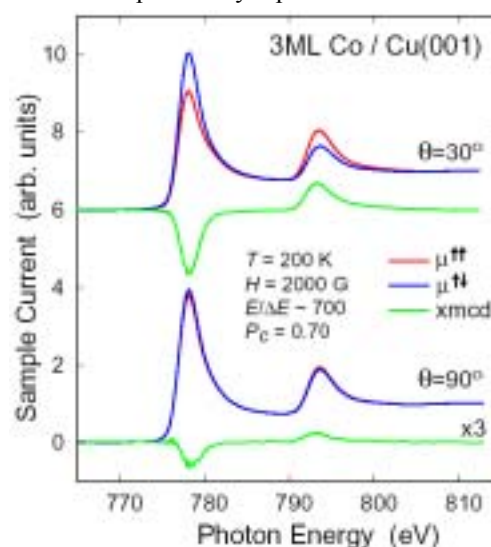Fig. 2   Co $L_{III,II}$-edge XMCD of 3 ML Co/Cu(001) at the x-ray incidence angles of 30° and 90°.

Fig. 1   Inside look of the UHV chamber.

INSTRUMENTAL
DEVELOPMENT

BL5U

Present Status of High-resolution Angle-resolved Photoemission Spectroscopy Apparatus at BL5U

T. Ito, S. Kimura, K. Takahashi[1], K. Soda[2], T. Takeuchi[3], K. Shinba[2], T. Kondo[3],
T. Nakagawa[4] and N. Kosugi

UVSOR Facility, Institute for Molecular Science, Okazaki 444-8585 Japan
[1]Synchrotron Light Application Center, Saga University, Saga 840-8502, Japan
[2]Department of Crystalline materials Science, Nagoya University, Nagoya 464-8603, Japan
[3]Research Center for Advance Waste and Emission Management, Nagoya University, Nagoya 464-8603, Japan
[4]Department of Molecular Structure, Institute for Molecular Science, Okazaki 444-8585, Japan

Functionalities (superconductivity, magnetism, etc.) originating from the electronic structure near the Fermi level (E_F), especially the Fermi surface of solids, thin films and surfaces. To pursue the experimental investigation of the functionalities of materials, we have constructed a new high-energy-resolution photoemission apparatus for the helical undulator beam line BL5U.

Figure 1 shows a present status of the apparatus installed at BL5U [1]. The most striking point is a new type hemispherical photoelectron analyzer, MBS-Toyama 'Peter A-1', with which we have achieved the world record of the experimental energy-resolution $\Delta E \sim 1.2$ meV, which has been evaluated from the fitting of the PES spectrum near E_F of Au by temperature-dependent Fermi-distribution-function broadened by Gaussian (Fig. 2).

To evaluate the improvement of the photoemission spectrometer for BL5U, the XPS spectrum of Si(111) 7x7 surface obtained by the present apparatus is compared with that by the previous one (Fig. 3). In Figure 3, the present spectrum seems to have some advantages to the previous one, *i.e.*, the better *S/N*, the sharper double peak structures originating from Si 2p spin orbit splitting, in spite of the compatible experimental conditions (photon energy, temperature, sizes of slits, surface preparation). The observed differences strongly suggest the improved efficiency as well as the energy resolution of the present spectrometer, though the upgrade of UVSOR is responsible for the better *S/N*.

Finally, we will briefly comment on the future issues for the experimental study of the functional materials at BL5U. After the upgrading UVSOR and the replacement of the photoemission apparatus, some weak points were revealed. Then, we plan the upgrade of BL5U in April 2004; (1) change of the spherical-mirror adjuster with high efficient water cooling, (2) installation of new spherical grating for normal incident region (hv=5~30 eV), and (3) installation the cooling system at the entrance slit.

[1] S. Kimura *et al.*, UVSOR Activity Report 2002, 75.
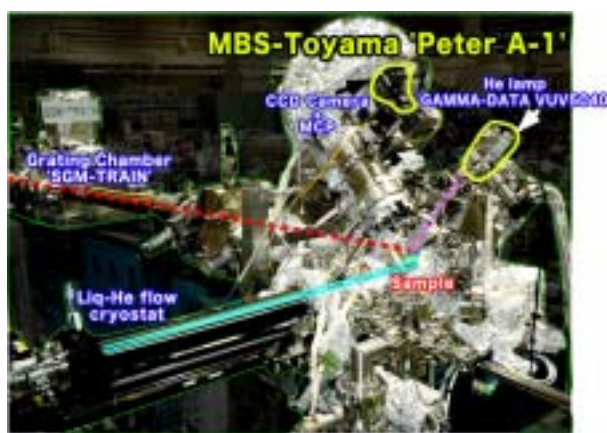

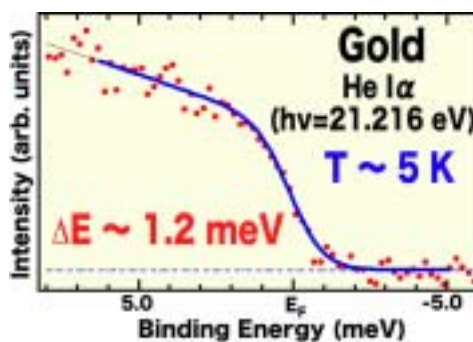Fig. 1 High-resolution photoemission spectroscopy apparatus at BL5U.

Fig. 2 PES spectrum around E_F of Au film obtained by using He Iα photons at 5 K (red circles). The results of fitting is superimposed (blue line).
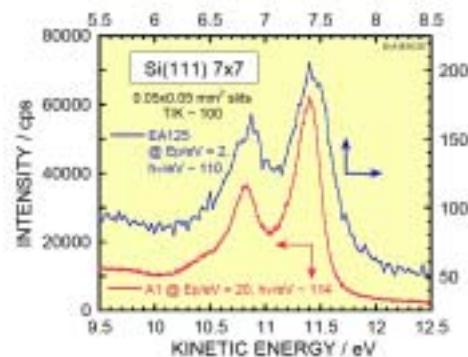

Fig. 3 Si 2p photoemission peaks obtained with the previous (blue) and present (red) apparatus installed at BL5U.

Construction of the new IR and THz beam line BL6B

S. Kimura[1,2], E. Nakamura[1], T. Nishi[2], K. Hayashi[1]

[1]*UVSOR Facility, Institute for Molecular Science, Okazaki 444-8585 Japan*
[2]*Department of Structural Molecular Science, Graduate University of Advanced Studies,*
Okazaki 444-8585, Japan

At the beginning of FY2004, the new infrared (IR) and terahertz (THz) beam line BL6B is constructed. The design concept and the expected performance have been already reported. [1,2] In this paper, the configuration of the Fourier interferometers and the end stations and the future plan are reported.

The configuration of the beam line is shown in Figure 1. IR-synchrotron radiation (IRSR) is collected by a perfect focusing mirror, so-called "magic mirror" set in the bending duct B6. IRSR is guided by two plane mirror and is focused at the first focusing point. The polarization is changed from horizontal at the emission point to vertical by the two plane mirrors. The first focusing point was shifted about 300 mm to the outside of the storage ring because of the installation of a newly installed radiation shield.

The ultra-high vacuum in the storage ring and in the front-end part is separated at the window exchanger with a diamond and a z-cut-quartz windows before the first focusing point. IRSR is guided to two interferometers, one is old Michelson FT-IR (Bruker IFS66v) and the other newly installed Martin-Puplett FT-FIR (JASCO FARIS-1). Since the new FT-FIR is rapid-scan type, higher accuracy of intensity is expected. The covering wave number range is from less than 10 cm^{-1} up to 20,000 cm^{-1}.

The IRSR after two interferometers is guided to the free port. Before the upgrading, a conventional sample chamber was located at the position. To support higher level experiments, users can set their own chambers to the port. The old conventional sample chamber and the old infrared magneto-optical apparatus can be also located, of course.

In the near future, a commercial IR microscope will be installed. The microscope will cover not only IR region but also THz region because the brilliance in the THz region is much higher than conventional light sources. The THz microscope will be a good probe for vibrations of large molecule in a small region and a metal-insulator imaging.

[1] S. Kimura *et al.*, UVSOR Activity Report 2002, *p.* 78 (2003).
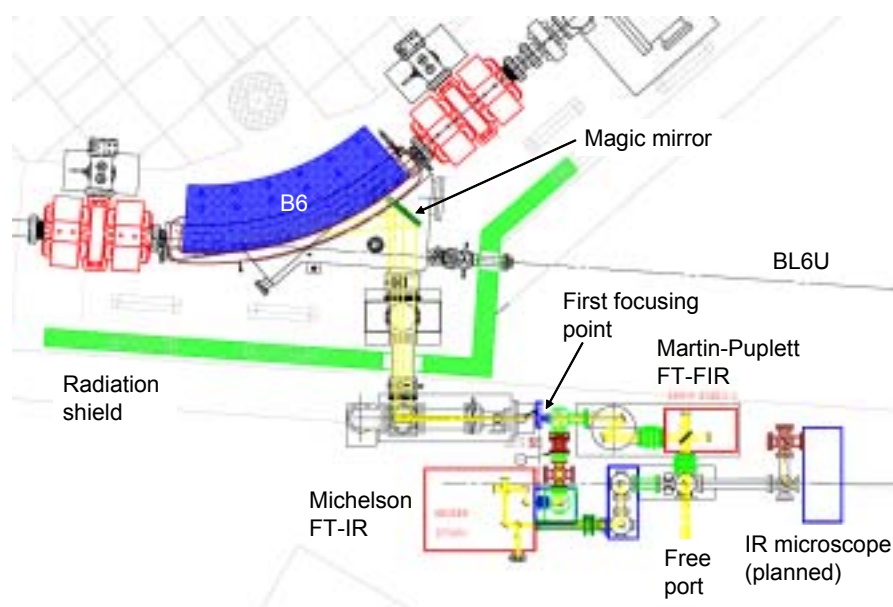[2] S. Kimura *et al.*, Proc. SRI2003.

Fig. 1. Schematic figure of top view of the new infrared and terahertz beam line BL6B.

INSTRUMENTAL
DEVELOPMENT

Carbon Contamination of SR Mirror

M. Tadano[1], E. Nakamura[2], M. Hasumoto[2],
T. Naito[1], J. Urakawa[1]

[1]*High Energy Accelerator Research Organization, 1-1OhoTsukuba 05-080, Japan*
[2]*Institute for Molecular Science, Okazaki 444-8585, Japan*

Carbon contamination on SR irradiated mirror was investigated as a series of the BL8A experiment Vacuum pump oil was checked as one factor as contamination to the mirror surface in the experiment of the preceding year.[1] We experimented by putting in oil in a vacuum in order to advance contamination on the surface of a mirror. Moreover, since it was assumed that oil dissociated to a carbon simple substance by irradiation, it tried how to apply an electric field to the processed thing. The effect of the electric field was investigated in this experiment by using the carburizing technique.

Although much time was spent on experiment preparation, the very interesting result was given. In the environment where electric fields differ, the result from which the amount of generation of a carbon contamination differs was obtained.(fig.1) The progress of the carbon contamination was measured under oil molecule existence that was apply the SR for 4 hours. Fig.2 shows the reflectivity reduction of the surface of the mirror in each condition. The reflectivity reductions were 73% for +1.5kV, 65% for without high voltage and 50% for -1.5kV, respectively. Fig.3 shows the profile of the SR irradiation mirror as a contour color plot. The clear electric field dependence was confirmed. From this result, we can conclude that the electric field at mirror surface is effective for reduce the carbon contamination. However, since there is few measurement data, the quantities talk is not made.

In this experiment, it is not experimenting in changing voltage etc. Change of the reflectance accompanying voltage change is an interesting point. It expects that the same data is obtained also in pure vacuum environment. More exact investigation is needed about dependence of the strength of an electric field, and dependence of vacuum conditions. Although this time was only found out delaying condition, things were not made to removing contamination. We need the further experiment for find out the other method of the carbon contamination.
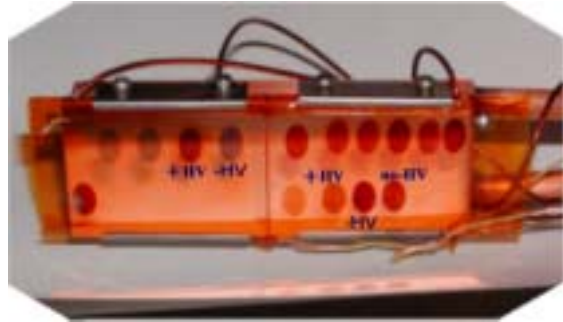
Fig.1. Picture of the contaminated copper mirror.
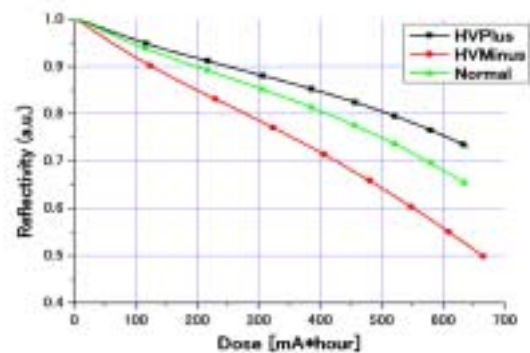
Fig.2. Reflectivity of irradiated mirror.
upper line: Plus High Voltage,
middle line: No High Voltage,
lower line: Minus High Voltage.
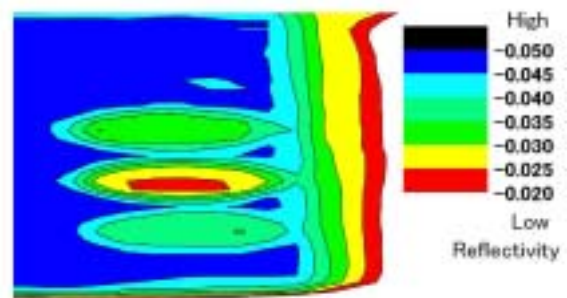
Fig.3. Mirror surface scan at after experiment.
upper round area: No High Voltage,
middle round area: Minus High Voltage,
lower round area: Plus High Voltage.
(unit at the time of measured [Volt].)

[1] M.Tadano et.al. UVSOR Activity Report2002 P80
[2] T.Naito et.al UVSOR Activity Report2000,P63

INSTRUMENTAL
DEVELOPMENT

Photofragmentation of C_{60} in Valence Ionization

J. Kou[a], T. Mori[a], Y. Haruyama[b], Y. Kubozono[b] and K. Mitsuke[a,c]

[a]*Department of Vacuum UV Photo-Science, The Institute for Molecular Science, Myodaiji, Okazaki 444-8585, Japan*

[b]*Department of Chemistry, Faculty of Science, Okayama University, Okayama 700-8530, Japan*

[c] *Graduate University for Advanced Studies, Myodaiji, Okazaki 444-8585, Japan*

It is well-known that dissociative ionization of C_{60} results in fragment ions with even numbered carbon atoms (C_{60-2m}^{q+}, $m=1,2,\ldots$). Experiments of laser multiphoton ionization[1] or electron impact ionization[2] have shown that these ions are produced via thermal fragmentation of C_{60} parent ions in highly excited vibrational states. Single photon excitation with a tunable synchrotron radiation is expected to be helpful in measuring the appearance energies of the fragment ions and investigating redistribution of internal energy of the parent ions, since one can estimate the magnitude of the vibronic energy initially deposited in the C_{60} system. However, no photoion yield curves for production of the fragment ions have been reported. As part of our recent studies on photoionization of fullerenes[3], we have measured the photoion yield curves of the fragment ions produced from C_{60} at $h\nu$ = 25 -150 eV to investigate mechanism of the photofragmentation of C_{60}.
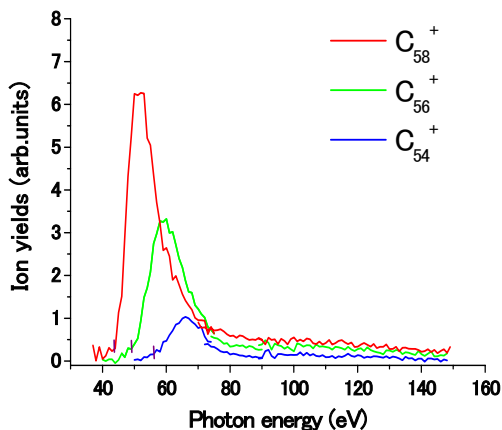

Fig. 1. Photofragment ion yields.

Yield curves for singly charged fragment ions are shown in Fig. 1. As the fragment ions become smaller, their appearance photon energies (AE) shift to higher energy side and curves rise more gently towards the peaks. All curves have long tails and a yield ratio of C_{58}^{+}: C_{56}^{+}: C_{54}^{+} keeps a constant value of approximately 4: 3: 1 at $h\nu \geq$ 90 eV. The maximum internal energy (Ei_{max}) of the parent ion produced via an excitation with the appearance photon energy is found by

$$Ei_{max} = AE + Ev – Ip.$$

Here Ev = 3.3 eV means the initial vibrational energy deposited in C_{60} at a heating temperature of 680 K applied to produce a C_{60} molecular beam and Ip = 7.6 eV the ionization potential of C_{60}. We obtained Ei_{max}

= 39.7±1, 44.7±1, and 51±1 eV for C_{58}^{+}, C_{56}^{+}, and C_{54}^{+}, respectively. These large internal energies are far beyond the adiabatic energies (E_0) for dissociation of $C_{60-2n}^{+}\rightarrow C_{60-2n-2}^{+}+C_2$ ($n = 0,1,2,\ldots$)……(1).

We applied the RRKM model to estimate the internal energies of the parent ions. The detail of the calculation is the same as that described in Ref [2]. Fig. 2 shows yield distribution of C_{58}^{+}, C_{56}^{+}, and C_{54}^{+} as a function of the internal energies of the parent ions. We adopted E_0 of 7.06, 6.78, and 6.60 eV for n =1, 2, and 3 in the reaction (1), respectively[2]. The internal energies for appearance thresholds of C_{58}^{+}, C_{56}^{+}, and C_{54}^{+} are 40.7, 47.3, and 51.7 eV, respectively. These values are in good agreement with the observed Ei_{max}. However, all curves in the calculation lie in a range from 40 to 70 eV and do not reproduce the long tails in the higher energy side. Minimum photon energy for the excitation to this internal energy range is $44.3 \leq$ $h\nu \leq 74.3$ eV. Therefore, the long tails observed at $h\nu \geq$ 90 eV indicate that photoelectron takes away a part of the excitation energy as a kinetic energy and leads to a production of the parent ion with an internal energy from 40 to 70 eV.

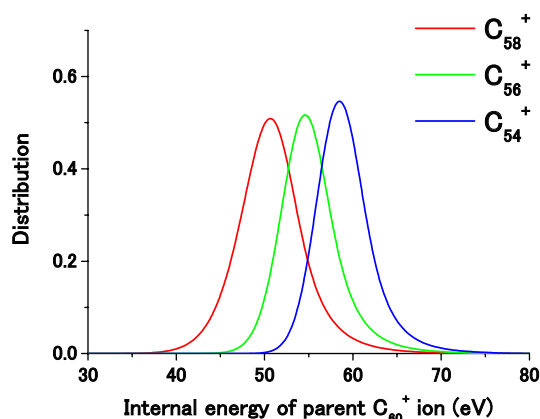

Fig.2 Distribution of fragment ions calculated with the RRKM model.

[1] P. Wurz and K. R. Lykke, J. Phys. Chem. **96,** 10129 (1992).

[2] R. Wörgötter, B. Dünser, P. Scheier, T. D. Märk, M. Foltin, C. E. Klots, J. Laskin, and C. Lifshitz,M. J. Chem. Phys. **104,** 1225 (1996).

[3] J. Kou, T. Mori, S. V.K. Kumar, Y. Haruyama, Y. Kubozono, and K. Mitsuke, J. Chem. Phys. **120,** 6005 (2004).

Absolute Photoabsorption Cross Section of C_{60}

T. Mori, J. Kou, Y. Haruyama*, Y. Kubozono*, K. Mitsuke

Department of Vacuum UV photo-science, Institute for Molecular Science, Okazaki 444-8585 Japan

*Department of Chemistry, Faculty of Science, Okayama University, Okayama 700-8530 Japan

Relative photoabsorption cross sections of C_{60} have been reported by several groups. Most of the authors focused their attention to photon energies below 25 eV or those around the carbon 1s edge (~ 280 eV). Furthermore, only a few experiments have been made on the absolute photoabsorption cross section σ_{abs} of C_{60}. The σ_{abs} curve can be estimated by direct absorption of synchrotron radiation in a cell filled with C_{60} vapor. Jaensch and Kamke measured σ_{abs} by using this method in the vacuum UV region [1]. They were confronted with several serious problems. First, the available energy range is crucially restricted by the material of the windows of the cell. Good transmission should be secured for the windows up to the highest photon energy of interest even at high ambient temperatures. Second, knowing the sample number density is prerequisite for calculating σ_{abs}, though the density is markedly unstable at high temperatures. With these difficulties, there has been no report on σ_{abs} at photon energies above 24.5 eV, where only relative absorption cross sections have been determined from the yields of positive ions produced from C_{60} [2,3].

In this report, we attempt to obtain the σ_{abs} curve of C_{60} from 25 to 180 eV by means of mass spectrometry. For this purpose, several essential devices have been exploited in combination with a high-temperature source of gaseous fullerenes: a grazing-incidence monochromator, a conical nozzle, a quartz-oscillator thickness monitor, and an efficient time-of-flight (TOF) mass spectrometer. The thickness monitor was used for the measurement of the C_{60} density. The detail of the apparatus has been described elsewhere [4].

We obtained the σ_{abs} curve by following equation.

σ_{abs} = (Ion count rate)/{(Photon flux)·(The sample density)·(Interaction length)·(Sensitivity of the spectrometer)·(Residence time)·(Pulse frequency)}

A pulse voltage rising from the ground level to +100 V was applied to the ion repeller electrode as start trigger for the TOF measurement. The duration and frequency of this pulse voltage were 5 μs and 5 kHz, respectively. Ions were drawn through a central hole 10 mm in diameter of the grounded extractor electrode. Photoions were detected with a microchannel plate (MCP) electron multiplier. The Photon flux was measured by a photodiode.

The vapor of the fullerene was discharged from the nozzle with a throat diameter of 0.5 mm and a diverging angle of 7.2 degree. The distance between the throat of the nozzle and the central point of the ionization region was set to 34.8 mm. The number density at the photoionization region is obtainable from the sublimation rate, beam size there (18.5 mm²), and the average of vertical velocity $\bar{v}$ of the C_{60} beam at the oven temperature T:

$$\bar{v} = \frac{1}{2} \cdot \sqrt{(8k_B \cdot T)/(\pi \cdot m)}$$

Where k_B is the Boltzmann constant and m is the mass of C_{60}. Assuming that the sublimation rate was 5 ng s⁻¹ at T = 743.15 K, the number density is estimated from $\bar{v}$ = 74 m s⁻¹ to be 0.765×10^9 molecules cm⁻³.

The sensitivity of our spectrometer is derived from the signal counts of Kr whose absolute photoionization cross section is given in the literature [5].

The obtained cross section of C_{60} is shown in Fig. 1. The σ_{abs} reported by Kamke were found to agree well with our data at 24 eV. The reliability of the Kamke's data appears to be degraded to some extent at $h\nu$ >25eV.
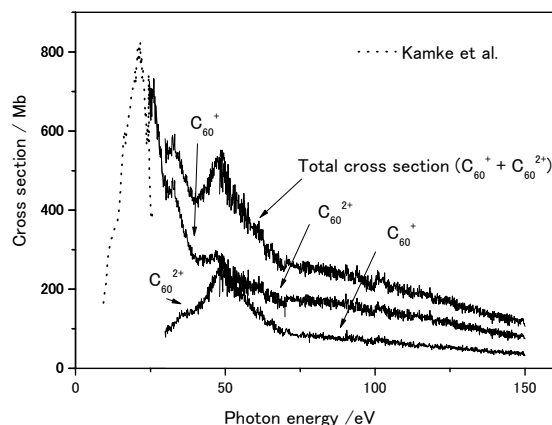

Fig. 1   Absolute cross section of C_{60}

[1] R. Jaensch and W. Kamke, Mol. Mat. 13, 143 (2000).
[2] I. V. Hertel et al. Phys. Rev. Lett. 68, 784 (1992)
[3] J. Kou et al. Chem. Phys. Lett. 374, 1 (2003)
[4] T. Mori et al. Rev. Sci. Inst., 74(8) 3769 (2003)
[5] J. A. R. Samson and W. C. Stolte, J. Electron Spectrosc. Relat. Phenom. 123, 265 (2002).

Autoionization and Neutral Dissociation of Superexcited HI Studied by Two-Dimensional Photoelectron Spectroscopy

Y. Hikosaka and K.Mitsuke*

UVSOR Facility, Institute for Molecular Science, Okazaki 444-8585
*Department of Vacuum UV Photoscience, Institute for Molecular Science, Okazaki 444-8585
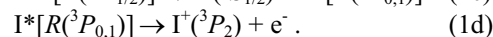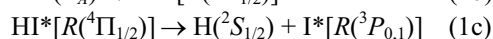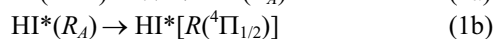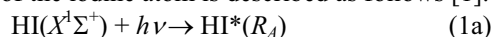
Superexcited states, which are defined as neutral states lying in ionization continua, occupy considerable amounts of oscillator strength in the extreme ultraviolet region of a molecule. Autoionization induced by interelectronic interaction is their major decay processes. However, in the case of molecular superexcited states with relatively narrow autoionization widths, other processes such as neutral dissociation compete with autoionization and have sizable fractions in the decay.

Hydrogen halides are one of the classes of molecules whose superexcited states attract considerable attention in the literature. As for HCl and HBr, series of Rydberg states converging to the ionic $A\,^2\Sigma^+_{1/2}$ states appear as extensive vibrational progressions on photoabsorption spectra. Characters of the involving states and branching ratios have been well accounted for from both experimental and theoretical sides. In contrast, less information has been gained on decay from the corresponding Rydberg states of HI, since the Rydberg states do not exhibit distinct vibrational progressions but broad and almost structureless features on photoabsorption and photoionization spectra. Even for the superexcited states with such broad profiles, two-dimensional photoelectron spectroscopy, in which the photoelectron yield is represented as a function of both photon energy $E_{h\nu}$ and electron kinetic energy E_k, may offer information on the decay dynamics. This is because, when the photon energy is tuned to a superexcited state, the vibrational distribution of the final ionic state on the photoelectron spectrum is closely related to the potential energy surface of this autoionizing state. In addition, photoelectron spectroscopy can probe neutral dissociation of the superexcited state if the neutral fragments undergo autoionization.

Figure 1(a) shows a two-dimensional photoelectron spectrum (2D-PES) of HI measured in the $E_{h\nu}$ region of 11.10 - 14.85 eV. The $E_{h\nu}$ region encompasses the Franck-Condon gap between the $X^2\Pi$ and $A^2\Sigma^+_{1/2}$ states of HI$^+$. Hence, the 2D-PES is expected to show the features arising from the decay of the Rydberg states HI*(R_A) converging to HI$^+$($A^2\Sigma^+_{1/2}$). Two intense diagonal stripes at $\Delta E \equiv E_{h\nu}$- E_k = 10.39 and 11.05 eV result from the formation of spin-orbit components of the v$^+$ = 0 level of HI$^+$($X^2\Pi$). In several $E_{h\nu}$ regions extensive vibrational excitation of HI$^+$($X^2\Pi$) up to v$^+$ ~ 12 are noticeable. A broad diagonal pattern spreading around ΔE = 14 - 14.5 eV is ascribed to the formation of the HI$^+$($A\,^2\Sigma^+_{1/2}$) state.

Figure 1(b) represents the curve obtained by summing electron counts over the whole E_k range as a function of $E_{h\nu}$. A broad peak centered at $E_{h\nu}$ ~ 12.3 eV can be seen on the curve. In analogy to HBr, this broad peak can be assigned to $5d\pi$ HI*(R_A) state. The 2D-PES exhibits strong vibrational excitation of HI$^+$($X^2\Pi$) over an $E_{h\nu}$ region from ~12 to 13.7 eV, which is attributable to autoionizing feature of the $5d\pi$ HI*(R_A) state [1]. In addition to the patterns due to molecular ionization, vertical stripes running parallel to the photon energy axis can be seen around ΔE = 13.5 - 14 eV. They are assigned as resulting from autoionization of the atomic Rydberg states I*[$R(^3P_{0,1})$] converging to I$^+$($^3P_0$ or $^3P_1$). The overall reaction scheme for the formation and autoionization of the iodine atom is described as follows [1]:

$$HI(X^1\Sigma^+) + h\nu \rightarrow HI^*(R_A) \qquad (1a)$$
$$HI^*(R_A) \rightarrow HI^*[R(^4\Pi_{1/2})] \qquad (1b)$$
$$HI^*[R(^4\Pi_{1/2})] \rightarrow H(^2S_{1/2}) + I^*[R(^3P_{0,1})] \quad (1c)$$
$$I^*[R(^3P_{0,1})] \rightarrow I^+(^3P_2) + e^- . \qquad (1d)$$

In process (1d) the electron kinetic energy is definitely determined by the energy difference between atomic energy levels of I*[$R(^3P_{0,1})$] and I$^+$($^3P_2$), and independent of the initial excitation energy in process (1a). As a consequence, autoionization of I*[$R(^3P_{0,1})$] should give rise to vertical stripes running parallel to the $E_{h\nu}$ axis on the 2D-PES.
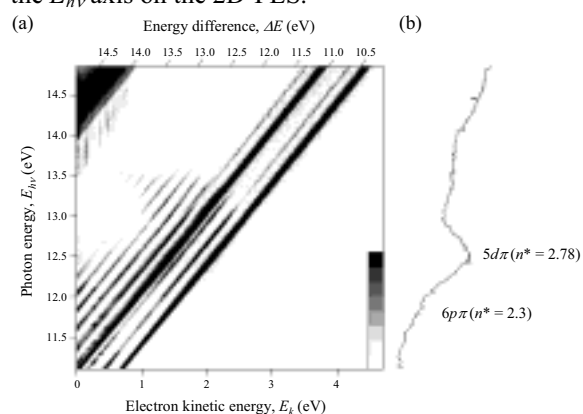
Fig. 1 (a) Two-dimensional photoelectron spectrum of HI in $E_{h\nu}$ = 11.10 - 14.85 eV. The electron yield, measured as a function of both $E_{h\nu}$ and E_k, is presented by the plots with eight tones from light to dark on a linear scale. Diagonal lines attached on the top of this figure denote the energy difference defined by ΔE = $E_{h\nu}$ - E_k. (b) The curve obtained by summing electron counts over the whole range of E_k as a function of $E_{h\nu}$.

[1] Y. Hikosaka and K. Mitsuke, J. Chem. Phys. submitted.

A Toroidal Electron Analyzer for Observing Anisotropic Electron Emissions Following Molecular Inner-Shell Photoabsorption

Y. Hikosaka and E. Shigemasa

UVSOR Facility, Institute for Molecular Science, Okazaki 444-8585

Molecular inner-shell photoabsorption processes leading to both discrete and continuum states are intrinsically anisotropic, since an anisotropic orientational distribution of molecules is determined by the orientation of the transition dipole moment relative to the electric vector of the light. This anisotropy is reflected in the angular distribution of the products created either from the initial core hole state or from states following the rapid decay. Processes like photoelectron emission, Auger electron ejection, fluorescence, and photodissociation, all bear the vestige of the symmetry of the initial excited state.

An electron analyzer with toroidal shapes is one of the most suitable analyzers to observe the anisotropic electron emissions, owing to the simultaneous multi-energy and multi-angle detection with a reasonably-high energy-resolution. Recently, a "double toroidal" electron analyzer, which has been originally developed by a French group [1], has been constructed. The analyzer consists of a four element electrostatic conical lens and two toroidal deflectors connected, as illustrated in Fig. 1. The conical symmetry of the lens system limits the detection angle of electrons to 54.7° with respect to the cylindrical symmetry axis of the analyzer. The incident electrons are focused by the lens, and then dispersed in energy between the double toroidal deflectors, and may reach a delay-line-type imaging detector (Siegmund Scientific) mounted on the output plane. The imaging detection without any exit slit enables us to observe electrons within an energy range more than 10 % of the pass energy. Figure 2 shows an observed image for Kr $M_{4,5}N_{2,3}N_{2,3}$ Auger lines with kinetic energies in 50-57eV. The Auger lines are partially resolved, and accordingly four or more concentric circles are seen on the image. Since we set the cylindrical symmetry axis of the analyzer to be parallel to the electric vector of the incident radiation, no anisotropy should essentially be observed along the concentric circles. However, the concentric circles in Fig. 2 are, in practice, far from isotropy; particularly, a lack of intensity is detected at the top-right part of the image, which is due to a potential distortion by a gas nozzle. The other minor intensity modulations on the concentric circles are probably due to a transmission-efficiency fluctuation depending on angle. Actually the analyzer has three supporting struts in the lens system to keep its geometrical structure appropriate, which may induce insensitive areas on the detector.

The acceptance solid-angle of the analyzer is estimated to be about 6×10^{-2} sr. Such large acceptance angle is suitable to coincidence measurements. One of our plans is to combine this electron analyzer with an imaging analyzer for ion momentum observation. The coincidence setup would enable us to observe anisotropic electron emissions in molecular frame.
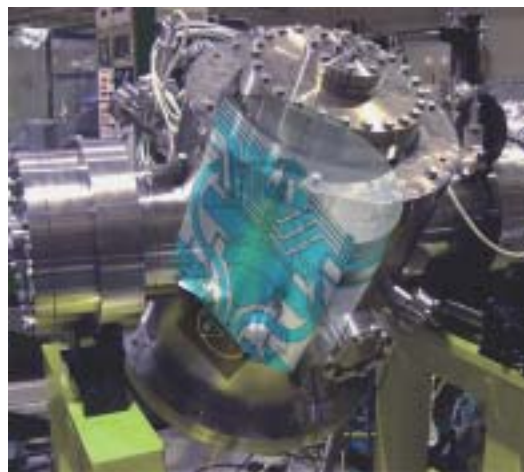
Fig. 1   A side view of the chamber with a schematic cutting image of the toroidal electron analyzer.
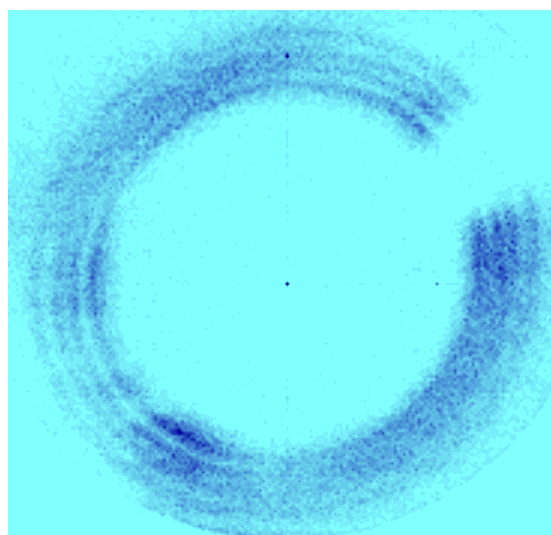

Fig. 2   An image observed by a delay-line-type imaging detector. The Kr $M_{4,5}N_{2,3}N_{2,3}$ Auger lines with kinetic energies in 50-57eV are partially resolved. A lack of intensity at the top-right part of the image is due to a potential distortion by the gas nozzle.

[1] C. Miron et al, *Rev. Sci. Instrum*. **68**, 3728 (1997).

Observation of Vacuum Ultraviolet Fluorescence Following the N 1s Excitations of N_2O

Y. Hikosaka and E. Shigemasa

UVSOR Facility, Institute for Molecular Science, Okazaki 444-8585

Resonant Auger is the dominant decay process of molecular core-excited states. The dynamics of the resonant Auger transition, which is closely related to the electronic structure of the core-excited state, has received considerable attention, often in connection with state-specific fragmentation induced by core-excitation. Electron spectroscopy is the standard means to investigate Auger final-states accessed from each core-excited state, and many interesting findings such as lifetime/vibrational interference, detuning effects, fragmentation dynamics etc., have been studied in great detail.

When the Auger final-states have sufficient internal energies, fluorescence may be emitted from either the molecular ions or fragments formed through dissociations of the molecular ions. The ultraviolet fluorescence may be a unique probe for identifying the multielectron processes such as double excitations in the core ionization continua, because it is expected that such processes may lead to highly-excited molecular ions, fragment ions, and neutral fragments produced after the Auger decays.

We have constructed a 0.3-m Seya-Namioka-type fluorescence spectrometer, for observing the vacuum ultraviolet fluorescence following the molecular inner-shell excitation. A photo of the spectrometer is shown in Fig. 1. The dispersed fluorescence is detected by a position sensitive detector composed of three microchannel plates and a resistive anode encoder, where the front microchannel plate is coated by CsI. The position sensitive detector enables us to observe the fluorescence spectrum with its spectral range about 300 Å simultaneously. The wavelength resolution is estimated to be about 5 Å.

As our first attempt, we have measured the vacuum ultraviolet fluorescence from N_2O at the N 1s excitation region. Figure 2 indicates dispersed fluorescence spectra at the incident photon energies of 401 and 424 eV, where the $\pi^*(N_t)$ and σ^* resonances lie, respectively. The wavelength region simultaneously-observed was set to 450-750 Å, though we did not calibrate the wavelength precisely; an error within a few tens of Å is anticipated in the wavelength scale of Fig. 2. Many fluorescence lines can be seen in the spectra. Most of the lines in the short wavelength region may be regarded as corresponding to the transitions between ionic states, probably the emissions from atomic fragment ions; however, at the present stage we do not attempt to assign the fluorescence lines, due to the anticipated error in the wavelength scale. The same fluorescence lines are observable in the two spectra, implying that the $\pi^*(N_t)$ and σ^* core-excited states result in

producing the same fluorescing species. In contrast, the Auger final states following these two core-excited states should be quite different from each other, according to the electronic properties of the core-excited states. The present observation suggests that most of the fluorescing species are not the molecular Auger final states, but the excited fragments produced by the dissociations after the core-hole relaxations. One interesting aspect seen in Fig. 2 is that the intensity ratios of several peaks between the two spectra are apparently different: the peaks at 460 and 510 Å in the spectrum of 424 eV is stronger than those of 401 eV, while the peaks at 610 Å exhibit the opposite behavior. This reflects different Auger final-states accessed by the resonant Auger processes.

Fig. 1   A photo of the vacuum ultraviolet fluorescence spectrometer.
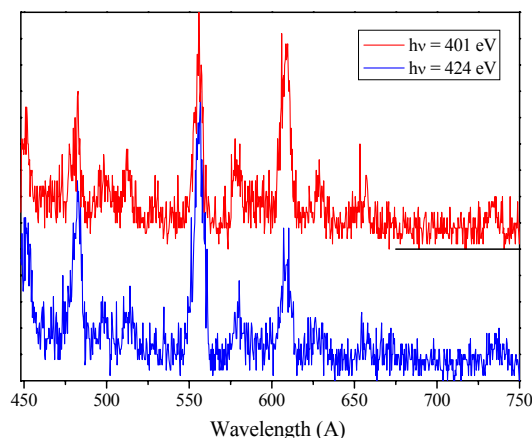

Fig. 2   Dispersed fluorescence spectra from N_2O measured at two different photon energies.

GAS PHASE SPECTROSCOPY

Blue Shift of UV Emission Band by Inner-core Excitation on InAlGaN

S. Naoe, K. Okada*, S. Hamaura*, S. Hamada*, K. Kimura*,
K. Fukui*, H. Hirayama**

Faculty of Engineering, Kanazawa University, Ishikawa 920-1192, Japan
* Research Center for Development of Far-Infrared Region, Fukui 910-8507, Japan
** The Institute of Physical and Chemical Research, Wako 351-0198, Japan

UV emission on InAlGaN where In takes a role increasing luminosity are obtained by band-to-band excitation and also by inner-core excitation. On the previous research [1], UV emission band (B band) excited by Al-K inner-core excitation showed shift of the peak position to the higher energy side with the wider half width of the band, by comparing with the B band excited by band to band energy region. This time, the measurement for N-K inner-core excitation was performed and the samples of several content of In element were examined

Experiments

A cryostat of Liq. He flow type was used, because the emission becomes remarkable at low temperature. Measurements were carried out at BL1A , BL8B1 and BL7B, for Al K core electron, N K core and band-to-band excitation regions, respectively. The luminescence was caught by an optical fiber inserted into vacuum chamber and detected by a CCD system attached to a spectrometer. This time, a hemispherical lens was set onto the tip of the optical fiber, so the intensity of signals was attained to increase by three times.

There is left an important technical problem to retain the same precision on calibrating the spectrometer among the each measurement on a different beam port, where the wavelength calibration is usually done to set a Hg lamp at the position of a sample holder, no changing the alinement of the optical system after the measurement.

The measurement to study B band in varying the luminance brightness is necessary, because the behavior of B band resembles to the case of the blue shift on semiconductors, where the blue shift is known to become on progress by increasing the luminance brightness of the excitation light. We tried measurement at such a time as just after beam injection, decrement state of beam current, preparation driving mode or single bunch driving mode of an accelerator and furthermore changed a monochromator crystal KTP to InSb or to Beta-alumina in BL1A.

Results

Results are shown in Fig.1. The B band is shown as B and the emission band in visible region as Y in the figure. The samples were grown on a substrate SiC. The exciting light becomes to reach at the substrate in proportional to the increase of the order of exciting light. The luminescence from SiC dose not existed in the energy region of B band, therefore the SiC substrate makes no matter for the study of B band. Similar results are obtained for $In_{0.05}Al_{0.12}Ga_{0.83}N$ and $In_{0.04}Al_{0.35}Ga_{0.61}N$. As seen from Fig.1, B band varies as the manner as if it would include the shape of the band itself toward to higher energy side by increasing the energy of the excitation light (4 to 400 to 1500eV). This behavior will be understood as that the band filling occurs in our samples in resemblance to the case of semiconductors.

Many electrons and holes (the order of 10^2) are produced due to the inner-core hole relaxation. They are concentrated to occupy the bottom part of conduction band or of the top part of the valence band. An electron occupied a state a little above the lowest energy state of conduction band becomes to make transition toward a hole in the valence band, emitting a photon whose energy value corresponds to the higher energy part of the B band on the axis of abscissa of luminescence spectra. Thus the blue shift of B band realizes in inner-core excitation. As the order of photon number in BL1A and BL8B1 is not enough to make band filling, then the transition will occur around the inner-core excited element before the electrons and holes fully relax to move into the whole area of the crystal.
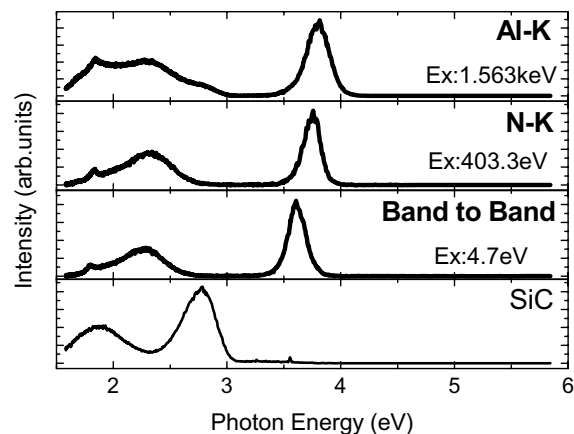

Fig. 1. UV and visible emission spectra on $In_{0.05}Al_{0.20}Ga_{0.75}N$. Energy values of excitation light correspond to band-to-band and inner-core excitation.

[1] K.Okada, K. Fukui, S. Naoe, S. Hamaura, H. Hirayama, Y. Aoyagi : UVSOR Activity Report 2002, 159 (2003).

UV Spectroscopy on Condensed Oxygen under Pressure

Y. Akahama, T. Moriwaki and H. Kawamura

Department of Material Science, Graduate School of Science, Himeji Institute of Technology, Kamigohri, Hyogo 678-1297, Japan

Recently, metal-insulator transition has been reported in highly condensed oxygen. Many arguments have also been made on the formation of O_4 molecular in condensed phase up to now. In order to understand the phenomena from the electronic structure of molecules, the study of electronic spectra on condensed oxygen is indispensable.

Our recent studies on VUV absorption spectra of condensed oxygen up to 13 GPa have revealed that in super-critical fluid of oxygen, a relatively strong absorption band was observed in a UV region between 5 eV and 7 eV and the valence band of the β solid phase was developed from the new UV band. Therefore, the nature of the new band holds the key to clarify the phenomena. In this study, detailed absorption experiments have been carried out in a wide temperature range from 15K to 300 K.

Experimental

Liquid oxygen was loaded in the sample chamber of a sapphire-anvil pressure cells and pressure was regulated at 300 K based on a ruby pressure scale. The typical thickness and diameter of the sample chamber were about 46 μm and 250 μm, respectively. The UV absorption measurements were developed over a range from 0.2 to 1.5 GPa using VUV source at the BL-B1. Low temperature measurements were also carried out in a liquid-He spray-type cryostat.

Results and Discussion

Figure 1 shows the absorption spectra of condensed oxygen at pressures up to 1.5 GPa at 300 K. The spectra were measured using a sapphire anvil cell. The absorption spectra show a photon energy dependence of $(E-E_0)^{3/2}/E$ corresponding to a forbidden transition between a direct band gap, E_0, in a solid. From the dependence, E_0 was estimated to be 4.7 eV and independent on pressure. The coefficient: α for a photon energy of 5.5 eV increased linearly with increasing pressure. The absorption cross-section, which was estimated from the molar volume vs pressure relation recently obtained from our x-ray diffraction experiments, were consistent with the earlier data to 20 atm [1].

Figure 2 shows the temperature dependence of the spectra. With decreasing temperature, the sample pressure of 0.41 GPa at RT deceases to 0.1 GPa at 90 K. The sample transformed to the γ-O_2 solid phase with cooling to 80 K and the β-O_2 phase to 60 K and further to the α-O_2 phase at 30 K. The spectra reflect the pressure change as well as these phase transitions. We should note that a dumping of transmitting light

occurred for the α-O_2 phase due to light-scattering at the crystal grains boundary.

One probable explanation of the nature for the new absorption band is that the Herzberg system of the $^3\Sigma_g^- \rightarrow ^3\Sigma_u^+$ or $^3\Delta_u$, $^1\Sigma_u^-$ transitions becomes allowed as the result of an intermolecular interaction, though it is basically forbidden by parity selection rules. The formation of $(O_2)_2$ molecular units may be enable to allow the transition. The fact that two molecules transition was observed relatively strong in the α-O_2 phase, means that the true character of the dimer is an antiferromagnetic O_2 pair. The pair is stabilized with increasing pressure.
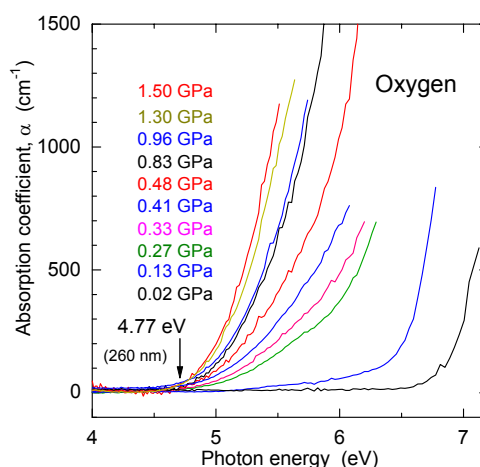

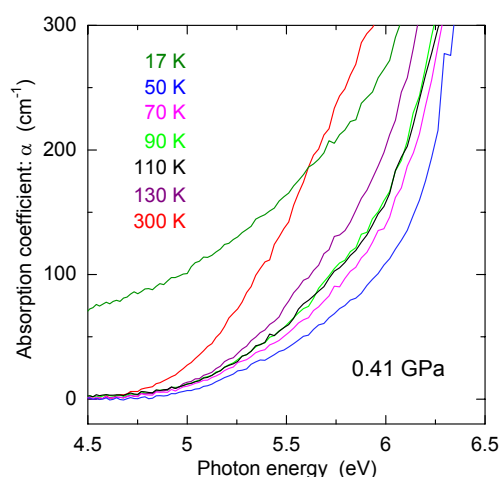Fig.1 UV absorption spectra of condensed oxygen at various pressures at RT.

Fig. 2 UV absorption spectra of condensed oxygen at various temperatures. Sample pressure was 0.41 GPa at room temperature.

[1] Shardamand, Phys. Rev**. 186**(1969)5.

Photoluminescence of Hydrogen-bonded Ferroelectrics CsH$_2$PO$_4$

T. Fuyuki, N. Ohno
K. Deguchi*

*Division of Electronics and Applied Physics, Graduate School of Engineering
Osaka Electro-Communication University, Neyagawa, Osaka 572-8530, Japan.
* Shizuoka Institute of Science and Technology, Fukuroi, Shizuoka 437-8555, Japan.*

Cesium dihydrogen phosphate CsH$_2$PO$_4$ (CDP) is one of hydrogen-bonded ferroelectrics. CDP shows a first-order ferroelectrics phase transition from monoclinic $P2_1/m$ to orthorhombic $P2_1$ at T_C = 156 K. The PO$_4^{3-}$ tetrahedra are linked to linear chains by hydrogen bonds along the b-axis, which is in contrast to well-known KH$_2$PO$_4$ (KDP) with the three-dimensional linkage of the hydrogen bonds.

The reflection and absorption spectra of CDP have been reported in the VUV region by our group [1]. The first reflection peak is observed at 10 eV. The spectrum near the fundamental absorption edge is quite similar to the previous results of KDP [2,3]. The absorption edge is located at 7.40 eV at 12 K. The temperature dependence of the absorption-edge energy was investigated in detail at around the T_C, showing an anomalous shift at T_C.

In the present study, photoluminescence and photo-excitation spectra of CDP have been investigated at the BL1B station. The optical measurements of KDP were also carried out for comparison. The specimens of CDP and KDP were grown at about 50°C by slow cooling of a saturated aqueous solution after several times of recrystallization.

Figure 1 shows the luminescence (left-hand side) and the excitation (right-hand side) spectra of CDP measured at 12 K. The luminescence spectrum was excited with 7.50 eV photons. Two luminescence bands are observed at 3.95 eV and 5.12 eV. The dash line in the figure is the absorption-edge spectrum at 12 K [1]. The 3.95 eV band is mainly induced at the excitation on the low-energy side of the absorption edge. On the other hand, the 5.12 eV band is stimulated with photons above the fundamental absorption edge. In the case of KDP, a single luminescence band is observed at 5.26 eV as shown in Fig. 2. The excitation spectrum of the 5.26 eV band of KDP is similar to that of the 5.12 eV band of CDP. These luminescence bands exhibits a Gaussian lineshape and a large Stokes shift, induced under the excitation into the fundamental absorption region. Thus, it is likely that these luminescence bands are intrinsic in origin.

The temperature dependence of the luminescence spectra was investigated for both materials. Unfortunately, these luminescence bands are found to be unstable at high temperatures; the luminescence bands are thermally quenched at ~ 80 K far below T_C.
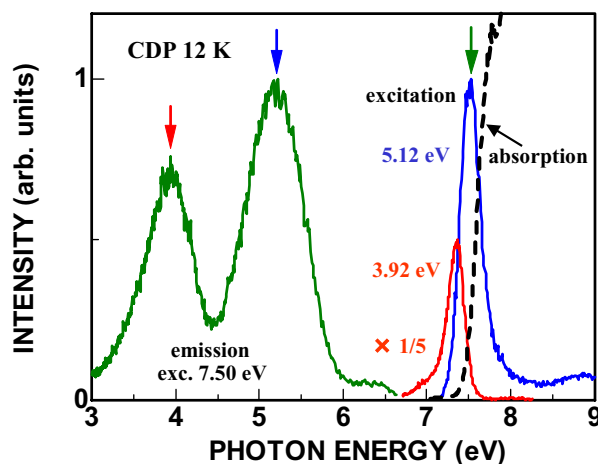
Fig. 1. Luminescence, excitation and absorption spectra of CDP at 12 K.
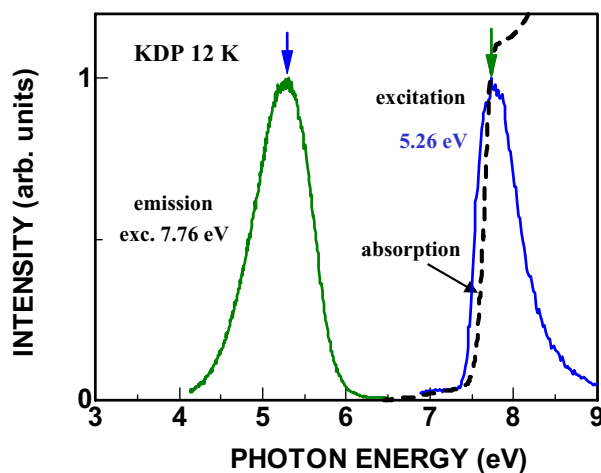

Fig. 2. Luminescence, excitation and absorption spectra of KDP at 12 K.

[1] T. Fuyuki, N. Ohno, K. Sasaki and K. Deguchi, UVSOR Activity Report 2002, **30** (2003) 106.
[2] S. Saito, K. Wada and R. Onaka, J. Phys. Soc. Jpn. , **37** (1974) 711.
[3] S. Matsumoto, M. Fujisawa and S. Suga, J. Electron Spectrosc. Relat. Phenom., **79** (1987) 615.

SOLD STATE
SPECTROSCOPY I:
IR AND VUV

Nonuniform Distribution of Adsorbed Dye at the Water Surface Probed by Photoionization Methods

T. Ishioka and A. Harata

Department of Molecular and Material Sciences, Kyushu University, Kasugakoen 6-1, Kasuga-shi, Fukuoka 816-8680, Japan

Photocurrent has been measured at a dye-adsorbed and hydrophobic-acid-modified water surface by synchrotron radiation and Nd:YAG laser irradiation. Photocurrent increase was observed when submonolayer amount of acid was added. It is suggested that the increased current is caused by aggregate formation of dye and acid molecules from large pulse-to-pulse fluctuation of photocurrent by laser two-photon ionization experiments.

SR light has a merit in measuring threshold energies by its inherent tunability in photon energy compared to lasers. However, it is hard to attain microscopic information at the water surface by SR because of the difficulties to focus the SR light to the μm level on the water surface by using conventional optics. If self-assembled or aggregated species are present at the water surface, local deviations should be large in photoionization intensities or threshold energies that are not observed in the conventional method.

A solute in a bulk solution is known to photoionize at a lower photon energy than the ionization potential in the gas phase due to neighboring solvent molecules. Lowering of the ionization threshold can also be observed in the case of adsorbed molecules at an aqueous solution surface though remarkable differences in energies are observed.[1] However, it is not clarified how a solute interacts on photoionization with its surrounding molecules in aggregated or self-assembled cases. Furthermore, formed surface structures might distort photoionization process itself because long alkyl chain or charged group can scatter electrons emitted by photoionization. In this study, photocurrent is measured of a water-soluble dye with an aliphatic acid that form surface-layer by single-photon ionization using SR and two-photon ionization using a Nd:YAG laser.

Experimental

The monochromated synchrotron light (4-8 eV) was obtained from BL1B at the UVSOR facility and emitted from the chamber to the He-purged cell through an MgF_2 window. The emitted light was reflected on an Al mirror and vertically irradiated on the aqueous solution surface through a Cu-mesh electrode. The electrode was set at 5 mm high above the liquid surface and high voltage (500 V) was applied. The photocurrent (~100 fA) was measured by a picoammeter. For two-photon ionization measurements, third-harmonic of a Nd:YAG laser was focused on the solution surface by a lens using the same cell and the transient photocurrent was amplified by a current amplifier. The signal was monitored by an oscilloscope.

The sample solutions were composed of surface-active dye (rhodamine B, 10 μM), a buffer electrolyte (HCl, pH 1.0), and water. The aqueous solution surface was modified with aliphatic acid (arachidic acid, $C_{19}C_{39}CO_2H$) by spreading as a benzene solution. The added amount was approximately within two monolayers at maximum that is calculated by the assumption that close-packed layer was formed on the aqueous solution surface.

Results and Discussion

Figure 1 shows the plot of the photocurrent against the added amount of arachidic acid measured by two-photon ionization. The current intensity remarkably increases when a small amount of acid is added and decreases to a constant value above monolayer formation level. These experimental results cannot be explained by a simple model that is described by the uniform monolayer formation and simple electron scattering through the aliphatic monolayer because this model needs monotonous decrease of photoionization current upon film formation. At the concentration range of increased photocurrent, it is found that pulse to pulse deviation is remarkably increased. The increased fluctuation suggests the presence of small domains that are comparable to the focused area (10-100 μm). From above results, aggregate formation and accumulation of dye molecules around the aggregate is a most probable explanation for the results.
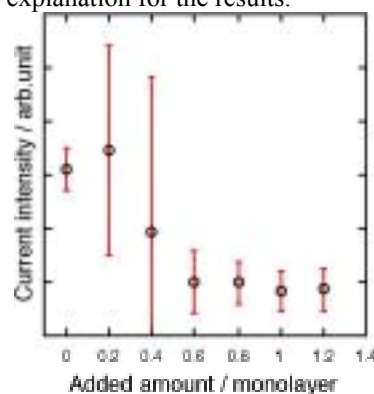

Fig. 1. Effect of arachidic acid addition on the photocurrent from the surface of rhodamineB aqueous solution by two-photon ionization. Bars indicate deviations of current intensities for each laser pulse.

[1] T. Ishioka, K. Seno, A. Harata, and Y. Hatano, *UVSOR Activity Report 2001*, 104.
[2] T. Ishioka, A. Harata, and Y. Hatano, *UVSOR Activity Report 2002*, 108.

Effects of Additives and Photodegradation on the Photoluminescence in Polypropylene

T. Ito, N. Fuse, Y. Ohki

Department of Electrical Engineering and Bioscience, Waseda University, Shinjuku-ku, Tokyo 169-8555 Japan

Photoluminescence (PL) and photoluminescence excitation (PLE) spectra were observed in polypropylene (PP) by irradiation of photons from synchrotron radiation (SR) at 300 K. The samples, some of which are additive free and the rest contain additives, are named as listed in Table 1.

Fig. 1(a) shows the PL spectrum induced in the sample PN by the irradiation of SR photons at 5.8 eV and its three Gaussian-fitted curves. Therefore, the sample PN has three PL component bands around 4.2, 3.6, and 3.1 eV, which are hereafter referred to as A1, A2, and A3, respectively. Fig. 1(b) shows the PLE spectra in the sample PN detected at 4.1 and 3.6 eV. Since curves 1 and 2 in Fig. 1(b) can be reasonably assumed to reflect mainly PLs A1 and A2 respectively, their respective PLE peaks are found to be around 6.2 and 5.3 eV. Note that the PLE spectrum of PN detected at 3.1 eV could not be obtained clearly with a good reproducibility since the PL component at 3.1 eV is very small and is superposed with the component at 3.6 eV. Further experiments have shown that all the other PP samples PA, PB, PC, and PD have similar PL and PLE spectra. Therefore, we conclude that the additives in PP do not contribute to the PLs.

In order to examine the effects of photodegradation on the photoluminescence, all the samples were pre-irradiated by 6.4-eV photons from the ArF excimer laser either in vacuum, air, or in oxygen. Fig. 2 shows the PL spectra induced by the irradiation of 5.6-eV photons in the pre-irradiated PN sample. The PL components A1, A2, and A3 are decreased by the pre-irradiation, and a new PL component, referred to as PL B, with its center around 2.9 eV is induced. The intensity of PL B becomes larger when the oxygen pressure during the pre-irradiation is lower. Note that similar results were observed in all the other samples. This result indicates that the same PL B appears in all the samples by the UV pre-irradiation.

At least two candidates are possible as the chromophores for PLs A1, A2, and A3. The first candidate is the α, β-unsaturated carbonyl, which is commonly present in impurities in organic polymers. This carbonyl has the following structure,

$$- CH_2 - CH = CH - C(=O) - CH_2 -.$$
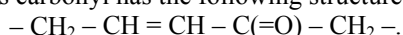
Namely, it has a pair of conjugated double bonds and is known to have a PL band around 4 eV, at an energy similar to PLs A1, A2, and A3. By the irradiation of UV photons, the α, β-unsaturated carbonyl becomes the β, γ-unsaturated carbonyl that has the following structure,

$$- CH = CH - CH_2 - C(=O) - CH_2 -.$$
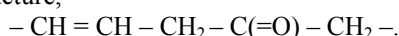
Namely, the two double bonds in the β, γ-carbonyl are not conjugated, and are not luminous. This may explain the disappearance of PLs A1, A2, and A3 in the pre-irradiated polymers. The other candidate is a polynuclear aromatic impurity, which is commonly present in organic polymers. Polynuclear aromatics are known to have a PL band around 4 eV, of which intensity decreases if the sample is subjected to irradiation of UV photons.

Table 1. Samples Examined.

Name	Polymer	Additive
PN	PP	Free
PA	PP	AO
PB	PP	N
PC	PP	SA
PD	PP	AO, N, SA

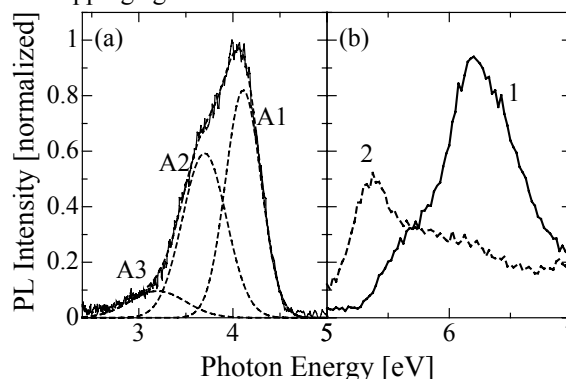(Note) AO: antioxidant; N: neutralizer; SA: slipping agent.

Fig. 1   (a) PL spectrum in the sample PN. (b) PLE spectra detected at 4.1 eV (curve 1) and 3.6 eV (curve 2) in the sample PN.
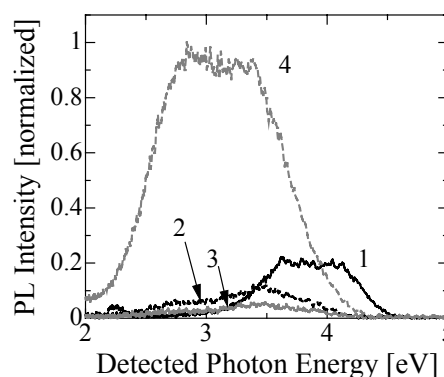

Fig. 2   Effects of pre-irradiation of UV photons in various atmospheres on PL spectra. Curve 1: as-received, 2: pre-irradiated in air, 3: pre-irradiated in oxygen, 4: pre-irradiated in vacuum.

Optical Properties of Ammonium Chloride Doped with Tl$^+$ Ions

T. Kawai, S. Hashimoto

Department of Environmental Sciences, Faculty of Science, Osaka Women's University,
Daisen- cho 2-1, Sakai City, Osaka 590- 0035, Japan

Ammonium halides are ionic crystals having the similar crystal and electronic structures as alkali halides. Since alkali halide crystals have played an important role as a host material for Tl$^+$- type ions such as Tl$^+$, Pb^{2+}, and Au$^-$ [1], ammonium halide crystals are also an attractive host material for a number of Tl$^+$- type ions. However, the optical properties of the Tl$^+$ ions doped in ammonium halides are comparatively less studied, especially up to the vacuum ultraviolet energy region.

Single crystals of NH$_4$Cl:Tl$^+$ were grown from saturated aqueous solution containing various TlCl concentrations from 10^{-2} to 10^{-6} mole %. Urea was added into the solution as a habit modifier in order to obtain the good cube shaped samples. Optical measurements up to the vacuum ultraviolet energy region were performed at a BL-1B beam line of UVSOR. The samples were mounted on the cold stage of a flow- type cryostat and cooled down to 13 K. The light beam from the 750 MeV electron storage ring of the synchrotron radiation was monochromatized through a 1 m Seya- Namioka type monochromator. The luminescence and excitation spectra were measured by using an optical detection system composed of a grating monochromator (Jobin Yvon HR320) and a photomultiplier (Hamamatsu R955).

In the NH$_4$Cl:Tl$^+$ crystals, the A and C absorption bands due to the cationic transition in the Tl$^+$ ion are observed at 5.22 and 6.59 eV, respectively [2]. Under the excitation on the A absorption band at 13 K, the broad luminescence band peaking at 4.35 eV is dominantly observed. When the C absorption band at 6.59 eV is excited, the luminescence band peaking at 3.37 eV appears in addition to the 4.35 eV band, as shown in Fig. 1 (a). Fig. 1 (b) shows the excitation spectra for both the luminescence bands. The excitation spectra for the 3.37 and 4.35 eV luminescence bands exhibit no response above the energy region of the intrinsic exciton transition and the strong one on the A and C absorption bands. Since there is the response on the lowest A absorption band in the excitation spectra, the luminescence bands should be ascribed to the reverse transition of the A absorption: the radiative transition from the relaxed excited states of $^3P_1$ in the Tl$^+$ ion. The 4.35 and 3.37 eV luminescence bands would be interpreted as the radiative transitions from the two Jahn-Teller minima having the trigonal (X) and tetragonal (T) symmetry on the adiabatic potential energy surface, respectively, from the analogy with the A$_X$ and A$_T$ luminescence bands of the Tl$^+$ center doped in the cesium halides [3].

By the way, the cesium halide crystals doped with the Tl$^+$ center exhibit the luminescence bands due to the perturbed self- trapped exciton in the visible region, in addition to the A$_X$ and A$_T$ luminescence bands [3]. The causes have been ascribed to the ion arrangements around the Tl$^+$ ion [3]. That is to say, the Tl$^+$ ion doped in CsCl- type cesium halides is surrounded by the eight nearest halogen ions in the different way from the Tl$^+$ ion surrounded by the six nearest halogen ions in NaCl- type alkali halides. However, the Tl$^+$ center doped in ammonium chloride with the CsCl crystal structure exhibits no luminescence band due to the perturbed self-trapped exciton even under the excitation on the higher absorption bands. The characteristic features of the luminescence and excitation spectra of NH$_4$Cl:Tl$^+$ are similar to those of the Tl$^+$ center doped in the NaCl- type alkali halides. This fact indicates that the luminescence bands due to the perturbed self- trapped exciton are not induced by the eight nearest halogen ions around the Tl$^+$ ion.
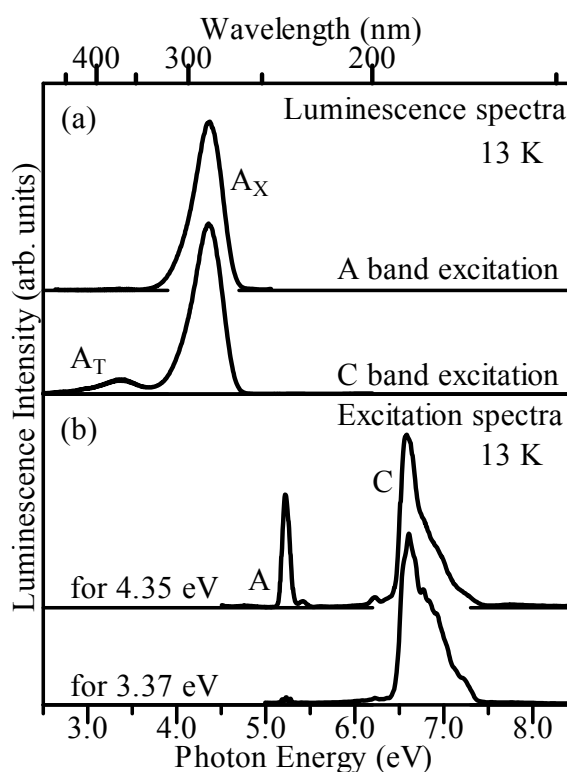

Fig.1. (a) Luminescence spectra
(b) Excitation spectra

[1] P. W. M. Jacobs: J. Phys. Chem. Solids **52** (1991) 35.

[2] T. Kawai and S. Hashimoto: J. Phys. Soc. Jpn. **21** (2002) 2566.

[3] S. Zazubovich, A. Voloshinovskii and G. Stryganyuk: phys. stat. sol. (b) **233** (2002) 238.

Vacuum-ultraviolet Reflectance Spectroscopy of Transition-metal Oxides and Chalcogenides

M. Matsubara[1], S. Miyasaka[1], Y. Shimada[1], and Y. Tokura[1,2,3]

[1] *Department of Applied Physics, University of Tokyo, Tokyo 113-8656*

[2] *Correlated Electron Research Center (CERC), National Institute of Advanced Industrial Science and Technology (AIST), Tsukuba 305-8562*

[3] *Spin Superstructure Project, ERATO, Japan Science and Technology Corporation (JST), Tsukuba 305-8562*

One of the most important characteristics for the correlated electron systems is the drastic re-construction of electronic structure over an energy scale of eV with changes of temperature, doping concentration, and/or external field. Therefore, optical reflectivity measurement over a wide energy range and the optical conductivity spectra derived from the reflectivity spectra provide us with very useful information about the strongly correlated electron systems.

In this beam time, we measured the reflectivity spectra of several transition-metal oxides and chalcogenides, including V, Cr, Mn, Fe and Mo, for an energy range of 4 eV < E < 35 eV at room temperature using the beam line BL1B. The measured reflectivity data, together with the lower-energy data below 6 eV, were used to derive the optical conductivity spectra or dielectric function via the Kramers-Kronig analysis. As an example, the imaginary part of the dielectric function of a single crystal of $GaFeO_3$, which is grown by a floating zone method, is shown below.

$GaFeO_3$ is a prototypical polar ferrimagnet and shows magneto-electric effect at low temperatures. The absorption bands indicated as A and B correspond to transitions from O $2p$ to Fe $3d$ state and the bands denoted as C and D are due to the transition between O $2p$ and Ga $4s$ levels. This system has two sites of Fe and Ga. The different sites of Fe and Ga may cause the splitting (A and B, C and D). The structure indicated as E corresponds to the transition from O $2s$ to Fe $3d$ state.
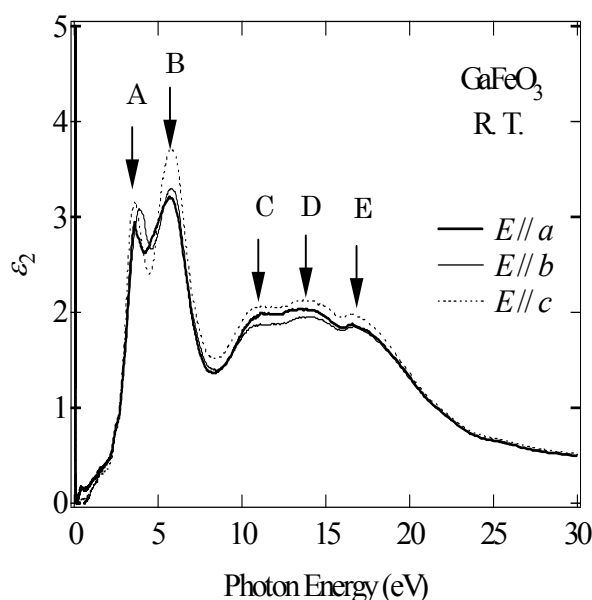

Figure. Imaginary part of dielectric function for polarization configurations of *E//a*-, *b*- and *c*-axis in $GaFeO_3$.

Reflection Spectrum and Auger-Free Luminescence in Cs$_2$ZnCl$_4$

A. Ohnishi, M. Kitaura* and M. Sasaki

Department of Physics, Faculty of Science, Yamagata University, Yamagata 990-8560 Japan
* Fukui National College of Technology, Geshi, Sabae 916-8507 Japan

Cs$_2$ZnCl$_4$ is orthorhombic and belongs to *Pnam* space group. In this material, thermo-chemical properties, dielectric properties and so on have been studied [1,2]. As for optical properties, however, there are only a few reports on absorption and emission spectra in the infrared region of a Cs$_2$ZnCl$_4$: Co^{2+} [3]. In this paper, we report the observation of the Auger free (AF) luminescence emitted from Cs$_2$ZnCl$_4$, in addition to that of the fundamental absorption.

Cs$_2$ZnCl$_4$ crystals were prepared by evaporating a stoichiometric mixture of solutions of CsCl and ZnCl$_2$. Experiments were performed at the BL1B of UVSOR equipped with a 1-m Seya-Namioka VUV monochromator. Reflection spectra were measured with a photomultiplier (Hamamatsu R105) coated by sodium salycilate phosphor. Luminescence from the sample was measured using a quartz lens, a grating monochromator (Jobin Yvon HR 320) and a photomultiplier (Hamamatsu R955).

Figure 1 shows the reflection spectrum of Cs$_2$ZnCl$_4$ at 10 K. Sharp bands are observed at 7.15, 7.67 and 8.78 eV. We tentatively assign the 7.15 eV band to the $n = 1$ exciton absorption, which is due to the transition from the Cl 3p valence band (VB) to the Cs 6s conduction band (CB) on the basis of the calculation of the electronic state for a [Cs$_3$ZnCl$_4$] cluster with the DV-Xα method. In the range of 13−14 eV, some weak peaks are observed. The transition energy of 13 eV is in almost agreement with the sum of the band gap energy E$_g$ = 7.95 eV and the energy difference E$_{vc}$ = 5.0 eV between the top of VB and that of the outermost core band. Thus, the peaks are attributed to the transitions from the core level to the conduction band.

It should be noticed that E$_g$ is larger than E$_{vc}$ in Cs$_2$ZnCl$_4$. This suggests the possibility that the AF luminescence is observable in this material. Figure 2 shows the emission spectrum observed at room temperature (RT) under excitation with 14.0 eV light. An intense luminescence band appears at 4.15 eV, along with a weak band at 3.31 eV.

In Fig. 3, the excitation spectrum for the 4.15 eV band is plotted. The excitation spectrum for the 3.31 eV band was practically the same as that for the 4.15 eV band. The spectrum rises from the energy position around 13 eV, and the intensity is almost constant in the range of 16−22 eV and increases above around 23 eV. It is noteworthy that the observed threshold energy corresponds to the onset of the transition between the outermost core level and the conduction band. On the basis of this, we suppose that both of the 4.15 eV and 3.31 eV bands come from the radiative recombination between the valence electron and the
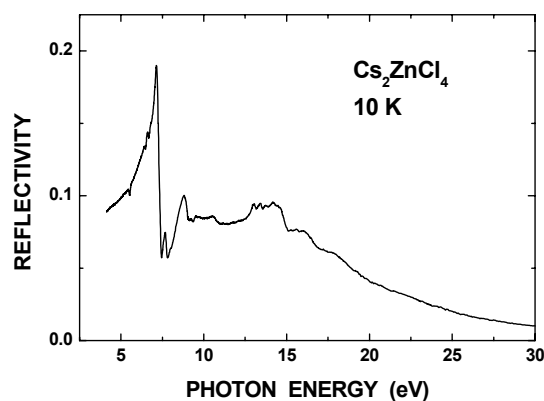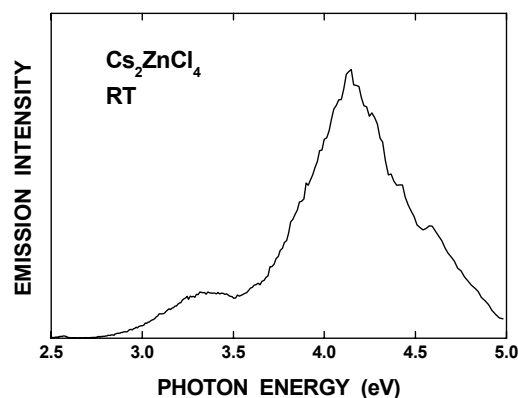
outermost core hole.

Fig. 1

Fig. 2

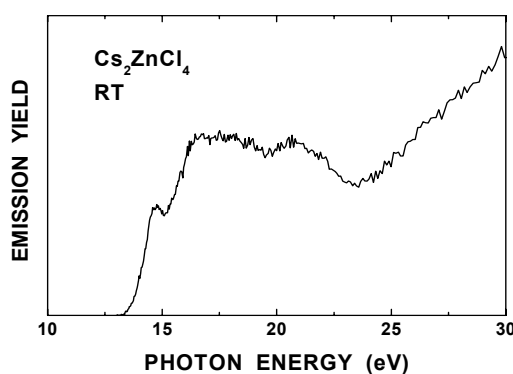**Fig. 3**

[1] F. Ying, L. Liangchao and Q. Songsheng: Thermochimica Acta **303** (1997) 187.
[2] A. Onodera, O. Watanabe, H. Haga, K. Kikuta, E. Suzuki, H. Yamashita and Y. Shiozaki: Ferroelectrics **125** (1992) 141.
[3] P. J. Deren, J. Derouet, P. Porcher and D. Svoronos: J. Mol. Struct. **404** (1997) 167.

Superlattice Structure and Optical Spectroscopy of SrMgF$_4$:Ce^{3+} Crystals

M. Yamaga[1], K. Itoh[1], S. Yabashi[1], Y. Masui[1], S. Ono[2], M. Sakai[2], and N. Sarukura[2]

[1]*Department of Electric and Electronic Engineering, Gifu University, Gifu 501-1193, Japan*
[2]*Institute for Molecular Science, Okazaki 444-8585, Japan*

Laser action was reported on interconfigurational transitions in LiYF$_4$:Ce^{3+} and LiCaAlF$_6$:Ce^{3+}. However, it has not been achieved for other fluorides crystals in spite of their high energy band gaps. We reported VUV spectroscopy of CaF$_2$ codoped with Ce^{3+} and Li$^+$/Na$^+$ at low temperature[1]. As Ce^{3+} substitutes for Ca^{2+} in CaF$_2$, charge compensators, for example, Li$^+$/Na$^+$ ions are required. It was found from the VUV spectra that several Ce^{3+} centers are perturbed by the charge compensators located at different nearest neighbors.

We have grown SrMgF$_4$ crystals doped with Ce^{3+} as a new laser material using the Bridgmann -Stockbarger method. The x-ray diffraction analyses for the SrMgF$_4$:Ce^{3+} crystals indicate the existence of superlattice structure. As the superlattice structure has several different Sr^{2+} lattice sites which are replaced by Ce^{3+}, it is expected to perform wider tuning. In this report, the relation between optical properties of various Ce^{3+} centers and the superlattice structure is discussed.

The optical absorption spectrum of the SrMgF$_4$:Ce^{3+} crystals in VUV range measured at 15 K is shown at the top of Fig. 1. There are several broadbands with peaks at 1400, 1500, 1800, 2200, 2500 and 2750 Å in the VUV and UV ranges.

The 140-nm VUV excitation produces two different luminescence bands with double peaks at (21500, 23500 cm^{-1}) and (24500, 26500 cm^{-1}), respectively, denoted by A and B. The 205-nm and 217-nm UV excitations produce different luminescence bands with double peaks at (30000, 32000 cm^{-1}) and (31500, 33500 cm^{-1}), respectively, denoted by C and D. The excitation spectrum of the A-band luminescence consists of two intense bands at 1800 and 2000 Å and weak three bands at 2500, 3150, 3800 Å. Similarly, the excitation spectra of the B, C and D luminescence bands are shown in Fig.1. Remarkable features of these luminescence and excitation spectra are as follow as.

(1) The luminescence spectra of A, B, C and D consist of two broadbands with separation energies of about 2000 cm^{-1}.

(2) The excitation spectrum of the A bands with lower energy peaks spread from 1700 to 3800 Å. On the other hand, the excitation spectrum of the D bands with higher energy is composed of five bands located at narrow range of 1500-2500 Å.

These results suggest relation between the superlattice structure of SrMgF$_4$ and crystal field of Ce^{3+}. The x-ray diffraction analyses show four different polyhedra of Sr coordinated with nine, ten and eleven fluoride ions. The large number of coordination may correspond to the large crystal filed splitting, resulting in red shift of the Ce^{3+} luminescence. Then, in the order of D, C, B and A, the crystal field splitting becomes small.

[1] M. Yamaga, S. Yabashi, Y. Masui, M. Honda, H. Takahashi, M. Sakai, N. Sarukura, J.-P.R. Wells, and G.D. Jones, J. Lumin. (2004) in press.
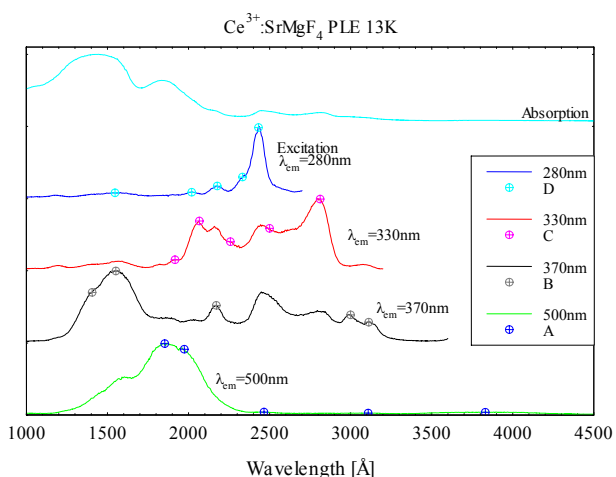
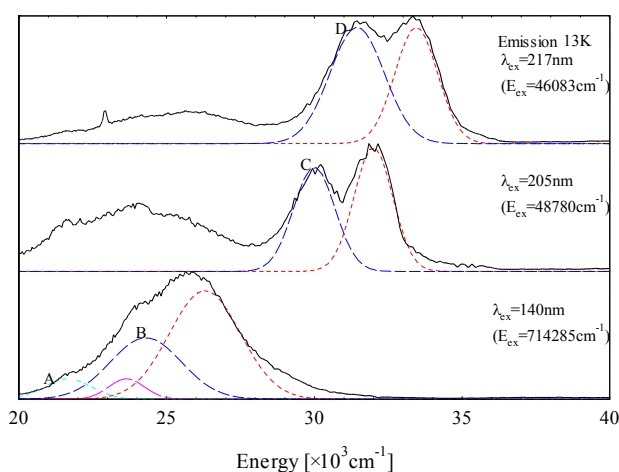Fig.1 Absorption and excitation spectra of Ce^{3+} in SrMgF$_4$

Fig.2 Luminescence spectra of Ce^{3+} in SrMgF$_4$

The Measurement of the Transmission Spectrum of an Amorphous Semiconductor Thin Film

K. Hayashi

Department of Electrical and Electronic Engineering, Gifu University, Gifu 501-1193, Japan

It is well known that amorphous semiconductor materials are very sensitive to the light and show a variety of photoinduced phenomena [1,2]. Therefore, amorphous semiconductor are very much expected as materials for optoelectronic devices, such as solar cells, thin film transistors, light sensors, and optical memory devices etc. These applications require an understanding of the physical properties of amorphous materials. In our recent study, we observed interesting photoinduced change in the photoconductivity and the total photoyield of amorphous chalcogenide films by the irradiation of the vacuum ultraviolet (VUV) light and the visible light with the energy corresponding to the optical bandgap [3]. To obtain a wide knowledge of the photoinduced phenomena, we investigated photoinduced effects in the VUV region by the reflection spectra. However the signal-to-noise ratio is not good in some cases in the reflection spectrum measurement. In present report, measuring method of the transmission spectrum was examined.

It is possible that the amorphous semiconductor sample for the measurement of the transmission spectrum easily makes a thin film by conventional evaporation technique. The ultrathin collodion film was used as a substrate for the measurement of the transmission spectrum. The ultrathin collodion films were prepared onto metal plates with a pinhole of the diameter of 1.5mm. The transmission spectrum was measured through this pinhole. The metal thin films are often used in order to eliminate the higher order light from the monochromator in the VUV region. It is important to investigate the annealing effects, when the photoinduced phenomena in the amorphous materials are studied. It can be used as a higher order light cutoff filter in the VUV region, and as a possible heat-treating substrate, a metal thin film is more useful than collodion film. At present, the transmission spectrum of amorphous materials has mainly planned the measurement in the wavelength region between 20nm and 35nm. An aluminum thin film is useful as a substrate, because it can be used as higher order cutoff filter in this wavelength region. In this report, the following was examined: optimum film thickness and performance as higher order light cutoff filter.

Aluminum thin films were prepared onto substrates of ultrathin collodion films by conventional evaporation technique. The film thickness was controlled by the filling quantity of the source material and the deposition time as a convenient method. The measurement of the transmission spectra in the VUV region was performed at room temperature at the BL5B beam line of the UVSOR facility of the Institute for Molecular Science.

Figure 1 shows the VUV transmission spectra in aluminum thin films with the different film thickness. The transmission spectrum of a commercial aluminum filter with 100nm film thickness supported by the metal mesh is also shown in Fig.1. In the figure, every transmission spectrum has not been normalized by the spectroscopic system response, and they have been normalized at the maximum value of the transmitted light strength. As can be seen in the figure, features of the spectrum observed in each aluminum film agree well to each other. In addition, the filter character that is equivalent to the commercial filter has been obtained in the prepared thin film. From present result, it is concluded that the aluminum thin film filter can be easily manufactured. The aluminum thin films will be used as substrates, and the amorphous semiconductor thin films are prepared onto them, and the transmission spectrum will be measured.

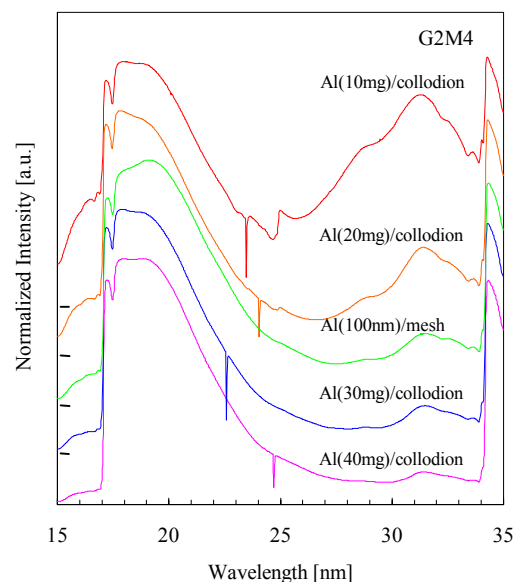

Fig. 1. Normalized transmission spectra of Al/collodion and Al/mesh.

[1] Ke. Tanaka, Rev. Solid State Sci., 4(1990)641.
[2] K. Shimakawa, A. Kolobov, and S. R. Elliott, Adv. Phys., 44(1995)475.
[3] K. Hayashi, A. Hirai, and K. Shimakawa, UVSOR Activity Report 1996(1997)116.

L-shell NEXAFS of Sulfur in amino acids: Cysteine and Methionine

F. Kaneko[1*], K. Nakagawa[2], T. Kitada[1], A. Kasahara[1]

[1]*Graduate School of Human Science and Cultural Studies, Kobe University, Kobe 657-8501 Japan*

[2]*Faculty of Human Development, Kobe University, Kobe 657-8501 Japan*

* fusae@radix..h.kobe-u.ac.jp

Using the upgraded UVSOR (UVSOR II), we measured L-shell NEXAFS of thin films of sulfur in metionine (Met, Fig. 1(A)) and cysteine (Cys, Fig. 1(B)), in an attempt to study the role of sulfur, the heaviest element in amino acids.

Cysteine and methionine powder was purchased from the Sigma Co. and used without further purification. These amino acids were evaporated carefully on BeCu substrates covered with 30nm Au. Thickness of sublimated amino acid films was measured by quarz oscillator to be 20nm and 150nm each other. Measurement was performed at BL-5B in energy region from 150eV to 270eV with the grating 2 and mirror 1. Wavelength resolution with the slit width of 0.05 mm was estimated to be 0.01nm from the half width of the 0-th order light spectrum.

We measured absorption spectra $A(\lambda)$ from the drain current $i(\lambda)$ divided by incident intensity $I_0(\lambda)$ monitored as drain current on Au mesh ($A(\lambda)= i(\lambda)/ I_0(\lambda)$). All measurements were carried out at 300 K. Typical drain current was 50 pA at 200 eV with 200 mA SR ring current. Obtained spectra are shown in Fig. 2, in which background signal due to other atoms was subtracted by linear extrapolation and only L-shell component was shown. Mass absorption coefficient was estimated by normalizing the intensity at 160 eV and 235 eV by Henke formula [1]. In the figure, photon energy was not calibrated.

According to the X-ray data booklet [2], L_1, L_2 and L_3 levels of sulfur is known to be at 230.9, 163.6 and 162.5 eV, respectively. Thus we concluded that peaks at 226.0 eV for Met and at 226.9 eV for Cys are due to L_1 transition. Doublet peaks at 163.8 eV and 164.6 eV for Met and peaks at 163.6 and 165.0 eV were ascribed to L_2 and L_3 transition which showed the clear spin-orbit splitting. It should be noted that sharp peak was observed at 166.6 eV for Met. The origin of this peak is not clear now. Quantum mechanical calculation is being planned.

References
[1] B.L. Henke, E.M. Gullikson, and J.C. Davis, Atomic Data and Nuclear Data Tables Vol. **54** (no.2), 181-342 (July 1993).
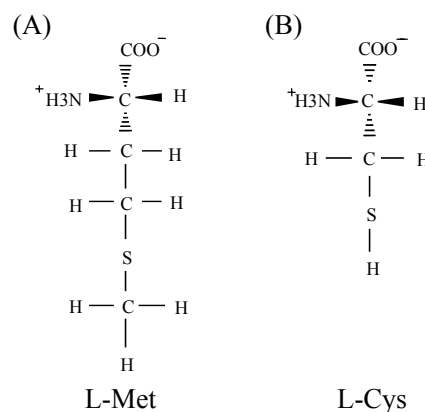[2] A. Thompson et al., "X-RAY DATA BOOKLET", ALS, 2001, p. 1-2.
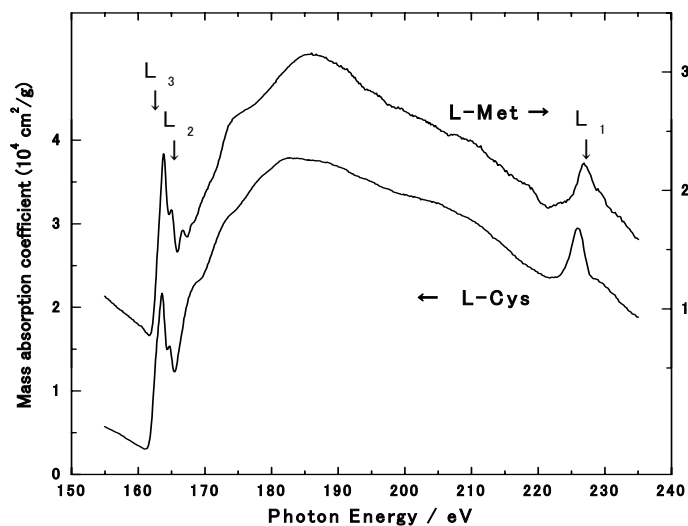
Fig.1. L-Methionine(A)andL-Cysteine(B).

Fig. 2. L-shell NEXAFS of Sulfur in L-Methionine and L-Cysteine.

Characterization of Freestanding Metal Optical Filters and GaN UV Detectors in VUV and SX Region

A. Motogaito[1], H. Watanabe[1], K. Hiramatsu[1]
K. Fukui[2], Y. Hamamura[3], K. Tadatomo[4]

[1]*Dept. of Electrical and Electronic Engineering, Mie University, Tsu 514-8507 Japan*
[2]*Research Center for Development for Far-Infrared region, Fukui University, Fukui 910-8507 Japan* [3]*Core Technology Center, Nikon Corporation, Sagamihara 228-0828 Japan*
[4]*LED Business Development Dept., Mitsubishi Cable Co. Ltd., Itami 664-0027 Japan*

The characterization of freestanding thin film filters and GaN based Schottky ultraviolet (UV) detectors were carried out from vacuum ultraviolet (VUV) to soft X-ray (SX) region (25-100 eV, 12.4-50 nm). The high order light from grating of monochromter was able to be eliminated by using Ti, Ti/Al/Ti and SiN thin films as a filter. Moreover, the transmittance of Schottky electrode Ni/Au calculated from that of Ti/Au membrane was about 50-70% in this wavelength region, and it is enough thin to transmit VUV and SX light. Measured using such a filter and transparent electrode, this detector can also detect VUV and SX light. The responsivity in VUV (30-50 nm) and SX region (@13 nm) was about 0.01 and 0.05 A/W, respectively.

UV detectors are one of the most attractive devices in the group III-nitride semiconductors. Currently, for the measurements of UV light, Si based photodiodes are mainly used. However, light sensitivity often deteriorates due to radiation damage in the vacuum ultraviolet (VUV) and soft X-ray (SX) region. To overcome this problem, several groups have reported on GaN- or AlGaN-based UV detectors such as photoconductor, the Schottky type, the Schottky-based metal-semiconductor-metal type, p-n or p-i-n type have been reported. However there are few reports for responsivity spectra in VUV and SX region [1].

On the other hand, there are few effective optical filters to remove higher order light generated by monochromter in VUV and SX region. Thus it is important to develop effective optical filters in VUV and SX region.

In this report, the characterization of optical filters by using membranes and GaN UV detectors are characterized in BL5B and comparing the results of simulation data.

The details of fabrication of optical filters and GaN UV detectors have already reported [1].

The optical characterization of SiN and Ti/Al/Ti are carried out. The experimental data and theoretical data are almost agreed. Thus, from these results, the measurement of UV detectors is able to in the range between 37 and 100 eV. The transmittance of Ni/Au electrode is about 0.5-0.7 in this measurement range [2].

Using these filters, the responsivity spectra of GaN UV detectors are carried out. Figure 1 shows the responsivity spectra of GaN UV detectors between near UV and SX region. No responsivity at the energy lower than 3.4 eV can be observed clearly. The ratio of responsivity between UV and visible (VIS) regions is about 5×10^3. The maximum responsivity of this detector is about 0.10 A/W at $h\nu$=3.5 eV. The responsivity in VUV region (10-50 eV) is about 0.01 A/W. The larger responsivity is found in VUV-SX region (>50 eV). The value of responsivity in SX region (@13 nm for EUV lithography system) is about 0.05 A/W. To consider the reason of increasing responsivity between VUV and SX region (50-100 eV), the transmittance spectra of Ni/Au Schottky electrode and penetration depth of GaN for VUV and SX light are evaluated. Above 50 eV, the transmittance of Ni/Au electrode and the penetration depth of GaN are increasing with photon energy. Therefore, the larger responsivity is obtained in SX region compared to VUV region.

[1] A. Motogaito et al., Phys. Stat. Sol (a) 200 (2003) 147.
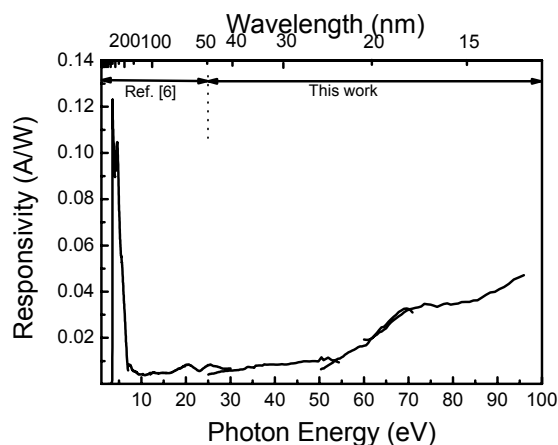[2] A. Motogaito et al., UVSOR ACTIVITY REPORT 2002 (2003) 132.

Fig. 1 The responsivity spectra of GaN UV detectors using SiN and Ti/Al/Ti optical filters in SX and VUV region.

Wide-Range Reflection Multilayer in 200-25nm Region

T. Ejima, A. Yamazaki, T. Banse, M. Watanabe

IMRAM, Tohoku University, Sendai, 980-8577 Japan

A new high reflectance mirror for normal incidence in wide wavelength region (200-25 nm) is designed and fabricated. Reflectance of the fabricated mirror in 5° of angle of incidence is comparable with that of Pt in 200-35 nm region, is higher than any materials in 35-25 nm region.

Introduction

The working wavelength range of normal incidence optical systems has been limited above 40 nm, because normal incidence reflectances of usual mirror-materials are small below 40 nm. Therefore, the development of multilayers to extend the working range to shorter wavelength region has been made [1]. In this study, the efforts were made to extend the short wavelength limit from 40 nm to 25 nm, and new high reflectance mirrors in this region are designed and fabricated.

Design

A conceptual structure of the wide-range multilayer is given in Fig. 1. It is composed of a top-single-layer (TSL) reflecting light in 200-65 nm region, a middle-aperiodic-layers (MAL) reflecting light in 65-25 nm region, and a bottom piled-double-layers (PDL) reflecting light around 25 nm.

The wide-range multilayers were designed as follows [2]. At first, the bottom PDL is designed to enhance the reflectance around 25 nm. At second, a material and its thickness of a TSL are chosen to have a high reflectance in the 200-50 nm range. Finally, an MAL is inserted between the PDL and the TSL to make the reflectance flat in 85-25 nm region.

One of the multilayer structure is a PDL of Mg 9.0 nm/Y_2O_3 4.8 nm with 14 periods, a MAL of Mg 12.6 nm/Y_2O_3 5.0 nm, and a TSL of SiC 5.0 nm.
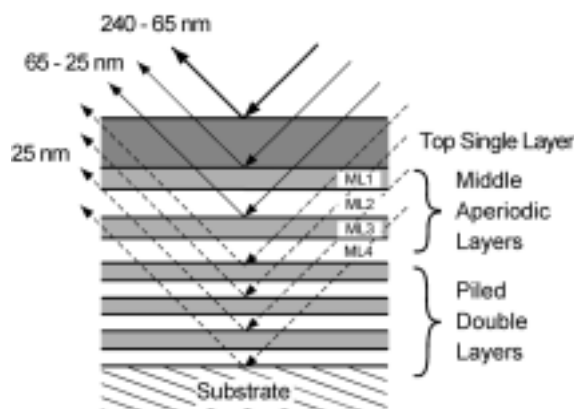

Fig. 1: Layer structure of the wide-range multilayer.

Experimental Results

Measured reflectance of the fabricated multilayer in 5° of angle of incidence is compared with the usual mirror materials in Fig. 2 (a). Measured reflectance of the multilayer is designated as the red curve, simulated reflectances of the materials are as the black curves. As can be seen in the figure, the measured reflectance of the fabricated multilayer is comparable with that of Pt in 200-35 nm region and is higher than any materials in 35-25 nm region.

Measured reflectance is also compared with the simulation results of the designed multilayer in Fig. 2 (b). The measured reflectance is lower than that of simulation in 200-62 nm region. This suggests that the fabricated thickness of the TSL, SiC, layer is thinner than the designed one. The reflectance in 62-41 nm and 31-23 nm regions is comparable with the simulation. These results suggest that the layer structure of the fabricated PDL fulfills the designed one. The lower reflectance in 41-31 nm region will be caused by the difference of the optical constants between the fabricated Y_2O_3 layer in MAL and the handbook data used in the simulations [3], because the Y-N absorption edge cannot be observed in the fabricated multilayer.

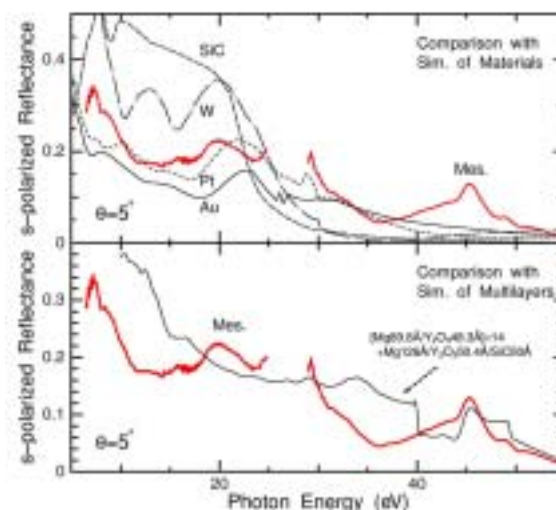Fig. 2: Measured reflectance of the wide-range multilayer with simulations.

References

[1] Y. Kondo, T. Ejima, K. Saito, T. Hatano, and M. Watanabe, Nucl. Inst. Meth. Phys. Res. A **467-468** (2001) 333.

[2] T. Ejima, K. Sudo, T. Hatano, and M. Watanabe, J. Phys. IV France, **104** (2003) 259.

[3] *Handbook of Optical Constants of Solids II*, Ed. by Edward D. Palik, Academic Press, Inc., 1991.

EUV Deterioration of Thin Filters

T. Murachi, K. Okada, M. Kanao, S. Kameda, H. Sagawa, and I. Yoshikawa

Institute of Space and Astronautical Science, Japan Aerospace Exploration Agency,
Sagamihara, Kanagawa 229-8510 Japan

When the satellites keep up observation in long term, the deterioration of observational equipments becomes important problem [1], [2]. It is indispensable for analyzing data to investigate the deterioration of equipments. Especially we should know the changes of the equipments' extreme-ultraviolet-region performance by the deterioration because our equipments have observed with the extreme ultraviolet (EUV) light. Therefore, we produce the samples simulated the deterioration in the Space, and investigate that.

It is said that main causes of deterioration in the Space is solar high-energy particles and solar ultraviolet (EUV) ray. We can list the deteriorative equipments as follows: Mirror, MicroChannel Plates, Filters, and Black paint inside the hood. This time, we simulate the solar EUV deterioration of Filters by the intense light of UVSOR BL5B (PGM 35). And we investigate changes of their transmittance.

We irradiated the light (radius: ~ 1 mm) of 20 ~ 100 nm to the filter (radius: ~ 5 mm), which consists of half area of Carbon/Aluminum (thickness: 368/1429 Å) and another half area of Al (thickness: 1429 Å) as Fig. 1. The 1st order light of 30.4 nm was irradiated to the place of ~ 2 mm (C/Al area) from edge of C/Al, and 0th order light (20 ~ 100 nm) was irradiated to ~ 4 mm (C/Al area) and ~ 8 mm (Al area). In case of 0th order, irradiated quantity of light is ~ 6.5×10^{-2} J/mm^2 (Irradiated at ~ 3.1×10^{11} photons/sec/mm^2 in 9 hours. Energy of 0th order light calculates as 30.4nm (~ 6.6×10^{-18} J/photon).), and in case of 1st order, that is ~ 2.2×10^{-4} J/mm^2 (~ 3.1×10^9 photons/sec/mm^2 in 3 hours.). As the solar He II (30.4nm) flux is ~ 2×10^{-9} W/mm^2, ~ 6.5×10^{-2} J/mm^2 is approximately 2 week amount.

After irradiation, the filter becomes as Fig. 1. The part of the C/Al filter where 0th order light was irradiated changes from brown to black.

Fig. 2 is the measurement result of filter transmittance before and after EUV irradiation. Transmittance was measured in every 1 mm from the edge of C/Al to the edge of Al by the lights (30.4nm, 46.2nm and 58.4nm) of radius: ~ 1 mm. Values of irradiated place (list above) are consistent with each values of horizontal axis. The transmittance of black place (~ 4 mm, C/Al area) irradiated 0th order light has decreased remarkably. At 30.4nm transmittance is reduced from 12.5 % to 4.6 %, at 46.2nm from 1.8% to 0.16 %, and at 58.4nm from 0.24 % to 0.056 %. Such decrease is not seen in Al area. We think this decrease is caused by structure change of carbon filter because carbon layer was heated in the vacuum.

We understand that intense light should not shine in the carbon filter. For example, in condensing optics filters are not arranged in focus.
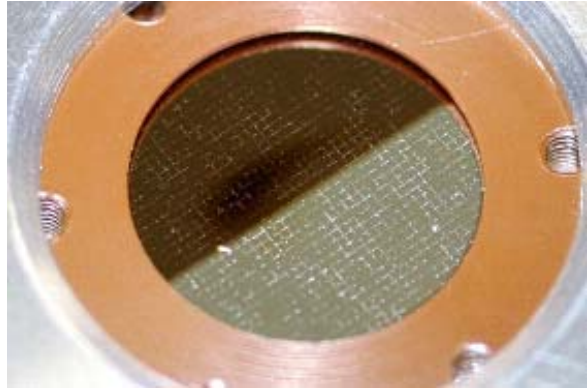
Fig. 1. The photograph of filter irradiated EUV. Upper brown half area is C/Al filter, and lower silver half area is Al filter. The black part in C/Al filter is where 0th light was irradiated.
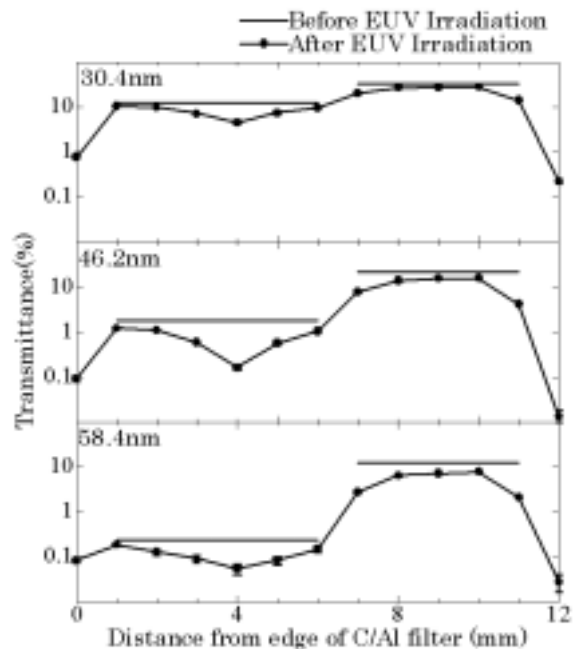
Fig. 2. Transmittance of filter before and after EUV irradiation. Measured wavelength is 30.4nm in top graph, 46.2nm in middle and 58.4nm in bottom. Horizontal axis represents distance (mm) from C/Al filter edge, and vertical represents transmittance (%).

[1] P. W. Vedder, J. V. Vallerga, J. L. Gibson, J. Stock, and O. H. W. Siegmund: Proc. SPIE **1742** (1992) 486.
[2] J. V. Vallerga, B. A. Roberts, J. Dupuis, and P. N. Jelinsky: Proc. SPIE **3356** (1998) 1001.

Millimeter Wave Reflection Measurements of

Secondary Battery Substance LiMn$_2$O$_4$

H. Ohta, H. Ishikawa[A], T. Hirano[A], Y. Nagasaka[A], T. Nanba[A], A. Hirano[B] and R. Kanno[C]

Molecular Photoscience Research Center, Kobe University, 1-1 Rokkodai, Nada, Kobe 657-8501

[A]*The Graduate School of Science and Technology, Kobe University, 1-1 Rokkodai, Nada, Kobe 657-8501*

[B]*Faculty of Engineering, Mie University, 1515 Kamihama-cho, Tsu 514-8507*

[C]*Interdisciplinary Graduate School of Science and Engineering, Tokyo Institute of technology, 4259 Nagatsuda, Midori, Yokohama 226-8502*

As LiCoO$_2$ and LiNiO$_2$, which are in commercial use and a promising material for the Li ion secondary batteries, respectively, have attracted much attention recently, we have been studying the millimeter wave reflection measurements of these substances and related substances using UVSOR to investigate the dynamical properties of Li ions [1-9]. The increase of reflection is observed in the low energy region above 300 K for LiNiO$_2$ and Li$_{1-x}$CoO$_2$, and we proposed that this increase of reflection is related to the motion of Li ion in the system. However, it turned out to be flat in the observed region for LiCoO$_2$ [8]. The investigation to clarify the relation between the reflection and the charge-discharge process is under progress. On the other hand, LiMn$_2$O$_4$ is considered as a new promising material for the positive electrode of the Li ion secondary battery from the economical point of view. Therefore, we made a reflection measurements of LiMn$_2$O$_4$.

The reflection measurements of LiMn$_2$O$_4$ sintered sample with a diameter of 10 mm have been performed in the spectra region from 5 to 60 cm^{-1} using the beam line BL6A1 of UVSOR. The low pass filter was used for the measurement below 22 cm^{-1}. The temperature was changed from 77 to 380 K. The gold plate was used as a reference and InSb detector was used as a detector.

Figure 1 shows the results of LiMn$_2$O$_4$. It is clear that the reflection is flat for the temperature region from 77 to 380 K. These results are similar to those of LiCoO$_2$ but different from LiNiO$_2$. The absolute reflection value is very close to that of LiCoO$_2$. In order to investigate the charge-discharge process in LiMn$_2$O$_4$, the millimeter wave reflection measurement of Li$_{1-x}$Mn$_2$O$_4$ is desired. However, as Li$_{1-x}$Mn$_2$O$_4$ is very fragile, we have not succeeded in observing Li$_{1-x}$Mn$_2$O$_4$. This remains as a future problem.
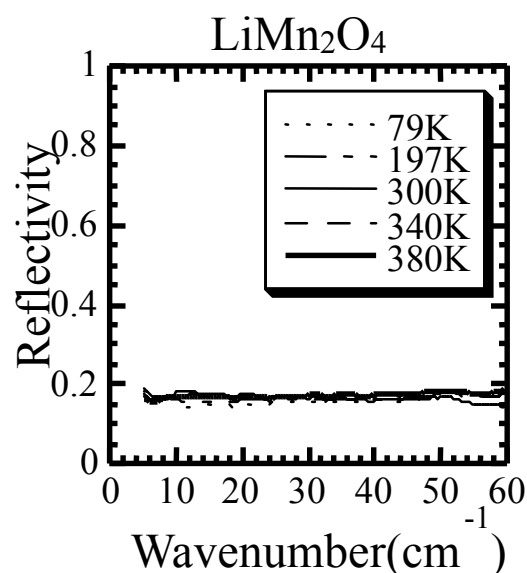
Fig. 1. Reflection spectra of LiMn$_2$O$_4$.

[1] H. Ohta *et al.*: UVSOR Activity Report 1996 (1997) 182.

[2] H. Ohta *et al.*: UVSOR Activity Report 1997 (1998) 128.

[3] H. Ohta *et al.*: UVSOR Activity Report 1998 (1999) 158.

[4] H. Ohta *et al.*: UVSOR Activity Report 1999 (2000) 93.

[5] H. Ohta *et al.*: UVSOR Activity Report 2000, (2001) 121.

[6] H. Ohta *et al.*: Jpn. J. Applied Phys. **39** (2000) Suppl. 39-1, 409-410.

[7] H. Ohta *et al.*: UVSOR Activity Report 2001, (2002) 138.

[8] H. Ohta *et al.*: UVSOR Activity Report 2002, (2003) 142.

[9] Y. Nagasaka *et al.*: J. Phys. Chem. Solids 64 (2003) 1949-1951.

SOLD STATE
SPECTROSCOPY II:
XAFS AND PES

Laser-induced Infrared Absorption of Carbon Nanotubes

J. Azuma, M. Itoh[A], M. Koike[A], T. Sakurai[A], M. Kamada and M. Endo[A]

Synchrotron Light Application Center, Saga University, Saga 840-8502, Japan
[A]*Faculty of Engineering, Shinshu University, Nagano 380-8553, Japan*

Since the discovery of carbon nanotube by Iijima [1], a new research field has been developed in material science. Many future applications can be expected from its interesting physical properties. For example, there are semiconducting and metallic carbon nanotubes, depending on their diameter and chirality [2,3]. The development of the sample synthesis of single-walled carbon nanotubes (SWNTs) has allowed detailed experimental studies of the electronic structure. It is important to measure the fundamental absorption of SWNTs for sample characterization. From the viewpoint of applications to electronic devices, it is also necessary to obtain the electronic properties of the metallic SWNT and of the photo-excited states in semiconducting SWNT.

In this paper, the optical absorption spectra of SWNTs prepared by two different chemical treatments are shown. The laser-induced change of the absorption spectra is also reported.

Experimentals

The absorption measurements were performed in the energy range of 400-15000 cm^{-1} with a rapid-scanning Michelson interferometer (Bruker, IFS-66V) by using a KBr or a quartz beam splitter. An HgCdTe photoconductive detector and a Si photodiode were used in the infrared and visible regions, respectively. Photo-excitation was performed by a Ti:sapphire laser (Coherent, Mira-900F) at 800 nm with 250 mW average power. The samples used in this experiment were prepared by dispersing two types of SWNT solutions onto BaF_2 substrates. One is the SWNT with iron impurity. The other is the SWNT in which iron impurity was chemically removed.

Results and Discussion

Fig. 1(a) shows absorption spectra of the two types of SWNTs at room temperature. The band-to-band transition of semiconducting SWNT is observed above 4000 cm^{-1}. On the other hand, the Drude tail of metallic SWNT appears below 3000 cm^{-1}. The absorption tail of the band-to-band transition increases slightly in the SWNT:Fe as compared with the Fe-removed SWNT. This increase is probably ascribed to the impurity state. The intensity ratio of the band-to-band transition to the Drude tail is also different between the two samples. The ratio might be changed by the difference in the chemical process of the impurity removal.

Fig. 1(b) shows the laser-induced change of the IR absorption spectra at room temperature. One can see that an additional absorption tail appears below 1000 cm^{-1}. This absorption tail is assigned to the Drude tail of the photo-excited carriers in semiconducting SWNTs. In usual, photoconductivity measurements using electrodes are required to obtain information about the photo-excited carriers. The present experiment demonstrates that it is capable to perform the photoconductivity measurement without electrodes by using tunable laser and brilliant IR light. This result is essentially important for the study on the electronic properties of SWNTs to which it is very difficult to attach the electrodes.
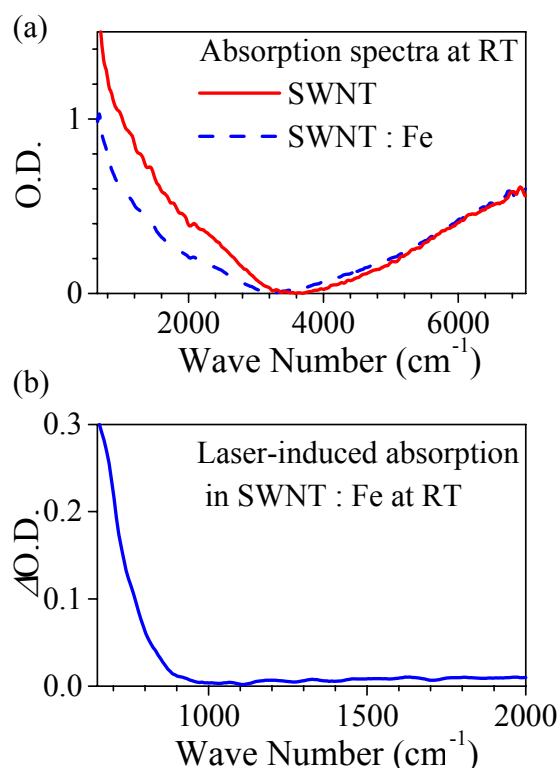
Fig.1 (a): Absorption spectra of two SWNTs.
(b):Laser-induced absorption in SWNT:Fe.

The detailed analysis of the laser-induced spectral change of SWNTs is in progress. Time-resolved experiment is necessary to obtain further information about the dynamics of photo-excited carriers.

Acknowledgement

[1] S. Iijima, Nature, **354** (1991) 56.
[2] X. Blasé, L.X. Benedict, E.L. Shirley, S.G. Louie, Phys. Rev. Lett., **72** (1994) 1878.
[3] J.W. Mintmire, C.T. White, Carbon **33** (1995) 893.

Optical Response of β-Na$_{0.33}$V$_2$O$_5$ and Its Electronic Structure

L. Chen, M. Matsunami, H. Okamura, T. Nanba, T. Yamauchi* and Y. Ueda*

Graduate School of Science and Technology, Kobe University, Kobe 657-8501, Japan
*Materials Design and Characterization Lab. ISSP, University of Tokyo, kasiwa 277-8581,Japan

β-Na0.33V2O5 is one of β-vanadium bronze compounds and attractive materials because it exhibits a quasi-one-dimensional (quasi-1D) metallic behavior and a metal-insulator transition (MIT) accompanying charge ordering at around 135 K[1]. The evidence for the charge separation into V+4 and V+5 states was obtained from NMR measurements[2] Up to now, however, the electronic states due to the MIT has not been made clear. In this paper, we report the temperature dependent optical spectra around the MIT and discuss the electronic structure very close to the Ff level.

Experimental

The temperature dependence of optical reflectivity spectra $R(\omega)$ at ambient pressure was measured in the wide photon energy range from 7 meV to 30 eV in the temperature range of 8-300 K. The measurements were performed using a Fourier-transform interferometer combined with a thermal light source and synchrotron radiation source at the beam line BL6B & 7B of UVSOR, Institute for Molecular Science. The optical conductivity $\sigma_1(\omega)$ and complex dielectric function $\varepsilon_1(\omega)$ were obtained from a standard Kramers-Kronig transformation of the measured reflectivity spectrum.

Results and discussions

Fig.1 shows the temperature dependence of the optical conductivity for E//b (upper) and E⊥b (lower). The electric resistivity data shows the conductivity in the b-axis due to the formation of a quasi-1D-chain by vanadium ions along the b-axis. Optical conductivity spectra for E//b show a clear Drude component by free carriers. The many spike structure were resolved below 0.1 eV even in the metallic phase. This means that the low density of free carriers in the conduction band which leads to the weak screening of the electric polarization for lattice vibration(phonon). On the other hand, the optical conductivity spectra for E⊥b shows a typical insulating profile. The onset of the interband transition locates at 0.1eV and the intense peak due to the transition from the V-3d initial state to the upper p state in the conduction band appears at 0.35 eV for E//b. On the other hand, for E⊥b the onset locates at 0.25 eV and the intense peak appears at 0.85 eV. This means the magnitude of the energy gap is smaller for E//b than E⊥b. The intense peak due to the transition from the O-2p state appears around 7 eV for both configuration. The same peak energy suggests the O-2p state has no anisotropy in band scheme.
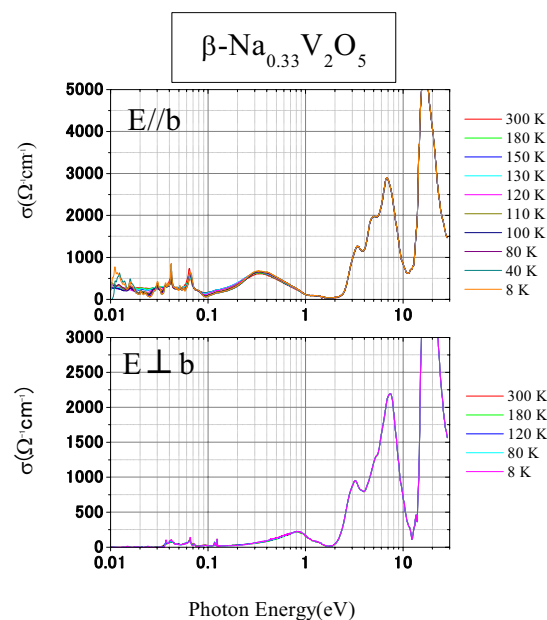

Fig. 1. The optical conductivity $\sigma_1(\omega)$ for E//b (upper) and E⊥b(lower).

[1] T,Yamauchi *et al*., Phys.Rev.Lett. 89(5) 057002-1 (2002).
[2] M.Itoh, *et al*. J.Phys.Soc.Jpn. 69 155(2000).

Infrared spectroscopy on CeSb at high pressure

T. Nishi[1], Y. Mori[2], Y. Sumida[2], Y.S. Kwon[3,4], H. Kitazawa[5], S. Kimura[1,3]

[1]*Department of Structural Molecular Science, Graduate University of Advanced Studies, Okazaki 444-8585, Japan*
[2]*Department of Physics, Okayama University of Science, Okayama 700-0005, Japan*
[3]*UVSOR Facility, Institute for Molecular Science, Okazaki 444-8585 Japan*
[4]*Department of Physics, SungKyunKwan University, Suwon 440-746, South Korea*
[5]*Nanomaterials Laboratory, National Institute for Materials Science, Tsukuba 305-0047, Japan*

CeSb has a complex magnetic phase diagram not only under magnetic fields [1] but also at high pressure. [2] The fundamental magnetic structure is double ferromagnetic layer along magnetic fields, for instance the magnetic structure at the antiferromagnetic state below 9 K at $B = 0$ T, $P = 0$ GPa is ++--, where +(-) is the ferromagnetic layer along the magnetic field. At $P =$ several GPa, single-layer antiferromagnetic phase (+-) appears. In the phase, the electric resistivity enhances one order higher than that at ambient pressure and it is strongly reduced by magnetic fields. [3] To investigate the electronic structure from which such anomalous physical property originates, the infrared reflection spectroscopy at high pressure was performed.

The experiment was done using an IR microscope and a diamond anvil cell (DAC) mounted on a liquid-helium-flow-type cryostat. The sample size was about $0.2 \times 0.2 \times 0.05$ mm^3. Because of the high brilliance of IR synchrotron radiation, The IR reflection from a sample in the DAC can be detected clearly.
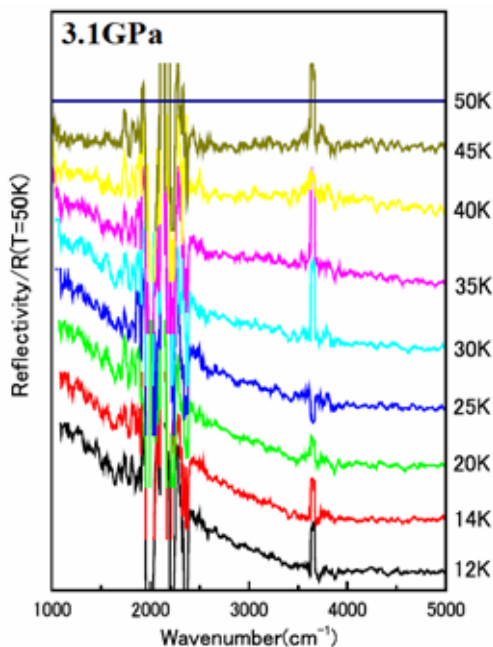
The obtained temperature dependence of the relative reflectivity spectrum of CeSb at $P = 3.1$ GPa are shown in Figure 1. The spectra are the reflectivity at each temperature divided by that at 50 K. Below 25 K, since all spectra are similar to one another, the electronic structure in the energy region as well as the magnetic phase does not change. Above 25 K, the spectrum gradually changes and then above 40 K the spectrum becomes flat. The temperature dependence is clearly indicated in the reflectivity at $\omega = 3000$cm^{-1} as shown in Figure 2. The slope changes at $T1 = 25$ and $T2 = 40$ K. This means that the electronic structure changes at these temperatures. This result originates from the magnetic phase diagram. According to the neutron scattering data [2], two phase boundaries appear at this pressure. The $T1$ and $T2$ are same as those detected by the neutron scattering.

The reflectivity spectra at the temperatures between $T1$ and $T2$ are gradually changes. This indicates that the magnetic interaction, in this case the *pf* mixing effect, gradually changes with temperature. The origin seems to the second order transition observed in CeBi at ambient pressure. [4]

Fig. 1. Temperature dependence of relative reflectivity spectrum of CeSb at $P = 3.1$ GPa.
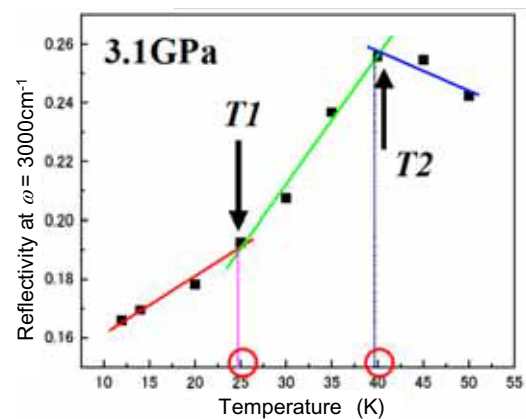

Fig. 2. Temperature dependence of the reflectivity intensity at $\omega = 3000$cm^{-1} of CeSb at $P = 3.1$ GPa.

[1] S. Kimura *et al.*, J. Phys. Soc. Jpn. **71** (2002) 2200.
[2] Osakabe *et al.*, Acta Phys. Pol. B **34** (2003) 1469.
[3] N. Môri *et al.*, JJAP Series 8 (1993) *p.* 182.
[4] S. Kimura *et al.*, submitted.

SOLD STATE SPECTROSCOPY II: XAFS AND PES

Far-infrared Reflectivity Measurement of SrTiO₃

H. Okamura, M. Matsubara, T. Nanba, K. Tanaka*

Graduate School of Science and Technology, Kobe University, Kobe 657-8501, Japan.
**Graduate School of Science, Kyoto Univeristy, Kyoto 606-8502, Japan*

$SrTiO_3$ (STO) has many interesting properties, and has been studied by condensed matter physicists for nearly half a century. STO is an insulator with an energy gap of about 3.4 eV and a static dielectric constant ε_0 of about 200 at room temperature. With decreasing temperature, ε_0 increases, and reaches ~ 20000 at liquid helium temperature. A Curie-Weiss plot suggests a Curie temperature of ~ 30 K, but it does not undergo a phase transition to a ferroelectric state. This absence of a ferroelectric transition in STO has been attributed to large quantum fluctuations of electric dipole moment, or equivalently strong zero-point oscillations of the ions. However, a clear softening of an optical phonon has been observed with infrared spectroscopy, which demonstrates a tendency toward ferroelectric ordering. Recently, it has been reported that a photoexcitation of STO across the band gap using UV light further increases ε_0 by a factor of 2 to 100 depending on the conditions of the photoexcitation [1,2]. This photo-induced enhancement of the dielectric properties has attracted a lot of interest, and several models have been proposed.

Besides the enhancement of dielectric properties at low temperatures, STO has other unique features. First, it gives a strong, white luminescence over a wide visible range by UV photo-excitation [4]. Since the band gap of STO is 3.4 eV, this means that the photo-generated carriers in STO experience large energy relaxation processes before recombination. Possibilities of polarons and self-trapped excitons have been discussed. Second, STO exhibits a very strong photoconductivity below the structural phase transition at 105 K [5]. At low temperatures, photo-excitations increase the conductivity of STO by several orders of magnitude. It has been suggested that the photoconductivity and the photo-enhancement of the dielectric properties are closely related to each other.

In order to probe the lattice dynamics of STO, we have carried out far-infrared reflectivity measurement of STO down to 10 cm⁻¹ at BL6B of UVSOR. The STO sample used had a (110) surface. Figure 1 shows the results. The spectra below ~45 cm⁻¹ were measured at BL6B using the synchrotron radiation source and a Martin-Puplett type interferometer, while those above 45 cm⁻¹ were measured at Kobe University using a conventional source and a Michelson type interferometer. At 295 K, there is a broad "dip" in the reflectivity below ~100 cm⁻¹. This corresponds to an optical phonon, which is very broad due to strong damping. The point where the reflectivity begins to decrease, ~100 cm⁻¹ for 295 K,

approximately corresponds to the frequency of the optical phonon. As the temperature is lowered, the dip becomes narrower and shallower. This result clearly demonstrates softening of the optical phonon. Although there is a previous report on the temperature-dependent soft phonon of STO [6], our present result covers much wider temperature and photon energy range. To make more detailed analyses on the data, we plan to perform the Kramers-Kronig analysis on the reflectivity data.
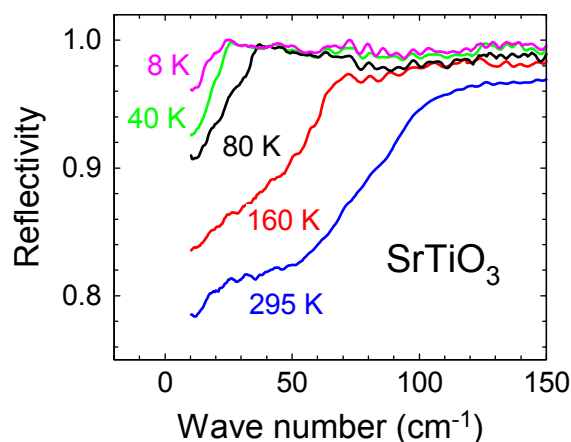
Fig. 1. The reflectivity spectra of SrTiO₃ at several temperatures. The spectra below 45 cm⁻¹ were measured at BL6B, and those above were measured at Kobe University.

[1] K. A. Muller and H. Burkard, Phys. Rev. **B** 19, 3593 (1979).
[2] M. Takesada, T. Yagi, M. Itoh, S. Koshihara, J. Phys. Soc. Jpn. **72**, 37 (2003).
[3] T. Hasegawa, S. Mouri, Y. Yamada, K. Tanaka, J. Phys. Soc. Jpn. **72**, 41 (2003).
[4] L. Grabner, Phys. Rev. **177**, 1315 (1969).
[5] H. Katsu, H. Tanaka, T. Kawai, Jpn. J. Appl. Phys. **39**, 2657 (2000).
[6] A.S. Barker and M. Tinkham, Phys. Rev. **125**, 1527 (1962).

Reflectivity Spectra and Electronic Structure of α-LiIO$_3$ Crystals

M. Kitaura, S. Kawabata[A], M. Kato[A], S. Matsumoto[A], H. Nakagawa[A], and M. Itoh[B]

Fukui National College of Technology, Sabae 916-8507
[A]*Department of Electrical and Electronics Engineering, Fukui University, Fukui 910-8507*
[B]*Department of Electrical and Electronic Engineering, Shinshu University, Nagano 380-8553*

Lithium iodate (LiIO$_3$) has two crystal structures, hexagonal (α-type) and tetragonal (β-type) ones, under normal conditions. From the viewpoint of technological application, the α-LiIO$_3$ crystal receives intense attention as a promising candidate for photorefractive (PR) substance. It has been generally accepted that the PR effect arises from trapping of photo-induced electrons and/or holes at some deep levels. The origin of the trap states is of great interest, but it has not yet been clarified in α-LiIO$_3$. This material is also known to be a quasi one-dimensional ionic conductor. The mobile ionic species are mainly lithium ions, the thermal migration of which is greatly enhanced by the super ionic phase transition at the temperature $T = 243$ K. As pointed out in Ref. [1], this phenomenon has a close relationship with the weakening of PR properties. It is thus supposed that interstitial Li$^+$ ions or Li$^+$ vacancies are linked to formation of the trap states responsible for the PR effect.

The optical spectra of pure crystals are necessarily required to study the effect of imperfections on the electronic structures. In pure α-LiIO$_3$, optical spectra have been investigated in the energy region lower than the fundamental absorption edge at around 4 eV. In order to understand the electronic structure, it is important to clarify the optical spectra in the energy region above 4 eV.

In the present study, polarized reflectivity spectra of α-LiIO$_3$ were measured in the energy range of 3-30 eV at room temperature. They were obtained for the polarization parallel ($E\|c$) and perpendicular ($E\perp c$) to the c-axis. The origin of the structures in the spectra is explained on the basis of the results of the DV-$X\alpha$ calculation.

Experiment

The crystals of α-LiIO$_3$ were grown by dissolving stoichiometric quantities of reagent grade iodic acid and lithium carbonate in distilled water. The obtained crystal was transparent, with a size of 6 mm in length and 2 mm in diameter.

The measurements of reflectivity spectra were carried out at BL7B using a 3-m normal incidence monochromator. The band-pass was set to be less than 0.3 nm. The incident angle of SR light for the sample surface was held at 15 degrees. The incident and reflected light were detected using a calibrated silicon diode sensor (IRD AXUV−100). The absolute values of reflectivity were determined by reference to the refractive indices at 3.5 eV in Ref. [2].

Results and Discussion

Figure 1 shows reflectivity spectra of α-LiIO$_3$ for $E\|c$ and $E\perp c$ configurations, which are indicated by solid and broken lines, respectively. The spectra exhibit remarkable difference in reflectivity. The spectral shape is also different especially in the energy region below 10 eV. In both configurations, there exist broad structures above 10 eV.

Our cluster calculation revealed that the valence band (VB) of α-LiIO$_3$ is built of the O 2p states with small admixture of I 5s and 5p characters. The base width of the VB is about 5 eV. The outermost core levels, composed of I 5s, O 2s and 2p orbitals, appear around −10 eV. On the other hand, the bottom of the conduction band (CB) is composed of Li 2s and I 5p orbitals. The higher-lying states are formed by Li 2p orbitals. The band gap is calculated to be 6.15 eV.

The reflectivity spectra are composed of two parts: I (5-10 eV) and II (10-20 eV). According to results of the present calculation, the structures in part I are ascribed to the electronic transitions from the VB of O 2p to the lower CB of Li 2s. The transitions of O 2$p \rightarrow$ I 5p are expected to be weak in the part I, because this type of transitions are electric-dipole forbidden. The structures in part II originate from the transitions from the top of the VB to the Li 2p conduction states and those from the outermost core levels to the lower CB.
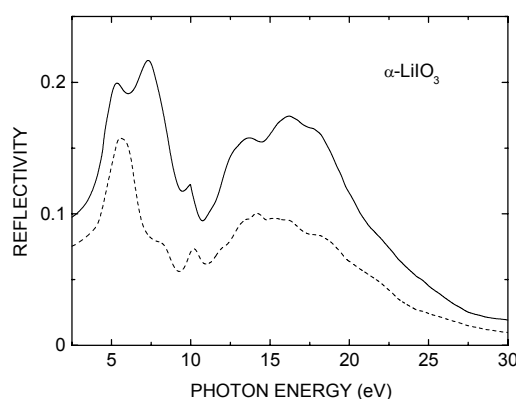

Fig. 1. Reflectivity spectra of α-LiIO$_3$ at room temperature for $E\|c$ (solid line) and $E\perp c$ (broken line) .

[1] J. Xu, X. Yue, and R. A. Rupp, Phys. Rev. B, **54** (1996) 16618.
[2] K. Takizawa, M. Okada, and S. Ieiri, Opt. Commun., **23** (1977) 279.

Reflectivity Spectra of Second-Group Metal Tungstate Crystals

M. Fujita
T. Maruyama*, S. Takagi*, N. Fujita*, M. Itoh*
Japan Coast Guard Academy, Wakaba, Kure 737-8512
* Department of Electrical and Electronic Engineering, Shinshu University, Nagano 380-8553

The second-group metal tungstate crystals are important materials because of their uses as a scintillation detector in medical applications, solid laser hosts and optical fibers. They crystallize into scheelite or wolframite structures. In the present study, reflectivity spectra of $CaWO_4$ and $BaWO_4$ crystals with scheelite structure and $CdWO_4$ with wolframite structure were measured in order to investigate the electronic structures of these tungstate compounds.

Experiment

Reflection measurements were carried out for oriented crystals of $CaWO_4$ and $CdWO_4$, and for unoriented crystal of $BaWO_4$ using a 3-m normal incidence monochromator at BL7B.

Results and Discussion

Figure 1(a) shows reflectivity spectra of $CaWO_4$ and $BaWO_4$ at 10 K. For each crystal, the lowest absorption band is observed at 6.0 eV. The band is rather broad compared with the exciton peak of $PbWO_4$ [1]. Several broad structures are seen in the region of 7–15 eV. In $CaWO_4$, the polarization dependence of the lowest peak is weak, while the structures in the 7–15 eV region show distinct dichroism. In $BaWO_4$, spectral features above 15 eV resemble those of BaF_2, indicating that the optical transitions from the Ba $5p$ core levels are involved in this high-energy region.

Reflectivity spectra of $CdWO_4$ crystal are shown in Fig. 1(b). In the 4–7 eV region is observed a broad band with weak fine structures. The small peak at 4.3 eV is probably assigned to the lowest exciton transition. Several sharp peaks are observed in the 7–11 eV region. In contrast to the case of $CaWO_4$, the spectral features below 7 eV depend strongly on the polarization. The difference in optical spectra is clearly seen between the scheelite and wolframite crystals.

The electronic structures of $CaWO_4$ and $CdWO_4$ were calculated by the DV-$X\alpha$ method. In Fig. 2 are shown the results for $[Ca_4WO_4]^{6+}$ and $[CdW_4O_{16}]^{6-}$ clusters. The valence band is mainly built of the O $2p$ state and the conduction band is composed of the W $5d$ state for both structures. In scheelite crystals, W ions are in almost tetrahedral O-ion cages to form WO_4 complex, which are isolated from each other. In wolframite crystals, W ions are in distorted WO_6 octahedra, which form chains by edge sharing. The difference of the spectral features between scheelite and wolframite might be attributed to the different coordination of O ions around W ions.

[1] M. Fujita, M. Itoh, M. Horimoto and H. Yokota, Phys. Rev. **B** 65 (2002) 195105.
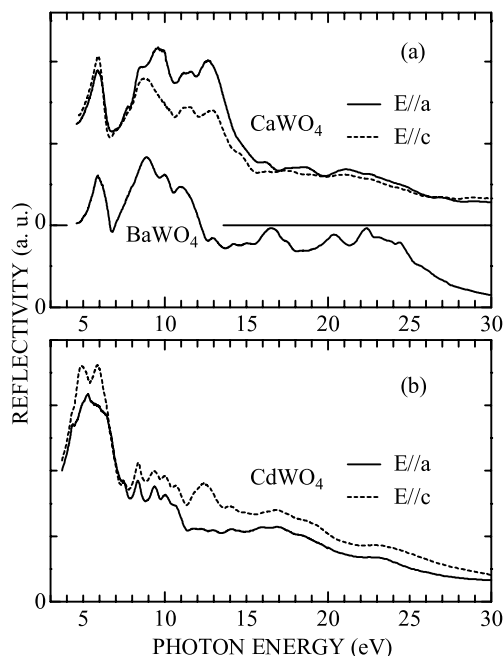

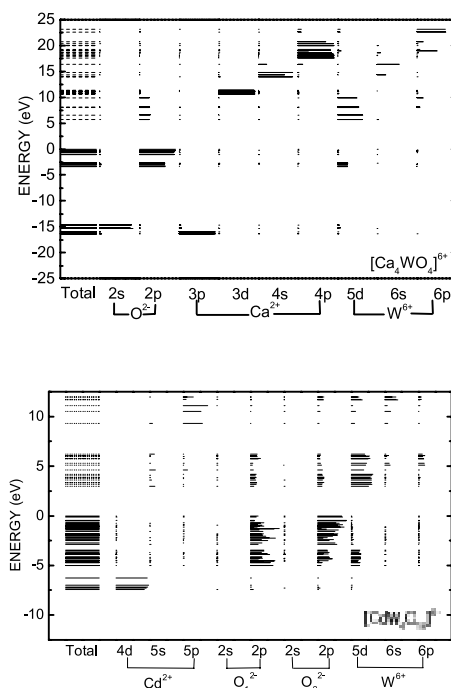Fig. 1. Reflectivity spectra of (a) $CaWO_4$ and $BaWO_4$, and (b) $CdWO_4$ at 10 K.

Fig. 2. Energy diagrams of $[Ca_4WO_4]^{6+}$ (upper) and $[CdW_4O_{16}]^{6-}$ (lower) clusters calculated by the DV-$X\alpha$ method.

Characterization of UV Detectors with n-AlGaN on AlN Epitaxial Films

K. Hiramatsu[1], Y. Shibata[1], H. Yasukawa[1], A. Motogaito[1], H. Miyake[1],
Y. Ohuchi[2], K. Tadatomo[2], T. Nomura[3], Y. Hamamura[3] and K. Fukui[4]

[1]*Dept. of Electrical and Electronic Engineering, Mie University, Tsu 514-8507 Japan*
[2]*LED Business Development Dept., Mitsubishi Cable Co. Ltd., Itami 664-0027 Japan*
[3]*Core Technology Center, Nikon Corporation, Sagamihara 228-0828 Japan*
[4]*Research Center for Development for Far-Infrared region, Fukui University, Fukui 910-8507
Japan*

Characterizations of transparent Schottky barrier n-$Al_{0.5}Ga_{0.5}N$ UV detectors on AlN epitaxial layer in the vacuum UV (VUV) region using synchrotron radiation are described. The high responsivity spectra were realized by using n-AlGaN Schottky UV detectors compared to GaN UV detectors.

Our group has reported on the responsivity spectra of GaN UV detectors in VUV region [1, 2] but they are lower than that in near UV region. To improve it, AlGaN UV detectors are attractive devices because of larger band gap compared with GaN. Furthermore, the advantages of III-nitride materials that are wide band gap and radiation proof will bring out the possibilities of better performance for detection of SX light instead of Si photodiode. If UV detectors can detect VUV and SX light, they will be used in the steppers for future photolithography systems.

In this report, characterization of GaN and AlGaN UV detectors with a transparent electrode in the VUV and SX region using synchrotron radiation are carried out and the comparison of device performance for these devices are described. These AlGaN UV detectors were fabricated on AlN epitaxial layer on (0001) sapphire substrate as shown in Figure 1. The latter structures consists of a 1-μm-thick n-$Al_{0.5}Ga_{0.5}N$ layer (n=2.0×10^{18} cm^{-3}) on (0001) AlN on sapphire substrate. These layers are grown by metalorganic vapor phase epitaxy (MOVPE). The details of growth of AlGaN on AlN are described in ref. [3-5]. The transparent Ni/Au Schottky electrode is formed on n-AlGaN layer. Its diameter is 0.8 mm. The transmittance of Ni/Au electrode is about 0.4-0.5 in the VUV region. The responsivity of UV detectors is estimated by measuring the photocurrent illuminating SR at the beam line 7B (BL7B). UV detectors are illuminated with the monochromatic light, which is between $h\nu$=2.2 eV (λ=564 nm) and $h\nu$=25 eV (λ=50 nm).

The responsivity spectra of $Al_{0.5}Ga_{0.5}N$ UV detectors in near UV and VUV (2-25 eV) are also characterized. Figure 5 shows the responsivity spectra of AlGaN UV detectors. In this figure, to compare the responsivity between GaN and AlGaN UV detectors, the responsivity spectra of unit illuminating area are shown. The band gap energy of $Al_{0.5}Ga_{0.5}N$ is 4.7 eV. Thus, the photon which energy is less than 4.7 eV is not absorbed. At 4.7 eV, the sharp cut-off characteristic is observed. The ratio of

responsivity between UV and VIS regions is about 5,000 – 10,000 like GaN UV detectors. The absolute responsivity at 5.0 eV and VUV region is 0.035 A/W and 0.015 A/W, respectively. Compared with responsivity spectra of GaN UV detectors, the high responsivity in VUV region is realized using AlGaN UV detectors. For example, at 6.5 eV (193 nm, corresponding to light emitting wavelength of ArF lasers), the responsivity of AlGaN (60 mW/A/mm^2) is 16 times as high as that of GaN (3.7 mW/A/mm^2). Therefore, $Al_{0.5}Ga_{0.5}N$ UV detectors have possibilities to detect VUV light with higher responsivity by improving crystal quality of AlGaN layer and device structures in the future.

[1] A. Motogaito et al., Jpn. J. Appl. Phys. 40 (2001) 368.
[2] A. Motogaito et al., Phys. Stat. Sol. (a) 188 (2001) 337.
[3] Y. Kida et al., Phys. Stat. Sol. (a) 194 (2002) 498.
[4] Y. Kida et al., Phys. Stat. Sol. (c) 0 (2003) 2128.
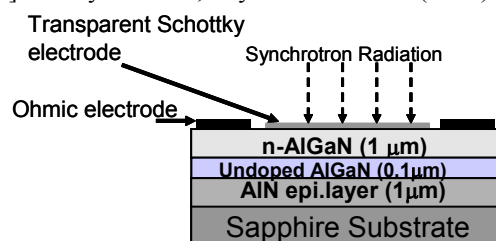[5] H. Miyake et al., Phys. Stat Sol. 200 (2003) 151.
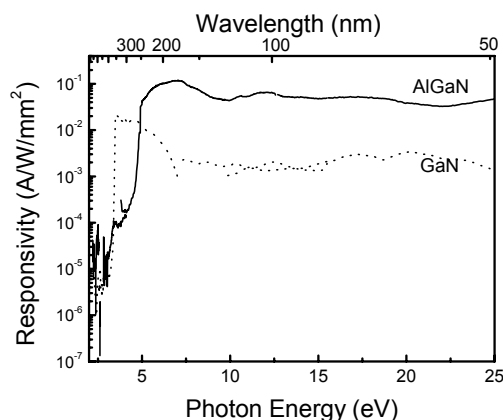
Fig. 1 The Schematic drawing of AlGaN UV detectors.

Fig. 2 Responsivity spectra of AlGaN UV detectors compared with GaN UV detectors [2].

BL7B **The 4f-5d Electronic Excitations in Reflectivity Spectra of LnMnO$_3$**

H. Kuroe, Y. Yagi, Y. Hirobe, H. Kuwahara and T. Sekine

Department of Physics, Sophia University, Tokyo 102-8554 Japan.

The orthorhombic LaMnO$_3$ has been extensively studied because this system has many kinds of interesting phenomena such as the orbital and antiferromagnetic orders. Recently, Ravindran *et al.* calculated the reflectivity spectra of LaMnO$_3$ with a generalized-gradient-corrected relativistic full-potential method [1]. They reproduced the reflectivity spectra observed by Jung *et al.* [2], Arima *et al.* [3] and Takenaka *et al.* [4]. Recently, the trivalent lanthanide ion (Ln^{3+} ion) dependence of the magnetic property also attracts much attention. [5,6]. When the ionic radius of Ln^{3+} ion is small enough, the crystal structure becomes hexagonal YMnO$_3$-type. In this work, we measured the reflectivity spectra in LnMnO$_3$ from visible to vacuum ultraviolet light.

Experiments

The single crystals of LnMnO$_3$ (Ln = Pr, Sm, Eu, Tb, Dy, Ho, Er and Yb) were prepared by floating-zone method. According to RIETAN2000 analysis of x-ray powder diffraction, the crystals of Ln = Yb, Er and Ho have a hexagonal YMnO$_3$-type structure and those of Ln = Tb, Eu, Sm and Pr have a orthorhombic GdMnO$_3$-type one. The single crystal of Ln = Dy contains the 24% YMnO$_3$-type and 76% GdMnO$_3$-type phases. The crystal axes were checked by Laue pattern. The samples were cut and polished with 0.05-μm Al$_2$O$_3$ powder carefully. The post annealing from 1000 $^\circ$C with a cooling rate of 10 $^\circ$C/hour was performed in O$_2$. The reflectivity spectra in the paramagnetic phase were measured with the 3-m normal incident monochromator in BL7B of UVSOR. We set the polarization of the light along to the pseudo-cubic lattice vector.

Results and Discussion

Figure 1 shows the observed spectra between 1.2 and 15 eV in LnMnO$_3$ (Ln = Pr, Sm, Eu, Tb, Dy, Ho, Er and Yb) in addition to those reported in Refs. [1-4]. The electronic configurations of the trivalent ions are $4f^0$ in La^{3+}, $4f^2$ in Pr^{3+}, $4f^5$ in Sm^{3+}, $4f^6$ in Eu^{3+}, $4f^8$ in Tb^{3+}, $4f^9$ in Dy^{3+}, $4f^{10}$ in Ho^{3+}, $4f^{11}$ in Er^{3+} and $4f^{13}$ in Yb^{3+}. The bold lines indicate the experimental conditions (grating: G1, G2 and G3), filters: O53, Pyrex(P), Quartz(Q) and LiF). The reflectivity peaks indicated by arrows around 1.2 and 3.5 eV in Fig. 1 are due to Mn–O charge-transfer process [3,4]. The line shapes of these peaks in the hexagonal crystals are similar to those in the orthorhombic ones. In our measurements, the peak structure from the intraionic $4f$ – $4f$ excitation, for example the structure between 4 and 5 eV when Ln = Pr, was superimposed on the peaks due to the Mn-O charge-transfer process.

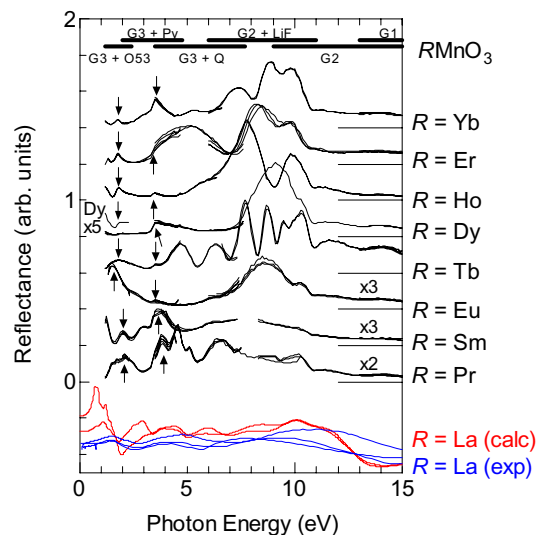We observed the large peaks between 3 and 10 eV

Fig. 1. Observed and calculated reflectivity spectra. The bold lines indicate the experimental conditions. The red and blue curves are the reflectivity spectra reported in Refs. [1-4]. The peaks indicated by arrows are due to the Mn-O charge-transfer exictation.

when Ln = Yb, Er, Ho, Dy and Tb. We assigned them to the reflectivity peaks due to the electronic excitation between $4f^n$ and $4f^{n-1}5d$. This process is electric-dipole allowed [7]. This $4f$ – $5d$ electronic excitation process was also observed in emission spectra in lanthanide-doped materials [8]. These peaks do not come from the breakdown of the selection rule, because the reflectivity peaks were clearly observed even when Ln = Tb, which has the GdMnO$_3$-type crystal structure. In the cases of Ln = Pr, Sm and Eu, we did not observe the peaks due to the $4f$ – $5d$ excitation process.

We also observed the reflectivity peaks due to electronic excitation between O2p and Ln5d orbitals which was reported in Ref. [3].

[1] Ravindran *et al.*, PRB **65**, 064445 (2002).
[2] J. H. Jung *et al.*, PRB **55**, 15489 (1997).
[3] Arima *et al.*, PRB **48**, 17006 (1993).
[4] K. Takenaka *et al.*, JPSJ. **68**, 1828 (1999).
[5] T. Kimura *et al.*, PRB **68**, 060403 (2003).
[6] T. Kimura *et al.*, Nature **426**, 55 (2003).
[7] M. F. Reid *et al.*, J. Alloys. Comp. **344**, 240 (2002).
[8] R. T. Weigh *et al.*, thesis (1999) and their references; R. T. Wegh *et al.* PRB **60**, (1999) 10822.

UV Reflection Spectra of Nanocrystalline β-FeSi$_2$

K.Takarabe, Y. Mori
K.Fukui*
T.Yoshitake**
Okayama University of Science, Okayama 700-0005 Japan
Fukui University, Bunkyo 3-9-1, Fukui 910-8507 Japan
***Department of Applied Science for Electronics and Materials, Kyushu University, 6-1 Kusaga, Fukuoka 816-8580 Japan*

Iron disilicide, β-FeSi$_2$, has attracted much attention as promising material for optoelctronic applications. β-FeSi$_2$ emits light of 1.55 μm(0.8 eV) suitable for SiO$_2$ optical fiber communicatios and can be grown epitaxially on Si. β-FeSi$_2$ is also known to be a Kankyo semiconductor(ecologically friendly semiconductor). A well annealed thin-film sample shows a highest hole mobility of 13000cm^2/Vs at 50 K, which exceeds the electron mobility. Room-temperature electroluminescence action has been already reported.

There are a growing number of studies of basic properties of β-FeSi$_2$. For example, Filonov et al. calculated the dielectric functions in a wide range of photon energies up to 5 eV, and compared these with the ellipsometric experiments. Takarabe et al. performed a first-principles calculation of the optical properties of β-FeSi$_2$ focusing on the near-edge absorption coefficient and reported on the high-pressure measurement of its absorption up to 5 GPa, and discussed the low pressure coefficient of the direct absorption edge of 15.9 meV/GPa, one seventh of that of GaAs, is the negative deformation potential of the valence-band maximum and due to the second largest bulk modulus of 243.5 GPa among common semiconductors. [1]

Exploration of advanced properties extends from the single crystal to nanocrystalline β-FeSi$_2$ in which we expect a quantum confinement effect and an increase of absorption coefficient near and below the band gap.

Sample

Pulsed-laser deposition(PLD) was applied to prepare nanocrystalline β-FeSi$_2$. This method produces a high-energitic particles and a quench of these particles on a low temperature substrate results in the amorphous and nanocrystalline β-FeSi$_2$[2].

Reflection spectra of nano β-FeSi$_2$

Reflection spectrum of the nano β-FeSi$_2$ shows some slightly broad but still developed reflection bands as shown in Fig. 1, it is understood as a finger print of a crystalline state with some degree of amorphous state. The structures are denoted from S0 to S4. In the reflection spectrum of the crystalline β-FeSi$_2$ measured in the energy of visible region, the well structured reflection band appears below 2.5 eV and also in the calculated reflectivity with a

first-principles calculation. However, this structure is completely smeared out in the nano β-FeSi$_2$. This indicates that the amorphous state affects strongly on the lower energy dielectric function than the higher-energy region. The structure at about 5 eV in the calculated reflectivity corresponds to the observed rise of reflectivity at the reflection band S0. One of the possibilities to interpret the S0 structure is the broadening of the calculated reflection band at 5 eV. The sharp reflection band at 20 eV in the calculated spectra is the plasma oscillation of the valence band of the crystalline β-FeSi$_2$. This is strongly damped in the measured reflectivity, although the S4 structure is close in energy. The structures S1 to S3 in the measured reflectivity have no counter part in the calculated reflectivity. In this sense this fact is inherent to the nanocrystalline β-FeSi$_2$.
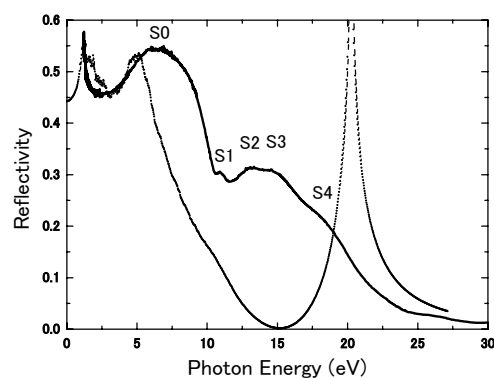
Fig. 1. Measured and calculated reflection spectra of nanocrystalline and crystalline β-FeSi$_2$, respectively.

The measured reflection spectrum of the nanocrystalline β-FeSi$_2$ shows a prominent difference from that of the crystalline state, at least the calculated spectra. The study to characterize the nanocrystalline state is at very early stage but this report shows the UV reflectivity is useful for this study.

[1] K.Takarabe et al., Phys. Rev.B, 65, 16215(2002); Y.Mori et al., phys. stat. sol(b) 235, 302(2003), and references therein.
[2]T.Yoshitake et al., Appl. Phys. Lett., 83, 3057(2003).

Formation of Active Mo Species Supported on SiO$_2$-Al$_2$O$_3$ for Dehydroaromatization:Mo L$_{III}$-edge XANES Study

H. Aritani,* M. Tamai,** K. Konishi,** S. Nishida,**
F. Nishimura,** and A. Nakahira**

*Faculty of Engineering, Saitama Institute of Technology, Okabe, Saitama 369-0293, Japan
**Faculty of Engineering & Design, Kyoto Institute of Technology, Kyoto 606-8585, Japan

MoO$_3$-modified H-MFI shows high activity for dehydroaromatization of methane, although strong deactivation cannot be avoided during the reaction. In this reaction, many workers have been revealed reduction of Mo species is brought about in contact with methane in the initial step. Deoxidated Mo ions react methane to form carbide species, Mo$_2$C, in the second stage. The carbide species is active for dehydroaromatization of methane to form benzene, however, deactivation is brought about by carbon deposition on the catalyst surface at the same time. It is likely the catalytic activity and its deactivation rate depend on the type of silica-alumina supports. Relation between silica-alumina support and active Mo species formed in the reaction is important to clarify the formation process of highly active Mo species and its red-ox behavior during the reaction. In fact, molybdena species supported on amorphous silica-alumina shows dehydroaromatization activity while it is very lower than that on H-MFI support. By comparing H-MFI with amorphous silica-alumina supports, reduction behavior of Mo ions before/after the reaction can be provided. Characterizaiton of those species by means of Mo L-edge XANES is appropriate for clarification of Mo ions with different valences. In this report, local structure of supported Mo ions on H-MFI and amorphous silica-alumina (SAH-1) and their redox changes after dehydroaromatization of methane or ethane at 973 K for 3 h is evaluated by Mo L$_{III}$-edge XANES.

Experimental

Mo L$_{III}$-edge XANES spectra were measured in BL1A of UVSOR-IMS in total-electron yield (TEY) mode, using the Ge(111) double-crystal monochromator ($2d = 0.6532$ nm). The photon energy was calibrated by using Mo metal sample at Mo L$_{III}$-edge (2520 eV).

Results and Discussion

Fig. 1 shows the XANES spectra of authentic Mo samples. It is clear that both intensity and energy positions of two white-lines are different between Na$_2$MoO$_4$ (consist of Mo^{6+}O$_4$ tetrahedra, T_d) and MoO$_3$ (Mo^{6+}-O$_6$ octahedra, distorted O_h) because of local symmetry around Mo^{6+} ions. In cases of Mo$_2$C (Mo^{2+}) and Mo metal, edge energy values of those XANES are lower than Mo^{6+} samples, however, difference of edge energy is unclear between Mo$_2$C and Mo metal. To clarify the difference, second derivative XANES were introduced, as shown in Fig. 2. As for the 2nd derivative waves, minimum peaks

are due to peak components of original XANES. The difference of energy value is significantly between Mo$_2$C (2524.2 eV as lowest energy) and Mo mettal (2523.5 eV). The assignment can be applied to the catalyst samples with reduced Mo ions. Fig. 3 shows the XANES spectra of MoO$_3$/SAH-1 and MoO$_3$/H-MFI catalysts before/after the reaction with CH$_4$ or C$_2$H$_4$ at 973 K. For MoO$_3$/SAH-1, it is concluded that reduced Mo species are formed after C$_2$H$_4$ reaction but not formad after CH$_4$ reaction. In case of MoO$_3$/H-MFI, which shows high catalytic activity for converting CH$_4$ to C$_6$H$_6$, several components due to Mo^{2+}- and Mo^{6+}- (peak at 2526.5 eV) species are overlapped after CH$_4$ reaction. This result suggests the formation of so-called "oxy-carbide species" as catalytically active species for dehydroaromatization of CH$_4$. After C$_2$H$_4$ reaction, Mo^{2+}-species is only formed and the component due to Mo^{6+}-species is scarcely seen. The reactivity for converting C$_2$H$_4$ to C$_6$H$_6$ is higher in MoO$_3$/SAH-1 than in MoO$_3$/H-MFI. In addition, crystallinity of MFI-phase in MoO$_3$/H-MFI became low only by the reaction with C$_2$H$_4$ by XRD analysis, suggesting catalytic deactivation during the reaction. Thus it is concluded that difference between H-MFI and SAH-1 supports gives the formation of Mo species with different reduction state after the reaction with CH$_4$. Partly reduced oxy-carbide species coexisting Mo^{2+} and Mo^{6+} ions are formed on H-MFI support after contact with CH$_4$, and this species can act as highly active species for CH$_4$ dehydroaromatization.
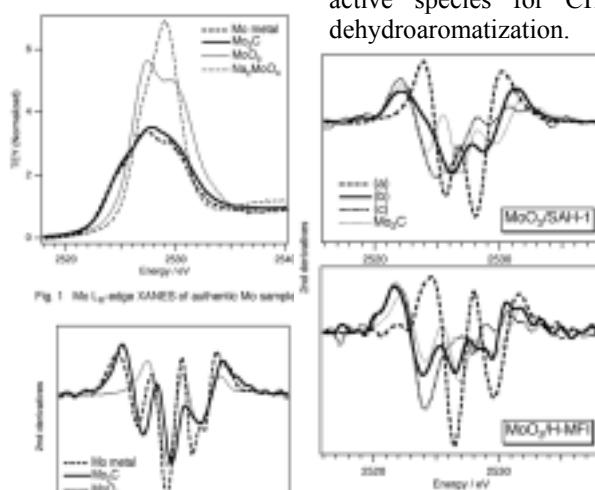

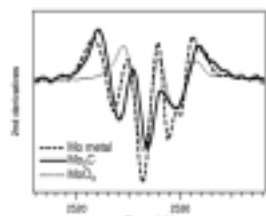Fig. 1 Mo L$_{III}$-edge XANES of authentic Mo samples

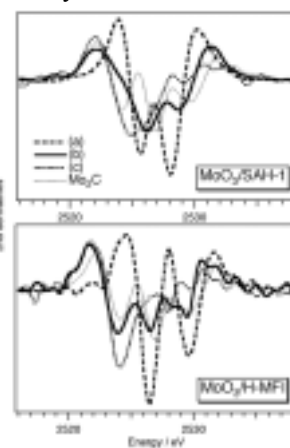Fig. 2 Second derivatives of Mo L$_{III}$-edge XANES on authentic Mo samples

Fig. 3 Second derivatives of Mo L$_{III}$-edge XANES on MoO$_3$/H-MFI and MoO$_3$/SAH-1.
(a) Before reaction.
(b) After reaction with CH$_4$ at 973K.
(c) After reaction with C$_2$H$_4$ at 973K.

Charging Mechanism of $Li_{1-x}Ni_{1/3}Mn_{1/3}Co_{1/3}O_2$ Cathode Materials for Lithium-ion Secondary Batteries from Transition Metal *L*-edge and Oxygen *K*-edge Spectroscopy

Y. Arachi, T. Asai, H. Kobayashi[†], S. Emura[††]

Faculty of Engineering, Kansai University, Osaka 564-8680, Japan
[†]*National Institute of Advanced Industrial Science and Technology(AIST),Osaka 563-8577*
[††]*ISIR, Osaka University, Ibaraki, Osaka 567-0047*

The alternatives to $LiCoO_2$ cathode material have been extensively searched due to small natural deposits of Co and its toxicity in the filed of Li-ion rechargeable batteries. Recently, $LiNi_{0.5}Mn_{0.5}O_2$ and $LiNi_{1/3}Mn_{1/3}Co_{1/3}O_2$ have been proposed as a new promising candidate.[1] Cell performance using Li exhibited good cycleability, and a reversible capacity of 150 mAh/g within the voltage range of 3.0 to 4.3 V, which corresponds to one-half of theoretical capacity (280mAh/g). We have employed the X-ray diffraction and XAFS measurement using synchrotron radiation source to investigate the structural change and the charging process of these materials.[2,3,4] In this study, the electronic structural change and the charging mechanism were investigated by XANES spectra of Co, Ni, Mn K- and L-edges, and O K-edge respectively.

Experiment

$LiNi_{1/3}Mn_{1/3}Co_{1/3}O_2$ was synthesized in air at 1273 K for 24 h using appropriate molar ratios of $LiOH \cdot H_2O$, $Mn(CH_3COO)_2 \cdot 6H_2O$, $Ni(CH_3COO)_2 \cdot 6H_2O$, and $Co(CH_3COO)_2 \cdot 6H_2O$ and de-lithiated samples were electrochemically prepared using coin-type cells with $Li/1M$ $LiPF_6$ in EC:DEC(1:1)/samples. The Ni/Mn/Co valence states of samples were determined by the Ni/Mn/Co *K*-edge XANES spectra. X-ray absorption measurements at the Co, Ni, Mn L-edges and O K-edge by total electron yield were performed on BL1A and BL8B1.

Results and Discussions

$LiNi_{1/3}Mn_{1/3}Co_{1/3}O_2$ showed a single phase adopted the α-$NaFeO_2$ structure like as $LiCoO_2$. The results of the Ni, Mn and Co K-edge XANES spectra showed that $LiNi_{1/3}Mn_{1/3}Co_{1/3}O_2$ could be represented as $Li(Ni^{2+}_{1/3}Mn^{4+}_{1/3}Co^{3+}_{1/3})O_2$. On the other hand, Neutron diffraction measurements demonstrated that the lattice parameters of $LiNi_{1/3}Mn_{1/3}Co_{1/3}O_2$ are $a = 2.860$ Å and $c = 14.22$ Å and that the chemical composition can be expressed as $[Li_{0.97}Ni_{0.03}]_{3a}[Li_{0.03}Mn_{0.33}Ni_{0.30}Co_{0.33}]_{3b}O_2$, referring to the Wyckoff positions 3*a* and 3*b* with space group *R3m*. Figure 1 shows the XANES spectra of Ni L-edge for charged $Li_{1-x}Ni_{1/3}Mn_{1/3}Co_{1/3}O_2$. A continuous chemical peak shifts corresponding to L_{III}, L_{II} to higher energy was observed up to $x = 0.7$ for showing charge capacity of 194 mAh/g. The results of K-edge were observed in the same way. In addition, that of Co L-edge showed a slightly higher shift and that of Mn L- and K-edges showed no chemical shifts for all the samples. However, a systematic change was not clearly observed in O K-edge absorption. On the basis of these results, we are constructing the band structure and investigating the charging mechanism for this material.
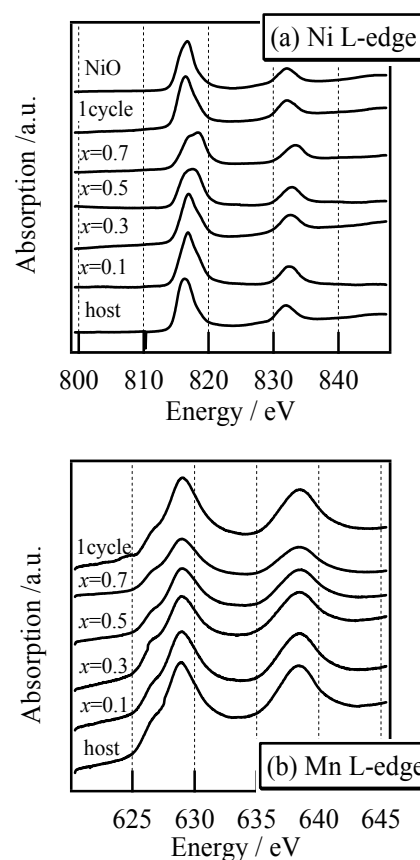

Fig.1 (a) Ni L- and (b) Mn L-edges XANES of $Li_{1-x}Ni_{1/3}Mn_{1/3}Co_{1/3}O_2$

1. T.Ohzuku and Y.Makimura,*Chem.Lett.*,(2001)744.
2. Y.Arachi, et al, *Chem.Lett.,* (2003)60.
3. H. Kobayashi et al., *J. Mater. Chem.*,14(2004) 40.
4. Y. Arachi et al., *Physica Scripta,* in press.

BL1A # Application of Synchrotron EXAFS on Studying Biomaterial

J. Ding[1,2], B. H. Sun[1], T. X. Fan[1], D. Zhang[1]

M. Kamada[3], K. Kuwahara[3], H. Ogawa[3], Q. X. Guo[4]

1. State Key Lab of MMCs, Shanghai Jiao Tong University, Shanghai 200030, P. R. China
2. Venture Business Laboratory, Saga University, Saga 840-8502, Japan
3. Synchrotron Light Application Center, Saga University, Saga 840-8502, Japan
4. Department of Electrical and Electronic Engineering, Saga Univ., Saga 840-8502, Japan

Porous materials are of scientific and technological interest because of their ability to interact with atoms, ions and molecules not only at their surfaces, but also throughout the bulk of the material [1]. These materials are extremely useful in catalysis and separation technologies [2]. Recently, novel porous morph-genetic ceramics synthesized from natural materials such as wood, fibers, surfaces of leafs, has recently attained particular interest [3, 4], because natural materials exhibit a hierarchically built anatomy optimized in the genetic evolution process, compared to artificial synthetic templates, and are abundant, cheap, renewable and environmentally conscious.

The porous morph-genetic ceramics is generally fabricated through sintering treatment at high temperature, after infiltrating various organic or inorganic solutions to the bio-template. Therefore, clarifying the mechanism of sintering process is indispensable for obtaining desired porous morph-genetic ceramics, because the sintering treatment plays a critical role for transforming the hierarchical cellular structure of bio-template into porous ceramics with specific functional properties. Unfortunately, it is impossible to reveal the dynamic transition during sintering process by using conventional analysis techniques such as scanning electron microscopy or X-ray diffraction. It is well known that extended X-ray absorption fine structure (EXAFS) is a powerful technique for determining the local structure with atomic selectivity in both crystalline and amorphous states. Therefore, we believe that it is possible to reveal the dynamic transition during sintering process by studying the local structure of atoms. However, to our best knowledge, no study of local structural properties of the porous morph-genetic ceramics has been reported up to now.

In this work, we investigate the local structural properties of the novel porous morph-genetic silicon carbide sintered at different temperatures by EXAFS for the first time. By measuring and analyzing Si K-edge EXAFS, it is found that the coordination number of nearest Si-Si shell dramatically changes when the structure is transformed from amorphous into crystalline, indicating the EXAFS technique is a useful tool to elucidate the synthesis mechanism for these novel porous morph-genetic ceramics.
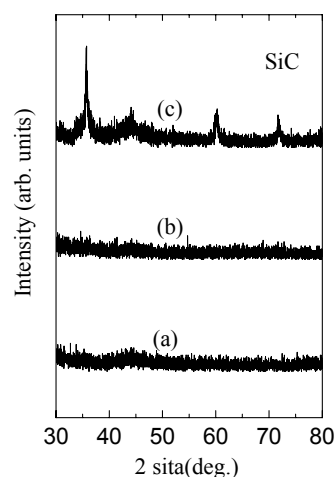
Fig. 1. XRD spectra of the samples sintered at temperatures of (a) 1273K, (b) 1473K, and (c) 1673K.
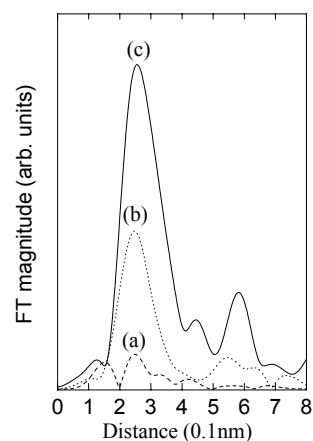
Fig. 2. Fourier transforms of Si K-edge EXAFS with weight κ^3, (a) 1273K, (b) 1473K, and (c) 1673K.

[1] M. E. Davis: Nature **417** (2002) 813.
[2] H. Yang, A. Kuperman, N. Coombs, S. Mamiche-Afara and G. A. Ozin: Nature **379** (1996) 703.
[3] P. Greil: J. Eur. Cera. Soc. **21** (2001) 105.
[4] A. Dong, Y. J. Wang, Y. Tang, N. Ren, Y. H. Zhang, Y. H. Yue and Z. Gao: Adv. Mater. **14** (2002) 926.

SOLD STATE
SPECTROSCOPY II:
XAFS AND PES

First-Principles Study of Al K-edge NEXAFS Spectra of AlN and Al_2O_3

T. Yamamoto*, T. Suga*, S. Yoshioka, S. Kameyama and I. Tanaka

*Fukui Institute for Fundamental Chemistry, Kyoto University, Kyoto 606-8103, Japan

Department of Materials Science and Engineering, Kyoto University, Kyoto 606-8501, Japan

It has been well established that the X-ray absorption near-edge fine structure (NEXAFS) measurement is a powerful tool to analyze electronic structures of materials, because spectral fine structure of the NEXAFS spectrum is very sensitive to a change in chemical environment. Recently we have succeeded the chemical state analysis of the ultradilute Ga dopant at a level of atomic p.p.m in MgO matrix by combined use of the experimental NEXAFS analysis and the first-principles calculations [1]. For the chemical state analysis of lighter dopant elements by the NEXAFS within the soft X-ray region, we have performed preliminary NEXAFS measurement and the first-principles calculations for Al_2O_3 and AlN at Al K-edge. Our present calculations could quantitatively reproduce both a) spectral fine structure and b) transition energy of the experimental NEXAFS.

Experiments and calculations

High-resolution X-ray absorption spectra at the Al K-edge of Al_2O_3 and AlN were measured using the BL1A beamline at UVSOR. The NEXAFS spectra were collected by the total electron yield (TEY) method. The incident photon beam was monochromatized using a KTP ($2d_{011}$=10.954Å) double-crystal monochromator. Commercially available high purity powders with corundum and wurtzite types of structures for Al_2O_3 and AlN, respectively, were attached to the first photocathode of the electron multiplier using adhesive carbon tape. The crystal structures and contaminants of the sample employed here were checked by the X-ray diffraction (XRD) measurements, which revealed the presence of only small amounts of contaminants.

The first-principles density functional theory (DFT) calculations were carried out by using the full-potential linearized augmented plane wave package, WIEN2k [2]. The core-hole effect was fully introduced in our present calculations by using the 2x2x1 and 3x3x2 supercells for Al_2O_3 (120 atoms) and AlN (72 atoms), respectively. The theoretical NEXAFS spectra were calculated within the electronic-dipole-allowed transitions in the core-hole state. Product of the radial transition probability and corresponding projected partial densities of the states (p-PDOS) represents the theoretical NEXAFS spectrum.

Results

The observed NEXAFS spectra of Al_2O_3 and AlN at Al K-edge are shown in Fig. 1(a). Seven peaks, labeled as peaks A to G for Al_2O_3 and peaks J to P for AlN, were found within this energy regime in both Al_2O_3 and AlN. Theoretical NEXAFS spectra are shown in Fig. 1(b). As shown in this figure, the theoretical spectral features showed fairly good agreements with experimental ones. It is noted that experimental threshold energy shift, i.e., chemical shift, by 4.3 eV was also well reproduced by our present calculations, although absolute transition energies were slightly overestimated by 4.0 eV ($\Delta E/E$ = + 0.25%).

In summary, we have carried out the NEXAFS measurements of Al_2O_3 and AlN at Al K-edge and the first-principles DFT calculations to interpret the spectral features and transition energy of experimental NEXAFS. Our present theoretical approach could give a quantitative reproduction of the experimental spectral fine structures and transition energies. This type of combined use of the experimental NEXAFS and the first-principles calculations must be a powerful tool for systematic and quantitative analysis of the chemical environment of the materials.
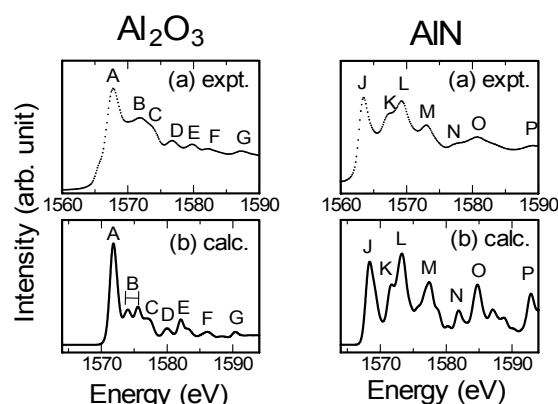

Fig. 1. Comparison of Al K-edge NEXAFS spectra of Al_2O_3 (left) and AlN (right) between (a) experiment and (b) calculation.

[1] I.Tanaka et al., Nature Materials 2 (2003) 541.
[2] http://www.wien2k.at

Cl K XANES Analysis of the Electronic Structure around Metal Ion in Metallotetraphenylporphyrin

H. Yamashige, T. Kurisaki, H. Wakita*

Department of Chemistry, Faculty of Science, Fukuoka University,
Nanakuma, Jonan-ku, Fukuoka 814-0180, Japan
*Advanced Materials Institute, Fukuoka University,
Nanakuma, Jonan-ku, Fukuoka 814-0180, Japan

The metallotetraphenylporphyrins (MTPPs) is of particular interest due to many possible applications, such as catalysts, electronic devices, gas sensors, and electroluminescent displays. MTPP have a large p-conjugated aromatic system. In order to elucidate chemical and physical properties of MTPP, it is necessary to determine their electronic structure [1].
In this work, we applied X-ray absorption near edge structure (XANES) spectroscopy to two type porphyrins, FeTPP-Cl and MnTPP-Cl. The results of the measurement indicate unoccupied and occupied electronic structure of MTPPs. The X-ray absorption spectra were measured at BL1A

of the UVSOR in the Institute of Molecular Science, Okazaki [2]. The ring energy of the UVSOR storage ring was 750MeV and the stored current was 110-230 mA. Cl K-edge absorption spectra were recorded in the regions of 2533-3733eV by use of two Ge(111) crystals. The absorption was monitored by the total electron yield using a photomultiplier.
The Cl K-edge XANES spectra for the MTPPs are shown in Figs. 1 and 2. A remarkable change of the spectral patterns was observed for the FeTPP-Cl and MnTPP-Cl. Comparison of observed and calculated spectra revealed that metal 3d and 4p orbits contribute to peak A and B. But, MnTPP-Cl did not contain contribution from the Cl4p and Cl5p orbits.
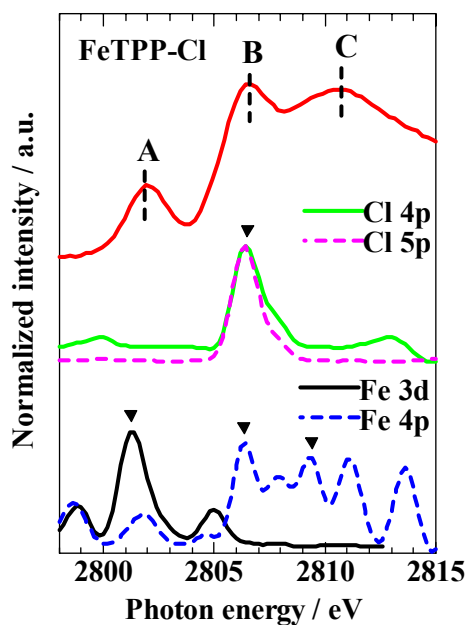

Fig. 1. Observed and calculated Cl K-edge XANES spectra of FeTPP-Cl.
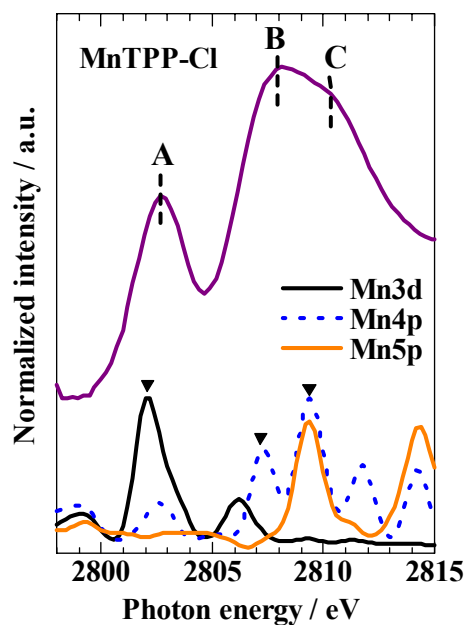

Fig. 2. Observed and calculated Cl K-edge XANES spectra of MnTPP-Cl.

[1] T. Okajima, Y. Yamamoto, Y. Ouchi and K. Seki, *Journal of Electron Spectroscopy and Related Phenomena*, 849 (2003)
[2] S. Murata, T. Matsukawa, S. Naoe, T. Horigome, O. Matsuodo, and M. Watatabe, Rev. Sci. Instrum., 63, 1309 (1992)

The Measurement of γ and Soft X-ray Excited Optical Luminescence of a Silica Glass

T. Yoshida[1], T. Tanabe[1] and H. Yoshida[2]

[1]Dept. of Nuclear Engineering, Graduate School of Nagoya University, Nagoya 464-8603
[2]Dept. of Applied Chemistry, Graduate School of Nagoya University, Nagoya 464-8603

In the present work, we have made in-situ luminescence measurements of silica glasses induced by γ-ray and soft X-ray, on silica. The main objects of this report are to clarify of the dynamic damaging process in silica which should be induced by the electron excitation, as well as the difference of the radiation effects between γ-ray and soft X-ray irradiations.

Experimental

The measurement of luminescence of the fused silica glass induced by soft X-ray irradiation (1.8-1.9 keV) was carried out on the beam line 7A at UVSOR, Institute for Molecular Science with a stored current of 100-200 mA. The size of soft X-ray beam was ca. 2 x 10 mm, and the flux was ca. 1×10^9 photons / mm^2/ sec / 100 mA. The luminescence was focused by a lens in the UHV chamber to the monochromator and detected by a multi-channel analyser.

Results and Discussion

Fig. 1 shows the soft X-ray induced luminescence of the fused silica glass. The 3.1 eV band attributed to $B_{2\beta}$ center was observed. One notes the significant deviation of the 3.1 eV band intensity profile for the different excitation energies of the incident soft X-ray. Irrespective of the incident energy of soft X-ray, fundamentally the same evolutions were observed. The intensity of the 3.1 eV band slightly increased in the early stage of the irradiation and then decayed gradually with irradiation time, similarly to the change of the 3.1 eV emission band in the γ-ray induced luminescence.
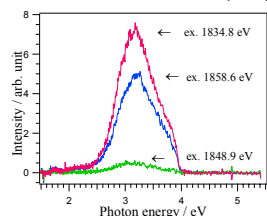

Fig.1 Optical luminescence spectra of a fused silica glass under the irradiation of soft X-ray with the energy of 1834.8 eV, 1848.9 eV and 1858.6 eV

Such changes of luminescence induced by the soft X-ray irradiations, must be discussed based on absorbed dose (Gy = J/kg) and absorbed dose rate. The absorbed dose rate (Gy/sec) for the γ-ray irradiation was evaluated as ca. 1.6 Gy/sec. On the other hand, in the case of soft X-ray irradiation, the absorbed dose rate changes drastically around the Si K-edge, because the penetration depth of the soft X-ray above the K-edge is much shorter than that below the K-edge in accordance with the change of the absorption coefficient (μ) of a silica glass. On the basis of the value of μ, we roughly estimated the penetration depths of soft X-ray below and above the edge as 5×10^{-3} and 2×10^{-4} cm, respectively. Accordingly the absorbed dose rates were estimated as ca. 2.6 and 12.9 Gy/sec, for 1834.8 eV and 1848.9 eV(1858.6 eV), respectively. Then we can obtain normalized luminescence yield from the intensities of the 3.1 eV emission band during both γ- and soft X-ray irradiations divided by the following two factors, i.e., (1) the volumes of the silica glass where γ- and soft X- rays were absorbed and (2) the detecting efficiencies of the spectrometers.

The normalized luminescence yields of the 3.1 eV band thus obtained are plotted against the absorbed dose in Fig. 2. One can note that all normalized yields show similar dependence on the absorbed dose, in spite of the large difference between γ- and soft X-rays energies. The normalized intensities rapidly increased and reached the maximum at around 3.5 kGy, followed by a gradual decrease. It is noteworthy that all the normalized yields are within a factor of 10, which is far less than the energy difference of γ-ray and X-ray (three order's of magnitude). This means that the luminescence is controlled by the absorbed dose, in other words, the luminescence is induced by the electron excitation from secondary electrons and photons with low energies, but not by the direct excitation of primary (Compton) or high energy electrons and photons.
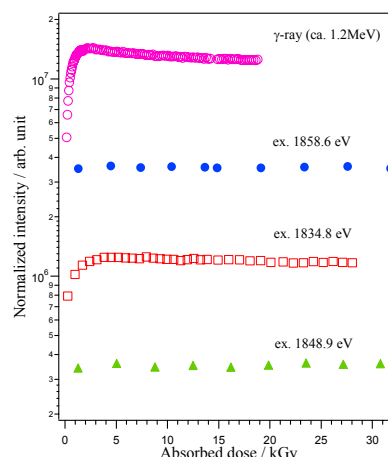

Fig.2 The variation of the normalized intensities of 3.1 eV band with the absorbed dose under the irradiation of γ-ray and soft X-ray with the energy of 1834.8 eV, 1848.9 eV and 1858.6 eV.

Photoemission Study for Initial Oxidation and Nitridation of ZrB$_2$

K. Takahashi, S. Tokudomi*, Y. Nagata*, K. Fukui**, M. Kamada

Synchrotron Light Application Center, Saga University, Saga 840-8502 Japan
*Faculty of Science and Engineering, Saga University, Saga 840-8502 Japan
**Research Center for Development of Far-Infrared Region,
Fukui University, Fukui 910-8507 Japan

Transition metal diborides are attractive materials due to its hardness, high-melting point and chemical stability. Among then, zirconium diboride (ZrB$_2$) has the hexagonal symmetry of the AlB$_2$-type structure with an in-plane lattice constant of 0.3168 nm which is very close to that of GaN. Recently, epitaxial growth of GaN film on ZrB$_2$ substrate has succeeded using the metal-organic vapor phase epitaxial method. In order to obtain epitaxial GaN film with good crystallinity, it is indispensable to elucidate the initial oxidation and nitridation processes. In addition, after the unexpected discovery of high temperature superconductivity in MgB$_2$, diborides have attracted renewed attentions. In this work, we have performed the photoemission study for clean ZrB$_2$(0001) surface obtained by in-situ annealing treatment and its initial oxidation and nitridation processes.

Experimental

Experiments have been performed at beamline BL2B1. The ZrB$_2$(0001) single crystalline sample was grown by floating-zone method. The ZrB$_2$(0001) sample was fixed on the molybdenum tile using a small molybdenum clip. The clean surface was obtained by the repetition of flash annealing around 1850ºC. The base pressure of the measurement chamber was about 2×10^{-8} Pa. The pressure during the flash annealing was kept better than 5×10^{-7} Pa. The O$_2$ and N$_2$ were exposed up to 100 Langmuir (1L $= 1\times10^{-6}$ Torr$\times$s) at 650ºC. The photoemission spectra were obtained using the double-pass cylindrical mirror analyzer. The overall energy resolution was about 1.3eV.

Results and Discussions

Figure 1 shows the photoemission spectra for B 1s and Zr 3d core-levels. The peaks at 179.0, 181.3 and 187.7 eV in binding energy correspond to Zr 3d$_{5/2}$, Zr 3d$_{3/2}$ and B 1s core-levels, respectively. Since the spectrum for the clean surface shows no structure originated from the oxidized component, we conclude that contamination free surface can be obtained using our cleaning procedure. The sample showed sharp hexagonal low-energy electron diffraction pattern after the cleaning procedure. We have also performed separated UPS measurements for clean ZrB$_2$(0001) surface. The work function of the clean ZrB$_2$(0001) surface is determined from the width of the photoemission spectra to be 5.1±0.1 eV, which is much larger than that of polycrystalline boron (4.5 eV). On a LaB$_6$(100) surface, the charge transfer occurs form La to B atoms and the dipole moment is directed from the surface into the bulk since the outermost layer of the LaB$_6$(001) surface consists of La atoms. As a result, the work function of LaB$_6$(001) is as small as 2.5 eV. From our result, it is considered that the clean surface of ZrB$_2$(0001) is terminated by graphitic-boron layer and the charge transfer form the second Zr layer to the first B layer exist. Because of the B atom at the ZrB$_2$(0001) surface, the dipole moment is directed outward, and the work function is increased. As shown in Fig.1, the new components appear at 182.0 and 184.3 eV in binding energy after a 11 L O$_2$ exposure at 650ºC. The chemical displacement of +3.0 eV is smaller than that between Zr and ZrO$_2$. The literature value of chemical shift is 4.2 eV for Zr 3d$_{5/2}$ between Zr and ZrO$_2$. On the other hand, the new components appear at lower binding energy after a N$_2$ exposure at 650ºC. It is found that the chemical displacement of Zr 3d$_{5/2}$ core-level is -0.7 eV. We have also performed the X-ray absorption measurement in the N 1s-2p threshold region for 10 L N$_2$ exposed surface. It is found that the X-ray absorption spectra show the dependence on the indent photon direction. In order to clarify the bonding orientation of the chemisorbed N atoms on ZrB$_2$(0001) surface, more detailed measurements is needed.
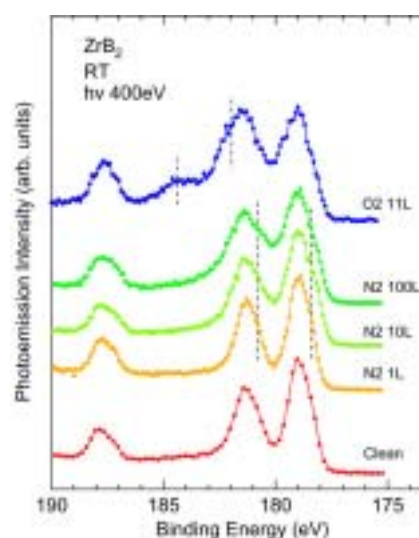

Fig. 1. Photoemission spectra for B 1s and Zr 3d core-levels.

Electronic Structure of DNA
Studied by Resonant Photoemission Spectroscopy

H. S. Kato, M. Furukawa, M. Kawai, M. Taniguchi*, T. Kawai*,
T. Hatsui**, N. Kosugi**

RIKEN (The Institute of Physical and Chemical Research), Wako 351-0198 Japan
*Institute of Scientific and Industrial Research, Osaka University, Ibaraki 567-0047 Japan
**UVSOR Facility, Institute for Molecular Science, Okazaki 444-8585 Japan

The characterization of electronic states near Fermi level of DNA duplexes has been desired to clarify the mechanisms of long-range charge migration in DNA, from the viewpoint of not only biochemistry but also molecular device materialization. With the recent progress in nanotechnology, the electric conductivity of DNA has directly been measured in molecular scale. However, these characterizations of the electric property are still indefinite, and there is no significant observation on the electronic states near Fermi level of DNA for understanding of the charge migration mechanism. In this study, therefore, we carried out resonant photoemission spectroscopy (RPES) experiments near Fermi level with resonance from N 1s to unoccupied states for both poly(dG)·poly(dC) (GC) and poly(dA)·poly(dT) (AT) DNA duplexes.

Experimental

Experiments were performed at the beamline BL4B of the UVSOR facility, in which the end-station (ultrahigh vacuum systems) is equipped with an electron energy analyzer and a retarding-field electron detector for XAS. We prepared thick GC- and AT-DNA films on SiO_2/p-Si(111) substrates in the atmosphere. The film thickness prepared was estimated to be 100 - 200 nm. These samples were introduced into the ultrahigh vacuum via a sample entry system from the atmosphere, without baking procedures.

Results and Discussion

An N K-edge X-ray absorption (XA) spectrum of GC DNA is shown in the inset of Fig. 1. In the XA spectrum, two 1s - π* resonant peaks at 399.7 eV and 401.9 eV and a broad 1s - σ* resonant peak at 407 eV were observed. The off- / on-RPE spectra near the Fermi level of GC DNA are shown in Fig. 1 as a function of kinetic energy. The RPE spectra were measured at each resonant absorption peak marked on the XA spectrum shown in the inset. On the comparison to the off-RPE spectrum, the on-RPE spectra are obviously involving additional components which is attributed to the N-KLL Auger electrons.

The Auger signals could be extracted from the on-RPE spectra by subtracting the off-RPE spectra in binding energy plots, as the dotted lines in Fig. 1. The differential spectra commonly show a broad bump. Normally, the Auger electrons keep an identical distribution in kinetic energy, independently of excitation photon energies. The obtained Auger

signals were, however, strongly affected by excitation energy; the lower photon energy light provides a higher kinetic energy distribution. This indicates that the excited electrons locate in the unoccupied states for, at least, a time scale of Auger transition and affect its final state of the transition.

In addition, an appended component was observed at the first π* resonance, as marked by a dagger in Fig. 1. We attribute the additional component to those of participant Auger transition. This finding again indicates that the excited electrons locate in the π* states for, at least, the time scale of Auger transition.

In the case of the molecules chemisorbed on metals, their RPE spectra do not show the drastic peak shift of Auger electrons in kinetic energy and also the participant Auger electrons. These are explained as that the molecular orbitals rehybridized with metal electronic states are delocalized, and the excited electrons in the chemisorbed molecules diffuse into the metal, immediately. In contrast, all features of the observed RPE spectra of DNA, as mentioned above, clearly show that the excited electron is localized at the excited orbitals. In other words, the unoccupied states of the bases in DNA duplexes are not delocalized. Hence, we conclude that the charge hopping model is suitable for electric conduction in DNA duplexes rather than the charge transfer model via delocalized states, when electrons pass through the π* states of the DNA bases.
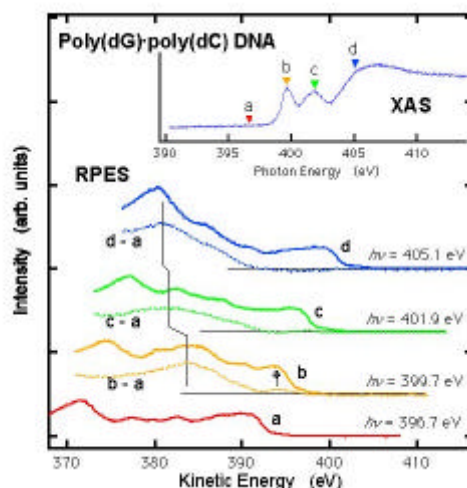

Fig. 1. Off- / on-RPE spectra of GC DNA. The inset shows an N K-edge X-ray absorption spectrum.

Excited States of Ar 2p in Ar Solid

H. Setoyama, T. Hatsui and N. Kosugi

Institute for Molecular Science, Okazaki 444-8585 Japan

Rydberg states in condensed phase are of interest since they are sensitive to external perturbation due to their large orbital radii. Several studies have been carried out on surrounding effects in the Ar 2p excited states using rare gas matrixes. Changes of the spectral features between another condensed phases are explained by the competition of two effects, namely, (i) the polarization stabilization of the ionization threshold, and (ii) the exchange repulsion of the Rydberg electron due to the valence electrons of the neighboring atoms/molecules. [1] In the present study, temperature dependence of the peak position of the bulk Ar $2p_{3/2}$-4s band has been measured to reveal the latter effect. The exchange repulsion is mainly influenced by the inter-atomic distance between the neighboring atoms. Different temperatures of Ar solid make different inter-atomic distances of neighboring Ar. The different inter-atomic distance between the neighboring Ar should reveal the effect.

The Ar solid was prepared by dosing Ar gas approx. 30 L to the gold coated copper plate of a cryostat at ~8K. The temperature of the Ar solid was monitored using a silicon diode thermostat and was adjusted to 8K or 16K by using a ceramic heater. Photoabsorption spectra were measured by a partial electron yield (Auger yield) method using an MCP detector with a retarding mesh (-180V). All spectra were taken at grazing incidence angle of 15 degree. The photoabsorption spectra were taken for several times since there was an energy drifting (~7 meV per hour) caused by the instability of the beamline monochromator.

Fig. 1 shows the observed energy position of the Ar $2p_{3/2}$ –4s for bulk Ar atom measured at different temperatures, 8K and 16K. The typical spectra for 8K and 16K are also shown as inset. Photon energy was calibrated by using the bulk Ar $2p_{3/2}$ –4s band (245.06eV) for 8K Ar solid. [1] As shown in the inset, the main band is observed with a shoulder structure at the lower photon energy side. The main band is assigned to the transition from Ar $2p_{3/2}$ to 4s band of bulk Ar atom and the shoulder structure is assigned to that of surface Ar atoms. [1] Comparing with the main bands for 8K and 16K spectra, it is clearly seen that the spectral features are very similar but the bulk band shows different excitation energy. To obtain the excitation energies of the $2p_{3/2}$ –4s band of the bulk Ar atom for 16K, the photoabsorption spectra were taken for several times and the bands are fitted with two Voigt functions. In Fig. 1, the vertical axis indicates the uncalibrated energy positions of the

Ar $2p_{3/2}$ –4s band. The horizontal axis indicates the measuring time. Error bars indicate 2σ of the peak fittings. The blue and red lines indicate the linear fittings for the energy driftings for 8K and 16K, respectively. The difference between the sections for both lines gives the excitation energy difference of 5 ± 1.5 meV.

The temperature increase causes an expansion of the lattice constant of the Ar solid. The Ar solid has a face-centered cubic structure with the lattice constants of 5.2890 Å and 5.2941 Å for 8K and 16K, respectively. [2] Neighboring Ar atoms with shorter inter-atomic distance are expected to have stronger perturbation (exchange repulsion) because the excited electron in 4s-Rydberg states is pushed to higher energy side by closer potential of the surrounding Ar atoms. This can be explained as stronger exchange repulsion by the surrounding atoms arisen from shorter inter-atomic distance of 8K than 16K. The bulk Ar $2p_{3/2}$-4s band at 8 K shows blue shift of 5 ± 1.5 meV from that at 16 K because of the increase of the exchange repulsion caused by the reducing the inter-atomic distance.
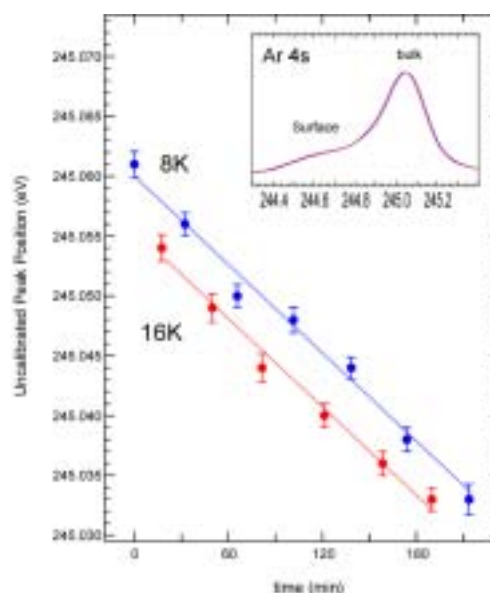

Fig. 1. The peak position of Ar 4s (bulk)

[1] T. Hatsui, M. Nagasono, N. Kosugi, *J. Electron Spectrosc. Relat. Phenom.,* in press.
[2] *Nonmetallic Solids*, Thermalphysical Proberties of matter, vol.13 Thermal expansion, Y.S.Touloukian, *et al.,* (IFI/Plenum, New York, 1997)

High-resolution Angle-resolved Photoemission Spectroscopy on CeSb

T. Ito, S. Kimura, H. Kitazawa*

UVSOR Facility, Institute for Molecular Science, Okazaki 444-8585 Japan
*Nano-Material Labolatory, National Institute for Materials Science (NIMS), Tsukuba 305-0047, Japan

The anomalously complicated magnetic phase transition on CeSb has been intensively studied by both experiment and calculation. The origin has long been believed to be understood under the framework of Ce 4*f*-Sb 5*p* mixing model (*pf* mixing model) [1,2]. On the other hand, the recent optical and magneto-optical experiments suggest the importance of the Ce 5*d*-Sb 5*p* mixing effect from the comparison with the band structure calculation based on the *pf*+*pd* mixing model [3,4]. Thus, we have performed high-resolution angle-resolved photoemission spectroscopy (ARPES) on CeSb at the para- and type-IA antiferro magnetic (AF) phase to elucidate the appropriate starting point of the complicated magnetic phase transition.

ARPES measurements were carried out using a MBS Toyama A-1 electron analyzer with a GAMMADATA discharge lamp and a toroidal grating monochromator. Ce 4*d*-4*f* resonant ARPES measurements have been performed at UVSOR-II BL5U with using the hν=115 eV and 122 eV photons (ΔE=100 meV, $\Delta\theta$=±0.1°), while high-resolution ARPES measurements with using He Iα photons (ΔE=15 meV, $\Delta\theta$=±0.1°). The single crystals were cleaved on the (001) plane *in situ* under vacuum of 2 x 10^{-8} Pa to obtain a clean mirrorlike surface. The Fermi level (E_F) of the sample was referred to a gold film evaporated onto the sample substrate.

Figure 1 (a) and (b) shows the valence band structure of paramagnetic CeSb obtained by plotting the intensity of Ce 4*d*-4*f* off (hν=115 eV)- and on (hν=122 eV)-resonant ARPES spectra as a function of the wave vector and the binding energy. Bright areas correspond to "bands". From the comparison of the experimental band structure in Fig.1, highly-dispersive features at E_F-2 eV enhanced on the off-resonant ARPES are dominated by the valence Sb 5*p* and Ce 5*d* electrons, while a non-dispersive feature at 3 eV by the localized Ce 4*f* states. Furthermore, the residual spectral weight near E_F of on-resonant ARPES spectra may suggest the existence of hybridization between Ce 4*f* states and valence *pd* electrons, as clearly seen in Fig. 1 (c).

To elucidate the change of band structure through magnetic phase transition, we have performed temperature-dependent high-resolution ARPES on CeSb with using He Iα photons. Figs. 2 (a) and (b) show the "band structure" near E_F of CeSb around the $\Gamma(X)$ point along the ΓX-XWX emission plane measured at the para- (T=30 K) and AF- (T= 5K) magnetic phase, respectively. Red and white areas correspond to "bands". From the para- to AF magnetic phase, we have observed two types of changes in the band structure near E_F. (1) The energy positions of the Sb 5*p* (A_1(') and A_2(')), and the Ce 5*d*

bands (A_3(')) around the $\Gamma(X)$ point approach each other (see Fig. 2(c)). (2) The additional band *B* with its top around 200 meV appears at AF-magnetic phase. While the former seems to be consistent with the *pf* mixing model, where the Sb 5*p* bands at the Γ point expect to be pushed up to E_F following the simultaneous downward shift of the Ce 5*d* bands [2], the latter is not explained by the model, since the band *B* is suggestive of the band energy-splitting, which has not been expected by the *pf* mixing model. On the other hand, we have found a qualitative agreement between the experiment and the recent calculation based on *pf*+*pd* mixing model [4], where the band energy-splitting originating in the *pf*+*pd* mixing effect along the ΓX axis has been expected. This result suggests the importance of the *pd* mixing effect to interpret the exact mechanism of the magnetic phase transition in CeSb other than the *pf* mixing effect.
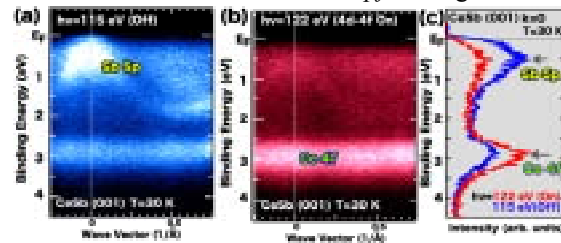
Fig. 1 (a, b) Comparison of the valence band structure of paramagnetic CeSb obtained by ARPES spectra with hν=115 eV (a) and 122 eV (b) photons.
(c) Comparison of normal emission ARPES spectra with hν=115 eV (blue line) and 122 eV (red

Fig. 2 (a, b) Experimental band structure of para- (a) and AF- magnetic (b) CeSb derived by ARPES. Dashed lines are guide for eyes.
(c) Comparison of normal emission ARPES spectra between AF- (blue line) and para-magnetic (red line) CeSb.

[2] H. Kumigashira *et al.*, Phys. Rev. B **56** (1997) 13654.
[3] S. Kimura *et al.*, J. Phys. Soc. Jpn. **71** (2002) 2200.
[4] S. Ishiyama and O. Sakai, J. Phys. Soc. Jpn. **72** (2003) 2071.

Pseudo-gap in $Zr_{55}Al_{10}Cu_{30}Ni_5$ Bulk Metallic Glass

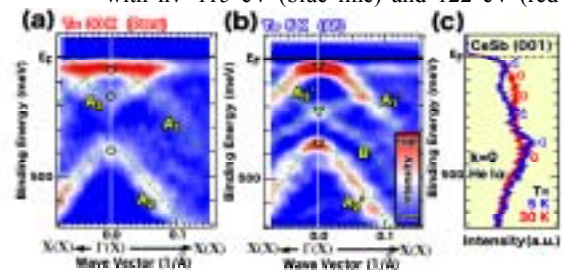K. Soda, K. Shimba, M. Kato, S. Yagi, T. Takeuchi,* U. Mizutani

T. Zhang,**M. Hasegawa,** A. Inoue,** T. Ito,*** S. Kimura***

Graduate School of Engineering, Nagoya University, Furocho, Chikusa-ku, Nagoya 464-8603
*Research Center for Advanced Waste and Emission Management, Nagoya University,
Furocho, Chikusa-ku, Nagoya 464-8603
**Institute for Materials Research, Tohoku University, Katahira, Aoba-ku, Sendai 980-8577
***UVSOR, Institute for Molecular Science, Myodaijicho, Okazaki 444-8585

Bulk metallic glasses have received much attention as new materials which possess useful engineering properties such as high mechanical strength, good ductility, and high corrosion resistance. In order to understand the origins of the large glass formation ability and unique properties of the bulk metallic glass from the microscopic point of view, we have studied the electronic structure of a $Zr_{55}Al_{10}Cu_{30}Ni_5$ bulk metallic glass [1] by photoelectron spectroscopy.

Experimental

Photoelectron spectra were recorded under an ultrahigh vacuum of 2×10^{-8} Pa at low temperatures with a high-resolution energy analyzer at BL5U. Total energy resolution and the origin of the binding energy E_B, *i.e.* the Fermi level E_F, were determined by the Fermi edge of an evaporated Au film.

Specimens were cut from an ingot of $Zr_{55}Al_{10}Cu_{30}Ni_5$ into a size of $3 \times 3 \times 2$ mm^3 and attached on a cupper plate by conductive glue. Clean surfaces for the photoelectron measurement were prepared by *in situ* scraping the specimen with a diamond file.

Results and Discussion

Figure 1 shows typical valence-band photoelectron spectra of $Zr_{55}Al_{10}Cu_{30}Ni_5$ recorded at 20 K with various excitation photon energies $h\nu$. They are normalized by the intensity integrated up to the binding energy $E_B = 10$ eV (exceptionally 7 eV for $h\nu$ ~22.3 eV). Three features at E_B ~0.6 eV, ~2.0 eV and ~3.7 eV in the valence band region are ascribed to the Zr 4d, Ni 3d and Cu 3d states, respectively, because of their $h\nu$ dependence [2]. An Auger line is also found at E_B ~ 8 eV for $h\nu$ = 66.8 eV.

Remarkable feature of the observed spectra is the highly symmetric shape of the transition metal d bands with the high binding energy and the narrow width in comparison with those of the crystalline transition metals. The Cu and Ni 3d band widths decrease from ~2 eV for crystalline Cu and Ni metals to ~1 eV for the glass. This is mainly due to the reduction in the neighboring atoms to hybridize with those transition metals in the glass. The symmetric shape may also arise from the lack of the crystalline periodicity.

In Fig.2, high-resolution spectra recorded with a He I light source ($h\nu$ = 21.2 eV) are presented for the valence-bands near E_F of the metallic glass and reference Au. Compared with Au, the intensity is reduced below E_B ~ 0.12 eV for the metallic glass. This suggests that a pseudo-gap is formed in this

metallic glass, which may stabilize the glass phase and contribute to its large glass formation ability.

At present, however, it is not clear whether these aspects are intrinsic for the glass phase of this alloy or not. Further study is intended on the crystalline counterpart and the glass with different compositions.
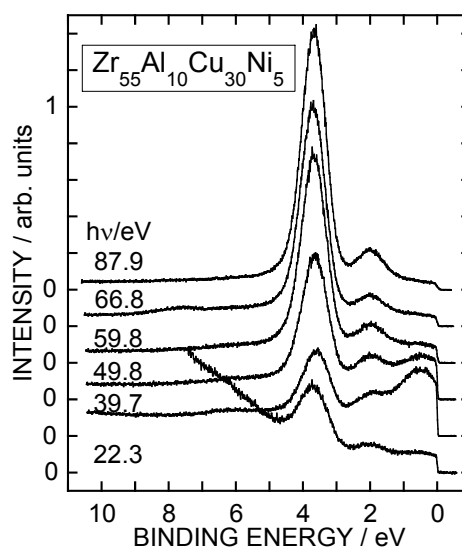

Fig.1 Valence-band spectra of $Zr_{55}Al_{10}Cu_{30}Ni_5$.
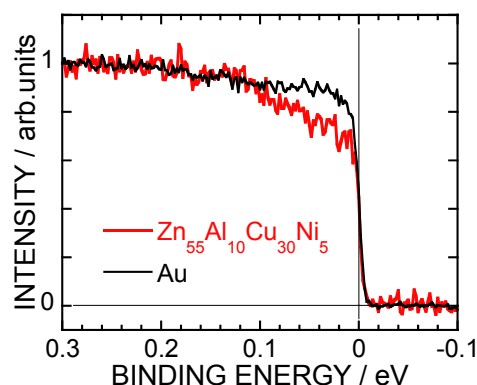The excitation photon energy $h\nu$ is indicated.

Fig.2 Valence-band spectra near the Fermi level of $Zr_{55}Al_{10}Cu_{30}Ni_5$ and Au.

[1] A. Inoue and T. Zhang, Mat. Trans. JIM **37** (1996) 185.

[2] J. J. Yeh and I. Lindau, Atom. Data Nucl. Data Tables **32** (1985) 1.

Evaluation of Thermoelectric Power in the Al-Mn-Re-Si 1/1-1/1-1/1 Approximant Using High-resolution Photoemission Spectroscopy

T. Takeuchi[1], T. Kondo[2], H.Takahashi[2], H. Sakagami[2], T. Otagiri[2], U. Mizutani[2], T. Itoh[3] and S. Kimura[3]

[1] *Research Center for Advanced Waste and Emission Management, Nagoya University, Nagoya 464-8603*
[2] *Department of Crystalline Materials Science, Nagoya University, Nagoya 464-8603*
[3] *UVSOR, Institute for Molecular Science, Okazaki 444-8585 Japan*

It has been widely believed that metallic compounds are inappropriate for their use as thermoelectric devices because their thermoelectric power, in general, possesses extremely small magnitude as low as a few μV/K. Recently, however, some metallic compounds such as quasicrystals and cobalt oxides were reported to show a large magnitude in the thermoelectric power. These experimental observations strongly motivated us to investigate the mechanism leading to the large thermoelectric power coupled with metallic electrical conduction.

Thermoelectric power of the metallic electrical conduction can be well explained by

$$S(T) = \frac{1}{eT} \frac{\int (\varepsilon - \mu) \sigma(\varepsilon) \frac{\partial f(\varepsilon)}{\partial \varepsilon} d\varepsilon}{\int \sigma(\varepsilon) \frac{\partial f(\varepsilon)}{\partial \varepsilon} d\varepsilon} \qquad (1)$$

where $\sigma(\varepsilon)$, μ, and $f(\varepsilon)$ indicate electrical conductivity, chemical potential, and Fermi-Dirac distribution function, respectively. Electrical conductivity in a isotropic system is determined by the following equation with in the context of the Boltzmann transport theory.

$$\sigma(\varepsilon) = \frac{e^2}{12\pi^3\hbar} S(\varepsilon) v(\varepsilon) \tau(\varepsilon) = \frac{e^2}{3\pi^3} N(\varepsilon) v^2(\varepsilon) \tau(\varepsilon) \qquad (2)$$

Here $N(\varepsilon)$, $v(\varepsilon)$, and $\tau(\varepsilon)$ represent electronic density of states, group velocity, and relaxation time, respectively. If $v(\varepsilon)$ and $\tau(\varepsilon)$ can be regarded as energy-independent in a narrow energy range where $\partial f(\varepsilon)/\partial \varepsilon$ has nonzero value while it turns out to possess negligibly small value at the outside of the energy range, $\sigma(\varepsilon)$ in eq.(1) can be simply replaced by N(e). In such a case, thermoelectric power can be evaluated using information about $N(\varepsilon)$. In this study, we employed high energy-resolution photoemission spectroscopy to investigate $N(\varepsilon)$ of the $Al_{74.6}Mn_{8.7}Re_{8.7}Si_8$ 1/1-1/1-1/1 approximant of the icosahedral quasicrystal. Thermoelectric power in the approximant was evaluated by the measured

photoemission spectrum. The energy resolution of the present measurements was better than 20 meV.

Photoemission spectra, in general, are believed to have information only about the valence band below the Fermi level (E_F). However, those measured at high temperature contain information about the conduction band up to a few above E_F. If the measured spectrum is divided by $f(\varepsilon)$, the resulting spectrum ($N'(\varepsilon)$) gives us information about electronic density of states across E_F.

We calculate the thermoelectric power by using eq.(1) and the deduced $N'(\varepsilon)$. Although its magnitude stays less than half of the observed value, the calculated $S(T)$ shows almost the same temperature dependence as that of the measured one. If we take an energy independent contribution of the surface or grain boundaries into accont, the magnitude of $S(T)$ is increased and the thermoelectric power can be perfectly determined from experi-mentally determined density of states. We have already applied this method for the layered cobalt oxides and the layered cuprates of the metallic electrical conduction and succeed in quantitatively evaluating their thermoelectric power.

As a result of these analyses on the thermoelectric power in terms of the electronic structure near E_F, we concluded that the large thermoelectric power with metallic electrical conduction is brought about by the characteristic electronic structure near E_F and is predictable if the electronic structure is precisely determined.
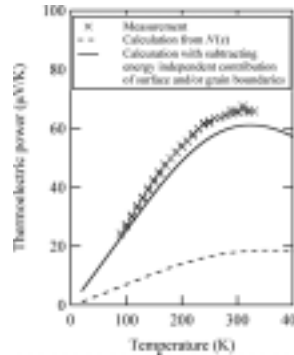

Figure 1 Measured and calculated $S(T)$. The calculated value with subtracting energy independent contribution of surface and /or grain boundaries form $N'(\varepsilon)$ shows extremely good consistency with the measured one.

Dynamic Final-State Effect on the Core-Level Photoemission of Surface-Passivated Au Nanoparticles on the Graphite Substrates

A. Tanaka, Y. Takeda, M. Imamura, S. Sato

Dept. of Physics, Graduate School of Science, Tohoku University, Sendai 980-8578, Japan

Recently, the surface-passivated nanoparticles have been chemically synthesized in the solution including surfactants. These surface-passivated nanoparticles exhibit closed-packed nanoparticle self-assemblies on the single-crystalline substrates, and therefore it is considered that they could be important constituents of future nanostructured devices. In order to elucidate their detailed intriguing properties and to develop the future devices, it is indispensable to understand the interactions with the substrates supporting the nanoparticles as well as their electronic structures. In this work, we have carried out a photoemission study of dodecanethiolate- (DT-) passivated Au nanoparticles.

The synthesis procedure of DT-passivated Au nanoparticles has been described elsewhere [1-3]. Photoemission measurements were carried out at BL-5A of UVSOR Facility. For the photoemission measurements, the synthesized DT-passivated Au nanoparticles were supported on HOPG substrates by evaporating the solvent (toluene) from the dispersion of DT-passivated Au nanoparticles on the single-crystalline HOPG cleaved surface in a nitrogen-filled glove bag directly connected to the ultrahigh-vacuum chamber. Photoemission measurements were performed with the incident photon energy of 180 eV at room temperature.

The Au $4f$ core-level spectra of DT-passivated Au nanoparticles consist of the two components, and the components with lower binding energy and higher binding energy originate from the inner Au atoms of Au nanoparticles (bulk component) and the surface Au atoms of Au nanoparticles bonded to surface-passivants of DT molecules (surface component), respectively [2]. An important point to note here is that the bulk components shift to higher binding energy side with decreasing the nanoparticle diameter (not given here). In our previous work [1], we have reported that the photoemission spectra in the vicinity of Fermi-level of DT-passivated Ag nanoparticles on the HOPG substrates are well characterized by the dynamic final-state effect due to the photohole with a finite lifetime left behind in the nanoparticles in the photoemission final state. This finite lifetime is determined by the coupling strength between the nanoparticle and substrate. Since the chemical states of both bulk components observed in the Au $4f$ core-level spectra for bulk Au crystallite and DT-passivated Au nanoparticles are considered to be equivalent, the bulk components in the DT-passivated Au nanoparticles on the HOPG substrates correspond to the shifted ones of bulk component observed in the bulk Au crystallite due to

the dynamic final-state effect. In order to analyze the present Au $4f$ core-level photoemission spectra of DT-passivated Au nanoparticles on the HOPG substrates, we apply the dynamic final-state model to Au $4f$ core-level photoemission spectra again. Figure 1 shows the comparison of experimental bulk component in the Au $4f_{7/2}$ core-level spectrum of DT-passivated Au nanoparticles with mean diameter of 3 nm on the HOPG substrates and calculated one from the experimental bulk component of bulk Au crystallite using dynamic final-state effect model. At the middle spectra in Fig. 1, the decomposed component denoted by red line shows the bulk component. The bottom spectrum shows the calculated bulk component based on the dynamic final-state effect on the bulk component of bulk Au crystallite. As shown in Fig. 1, the calculated bulk component reproduces the experimental one of DT-passivated Au nanoparticle on the HOPG substrate fairly well. Therefore, it is concluded that the experimental core-level photoemission spectral features of the present DT-passivated Au nanoparticles on the HOPG substrates can be also quantitatively characterized by the dynamic final-state effect model.
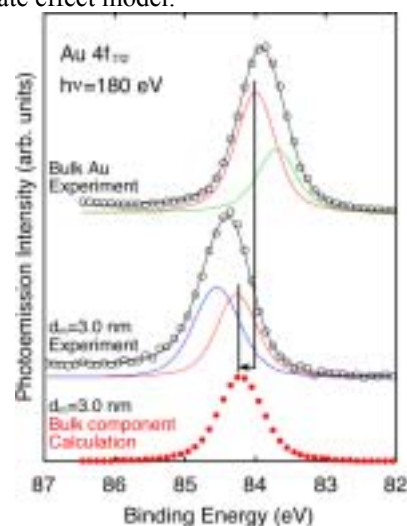
Fig. 1. Comparison of experimental Au $4f_{7/2}$ core-level spectrum of DT-passivated Au nanoparticles on the HOPG substrates and calculated one using dynamic final-state effect model.

[1] A. Tanaka, Y. Takeda, T. Nagasawa, and S. Sato, Phys. Rev. B **67**, 033101 (2003).
[2] A. Tanaka, Y. Takeda, T. Nagasawa, and K. Takahashi, Solid State Commun. **126**, 191 (2003).
[3] A. Tanaka, Y. Takeda, M. Imamura, and S. Sato, Phys. Rev. B **68**, 195415 (2003).

Soft X-ray Absorption Spectra of Dilute Magnetic Semiconductor GaCrN

S. Emura[1], M. Hashimoto [1], H. Tanaka[1], M. S. Kim[1], S. Kimura[1], Z. Yikai [1], H. Asahi [1],
Y. Arachi[2], H. Kobayashi[3]

[1]*ISIR, Osaka University, Mihoga-oka 8-1, Ibaraki, Osaka 567-0047,*
[2]*Faculty of Engineering, Kansai University, Suita Osaka 564-8680*
[3]*National Institute of Advanced Industrial Science and technology, Ikeda, Osaka 563-8577*

In present society, infrastructures of communication are demanded to expand in the speed and the quantity. One of future devices in this field is a spin-related device. Several candidates are considered and a part of those starts in fundamental research. Theoretical study also reveals the possibility of dilute magnetic semiconductor that exhibits ferromagnetism at room temperature and predicted that GaN-based dilute magnetic semiconductors, especially Cr-doped GaN, are highly potential candidates for those materials. This material, Cr doped wide gap semiconductor, shows ferromagnetic properties even at 400K experimentally. This is one of highest Curie temperatures at present in dilute magnetic semiconductors. Furthermore, GaCrN substance emits luminescence at the energy of near the band gap of Ga. We have, thus, three independent characters for GaCrN, semiconductor nature, ferromagnetism, and optical feature.
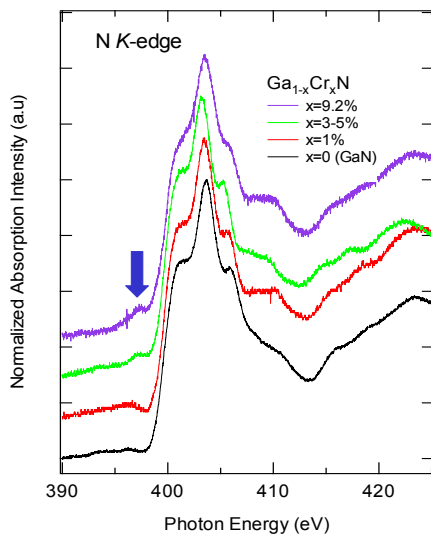

Fig.1 Absorption spectra around N K-edge of GaCrN.

Here, we observed the absorption spectra around N K-edge and Ga $L_{III, II}$-edge to try to reveal the origin of ferromagnetism of GaCrN. Figure 1 shows the absorption spectra around N K-edge. We found .a weak peak at 398eV lower than the fundamental N K-shell absorption edge for high Cr concentration specimens studied here. A blue arrow in Fig.1 indicates the peak. The intensity of the peak increases with the concentration of Cr atom. The $3d$-orbitals of the doped Cr atom partially hybridize with the N $2p$-orbitals to construct a valence band of GaCrN (Fig.2), and the other part makes a state in the band gap of GaCrN as the result of crystal field splitting. We tentatively assign the peak to a transition to the $3d$-orbitals of Cr atom making the in-band gap state, which is essentially dipole-forbidden, but becomes partially dipole-allowed owing to the hybridization

with the N p-orbital. The electrons in the in-band gap state may play the main role of ferromagnetism of GaCrN in connection of the hole of the valence band.
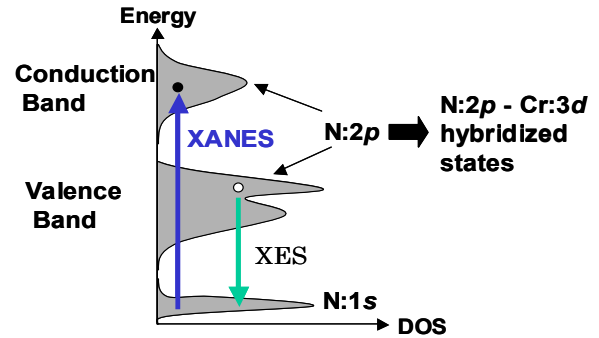

Fig.2 Schematic DOS of GaCrN and optical transition.

On the other hand, while a slight modification of the spectrum was found, indicated by a blue arrow, we did not observe the large change in the absorption spectrum around Ga L_{III}- and L_{II}-edges as shown in Fig.3. This observation means that the Ga and N s-orbital constructing the conduction band of GaCrN are not strongly affected by doping the Cr atom. By the way, the doped Cr atom states as trivalent ion in the GaN and constructs the alloy GaCrN. The configuration circumstance around the Cr ion has been elucidated with XAFS measurement, and the analysis indicates that the Cr ion locates substitutionally, but the first nearest neighbor configuration is somewhat complex.
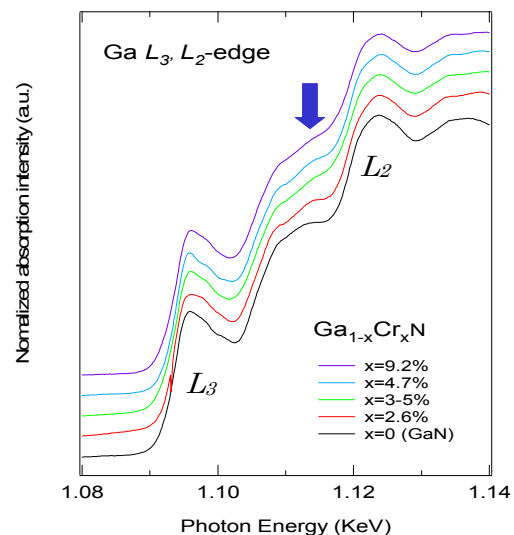

Fig.3 Absorption spectra around Ga L_{III} and L_{-II}-edge of GaCrN.

Study of Ar Cluster Ion Incident Angle for Super Hard Diamond Like Carbon Film Deposition

T. Kitagawa[1,2], K. Miyauchi[1], K. Kanda[2], Y. Shimizugawa[2], N. Toyoda[2], S. Matsui[2], H. Tsubakino[1], and I. Yamada[2,3]

[1] *Faculty of Engineering, Himeji Institute of Technology, Himeji, Hyogo, Japan*
[2] *Laboratory of Advanced Science and Technology for Industry, Himeji Institute of Technology, Kamigori, Hyogo, Japan*
[3] *Collaborative Research Center for Cluster Ion Beam Process Technology, Osaka Science and Technology Center, Osaka, Japan*

We have demonstrated that gas cluster ion beam (GCIB) assisted deposition was useful for forming super hard DLC films (> 50 GPa) with a smooth surface and low content of sp^2 orbital at room temperature [1,2].

In our case, the DLC films were formed with irradiation of Ar cluster ion beam during evaporating C_{60} as a carbon source. These films were deposited with a perpendicular irradiation of Ar cluster ions [3]. In this paper, effects of the irradiation angle of the Ar cluster ion beam on carbon film properties were studied, in order to develop this deposition technique and to optimize the angles for the super hard DLC film formation.

Result and Discussion

Figure 1 shows the NEXAFS spectra of the films irradiated with various incident angles of Ar cluster ion at the acceleration energy of 5 keV. Additionally, the spectra of the conventional DLC film formed with RF plasma and a diamond film formed with microwave plasma are also shown as references.

A significant difference of the spectra between DLC films and the diamond film was the pre-edge peak at 285.3 eV. This pre-edge resonance is due to transitions from a C_{1s} orbital to an unoccupied π^* orbital originating in sp and sp^2 orbitals. Thus, the NEXAFS spectrum of the diamond film, which has no- sp^2 orbital, did not present the pre-edge peak at all. This pre-edge peak is usually considered as a marker for presence of the sp^2 orbital, as the sp orbital is unstable. The increasing of the sp^2 content in the DLC film indicates the increasing the graphitic bond in the film. Therefore, in order to obtain higher hardness, the fraction of the sp^2 content in the DLC film should decrease. In the DLC films deposited with Ar cluster ion beam assistance, the peak shape at pre-edge of 285.3 eV was different between 0° and 60°. In comparison with the film at the normal incidence, the spectra of the film formed with incident angle of 60° presented an increase of the peak width with the same peak intensity. Therefore, from Fig.1, the sp^2 content at 60° was higher than that at normal incident angle. At 40°, the shoulder peak around 287 eV was also higher than that at normal. This increase is also concerned with increasing of sp^2 content, because the spectrum of the diamond does not have this shoulder peak. Thus,

increasing of the incident angle increased the sp^2 content. Additionally, it should be noted that the sp^2 content of the film formed with normal incident angle was lower than that of RF plasma film.

Acknowledgements
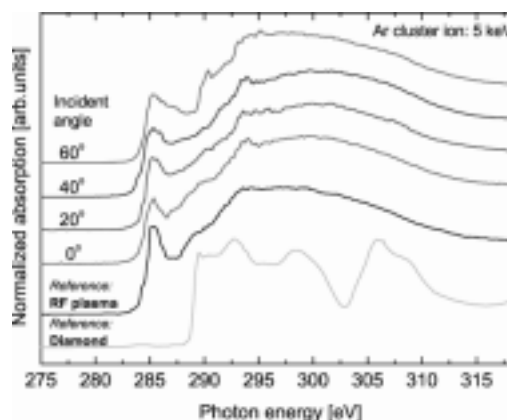
Figure 1: NEXAFS spectra of DLC films formed by Ar cluster ion beam assisted irradiation with oblique incident angles.

[1] Yamada, T. Kitagawa, J. Matsuo, and A. Kirkpatrick: Proceedings of the International Conference on the Mass Charge Transport in Inorganic Materials (2000) 957.

[2] T. Kitagawa, I. Yamada, N. Toyoda, H. Tsubakino, J. Matsuo, G.H. Takaoka, and A. Kirkpatrick: Nucl. Instrum. Methods Phys. Res. B **201** (2003) 405.

[3] T. Kitagawa, K. Miyauchi, K. Kanda, Y. Shimizugawa, N. Toyoda, H. Tsubakino, S. Matsui, J. Matsuo, and I. Yamada: Jpn. J. Appl. Phys. **42** (2003) 3971.

Angle-resolved UV Photoelectron Spectra of Thin Films of Perylene-3,4,9,10-tetracarboxylic Bisimidazole on GeS(001)

H. Yamane, M. Ohyama, H. Fukagawa, S. Kera*, D. Yoshimura**
K. K. Okudaira, A. Kahn***, K. Seki**, and N. Ueno
Faculty of Engineering, Chiba University, Chiba 263-8522 Japan
*Institute for Molecular Science, Okazaki 444-8585 Japan
**Research Center for Materials Science, Nagoya University, Nagoya 464-8602 Japan
***Department of Electrical Engineering, Princeton University, New Jersey 08544 USA

Recently, we observed the intermolecular energy-band dispersion of the oriented perylene-3,4,9,10-tetracarboxylic dianhydride (PTCDA) multilayer[1]. The observed energy-band dispersion gave that the transfer integral for the π-π interaction (0.05 eV), the effective mass of HOMO hole (5.28 m_0), and the hole mobility (> 3.8 cm2/V s, when $\tau > \hbar/k_BT$), which are the fundamental basis for the understanding of electronic and optical properties of organic solids[1]. This was the first observation of the intermolecular energy-band dispersion of a conventional single-component organic semiconductor only with the weak intermolecular van der Waals interaction.

In this work, in order to obtain information on the intermolecular interaction of perylene-3,4,9,10-tetracarboxylic bisimidazole (PTCBI), we characterized the film structure of PTCBI thin films prepared on GeS(001) single crystal surface by measuring the take-off angle (θ) and the azimuthal ( ) dependencies of angle-resolved UV photoelectron spectroscopy (ARUPS).

Experiments

ARUPS spectra were measured at photon incidence angle $\alpha = 0°$, $h\nu = 40$ eV, and T = 295 K. θ and ϕ dependencies of ARUPS spectra were analyzed using the independent-atomic-center (IAC/MO) and the single-scattering (SS/MO) approximations combined with molecular orbital calculation[2].

A GeS(001) was cleaved in UHV. The cleanness of GeS(001) was confirmed by measuring ARUPS and low-energy electron diffraction (LEED). The purified PTCBI was carefully evaporated onto GeS(001). The film thickness and the deposition rate (< 1.0 Å/min.) were measured with a quartz microbalance.

Results and Discussion

Figure 1 (a) shows θ dependence of ARUPS of PTCBI (3Å) on GeS(001) substrate surface, where the intensity is normalized to the incidence photon flux, and the binding energy (E_B) is measured from the Fermi level of the substrate (E_F^{sub}). θ dependencies of ARUPS spectra are clearly seen. From MO calculation, the highest occupied molecular orbital (HOMO, $E_B = 1.8$ eV) band is assigned to a single π MO as shown in Fig. 1. This HOMO-band intensity showed maximum at $\theta = 30 \sim 33°$.

Figure 1 (b) shows the comparison between

observed and calculated θ dependencies of the HOMO-band intensities with the SS/MO (PM3) for the molecular tilt angle of $\beta = 0°$, which gave the best agreement with the observed θ pattern. It indicates that PTCBI molecules orient with their molecular plane parallel to the GeS(001) substrate surface. Furthermore, LEED measurements showed similar pattern from 3-Å- to 50-Å-PTCBI (not shown). Therefore, the strong intermolecular π-π interaction in PTCBI multilayer can be expected.

In order to obtain the energy-band dispersion in PTCBI multilayer, the measurements of θ, ϕ, and $h\nu$ dependencies as a function of PTCBI deposition amounts are now in progress.
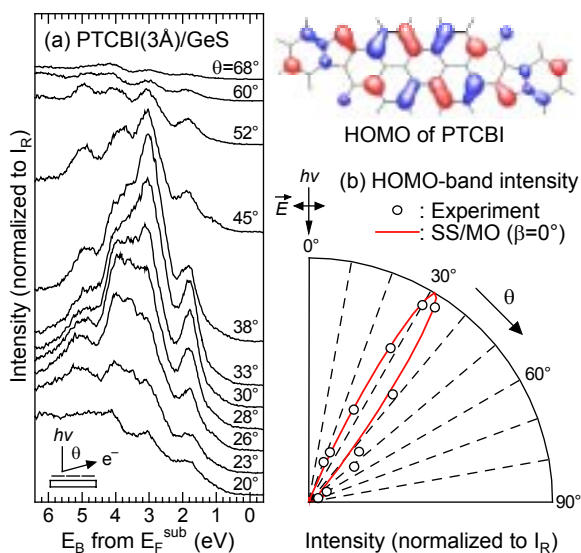
Fig. 1. (a) The take-off (θ) angle dependence of the ARUPS of the 3-Å-PTCBI on GeS(001). The intensity is normalized to the incidence photon flux. The binding energy (E_B) is measured from the Fermi level of the substrate (E_F^{sub}). (b) Comparison between observed and calculated θ dependencies of the HOMO-band intensities with the SS/MO ($\beta = 0°$).

[1] H. Yamane, S. Kera, K.K. Okudaira, D. Yoshimura, K. Seki, N. Ueno: Phys. Rev. B, 68 (2003) 033102.
[2] N. Ueno, A. Kitamura, K.K. Okudaira, T. Miyamae, Y. Harada, S. Hasegawa, H. Ishii, H. Inokuchi, T. Fujikawa, T. Miyazaki, K. Seki: J. Chem. Phys., 107 (1997) 2079.

Shrinking of Spin-on-Glass Films Induced by Synchrotron Radiation and Its Application to Three-Dimensional Microfabrications

Md. Mashiur Rahman, Ryugo Tero*, Tsuneo Urisu*

The Graduate University for Advanced Studies, Okazaki 444-8585 Japan
Institute for Molecular Science, Okazaki 444-8585 Japan

In this work, we have performed experiments on the SR etching of SOG using a Co thin film as an etching mask and a mixture of SF_6 and O_2 as an etching gas. It was found that the thickness of SOG under the Co mask was also reduced by irradiation with the SR beam. The shrinkage phenomenon is a photoinduced process caused by SR permeating through the Co mask due to the high-energy photons rather than a thermal process, because the SOG is pre-annealed at 425°C before irradiation with SR. The shrinkage of SOG was attenuated by increasing the Co thickness. An application of this phenomenon to a three-dimensional (3-D) microfabrication process using Co masks of varying thickness has also been demonstrated. Atomic force microscopy (AFM) observations showed that the surface of the shrunken SOG was as flat as a mirror-polished level. We have also investigated the mechanism and the characteristics of the shrinkage process by Fourier-transform infrared spectroscopy (FT-IR).

The Co contact mask was deposited in two steps as shown in Fig. 1a. First a line-and-space pattern was formed by photolithography and the lift-off technique (mask A). Then a rectangular Co layer was deposited using a stainless mask (mask B). The thickness of the former and the latter masks were 315 nm and 245 nm, respectively. Thus the SOG surface was covered with Co masks 560, 315 and 245 nm thick which are represented by areas 1-3 in Fig. 1a, respectively. The area without the Co mask is represented by area 4 in Fig. 1a. Figure 1b shows the SEM image of the SOG/Si surface after exposure to 2.00×10^4 mA min of SR using the Co mask shown in Fig. 1a, followed by removal of the Co mask with aqueous HNO_3 (0.1 N). The 3D structure of SOG is successfully obtained with only one SR irradiation, because the thinner the Co mask is, the deeper the SOG shrinks.

We have found that the thickness of the SOG film on the Si(100) surface is reduced by SR irradiation under a Co mask. This shrinkage phenomenon is a photoinduced process occurring due to the transmission of SR through the Co mask. A 550 nm thick SOG film shrinks by 152 nm under the Co mask that is 230 nm thick after exposure to 2.0×10^4 mA min of SR. Without the Co mask, the etching depth of SOG increased with the SR dose and the SOG film was completely removed by the exposure of 1.8×10^4 mA min. The shrinkage of SOG decreased with an increase in the Co mask thickness.
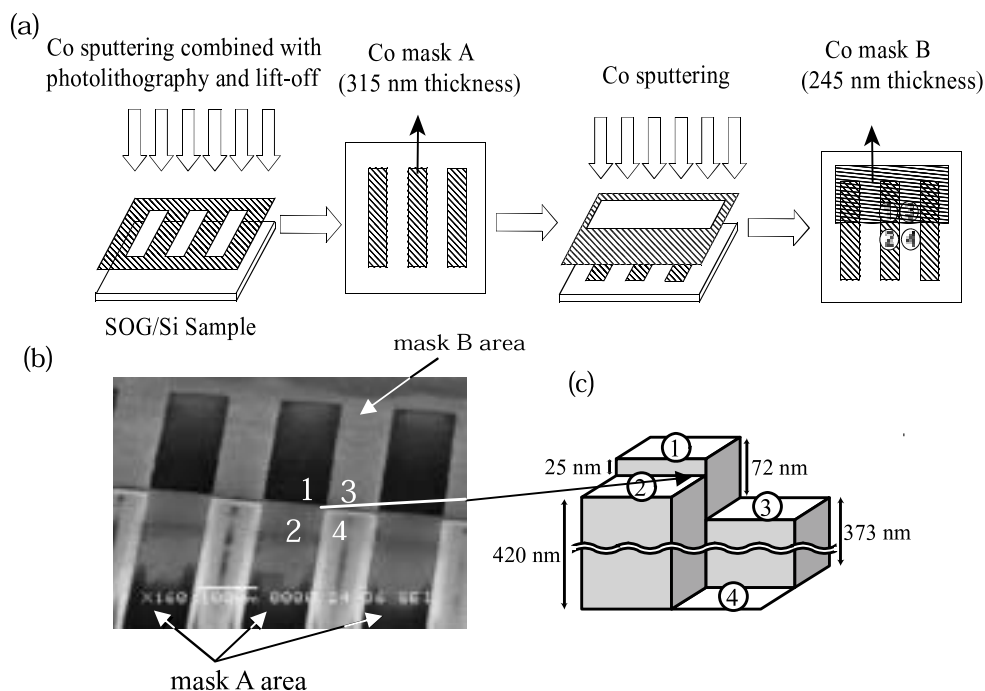

Fig. 1. Fabrication process of the Co contact mask. Mask A (315 nm thick) and mask B (245 nm thick) were overlapped. (b) SEM image of the 3D structure of SOG on Si fabricated by exposure to 2.00×104 mA min of SR using the Co contact mask in (a). (c) The schematic drawing of the 3-D structure.

X-ray Magnetic Circular Dichroism Study on Cu Capping on Ni/Cu(001)

T. Nakagawa, H. Watanabe, T. Yokoyama

Department of Molecular Structure, Institute for Molecular Science, Okazaki 444-8585 Japan

Ultrathin Ni/Cu(001) films are well known to show unique magnetic properties. The spin reorientation transition occurs twice by varying the Ni thickness; at <8 ML (monolayer) the easy axis is in plane, at 8-40 ML it is perpendicular, and at >40 ML it is again in plane. O'Brien *et al*. [1] reported previously that the Cu capping stabilizes perpendicular magnetic anisotropy. They showed that the critical thickness for the first transition (~8 ML) is reduced by ~2 ML using Ni *L*-edge x-ray magnetic circular dichroism (XMCD). Although these results seem established, a recent work by Zhao *et al*. [2] shows essentially contradictory findings by means of magneto-optical Kerr effect (MOKE); the critical thickness increases upon the Cu capping. In this work, we tried to confirm the effect of Cu capping on Ni/Cu(001) by using both XMCD and MOKE.

Experiments

Ni was deposited on clean and ordered Cu(001) at room temperature in ultrahigh vacuum chambers. The thickness was monitored with the RHEED oscillations. Cu was subsequently deposited on Ni/Cu(001). Ni *L*-edge XMCD was taken at BL4B [3]. For XMCD films with an uniform thickness were prepared, while those for MOKE were wedge shaped.

Results

Figure 1 shows the polar MOKE intensity (only perpendicular magnetization was detected) as a function of the Ni thickness. These data were taken at room temperature. It is apparent that the critical thickness decreases with the Cu capping, being consistent with the results by O'Brien *et al* [1].

Figure 2 gives the Ni *L*-edge XMCD of 5.5 ML (in-plane magnetization) and 11 ML (perpendicular) Ni/Cu(001) before and after Cu deposition, taken at a
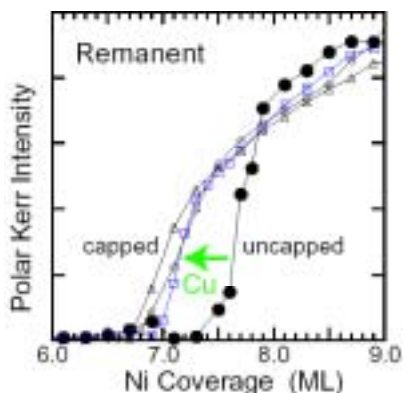
temperature of 100 K and a magnetic field of 1000 G. It is easily found that the 11ML Ni does not show any significant change with the Cu deposition, while the 5.5ML film gives gradual reduction of the L_{III} XMCD intensity leaving the L_{II} intensity rather constant. These findings imply that the in-plane orbital magnetic moment (5.5 ML) is suppressed, while the perpendicular one is kept unchanged (11 ML). Figure 3 shows the results of the orbital magnetic moments given by the sum-rule analysis. It can be concluded that the in-plane magnetic anisotropy is unstabilized compared to the perpendicular magnetic anisotropy upon the Cu capping.

[1] W. L. O'Brien *et al*. *Phys. Rev.* **B54** (1996) 9297.
[2] H. W. Zhao *et al*. *Phys. Rev.* **B66** (2002) 104402.
[3] T. Nakagawa *et al*. this volume.
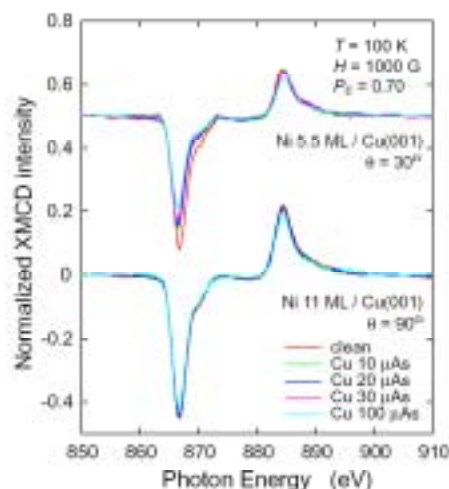
Fig. 2 Ni *L*-edge XMCD of 5.5 ML (in-plane magnetization, grazing x-ray incidence) and 11 ML (perpendicular, normal incidence). The amount of Cu deposition approximately corresponds to 1 ML to 100 µAs.

Fig. 1 Polar MOKE intensity (remanence) as a function of Ni thickness. The thickness of the Cu capping layer increases as a sequence of filled circle (clean), square, diamond, and triangle.

Fig. 3 Orbital magnetic moments of the Cu-capped Ni/Cu(001) as a function of Cu coverage (100 µAs is approximately 1 ML).

BL4B

X-ray Magnetic Circular Dichroism Study on NO Adsorbed Co and Ni Ultrathin Films on Cu(001)

T. Nakagawa, H. Watanabe, T. Yokoyama

Department of Molecular Structure, Institute for Molecular Science, Okazaki 444-8585 Japan

NO is well known as an effective magnetic killer since NO interacts with magnetic metal surfaces very strongly and the unpaired electron couples with the metal spins antiferromagnetically. In this work, we have investigated the effect of NO adsorption on ultrathin Co and Ni/Cu(001) films from the view point of magnetic anisotropy.

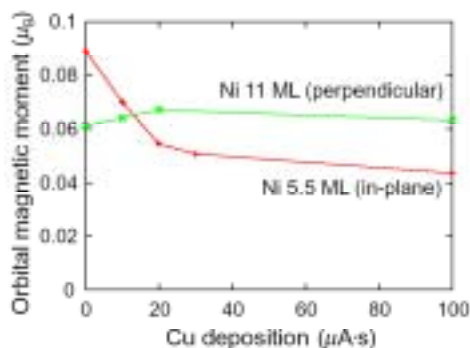## Experiments

Co and Ni were deposited on clean and ordered Cu(001) at room temperature in an ultrahigh vacuum chamber. The thickness was monitored with the RHEED oscillations. The obtained metal films were subsequently dosed with 0.5-1.0 L NO (1 L = 1×10^{-6} Torr·s) at 200 K. Co and Ni L-edge XMCD was taken at BL4B [1] at a temperature of 200 K.

Results

Figure 1 shows the Co L-edge XMCD of 3 ML (monolayer) in-plane magnetized Co/Cu(001) at the x-ray incidence angles θ of 30° (grazing incidence, close to the easy axis) and 90° (normal incidence, along the hard axis) before and after NO adsorption. It is apparently found that in the 30° spectra the magnetization is reduced drastically upon NO adsorption. On the contrary, the magnetization along surface normal (hard axis) is not so much reduced on NO adsorption, although the magnetization is not saturated under a magnetic field of 2000 G.

Figure 2 depicts the Ni L-edge XMCD of 5.5 and 9 ML Ni/Cu(001). In the case of in-plane magnetized 5.5 ML Ni/Cu(001), both θ=30° and θ=90° spectra were taken at a magnetic field of 1000 G. The θ=30° spectra show noticeable reduction of the magnetization on NO adsorption, while less prominent suppression is found in the θ=90° spectra.
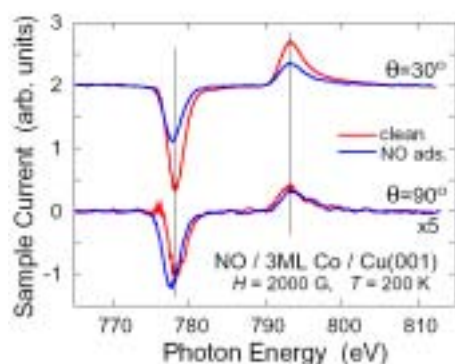
This finding is similar to the NO/Co/Cu(001) case. The 9 ML spectra show much less change between clean and NO-adsorbed Ni along the easy axis, being different from the 5.5 ML case.

The results of the sum rule analysis are summarized in Table 1. In the in-plane magnetized films of 3 ML Co and 5.5 ML Ni, the in-plane orbital moments m_l (see 30° data) are significantly suppressed on NO adsorption, while perpendicular m_l (see 90° data) show much less change. The Ni 9 ML films give again almost no change in perpendicular m_l. These results imply that NO suppress the in-plane orbital moment drastically, while the perpendicular orbital moment is much less influenced. Namely, NO relatively stabilizes perpendicular magnetization effectively.

[1] T. Nakagawa *et al*. this volume.

Table 1　Results of the sum rule analysis.

Sample	State	θ(°)	m_l (μ_B)	m_s (μ_B)
Co 3 ML (in-plane)	Clean	30	0.164	1.65
	NO	30	0.095	0.82
	Clean	90	0.0169	0.18
	NO	90	0.039	0.18
Ni 5.5 ML (in-plane)	Clean	30	0.125	0.63
	NO	30	0.057	0.33
	Clean	90	0.024	0.30
	NO	90	0.020	0.17
Ni 9 ML (perpen.)	Clean	90	0.055	0.56
	NO	90	0.052	0.50

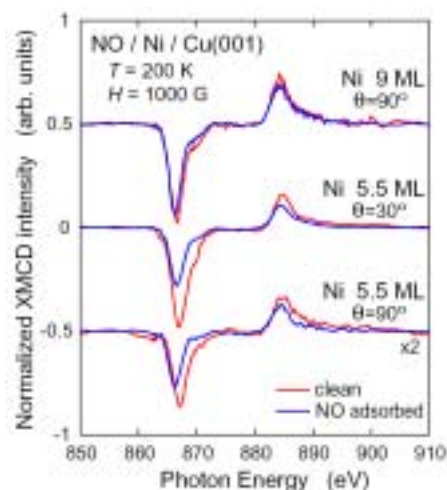Fig. 1　Co L-edge XMCD of 3 ML Co/Cu(001) before and after NO adsorption. The x-ray incidence angles were θ=30° and 90°.

Fig. 2　Ni L-edge XMCD of 5.5 and 9 ML Ni/Cu(001) before and after NO adsorption. The x-ray incidence angles were θ=30° and 90° for 5.5 ML Ni and θ=90° for 9 ML Ni.

SURFACE AND PHOTOCHEMISTRY

Surface Photo-voltage Effect on *n*-GaAs(100) Surface Studied by Combination of SR and Laser

K. Takahashi, Y. Nagata*, S. Tokudomi*, S. Katayama**, N. Takahashi**,
J. Azuma, and M. Kamada

Synchrotron Light Application Center, Saga University, Saga 840-8502 Japan
*Faculty of Science and Engineering, Saga University, Saga 840-8502 Japan
**Faculty of Education, Kagawa University, Kagawa 760-8522 Japan

Electronic non-equilibrium in the surface layer of photo-excited semiconductors has been attracting much interest from the basic scientific point of view and also from the practical applications for photo-electronic devices. In order to elucidate the electronic non-equilibrium in the surface layer of photo-excited semiconductors, it is indispensable to understand the transient state of photo-excited semiconductor surface. In this work, we have performed time-resolved photoemission spectroscopy in nano-second region with the combinational use of synchrotron radiation and laser.

Experimental

Experiments were performed at BL5U. An As-capped *n*-type GaAs(100) (Si-doped, 3.0×10^{16} cm^{-3}) was used for the measurements. An As capping layer was removed by heating the sample in the ultra-high vacuum. We used the mode-locked Ti:Sapphire laser (COHERENT Mira 900-F) which is synchronized with the synchrotron radiation in the multi-bunch operation. The time-resolved photoemission measurements in nano-second region were performed by the so-called pump-probe technique with the synchrotron radiation and laser. The laser light was transported to the viewport of the main experimental chamber using an optical fiber. The laser light was then focused onto the sample surface with a 3 mm radius spot. The spatial overlap of the laser with the synchrotron radiation was adjusted by eyes.

Results and Discussions

Figure 1 shows the Ga *3d* photoemission spectra with and without laser illumination measured at room temperature. The delay time between laser and SR is 0 ns. As shown in Fig. 1, it is clearly seen that the peak position of the Ga *3d* spectrum is shifted to lower kinetic energy under the laser excitation. From the conjunction with our previous studies, we have concluded that the present core-level shift is originated from the surface photo-voltage (SPV) effect. The SPV effect is closely related to the concept of the band bending in semiconductor surfaces. The intrinsic or extrinsic charges in the surface states are compensated by the underlying bulk charges, thus resulting in the band bending. When electrons and holes are produced in n-type semiconductors by laser excitation, the photo-excited holes move toward the surface and the electrons go into the bulk according to the potential curves due to the band bending. This charge separation in space produces another electric field in the space-charge region, and changes the magnitude of the band bending.

In addition to the peak shift caused by the SPV effect, it should be noted that the spectral shape changes under laser excitation. As shown in Fig. 1, it is clearly seen that the dip between two spin-orbit splitting components become shallow under laser illumination. The change of the spectral shape has been clearly observed for the first time by the high energy resolution measurements. We have confirmed that the change of the spectral shape is reproducible phenomena. Therefore, the decomposition of the surface stoichiometry due to the laser illumination can be excluded as the origin of the measured change of the spectral shape. It has been reported that the decapped GaAs(100) surface produces a Ga-rich composition which shows the (4x2)-c(8x2) low-energy electron diffraction pattern. In this case, two surface components on ether side of the bulk component are necessary to reproduce the observed spectral shape of the Ga *3d* core-level. These surface components correspond to the inequivalent surface Ga sites in the (4x2) unit cell. It is considered that the change of the spectral shape observed in this work can be explained by different SPV shift for each Ga site. In order to clarify the site dependent SPV effect and its time dependence, the detailed analysis including the line-shape analysis using a least-squares-fitting is in progress.
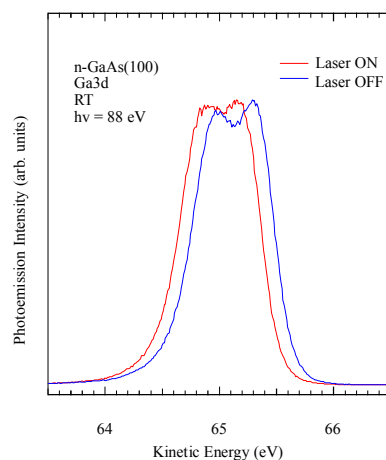

Fig. 1. Ga *3d* photoemission spectra with and without laser illumination.

BL5U

Photoelectron Spectroscopy of ErAs/GaAs(100)

H. Murayama, K. Shimba, M. Kato, S. Yagi, K. Soda, T. Yamauchi, A. Nakamura

Graduate School of Engineering, Nagoya University,
Furo-cho, Chikusa-ku, Nagoya, 464-8603 Japan

Introduction

In recent years much attention has been focused on the quantum size effect in thin films on semiconductor. The electron confinement induced by the quantization of its states was found in thin ErAs films epitaxially grown on the GaAs(100) surface [1]. A semimetal to semiconductor transition has been also predicted as the ErAs film thickness is decreased [2]. In this report, we will present results of angle-resolved photoelectron spectroscopic study on the electronic structure of ultrathin ErAs films on GaAs(100).

Experiments

Photoelectron measurements were carried out in the normal emission angle-resolved mode with the angle acceptance of ±1˚ at BL5A of UVSOR. Thin ErAs films were grown on GaAs(100) substrates with a 200 nm thick GaAs buffer layer by molecular beam epitaxy, and then capped with a thick As overlayer to prevent oxidation. This overlayer was removed by annealing in an ultrahigh vacuum just before the photoelectron measurement, as shown below. A clean GaAs(100) surface was also prepared by an Ar^+ ion sputtering and annealing procedure.

Results and Discussion

Figure 1 shows typical spectra recorded with the excitation photon energy $h\nu$ = 120 eV for 9 ML thick ErAs films on GaAs(100) at different stages of successive annealings, each of which was made at the temperature indicated in the figure for 10 min. The spectrum of the clean GaAs(100) is also presented for comparison. Features around the binding energy E_B of 20, 41 and 45 eV are ascribed to the Ga 3d and As 3d states of ErAs/GaAs and the As 3d one of the As oxides in the overlayer, respectively. No lines due to Ga oxides are observed. After annealing, the As 3d line at ~41 eV increased, while the As oxide line at ~45 eV decreased. The Er 5p line at E_B ~ 32 eV and the Er 4f multiplets around 4~11 eV also appear after annealing. These results show that the As overlayer can be removed by the longer annealing at 740 K.

In Fig.2, we compare the valence band spectra of 2 ML and 9 ML thick ErAs/GaAs (100) after the 740 K annealing with that of a thick ErAs layer reported by Komesu *et al*. [3]. Here, the 2 ML-ErAs/GaAs spectrum was recorded with a He I light source. It shows the less noticeable Er 4f features because of its small ionization cross section at $h\nu$ = 21.2 eV and of the low Er concentration. As for the electronic structure near the Fermi level (E_B = 0 eV), the thick ErAs reveals the definite intensity at the Fermi level, representing a semimetallic electronic structure, while

the ultrathin 2 ML-ErAs/GaAs indicates an energy gap. This implies that the semimetal-semiconductor transition may occur at some thickness, though the detailed thickness dependence of the electronic states of ErAs/GaAs has not been clarified at present.
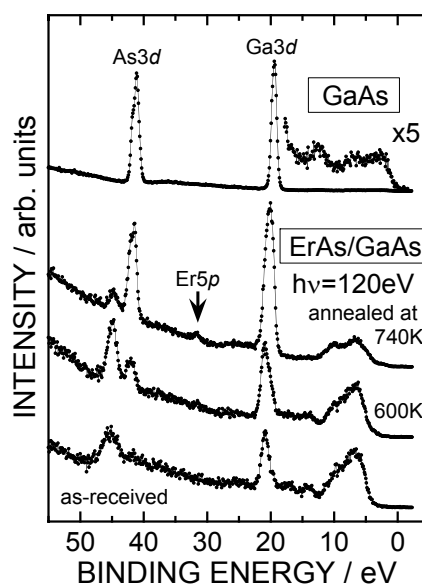

Fig. 1 Photoelectron spectra of ErAs/GaAs(100) at different annealing stages. A spectrum for a clean GaAs(100) is presented for comparison.
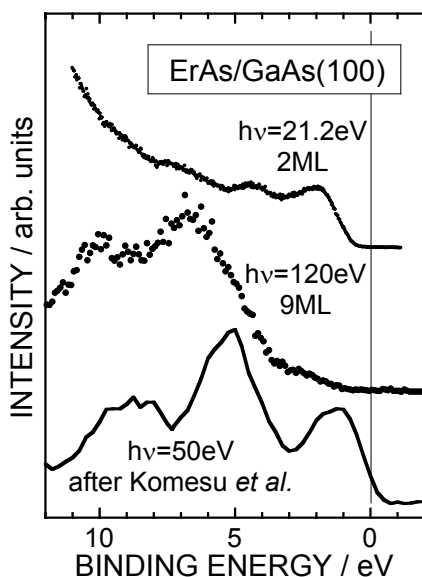

Fig.2 Valence band spectra of ErAs/GaAs(100).

[1] L. Ilver *et al*. Phys. Rev. Lett. **77,** 4946 (1996).
[2] S. J. Allen *et al*. Surf. Sci. **228,** 13 (1990).
[3] T. Komesu *et al*. Phys. Rev. B **67**, 035104 (2003).

Atomic Arrangement of Si(111) 2√7×3-(Pb,Sn) Surface

K. Shimba, H. Miyazaki, S. Ota, H. Murayama, J. Yuhara, M. Kato, S. Yagi, K. Soda
T. Ito*, S. Kimura*

Graduate School of Engineering, Nagoya University, Chikusa-ku, Nagoya 464-8603 Japan
**UVSOR, Institute for Molecular Science, Myodaiji-cho, Okazaki 444-8585 Japan*

Binary metal adsorbing system on a semiconductor surface possesses a possibility of showing unique atomic arrangement and electronic properties, which are different from those for a single adsorbate system. Recently, we have found a new superstructure, a Si(111) 2√7×3-(Pb,Sn) surface, on the coadsorption of Pb and Sn at their coverages, θ_{Pb} and θ_{Sn}, of 0.25 and 0.5 ML, respectively [1]. Here, 1 ML is defined as 7.8×10^{14} atoms·cm^{-2}. However, its detailed atomic arrangement has not been clarified yet. In this study, we have measured the Pb 5d and Sn 4d photoelectron spectra of the Si(111) 2√7×3-(Pb,Sn) surface and proposed its atomic arrangement model.

Experimental

An n-type Si(111) wafer of 5 Ωcm and 5×10×0.5 mm^3 in size was used for a substrate of the Si(111) 2√7×3-(Pb,Sn) surface. This surface was prepared by annealing at 620 K after deposition of ~ 1 ML Pb onto a Si(111) √3×√3 + faint 2√3×2√3-Sn surface at θ_{Sn} = 0.5 ML, which was made by deposition of 1 ML Sn onto a clean Si(111) 7×7 surface and subsequent annealing at 970 K. The completion of the surface was confirmed by low energy electron diffraction. Photoelectron spectra were recorded at the normal emission at 100 K with the excitation photon energy of 52 eV, the angle acceptance of ±1° of an electron analyzer, and total energy resolution of ~80 meV.

Results and Discussion

Figure 1 shows typical Pb 5d and Sn 4d core-level spectra for the Si(111) 2√7×3-(Pb,Sn) surface. The Pb 5d spectrum consists of single component, while the Sn 4d one exhibits two components C1 and C2, the ratio of which is C1:C2 = 100:31. This suggests that the Pb atoms are located at single adsorption site and the Sn atoms are adsorbed on two inequivalent sites at their ratio of 100:31. Taking account of results of scanning tunneling microscopy (STM) as well, we propose a model for the atomic arrangement of the Si(111) 2√7×3-(Pb,Sn) surface in Fig.2. Here, typical STM image for the surface is also presented for a filled state of -0.8 V sample bias in a scanned area of 50×50 Å^2. In this model, all dangling bonds of the first Si layer are terminated by metal adsorbates and the number of Pb and Sn atoms per unit cell are 4 and 8, corresponding to the coverages θ_{Pb} = 0.22 and θ_{Sn} = 0.44 ML respectively.

[1] J. Yuhara *et al*., Nucl. Instrum. Methods B **199** (2003) 422.

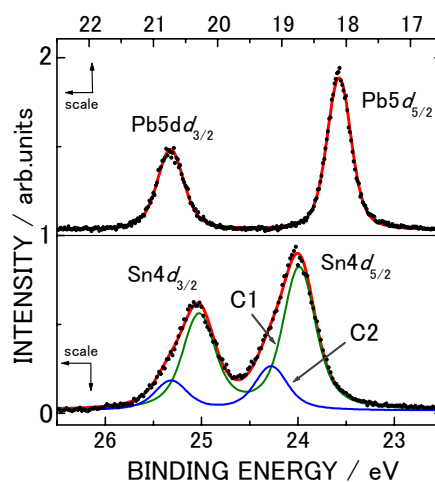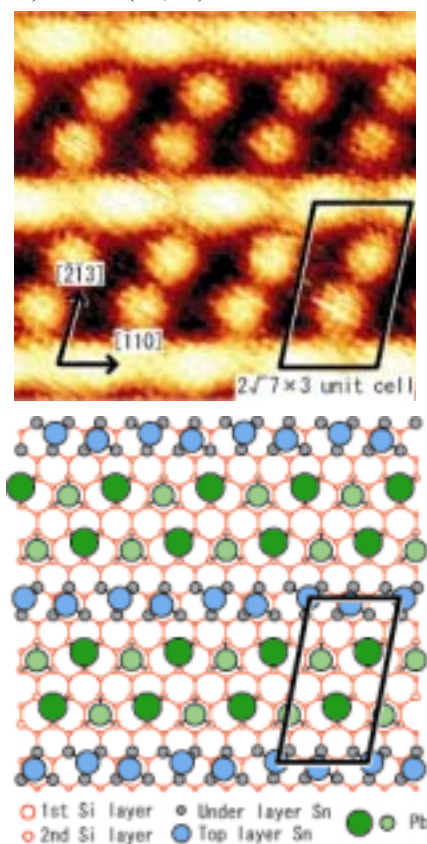Fig.1. Pb 5d and Sn 4d photoelectron spectra of the Si(111) 2√7×3-(Pb,Sn) surface.

Fig.2. STM image and atomic arrangement model for the Si(111) 2√7×3-(Pb,Sn) surface.

BL5B **Photodesorption of Ionized Clusters from Water Physisorbed on Rare Gas Solids: Measurements of the Desorption Yield**

T. Tachibana[1], Y. Yamauchi[1], H. Nagasaki[1], T. Miura[1],
T. Hirayama[2], M. Sakurai[3] and, I. Arakawa[1]

[1]Dept. Phys., Gakushuin Univ., Mejiro, Toshima, Tokyo 171-8588, Japan
[2]Dept. Phys., Rikkyo Univ., Nishiikebukuro, Tokyo 171-8501, Japan
[3]Dept. Phys., Kobe Univ., Rokkodai, Nada, Kobe 657-8501, Japan

A variety of studies have been made on electron- and photon-stimulated desorption (ESD/PSD) of water adsorbed on various substrates, and the mechanisms of desrobed species have been discussed. Recently, Souda has examined D_2O adsorbed on rare gas solids by means of ESD and found $(D_2O)_nD^+$ [n=1-10]. The result is interpreted that the desorption of the cluster are due to Coulombic expulsion between valence holes in the water cluster[1].

We have studied PSD of $(H_2O)_nH^+$ from water physisorbed on rare gas solids Ar through Xe by using synchrotron radiation and by a laser-plasma ultraviolet light source (LPLS). Previous PSD experiment of the threshold for the desorption of $(H_2O)_nH^+$ from the substrate Ar was found to 240 eV, and the desorption yield dependence on the incident energy after the threshold is clearly corresponds to the absorption spectrum of solid Ar near the onset of 2p transitions. In the present study, the desorption yields of $(H_2O)_nH^+$ from water adsorbed on solid Xe and on solid Kr were measured as a function of the incident photon energy. The same as a result of H_2O / Ar, the results indicated that the core excitation of rare gas atoms leads the desorption of clusters.

Experimental

The PSD-experiments have been carried out in two independent ultra-high vacuum systems; One at the Gakushuin University and the other at the beam line 5B at UVSOR in Institute for Molecular Science, Okazaki. The mass spectrum of PSD ions was measured by a time-of-flight (TOF) technique. The desorption yield was normalized by the light intensity, which was continuously monitored by the photoelectronic current from a gold-plated mesh, inserted in the beam lines.

In Gakushuin, the experiments were performed with the ultrahigh-vacuum instrument attached to LPLS, which was developed for purpose of using it as an excitation light source in exprimental studies of DIET. Radiation is produced by plasma on a Ta surface which is induced by YAG-laser irradiation focused on the surface. The photon energy was monochromatized using troidal grating monochromators and a exist slit in the range of 11.5 to 310 eV. The pulse width of the order of 10 ns makes it possible to obtain higher time resolution in a TOF measurement of desorbed particles. Water was physisorbed on the rare gas solids which was condensed on a Copper substrate attached to the He gas flow cryostat. The samples were held at ~17 K.

In UVSOR, The sample film was prepared on a Pt(111). This was fixed to a liquid He cryostat and cooled down to 6 K. the cryostat surrounded by a liquid N_2 cooled heat shield. Monochromatized synchrotron radiation in the range of 6 to 1000 eV was focused on the sample. The incident angle of the photon beam was 20 deg from the normal direction of the sample surface. A voltage pulse was applied to the sample, and the desorbed cations extracted into the drift tube were detected by a channeltron electron multiplier, which was placed at off-axis with respect to the surface normal.

Results

The results of the $(H_2O)_nH^+$ desorption yield from a surface of (a)Kr and (b)Xe were shown fig. 1. The desorption yield is quite similar to the absorption spectrum near the onset of 4d (3d) transitions of solid Xe (Kr)[2]. However, there was no increasing of the desorption yield 20-40 eV incident photon energy, which was reported as the desorption threshold of the H^+ for bulk water[3]. We can conclude that the inner-shell ionization of the rare gas atom plays a important role as a primary excitation which leads to the desorption of the $(H_2O)_nH^+$ at the rare gas solids.

[1] R. Souda, Surf. Sci. 511, 147 (2002)
[2] Hansel at el., J. Phys. **32**, 236 (1971)
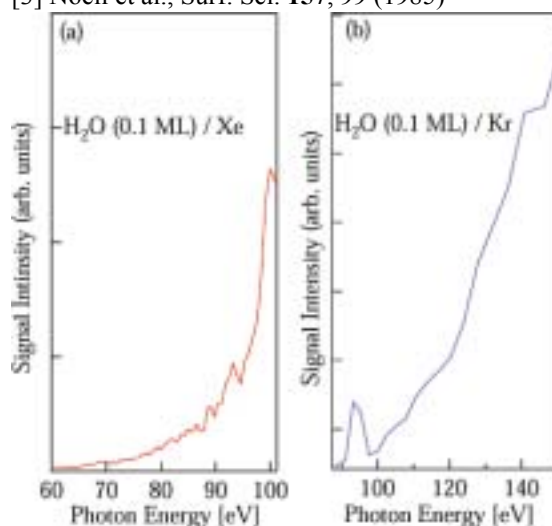[3] Noell et al., Surf. Sci. **157**, 99 (1985)

Fig. 1. Excitation energy dependence of the PSD cluster ion yield from adsorbed on (a)solid Xe and (b)solid Kr.

Construction of BL7U and STM Observations of H-Si (111)

Y. Nonogaki and T. Urisu

Dept. Vaccum UV Photoscience, Institute for Molecular Science, Okazaki 444-8585 Japan

SR stimulated etching and deposition have been attractive for fabrications of semiconductor devices with nanometer-scale fine structures due to their high spatial resolution and low damage properties. From the viewpoint of photochemistry, they are also very important because there are a few reports of STM observation of surface reactions stimulated by SR irradiation[1]. Particularly, STM observations of their excitation energy dependence are much interesting.

BL7U was designed that the 1st order harmonic of the undulator radiation was changed from 70 eV to 140 eV with high photon flux achieving to 10^{20} phot. cm^{-2} on the sample surfaces. Two Pt-coated cylindrical mirrors were used for vertical and horizontal focusing. These two mirrors also suppress the higher harmonics of the undulator radiation into ~10% with respect to the first harmonic. The spectral resolution of this beamline is determined by the light source characteristics of the undulator radiation and an aperture stop set at the point 4810 mm downstream from the middle of the undulator. The calculated FWHMs at K parameter of 0.985 (1st harmonic at ~100 eV) are 9.3 eV and 4.5 eV for the radiation divergences of 500 µrad and 250 µrad respectively.

The UHV-STM system (UNISOKU Sci. Instrument) was installed at the end station and the atomic images of the clean Si (111) and H-adsorbed Si (111) surfaces were observed as a preliminary experiment. For a simplicity of the H/Si system, observation of SR irradiation effects and its excitation energy dependence by STM are interesting research targets.

The STM observations of H-Si (111) surfaces before undulator irradiation were carried out in the UHV chamber with a base pressure below 1×10^{-10} Torr. Although there are a lot of reports about the studies of H-Si (111) surfaces[2-4], interaction between rest-atom monohydride and H-atoms is still unclear. To observe the interaction of rest-atom monohydride and H-atoms, we used monohydride surfaces that were prepared by H-atom exposure on the Si 7x7 surface at a sample temperature of ~400°C.

Figure 1 shows 11 nm x 11 nm STM images that were recorded with a sample voltage of -2.00 V at a constant current of 0.25 – 0.30 nA. A sufficiently clear image of Si (111)-7x7 was obtained as shown in Fig. 1 (a). Figure 1 (b) shows a monohydride surface with several adatom islands prepared by 1000 L H-exposure at a sample temperature of ~400°C. It is observed that the area of the faulted regions is reduced. Further exposure of H atom of 1000 L at RT, shown in Fig. 1(c). The vacancies of the rest-atom are observed near the boundary of the faulted and unfaulted domains, which indicates that rest-atom etching occurred by H-exposure at RT.

At ~400°C, the H-exposure on clean Si 7x7 surface terminates the dangling bonds on the Si surface. The adatom hydrides move around on the rest-layer monohydride surface, fill the defects and enlarge the unfaulted domain, or form adatom islands. Excess H-atoms would partly contribute to the enlargement of the unfaulted domains and partly desorb by forming H_2 since the sample temperature is above the H_2 desorption threshold of 325°C [10]. However, at RT where H_2 desorption rate is low, excess H-atoms would break Si-Si bonds in the rest-atom layer and in adatom islands. Subsequential Si-Si bond breaking can lead the formation of SiH_4, which is then removed from the surface.

We are planning to investigate photon-stimulated desorption of a H-Si (111) surface, and the etching reaction by inner-shell excitation of the H-Si (111) surface and its excitation-energy dependence in the next experiments at BL7U.
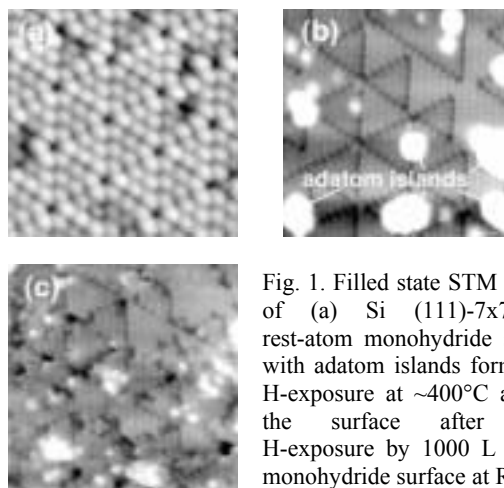
Fig. 1. Filled state STM images of (a) Si (111)-7x7, (b) rest-atom monohydride surface with adatom islands formed by H-exposure at ~400°C and (c) the surface after more H-exposure by 1000 L on the monohydride surface at RT.

[1] Miyamae, T., Uchida, H., Munro, I.H., and Urisu T., J. Vac. Sci. Tehnol. A17, 1733-1736 (1999).
[2] Mortensen, K., Chen, D.M., Bedrossian, P.J., Golovchenko, J.A., and Besenbacher, F., Phys. Rev. 43, 1816-1819 (1991).
[3] Boland, J.J., Surf. Sci. 244, 1-14 (1991).
[4] Owman, F., and Mårtensson, P., Surf. Sci. 324, 211-255 (1995).

Investigation of Synchrotron Radiation
Induced Etching of Polytetrafluoroethylene

H. Okada, H. Yamada, A.Yoshida and A.Wakahara

Department of Electrical and Electronic Engineering, Toyohashi University of Technology,
Tempaku-cho, Toyohashi 441-8580, Japan

Polytetrafluoroethylene (PTFE) has many unique properties such as high thermal and chemical stability, low coefficient of friction, high electrical resistively, hydrophobicity (contact angle ~108°), and so on. By taking advantage of these characteristics, this material is expected for applications in various fields such in chemical, mechanical, electronics and so on. Recently, some reports about high aspect ratio fabrication for PTFE by synchrotron radiation (SR) are reported.[1,2] However the etching mechanism of PTFE by SR beam irradiation is not well understood yet. Adding to this, properties of the SR beam irradiated surface should be characterized for further application. In this study, etching of the PTFE by SR and surface characteristics after the processing was investigated.

In this study, etching of PTFE was made using SR of UVSOR facility with various holder temperatures (150~250°C) and photon fluxes ($1.5 \times 10^{17} \sim 3.1 \times 10^{17}$ /s/cm^2). SR beam induced etching was done in the vacuum chamber having turbo molecular pump. For the PTFE target, Naflon by Nichias was used. Chemical composition of the etched surface was analyzed by XPS system in author's group laboratory

Figure 1 shows the etching rate dependence on the photon flux for various holder temperatures. Higher etching rate was obtained with higher photon flux. Higher etching rate was also observed in higher holder temperature, however, after the SR beam irradiation at 150°C , the etching rate was noticeably low and surface color change into brown was observed.

To clarify this point, XPS spectrum of PTFE surface before and after the SR beam irradiation was investigated. As shown in Fig. 2, C$_{1s}$ spectrum of bulk PTFE before the irradiation showed two major peaks marked as A and C. Here, the peak A and the peak C correspond to CF$_2$ and C-C component, respectively.
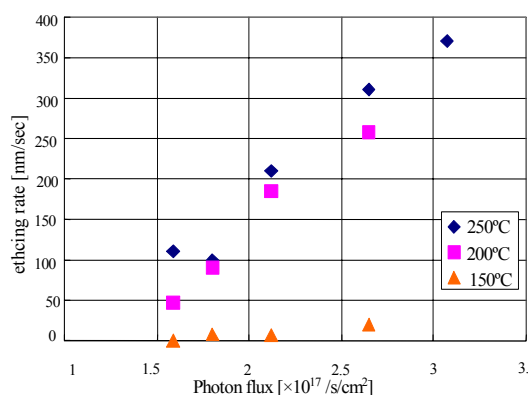
After the irradiation at holder temperature of 150°C, the peak A became ambiguous, and the peak C became major. Additional signal was also found at around the binding energy of 295 eV. After the irradiation at holder temperature of 250°C, the peak A suggesting CF$_2$ component became major again, and the peak C was not seen. Around 295 eV, peak B was seen and was thought to be –C-CF$_3$ component.

From XPS, surface after the SR beam irradiation at higher temperatures is close to the bulk PTFE. On the other hand, SR beam irradiation at 150°C, marked composition change suggests that removal of fluorine from the surface. SR beam irradiation at lower temperatures causes carbon-rich surface which prevents further PTFE etching by SR beam irradiation. In the case of the irradiation in 200-250°C, some dissociation mechanism by heat may assist the etching process. Thus, the holder temperature is a key parameter for SR beam induced etching of PTFE by means of surface composition control because which affects chemical properties and hydrophobicity of the surface.

[1] T.Katoh, Y.Zhang, Appl. Phys. Lett. 68 (1996) 865.
[2] T.Katoh, D.Yamaguchi, Y.Satoh, S.Ikeda, Y.Aoki, M.Washio, Y.Tabata, J. Appl. Surf. Sci. 186 (2002) 24.
[3] A.Yoshida, E.Matsumoto, H.Yamada, H.Okada and A.Wakahara, Nucl. Inst. and Meth. in Phys. Res. B 199 (2003) 370-374.
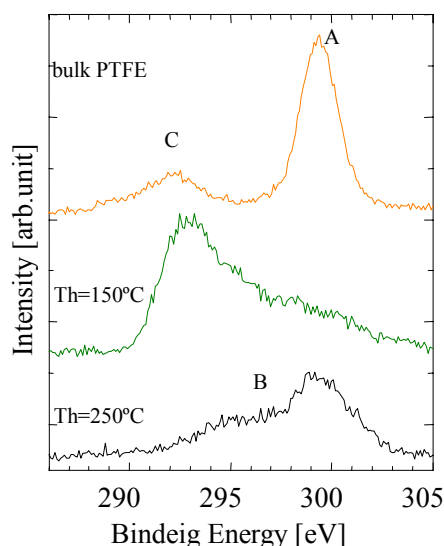
Fig.1 Etching rate vs. photon flux for various holder temperatures

Fig.2 XPS spectrum of PTFE before and after the beam irradiation

Synchrotron Radiation-excited Etching of ZnTe Using Ar Gas

T. Tanaka, Y. Kume*, S. Fukui*, K. Hayashida**, M. Nishio*, Q. Guo*, and H. Ogawa

Synchrotron Light Application Center, Saga University, Saga 840-8502, Japan
*Dept. of Electrical and Electronic Engineering, Saga University, Saga 840-8502, Japan
**Venture Business Laboratory, Saga University, Saga 840-8502, Japan

Synchrotron radiation (SR) is an ideal light source for the photo-excited process. Many studies on the technological utilization of SR-stimulated reactions, such as chemical vapor deposition [1,2], etching [3,4], and epitaxy [5,6] have been carried out so far. Concerning the SR-excited etching, the materials for integrated circuit such as Si, SiO_2, SiC, *etc*, have been studied actively using SF_6 as a reaction gas together with Ar gas [3]. SF_6 seems to be useful for SR-excited etching. On the other hand, few papers concerning the etching of compound materials such as III-V and II-VI semiconductors have been published to date in spite of their importance in optoelectronic application [7]. As II-VI semiconductors, *e.g.* ZnTe, with good quality can be grown by SR-excited growth [6], the study on the SR etching of them is the important next step to make the electronic devices by SR. In this study, we have described the SR-excited etching of ZnTe using SF_6 and Ar gas.

Experiments

The irradiation experiments were performed at beam line, BL-8A, in UVSOR. The focused SR from the bending magnet field of the 750 MeV electron storage ring was shone upon ZnTe (100) in Ar gas atmosphere. The spot size of SR on the sample was about 2×4 mm. A Ni mesh of 100 lines/in. and 80% transmittance, which is used as a mask, was placed on the sample surface. The synchrotron light is irradiated perpendicularly to the surface at room temperature (RT). The electric current for the SR emission in the storage ring was varied up to 300 mA. After the reaction chamber was evacuated to less than 10^{-7} Torr, the etching gas was fed into the chamber. The pressure in a reaction chamber was changed between 10^{-2} and 10^{-1} Torr. The substrate was negatively biased against the reaction chamber. A large pressure difference was sustained between the storage ring and the reaction chamber using multiple differential vacuum pumping system.

Results

ZnTe was etched by the irradiation of the SR beam under the negative bias to the sample. The surface step profile of this sample is shown in Figure 1. The shadow area due to 50 μm wide Ni wires is not etched but the irradiated area is etched. The pattern of metal mask was found to be transferred exactly. In this experiment, we used focused SR beam as mentioned above, and the center area of the beam was etched deeply, indicating that the etching rate depends on the photon flux. The maximum etching rate was estimated to be around $4.5×10^{-2}$ Å/mA·min. The etching is supposed to be proceeded by the excitation of Ar gas by high-energy SR beam, followed by the bombardment of Ar ion to the surface of ZnTe due to the negative bias. Since the etched area was relatively large compared with the beam spot size (2×4 mm), the physical etching process is considered to be dominant rather than chemical process with surface excitation. Further investigation will be required to clarify the mechanism and improve the etching rate.
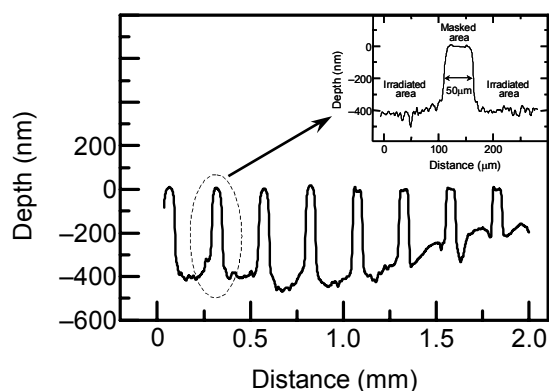
Fig. 1. Surface step profile of ZnTe etched in Ar atmosphere under negative bias to the sample.

[1] D. C. Mancini, S. Varma, J. K. Simons, R. A. Rosenberg, and P. A. Dowben, J. Vac. Sci. Technol. B 8, 1804 (1990).

[2] D. Byun, S. D. Hwang, P. A. Dowben, F. K. Perkins, F. Filips, and N. J. Ianno, Appl. Phys. Lett. 64, 1968 (1994).

[3] Y. Utsumi, J. Takahashi, and T. Urisu, J. Vac. Sci. Technol. B 9, 2507 (1991).

[4] K. Shobatake, H. Ohashi, K. Fukui, A. Hiraya, N. Hayasaka, H. Okano, A. Yoshida, and H. Kume, Appl. Phys. Lett. 56, 2189 (1990).

[5] J. Takahashi, Y. Utsumi, H. Akazawa, I. Kawashima, and T. Urisu, Thin Solid Films 218, 40 (1992).

[6] T.Ogata, S.I.Gheyas, M.Ikejiri, H.Ogawa, and M.Nishio, J.Crystal Growth, 146, 587 (1995).

[7] S.Terakado, J.Nishino, M.Morigami, M.Harada, S.Suzuki, K.Tanaka, and J.Chikawa, Jpn.J.Appl.Phys. 29, L709 (1990).

Surface Properties of Synchrotron Radiation Irradiated PTFE

A.Yoshida, H.Yamada, H.Okada, and A.Wakahara

Department of Electrical and Electronic Engineering, Toyohashi University of Technology,
Tempaku-cho, Toyohashi 441-8580, Japan

High hydrophobicity of polytetrafluoroethylene (PTFE) is a one of the standing feature of this material. With this unique feature together with its high chemical stability, PTFE is quite useful for the application to bio-sensors, tissue engineering and so on. SR beam induced etching of PTFE have a high potential for micro fabrication of this material[1]. In this study, we have studied surface properties of PTFE after the synchrotron radiation (SR) beam irradiation.

In this study, commercially available PTFE bulk was used for the experiments. SR beam irradiation onto the PTFE was made in vacuum chamber which was connected to the UVSOR beam line, as mentioned in previous report.[2,3] PTFE samples were placed on the sample holder having a heater. In this study, holder temperature was changed in the range of 150°C to 250°C. Characterization of SR beam irradiated PTFE was made by SEM observation, and XPS measurement. To evaluate the surface hydrophobicity, measurement of the contact angle of the PTFE surface was done following JIS R3257.

Figure 1 shows SEM image of SR beam irradiated PTFE surface at 250°C. As reported in our previous report, SR beam induced etching of PTFE was clearly found. From the SEM observation of the etched surface, some microstructures were found. Roughness of the structure became large with increasing an irradiation time, photon flux and holder temperature.

Contact angle of the irradiated surface became as high as 156°, which is clearly exceeded that of bare PTFE surface. According to Wenzel's model, an introduction of fine structures on the surface enhances the hydrophobicity of the surface. Although the mechanism of the fine structures on SR beam irradiated surface of PTFE, observed enhancement of hydrophobicity is thought to be come from the introduction of surface structures as shown in Fig. 1.
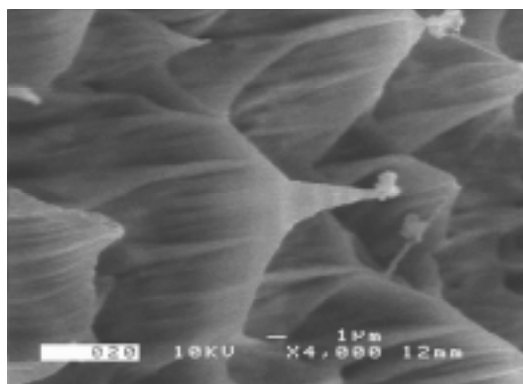
Irradiation time dependence on the contact angle was characterized. Contact angle became larger with irradiation time. Here, increase of the contact angle was observed up to 156°. As compared with the case of holder temperature of 200°C, result of holder temperature of 250°C showed rapid enhance of hydrophobicity with short irradiation time. This suggests that the surface decomposition process of PTFE by SR beam irradiation affects the hydrophobicity of PTFE.

Then, to investigate a relation between the hydrophobicity and the compositional change by the SR beam irradiation, XPS measurements of the PTFE surfaces were made. As shown in Fig. 2, chemical composition of the PTFE surface clearly depend on the holder temperature. Namely, SR beam irradiated samples at lower temperature showed F-poor (C-rich) surfaces as compared with bare surfaces. However, as area ratio of XPS peak of fluorine and carbon (F/C ratio) increased in higher temperatures, contact angle becomes higher. This suggests that the hydrophobicity enhancement by SR beam irradiation is not only from the introduction of the fine structures on the surface, but also the control of the chemical composition of PTFE surfaces.

[1] T.Katoh, Y.Zhang, Applied Physics Letters 68 (1996) 865.
[2] A.Yoshida, E.Matsumoto, H.Yamada, H.Okada and A.Wakahara, Nucl. Inst. and Meth. in Phys. Res. B 199 (2003) 370-374.
[3] H.Okada, H.Yamada, A.Yoshida, and A.Wakahara, UVSOR Activity Report 2003 (2004)
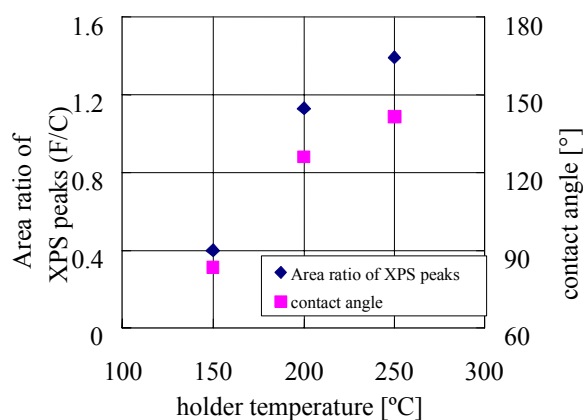
Fig.1 SEM image (tilted) of UVSOR irradiated surface.

Fig.2 Holder temperature dependence on the area ratio of XPS peaks (F/C) and contact angle.

Chalcogen-Au Bonding State of Self-assembled Monolayers on Au(111)

T. Miyamae, T. Nakamura, D. Yoshimura*, N. Kobayashi, M. Matsumoto, H. Nozoye

Nanotechnology Research Institute, National Institute of Advanced Industrial Science and Technology, Tsukuba, Ibaraki 305-8565, Japan
*Research Center for Materials Science, Nagoya University, Chikusa, Nagoya 464-8602 , Japan

Self-assembled monolayers (SAMs) on metal surfaces present many interesting aspects in resent years from the viewpoints of both basic science and practical applications. Although a variety of substrates and functional groups are known to form SAMs, the thiol/disulfide monolayer on Au has received considerable attention due to its simplicity and ease of preparation. In contrast to the many reports of monolayers derived from organosulfur reagents containing functional groups in the ω-position, there has been relatively little work done to build organic monolayers on metals without using sulfur as the anchor group. Moreover, there is little attention for the electronic states which originate from anchored part of adsorbed SAM molecules adsorbed on metal surfaces. In this report, we have studied the molecular conformation and the electronic structural study of dialkyl telluride adsorption on Au(111) with ultraviolet photoelectron spectroscopy (UPS).

Experiments

The Au(111) substrates were prepared by thermally evaporated on mica. The substrate was immersed into a try toluene diluted Oc_2S_2 or Oc_2Te_2 solution at a concentration of about 1 mM for 24 h in dry nitrogen atmosphere. After removal from the solution, the samples were rinsed and stored in dried ethanol until measurements under dark condition. ARUPS measurements were carried out at the beamline 8B2 of the UVSOR facility.

Results and Discussion

Figure 1 shows the UPS spectra of Oc_2S_2 and Oc_2Te_2 monolayers adsorbed on Au(111) at the incident photon energy $h\nu = 40$ eV on a binding energy scale relative to the Fermi level. Bands A and B are ascribed to pseudo-π and C2s orbital distributed on the alkyl chain, respectively. ARUPS spectra of Oc_2S_2 on Au(111) exhibit polarization dependence suggestive of formation of a well-oriented film. In contrast, the bands A and B of Oc_2Te_2 on Au does not show polarization dependence, indicating that the conformation of the alkyl chain is more randomly oriented than that of Oc_2S_2. In Fig, 2, we show the UPS spectra of clean Au(111), and Oc_2S_2 and Oc_2Te_2 monolayers near the Fermi level. In the case of the clean Au(111), the Shockley surface state is clearly observed just below the Fermi level. The quenching of the surface state and the emergence of additional bands attributed to the MOs of the dialkyl dichalcogenide-

derived adsorbates. In the case of the Oc_2S_2, a low intensity feature is observed at approximately 1.5 eV below Fermi level and prior to the Au 5d band onset. We measured with the different photon energies thus changing the relative cross section between Au 6s and the binding orbital (largely S 2p), and the band has a small contribution of Au 6s. Similar low intensity bands are also observed at around 1.5 eV for the Oc_2Te_2 on Au. These band observed at around 1.5 eV for dioctyl dichalcogenide adsorbed on Au(111) can thus be taken as evidence of Au-chalcogen bonding.

In our previous report for the Oc_2Te_2 monolayer, the ditelluride derived adsorbed layer is easily oxidized in air atmosphere than the disulfide and diselenide adsorbed monolayers [1]. By exposing to air for Oc_2Te_2 monolayer, this band is completely disappeared, indicating that the Au-Te bonding cleavage proceeds by the oxidation in the atmosphere.

[1] T. Nakamura et al, *J. Am. Chem. Soc.*, **124** (2002) 12642.
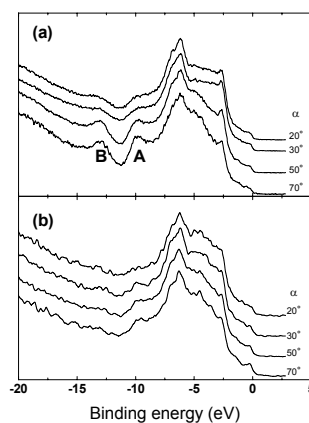
Fig. 1. Normal emission UPS spectra of Oc_2S_2 and Oc_2Te_2 on Au(111) as a function of photon angle of incidence α.
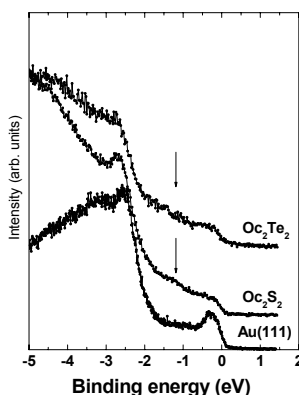

Fig. 2. Expanded normal emission UPS spectra of Oc_2S_2 and Oc_2Te_2 on Au(111) and clean Au(111) surface.

List of Publications 2003

M. Katoh, M. Hosaka, A. Mochihashi, J. Yamazaki, K. Hayashi, Y. Hori, T. Honda, K. Haga, Y. Takashima, T. Koseki, S. Koda, H. Kitamura, T. Hara, T. Tanaka

Construction and Commissioning of UVSOR-II

* AIP Conference Proceedings **705** (2004) 49.

M. Hosaka, M. Katoh, A. Mochihashi, J. Yamazaki, K. Hayashi, Y. Takashima, T. Gejo, E. Shigemasa, E. Nakamura

Status and Prospects of User Applications of the UVSOR Storage Ring Free Electron Laser

*AIP Conference Proceedings **705** (2004) 61.

A. Mochihashi, M. Katoh, M. Hosaka, TK. Hayashi, J. Yamazaki, Y. Takashima, Y. Hori, H. Kitamura, T. Hara, T.Tanaka

In-Vacuum Undulators in UVSOR Electron Storage Ring

*AIP Conference Proceedings **705** (2004) 259.

Y. Nonogaki, M. Katoh, E. Shigemasa, K. Matsushita, M. Suzui, T. Urisu

Degign and Performance of Undulator Beamline (BL7U) for In-Situ Observation of Synchrotron Radiation Stimulated Etching by STM

*AIP Conference Proceedings **705** (2004) 368.

S. Kimura, E. Nakamura, J. Yamazaki, M. Katoh, T. Nishi, H. Okamura, M. Matsunami, L. Chen, T. Nanba

New Infrared and Terahertz Beam Line BL6B at UVSOR

*AIP Conference Proceedings **705** (2004) 416.

T. Hatsui, E. Shigemasa, N. Kosugi

Design of a Transmission Grating Spectrometer and an Undulator Beamline for Soft X-Ray Emission Studies

*AIP Conference Proceedings **705** (2004) 921.

E. Shigemasa, E. Nakamura, T. Gejo

New Molecular Inner-Shell Spectroscopy for Probing Multiple Excitations

*AIP Conference Proceedings **705** (2004) 1118.

---

*in proceedings of SRI2003, California (USA), Aug. 2003.

T. Ejima, Y. Muramatsu, H. Kakenaka, M Watanabe

Simulation Study of Total-Electron-Yield X-Ray Standing-Wave Spectra of Mo/SiC/Si/SiC and Mo/Si Multilayers

* AIP Conference Proceedings **705** (2004) 1126.

M. Hosaka, M. Katoh, A. Mochihashi, J. Yamazaki, Y. Takashima, H. Hama

Q-switching Operation of the UVSOR-FEL

Nucl. Instr. and Meth. A **507** (2003) 289.

M. Itoh

Radiative and Nonradiative Decay Processes of Core Holes in Shallow-lying Inner Shells

Recent Res. Devel. Phys. **4** (2003) 205.

M. Itoh, Y. Inabe

Optical Properties and Electronic Structure of Yttrium Oxysulfide

Phys. Rev. B **68** (2003) 035107.

K. Kanda, Y. Shimizugawa, Y. Haruyama, I. Yamada, S. Matsui, T. Kitagawa, H. Tsubakino, T. Gejo

NEXAFS Study on Substrate Temperature Dependence of DLC Films Formed by Ar Cluster Ion Beam Assisted Deposition

Nucl. Instr. And Meth. B **206** (2003) 880.

S. Kimura, H. Iwata, K. Kanai, S. Shin, G. Schmerber, J. P. Kappler, J. C. Parlebas

Collapse of Kondo Lattice in Ce$_{1-x}$La$_x$Pd$_3$(x=0, 0.03)

Acta Physica Polonica B **34** (2003) 975.

T. Misaki, A. Wakahara, H. Okada, A. Yoshida

Optical Properties of ZnGeN$_2$ Epitaxial Layer

phys. stat. sol. (c) **0**, No.7 (2003) 2890.

A. Motogaito, H. Watanabe, K. Hiramatsu, K. Fukui, Y. Hamamura, K. Tadatomo

Characterization of GaN Based Schottky UV Detectors in the Vacuum UV (VUV) and the Soft X-ray (SX) Region (10-100 nm)

phys. stat. sol. (a) **200**, No.1 (2003) 147.

**in proceedings of SRI2003, California (USA), Aug. 2003.*

H. Miyake, H. Yasukawa, Y. Kida, K. Ohta, Y. Shibata, A. Motogaito, K. Hiramatsu, Y. Ohuchi, K. Tadatomo, Y. Hamamura, K. Fukui

High Performance Schottky UV Detectors (265-100 nm) Using n-Al$_{0.5}$ Ga$_{0.5}$N on AlN Epitaxial Layer

phys. stat. sol. (a) **200**, No.1 (2003) 151.

Y. Nagasaka, H. Ohta, K. Kawakami, A. Ueda, S. Ono, Y. Ikeuchi, T. Nanba, A. Hirano, R. Kanno

Millimeter Wave Spectroscopy of Secondary Battery Substance Li$_{1-x}$Ni$_{1+x}$O$_2$

J. Phys. Chem. Sol. **64** (2003) 1949.

K. G. Nath, Y. Ufuktepe, S. Kimura, Y. Haruyama, T. Kinoshita, T. Matsumura, T. Suzuki, H. Ogasawara, A. Kotani

Photoemission Study of Mixed-Valent Tm-Monochalcogenides: Evidence of Electron-Correlation Effect in Different Tm-Core Levels

J. Phys. Soc. Jpn. **72** No. 7 (2003) 1792.

K. Okada, S. Tanimoto, T. Morita, K. Saito, T. Ibuki, T. Gejo

Molecular Size Effect on the Site Dependent Photofragmentation of N and O K-Shell Excited CH$_3$CO(CH$_2$)$_n$CN (n = 0-3)

J. Phys. Chem. A **107** (2003) 8444.

A. Ohnishi, M. Kitaura, T. Otomo and M. Sasaki

Reflection Spectrum and Auger-Free Luminescence in Molecular Ionic Crystals of Cs$_2$ZnCl$_4$

J. Phys. Soc. Jpn. **72**, No. 9 (2003) 2400.

J. Sichelschmidt, V. Voevodin, S. Paschen, W. Carrillo-Cabrera, Y. Grin, F. Steglich, S. Kimura

Optical Reflectivity of the Clathrate Compound Ba$_6$Ge$_{25}$

Acta Phys. Pol. B **34** (2003) 613.

A. Tanaka, Y. Takeda, M. Imamura, S. Sato

Dynamic Final-state Effect on the Au 4f Core-level Photoemission of Dodecanethiolate-passivated Au Nanoparticles on Graphite Substrates

Phys. Rev. B **68** (2003) 195415.

H. Yamane, S. Kera, K. K. Okudaira, D. Yoshimura, K. Seki, N. Ueno

Intermolecular Energy-band Dispersion in PTCDA Multilayers

Phys. Rev. B **68** (2003) 033102.

L. F. Jiang, W. Z. Shen, H. Ogawa, Q. X. Guo,

Temperature Dependence of the Optical Properties in Hexagonal AlN

J. Appl. Phys. **94**, No. 9 (2003) 5704.

Q. X. Guo, M. Nishio, H. Ogawa, A. Yoshida,

Temperature Dependence of Alminium Nitride Reflectance Spectra in Vacuum Ultraviolet Region

Solid State Communications **126** (2003) 601.

N. Kosugi,

Exchange Interaction in Core Excitation of Diatomic Systems

Chem. Phys. **289** (2003) 117.

T. Hatsui and N. Kosugi

Metal-to-ligand Charge Transfer in Polarized Metal L-edge X-ray Absorption of Ni and Cu Complexes

J. of Electron Spectrosc. and Relat. Phenom. **136** (2004) 67.

T. Hatsui, T. Yamamoto, H. Tajima and N. Kosugi

Cu L-edge X-ray absorption spectra of $(Me_2\text{-}DCNQI)_2Li_{(1-x)}Cu_x$ alloys

Chem. Phys. **298** (2004) 189.

M. Yamaga, S. Yabashi, Y. Masui, M. Honda, H. Takahashi, M. Sakai, N. Sarukura,

J.-P. R. Wells, G. D. Jones

Optical, Infrared and EPR Spectroscopy of CaF_2:Ce^{3+} Crystals Co-doped with Li^+ or Na^+

Journal of Luminescence **108** (2004) 307.

Published Papers (before 2003)

Q. X. Guo, M. Nishio, H. Ogawa,

Temperature Effect on the Electronic Structure of AlN

Phys. Rev. B **64** (2001) 113105.

Books

K. Seki, H. Ishii, Y. Ouchi

Functional Organic Materials Studied Using UPS and NEXAFS

in *Chemical Application of Synchrotron Radiation*, p. 386.

H. Ishii, K. Seki

Energy Level Alignment at Organic-Metal Interfaces

in *Conjugated Polymer and Molecular Interfaces*, p. 293.

In Japanese

K. Isari, H. Yoshida, T. Gejo, E. Kobayashi, K. Mase, S. Nagaoka, K. Tanaka

Construction and Evaluation of Coaxially Symmetric Mirror Electron Energy Analyzer with High Sensitivity, and Its Application to Coincidence Spectroscopy

J. Vac. Soc. Jpn. **46** (2003) 377.

H. Watanabe, A. Motogaito, K. Hiramatsu, K. Fukui, Y. Hamamura, K. Tadatomo

Characterization of Optical Filters and GaN Based Schottky Ultraviolet Detector in Vacuum Ultraviolet and Soft X-ray Region

Technical Report of IEICE **103** (2003) 5.

S. Kameda, H. Sagawa, T. Murachi, A. Yamazaki, I. Yoshikawa, M. Nakamura

Development of Multilayer Gratings for Spectroscopy of Mercury's Atmosphere

ISAS Res. **124** (2003) 1.

E. Kobayashi, K. Isari, M. Mori, K. Mase, K. Okudaira, K. Tanaka, N. Ueno

Construction and Evaluation of Polar-Angle-Resolved Miniature Time-of-Flight Ion Mass Spectrometer, and Its Application for Electron-Ion Coincidence Spectroscopy

J. Vac. Soc. Jpn **47**, No. 1 (2004) 14.

UVSOR Twentieth Anniversary

Report for Upgraded UVSOR

December 2, 2003

Okazaki Conference Center

11:30~	**Facility Tour**	**for Guest Persons**
14:45~	**Report for Upgraded UVSOR :**	
	Future for the UVSOR Facility	**N. Kosugi (UVSOR)**
	Upgrade of UVSOR Light Source	**M. Katoh (UVSOR)**
	Upgrade of Users' Research I : **in Photochemistry**	**E. Shigemasa (UVSOR)**
	Upgrade of Users' Research II : **in Photophysics**	**S. Kimura (UVSOR)**
16:30~	**Special Talk :** **Expectation for UVSOR**	**T. Matsushita** **(President of the Jpn. Soc. for** **Synchrotron Radiation Research)**
17:30~18:30	**Banquet**	

UVSOR Users' Meeting

December 3, 2003

Okazaki Conference Center

9:00~9:10	**Opening**	**K. Nakagawa (Kobe Univ.)**
9:10~	**Photoionization Process of Fullerene in UV Region**	**J. Kou, T. Mori, S. V. K. Kumar,** **M. Ono, Y. Haruyama, Y. Kubozono,** **K. Mitsuke (IMS)**
9:35~	**Search for Conductive Mechanism of DNA with SR**	**M. Furukawa, H. Kato,** **M. Kawai (RIKEN)**
10:00~	*Break*	
10:10~	**Optical Spectra of Tungstate Crystals in VUV Region**	**M. Fujita** **(Japan Coast Guard Academy),** **M. Itoh, T. Maruyama (Shinshu Univ.)**

10:35~	**Time-resolved Spectroscopy combined with SR and Laser**	**T. Tsujibayashi (Osaka Dental Univ.)**
11:00~	*Break*	
11:10~	**Crystal Growth and Etching process of Compound Semiconductor with SR**	**M. Nishio (Saga Univ.)**
11:35~	**Development and Application of VUV/Soft X-ray Multilayer**	**M. Watanabe (Tohoku Univ.)**
12:00~	*Lunch Time*	
13:00~	**Poster Session***	
15:00~	**Research for Solid Materials using Soft X-ray**	**T. Yoshida (Nagoya Univ.)**
15:25~	**A Proporsal for Helical Switching Undulator for VUV Region**	**K. Nakagawa (Kobe Univ.)**
15:50~	**Research for Bulk Zr Alloy System and Si Surface 2-dimensional Metal System, and Expectation for BL5U**	**K. Soda (Nagoya Univ.)**
16:15~16:30	**Summary and Closing Remark**	**K. Nakagawa (Kobe Univ.)**

* Total 70 Posters
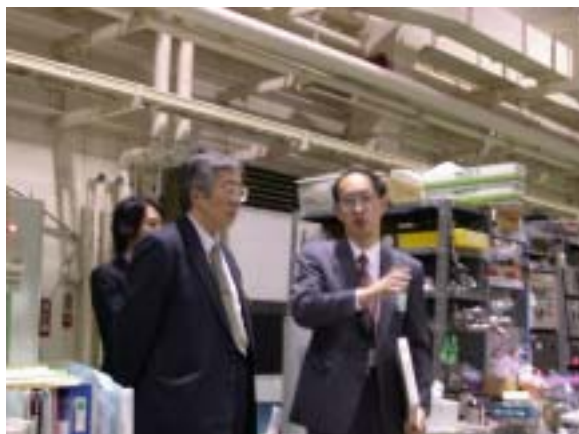
UVSOR Lunch Seminar

FY2002

May 22   Dr. J. Sichelschmidt, Max-Planck-Institut für Chemische Physik fester Stoffe, Dresden, Germany

Optical conductivity of the clathrate compound Ba_6Ge_{25}

June 12   Dr. H. Hara, National Astronomical Observation of Japan

Observation of sun from space and calibration of instruments at UVSOR

July 10   Prof. K. Fukui, Fukui University

SR study on Nitride semiconductors

July 24   Dr. K. Saito, Tohoku University

Magnetic dichroism in the XUV region using multilayer polarizer

Sept. 18   Prof. T. Miyazaki, Ehime University

UV photoemission spectra of Li-Ni complex oxides

Nov. 6   Prof. V.G. Stankevich, Kurchatov Synchrotron Radiation Source, RRC Kurchatov Institute, Russia

Present Status and Scientific Program of the Kurchtov SR Center

Dec. 4   Dr. S. Tanaka, Graduate University for Advanced Studies

Study on surface photovoltage using time-resolved photoemission

Jan. 15   Prof. I. Arakawa, Gakushuin University

Study on desorbed water cluster ions induced by electronic transitions from adsorbed water on solid rare gases

FY2003

Sept. 24   Prof. H. Namba,, Ritsumeikan University

Present status of Rits SR

Oct. 2   Dr. G. L. Carr, National Synchrotron Light Source, Brookhaven National Laboratory, USA

Characteristics of Far-infrared and THz Synchrotron Radiation at the National Synchrotron Light Source

Nov. 12   Prof. K. Nakagawa, Kobe University

What energy does synchrotron radiation change to a radiant ray?

Feb. 4   Prof. T. Urisu, Department of Vacuum UV Photoscience

SR etching and relativistic theory (Schwinger equation)

Mar. 3   Prof. K. Hayashi, Gifu University

On the photo induced phenomena in amorphous semiconductors